CRANFIELD UNIVERSITY

ROBERT CHRISTIE

# LATERAL JET INTERACTION WITH A SUPERSONIC CROSSFLOW

SCHOOL OF ENGINEERING

MSc by Research
Academic Year: 2009 - 2010

Supervisor: Dr D. G. MacManus
October 2010

CRANFIELD UNIVERSITY

SCHOOL OF ENGINEERING

MSc by Research

Academic Year 2009 - 2010

ROBERT CHRISTIE

# LATERAL JET INTERACTION WITH A SUPERSONIC CROSSFLOW

Supervisor: Dr D. G. MacManus

October 2010

# ABSTRACT

A lateral jet in a supersonic crossflow creates a highly complex three-dimensional flow field which is not easily predicted. The aim of this research was to assess the use of a RANS based CFD method to simulate a lateral jet in supersonic crossflow interaction by comparing the performance of available RANS turbulence models.

Four turbulence models were trialled in increasingly complex configurations; a flat plate, a body of revolution and a body of revolution at incidence. The results of this numerical campaign were compared to existing experimental and numerical data. Overall the Spalart-Allmaras turbulence model provided the best fit to experimental data. The performance of the lateral jet as a reaction control system was assed by calculating the force and moment amplification factors. The predicted flowfield surrounding the interaction was analysed in detail and was shown to predict the accepted shock and vortical structures. The lateral jet interaction flowfield over a body of revolution was shown to be qualitatively the same as that over a flat plate.

An experimental facility was designed and manufactured allowing the study of the lateral jet interaction in Cranfield University's 2 ½" x 2 ½" supersonic windtunnel. The interaction was studied with a freestream Mach number of 1.8, 2.4 & 3.1 and over a range of pressure ratios (50≤PR≤200). Levels of unsteadiness in the interaction were measured using high bandwidth pressure transducers. The level of unsteadiness was quantified by calculating the OASPL of the pressure signal. OASPL was found to increase with increasing levels of PR or MPR and to decrease with increases of Mach number. The levels of unsteadiness found were low with the highest levels found downstream of the jet.

Keywords:
High speed aerodynamics, sonic, underexpanded jet, reaction control system, side jet

# ACKNOWLEDGEMENTS

It would have been impossible to write this thesis without the help and support of those around me. I owe my deepest gratitude to Dr. David MacManus for his guidance and support and for always being available and approachable.

I would like to acknowledge the financial support of the Dstl who funded this research.

I would like to express my gratitude to Dr. Ross Chaplin for his help regarding Gridgen and Cobalt.

Many thanks to Camille Battisti it was a pleasure to collaborate with her during this project.

The experimental work would not have been possible without the expertise of Paul Dancer both in the design and manufacturing stages. I would also like to thank all the technical staff; Jenny Holt, Lynton Banks-Davies and John Thrower for their generous assistance.

I would also like to thank to Dr Les Oswald for his continuous high performance computing support.

Finally I would like thank Ann-Marie for her personal support and great patience at all times and all my family for their love and support throughout the year.

# Table of Contents

# Table of Figures

# Table of Tables

# Nomenclature

## English symbols

| | |
|---|---|
| A | Area |
| $C_D$ | Drag Coefficient |
| $C_f$ | Skin friction coefficient |
| $C_m$ | Pitching moment coefficient |
| $C_N$ | Normal force coefficient |
| $C_p$ | Pressure coefficient |
| $C_{p\ diff}$ | Differential pressure coefficient |
| D | Body diameter |
| D | jet diameter |
| F | Frequency |
| $F_i$ | Interaction force |
| $F_j$ | Jet thrust force |
| $F_s$ | Factor of safety |
| H | Penetration height |
| H | Shape factor |
| $K_F$ | Force amplification factor |
| $K_M$ | Moment amplification factor |
| K | Thermal diffusivity/Turbulent kinetic energy |
| l | Distance from c.g. |
| L | Separation length |
| M | Mach number |
| $M_i$ | Interaction pitching moment |
| $M_j$ | Jet induced pitching moment |
| $\dot{m}$ | mass flow rate |
| N | Window length minus one |
| P | Static pressure |
| $P_0$ | Total pressure |
| $P_b$ | Back pressure |
| $p_{con}$ | Observed level of convergence |
| Pr | Prandtl number |
| $P_w$ | Wall pressure |
| R | Gas constant |
| R | Recovery factor |
| R | Grid refinement ratio |
| Re | Reynolds number |
| S | Area |
| T | Static temperature |
| T0 | Total pressure |
| V | Velocity/Voltage |
| W | Window function |
| Y+ | Non-dimensional wall distance |
| $Y_1$ | First cell distance |

## Greek symbols

| | |
|---|---|
| α | Angle of incidence |
| γ | Gamma ratio of specific heats |
| δ | Boundary layer thickness |
| δ* | Displacement thickness |
| δ3 | Energy thickness |
| ε | Turbulent kinetic energy dissipation |
| θ | Momentum thickness |
| μ | Viscosity |
| ρ | Density |
| ϕ | Circumferential position |

## Subscripts

| | |
|---|---|
| aw | Adiabatic wall |
| 0 | Total |
| 1 | Upstream of shock |
| 2 | Downstream of shock |
| ' | Fluctuating |
| ∞ | Freestream |
| avg | Average |
| b | Back |
| D | Body diameter |
| e | Exit plane |
| e | Effect of boundary layer |
| F | Force |
| fluc | Fluctuating |
| g | Grid refinement level |
| i | Interaction |
| j | jet |
| L | Characteristic length |
| M | Moment |
| p | Pressure |
| r | Reservoir |
| ref | Reference |
| s | Safety |
| s/block | samples pre block |
| sep | Separation |
| tip | Nose tip |
| u | Upstream |
| w | wind axis |
| x | x axis direction |
| y | y axis direction |
| z | z axis direction |

# Acronyms

| | |
|---|---|
| AN | Attachment node |
| aoa | Angle of attack |
| AR | Asymptotic range |
| c.g. | Centre of gravity |
| DLR | German Aerospace Centre |
| GCI | Grid convergence index |
| GSL | Global Separation line |
| ISL | Institute of Saint-Louis |
| JICF | Jet in crossflow |
| MPR | Momentum parameter ratio |
| OASPL | Over all sound pressure level |
| PR | Pressure ratio |
| PRL | Primary reattachment line |
| PSD | Power spectral density |
| RL | Reattachment line |
| SA | Spalart-Allmaras |
| SARC | Spalart-Allmaras with rotation correction |
| SP | Saddle point |
| SPL | Sound pressure level |
| SST | Shear stress transport |
| SW | Shock wave |

# 1 Introduction

The area of lateral jet interaction has been under investigation since the 1950's. The main applications for lateral jets in supersonic crossflow are in the mixing of fuel and air in supersonic air breathing engines and as reaction control jets for missile control. Control systems for future tactical missiles must have a very short response time (0.1ms), be highly manoeuvrable and have significant effectiveness at low dynamic pressure (i.e. low speeds or high altitude) (Champigny and Lacau, 1994). These requirements cannot always be met by conventional control solutions, such as aerodynamic surfaces. Control surfaces are limited in their response time which can range from one tenth to some tenths of a second depending on altitude and in their manoeuvrability at low dynamic pressure (Champigny and Lacau, 1994). To meet these requirements supersonic interceptor missiles (e.g. THAAD missile, Figure 1) generally employ several lateral jets for divert and/or attitude control instead of, or alongside more conventional control solutions (Dennis, 2007). Lateral jets also have the advantage of low drag in straightforward flight.

Figure 1 Terminal High Altitude Area Defence (THAAD) missile system which uses a reaction jet control system (Brown, 2002).

A lateral jet exhausting into a supersonic freestream creates a highly complex three-dimensional flowfield. The flowfield includes shock and vortical structures as well as regions of flow separation and reattachment (Figure 2). The net force and moment generated by a lateral jet is a sum of the jet thrust and the pressure distribution on the airframe due to the complex interaction of the lateral jet with the flowfield. There is a relatively high uncertainty and risk in magnitude of the jet interaction force (Fleeman, 2006). This interaction force does not always augment the jet thrust. In extreme cases the interaction force may be

larger than the jet thrust and act in an opposite sense. In this scenario, known as control reversal the body will move in the opposite to intended direction. Accurate characterisation of the interaction is necessary for autopilot design.

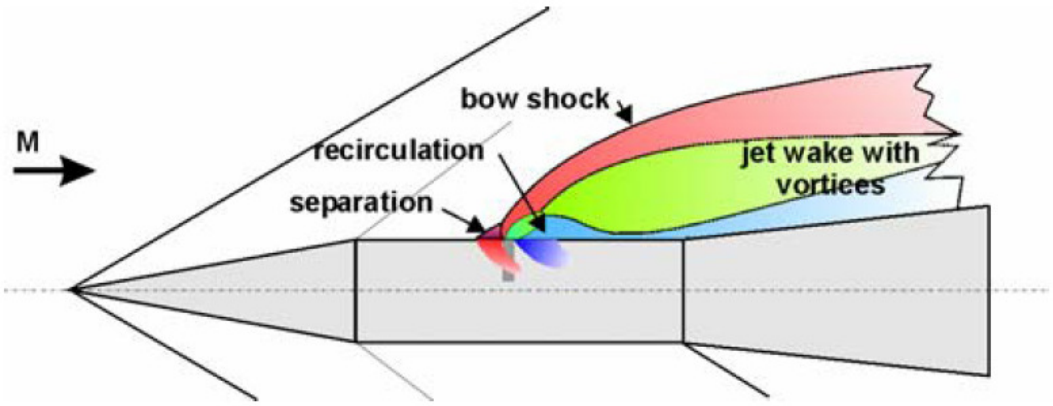


Figure 2 Lateral jet interaction with a supersonic cross-flow (Gnemmi & Schafer 2005).

This project builds upon a previous MSc project. Dessaint (2008) conducted numerical analysis on lateral jets and performed a basic analysis of the interaction. The lateral jet interaction has been investigated extensively both numerically and experimentally in this thesis. Initial numerical investigations were carried out on a flat plate. The flowfield structure of a jet exhausted from a body of revolution is qualitatively the same as that over a flat plate (Dennis, 2007) and is often used in idealised simulations. The numerical studies increased in complexity as they were extended first to a body of revolution and then to a body of revolution at incidence. The numerical method used Reynolds averaged Navier-Stokes based turbulence models. This approach is only valid for flows which have little or no unsteadiness. It is accepted that the lateral jet interaction is inherently unsteady, but as far as the author is aware no quantitative measurement of this unsteadiness has been carried out. The experimental campaign consisted of high bandwidth pressure measurements to capture this unsteadiness.

## *1.1 Aims & Objectives*

### 1.1.1 Research aim

The overall research aim is to assess the use of a RANS based CFD method to simulate a lateral jet in supersonic crossflow interaction by comparing the performance of available RANS turbulence models.

### 1.1.2 Research objectives

To meet the research aim the following objectives were established:

1. Conduct a numerical campaign consisting of simulating the lateral jet in supersonic crossflow interaction over a flat plate, a body of revolution and finally a body of revolution at incidence.
2. Evaluate the ability of RANS based turbulence models to predict the lateral jet in supersonic crossflow interaction
3. Compare the results of this numerical campaign to existing experimental and numerical data.
4. Conduct a detailed flowfield analysis to assess whether the CFD method predicts all the expected flow structures.
5. Investigate the aerodynamics and performance of a lateral jet in a range of configurations.
6. Design and manufacture a system to deliver a sonic jet to the Cranfield University's 2 ½" x 2 ½" supersonic windtunnel.
7. Measure the levels and location of unsteadiness in the lateral jet in supersonic crossflow interaction using Cranfield University's 2 ½" x 2 ½" supersonic windtunnel.

## *1.2 Background*

### 1.2.1 Missile Control

The conventional missile control solutions (tail, canard, wing, thrust vector / reaction jet control) area shown in Figure 3 . A tail configuration can either be cruciform with four surfaces or tri with three and can also integrate some form of forward surface like wings, strakes or canards. Canard control or wing control requires three or more tail surfaces for static stability. There are a number of limitations to the use of conventional missile control. The response time between control input and execution can be slow and the range of incidence may be limited by stall issues (Fleeman, 2006).

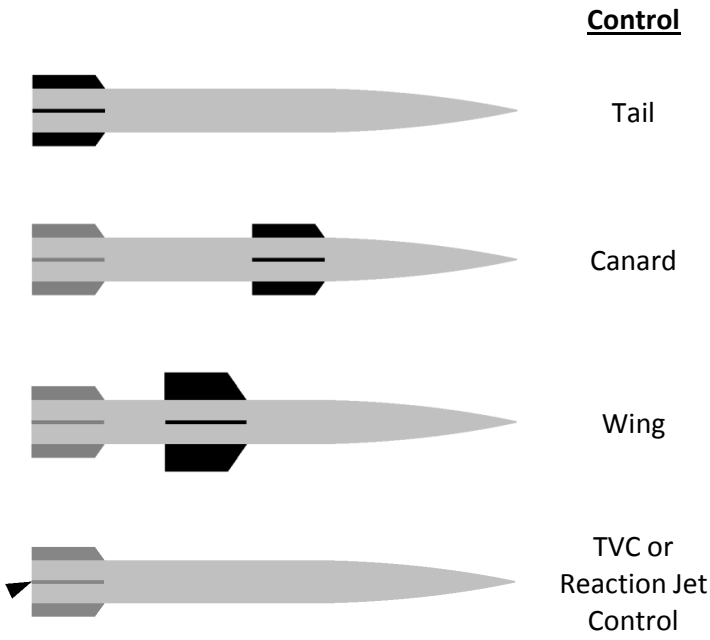


Figure 3 Types of Missile Flight Control

The use of a lateral jet, the subject of this study, is considered an unconventional missile control solution. The use of a lateral jet as a reaction control systems has some advantages over conventional control systems and a few disadvantages. Lateral jets can have a higher response time and when not in use present no obstacle to the freestream lowering drag with respect to a fixed control surface. These higher response times offer increased agility and enhanced maneuverability. The lateral jet also has an advantage over conventional systems in starting phase or at high altitudes as the direct thrust is independent of the outer stagnation pressure. In some designs the lateral jet can only be employed for a short time

due to the high pressure required this allayed with the fact that the performance of lateral jet control and its interaction with the fuselage boundary layer still cannot be predicted with sufficient accuracy. (Stahl et al. 2008)

The lateral jet can be used in two ways as a control system. It can be located at the centre of gravity of the body hence controlling translation only without pitching. Placing the jet away from the centre of gravity allows it to produce a moment be it pitch or yaw much in the same way as a conventional control surface would. These design options are shown in Figure 4.

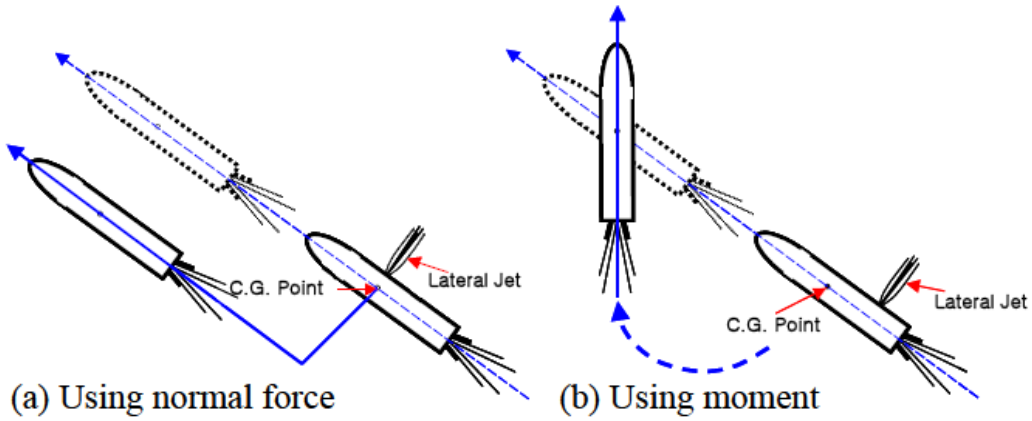


Figure 4 Missile attitude control using lateral jet (Lee, 2004).

### 1.2.2 Evaluating jet interaction design

Attitude control systems are designed to create attitude trim moments and to sustain them over a specified time. Optimally designed control systems utilize the solution which minimizes weight, volume and energy expenditure. For reaction control systems these criteria generally lead to the selection of the configuration needing minimum thrust (Cassel 2003). For rotational control this is achieved by placing the control as far as possible away from the body's centre of gravity, maximizing the moment arm. The mass distribution of the bodies of revolution (ISL and DLR test bodies) studied in this thesis is unknown. It is assumed that the centre of gravity is located at the intersection of the jet nozzle axis with the body of revolution axis. In this configuration the objective of the reaction control system is to control translational movement without rotation.

The efficiency of the jet interaction is commonly assessed using the force and moment amplification factors $K_F$ and $K_M$. $K_F$ is calculated using Equation 1:

$$K_F = \frac{F_i + F_j}{F_j} \qquad \text{Equation 1}$$

Where $F_i$ is the interaction force calculated by subtracting the forces on the body with no jet from the forces on the body with the jet on. $F_{j,}$ the jet thrust force is calculated Equation 2:

$$F_j = S_j\left[\rho_j \cdot V_j^2 + P_J - P_\infty\right] \qquad \text{Equation 2}$$

The moment amplification factor $K_M$ is evaluated using Equation 3:

$$K_M = \frac{M_i + M_j}{M_j} \qquad \text{Equation 3}$$

The moment due to the jet force, $M_j$, is sometimes calculated by multiplying the jet thrust force $F_j$ by $l_j$, where $l_j$ is the distance between the centre of gravity, (c.g.), and the jet nozzle axis (Equation 4).

$$M_j = F_j \cdot l_j \qquad \text{Equation 4}$$

The c.g. for both the ISL and DLR bodies of revolution is unknown. It is assumed that the c.g. is located at the intersection of the jet nozzle exit axis and the body axis. For cases where the jet is located at the body c.g. Equation 4 is modified with the moment arm $l_j$ being replaced by the body diameter, D. This modification leads to Equation 3 becoming Equation 5:

$$K_M = 1 + \frac{M_i}{F_j \cdot D} \qquad \text{Equation 5}$$

The force and moment sign convention is shown Figure 5. The interaction force is taken to act in the opposite direction to the jet thrust force.

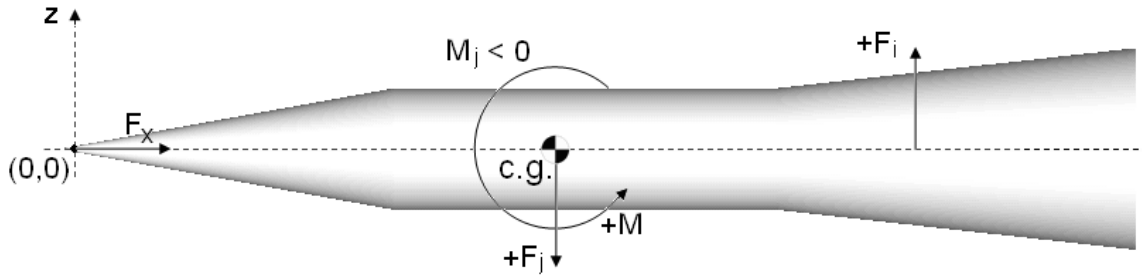


Figure 5 Sign Convention for aerodynamic forces and moments

The coordinate system when the body of revolution is at incidence is shown in Figure 6.

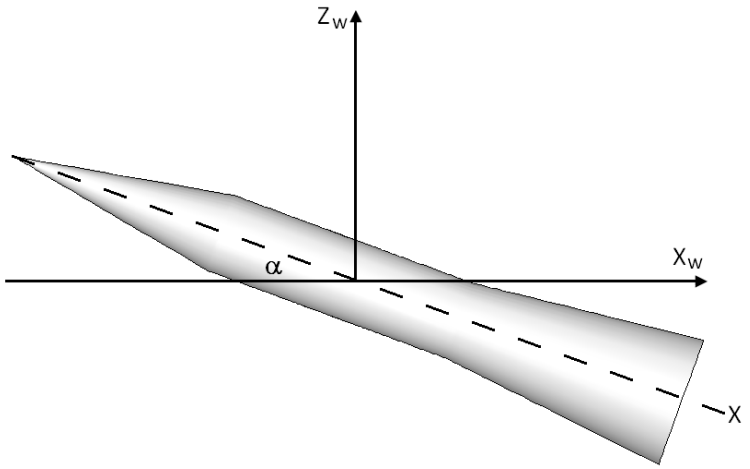


Figure 6 Angle of the body centreline (dashed) relative to wind axes reference frame (solid) for positive angle of attack.

Efficient jet interaction control systems are realized by achieving high positive amplification factors where the interaction force and moment augments the jet thrust force and moment. Typical values for a lateral jet exhausted from a flat plate are given in Figure 7 (Spaid & Cassel, 1973). Aerodynamic interference forces can often be larger than the jet thrust force data, as seen in this data.

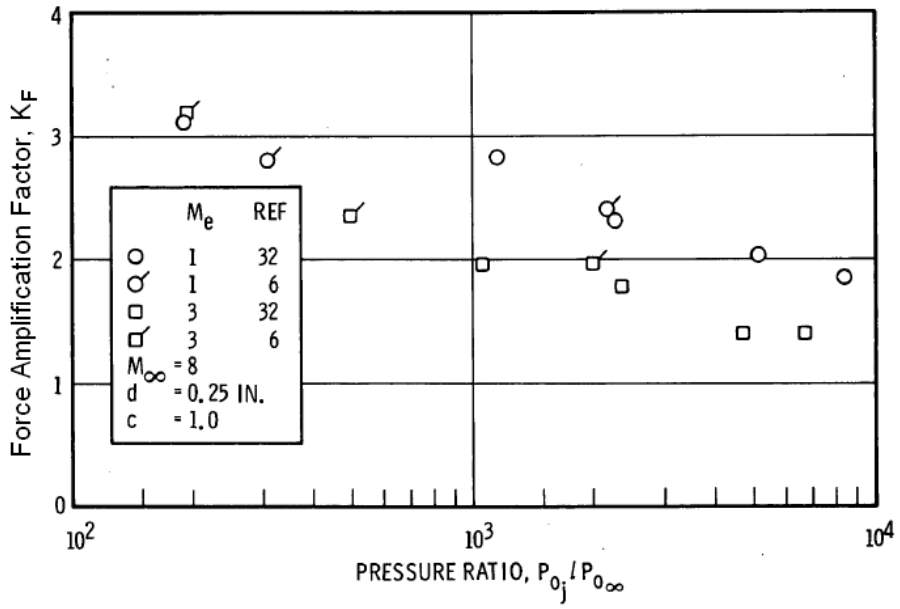


Figure 7 Typical force amplification factors on a flat plate (Spaid & Cassel, 1973).

Seiler et al. (2003) simulated the lateral jet interaction over a body of revolution. The variation of the force and moment amplification factors with changes in freestream pressure and Mach number was calculated (Table 1 &Table 2). The jet was found to be more efficient at positive angles of attack. An increase in Mach number lead to an increase in the force amplification factor however the moment amplification factor dropped. Rising air pressure reduced both the force amplification factor but increased moment amplification factor.

| $M_\infty$ | $P_{0j}/P_{0\infty}$ | $C_D$ | $K_F$ | $K_M$ |
|---|---|---|---|---|
| 3.5 | 0.43 | 0.0959 | 1.11 | 1.53 |
| 4 | 0.34 | 0.0903 | 1.21 | 1.49 |
| 4.5 | 0.27 | 0.0858 | 1.31 | 1.45 |

Table 1 Amplification factor vs. Mach number (Seiler et al. 2003).

| Atmospheric pressure (kPa) | $P_{0j}/P_{0\infty}$ | $C_D$ | $K_F$ | $K_M$ |
|---|---|---|---|---|
| 65 | 0.27 | 0.0858 | 1.31 | 1.45 |
| 70 | 0.25 | 0.0853 | 1.29 | 1.48 |
| 75 | 0.24 | 0.0849 | 1.26 | 1.5 |
| 85 | 0.21 | 0.0841 | 1.22 | 1.57 |

Table 2 Amplification factor vs. air pressure (Seiler et al. 2003).

The performance of a lateral jet acting as a reaction control system on a body of revolution was assessed by calculating force and moment amplification factors. These results are present in §4.4 for a range of configurations.

### 1.2.3 Jet and cross flow interaction

#### 1.2.3.1 Jet flow into a quiescent medium

For choked flow the flow upstream of the throat does not change with changes in static exit pressure ($P_e$) and the mass flow rate remains the same. As the area increases downstream of the nozzle the flow is accelerated and the pressure decreases. A normal shock forms in the duct, which moves downstream if $P_e$ is reduced. By sufficiently reducing $P_e$ the jet exit flow can be made supersonic. Here the static exit pressure ($P_e$) does not necessarily equal the static pressure of the surrounding air, known as the back pressure ($P_b$).

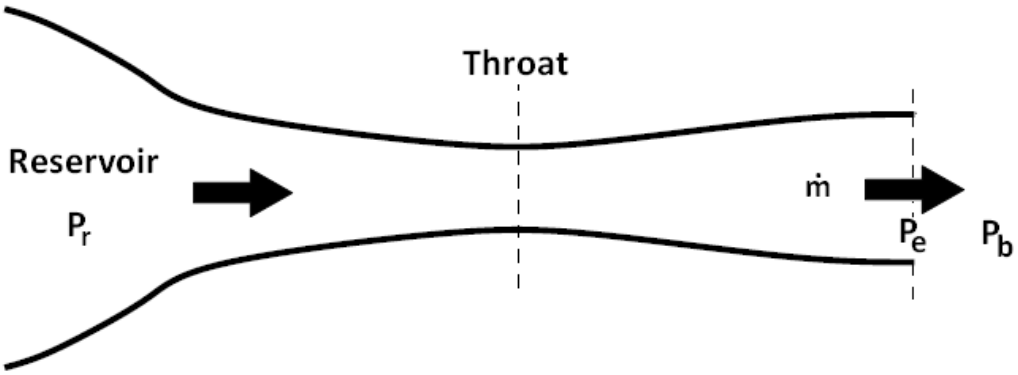


Figure 8 Schematic of a converging-diverging nozzle.

For supersonic jet exit flow there are three possible scenarios; overexpanded, pressure matched and underexpanded nozzle flow. When $P_b > P_e$, the flow must adjust to a higher pressure. This is done through oblique shocks attached to the duct nozzle edges. The streamline at the edge of the jet behaves much like a solid wall, whose turning angle adjusts itself so that the post-shock pressure is equal to $P_b$. When $P_b = P_e$. The duct nozzle flow comes out at the same pressure as the surrounding air, and hence no turning takes place. If $P_b < P_e$. The duct nozzle flow must expand to reach $P_b$, which is done through expansion fans attached to the duct nozzle edges.

In the underexpanded and overexpanded nozzle flows, each initial oblique shock or expansion fan impinges on the opposite edge of the jet, turning the flow away or towards the centerline. The shock or expansion fan reflects off the edge, and propagates back to the other side, repeating the cycle until the jet dissipates though mixing. These flow patterns

are known as shock diamonds, which are often visible in the exhaust of rocket or jet engines. All the lateral jets discussed in this thesis are underexpanded jets.

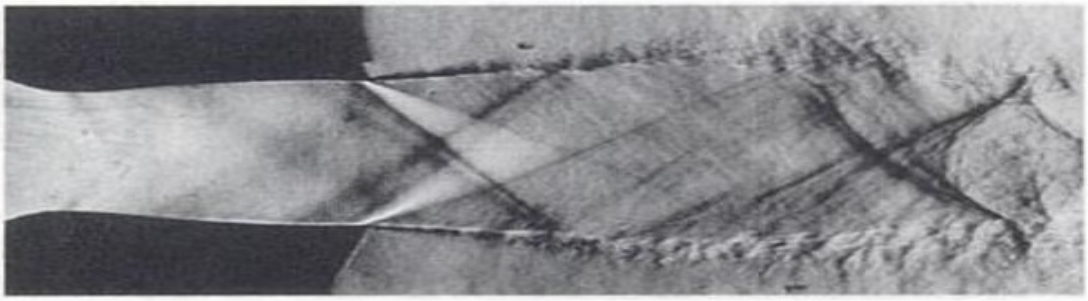

a) Schlieren visualisation of an underexpanded jet, PR=1.5.

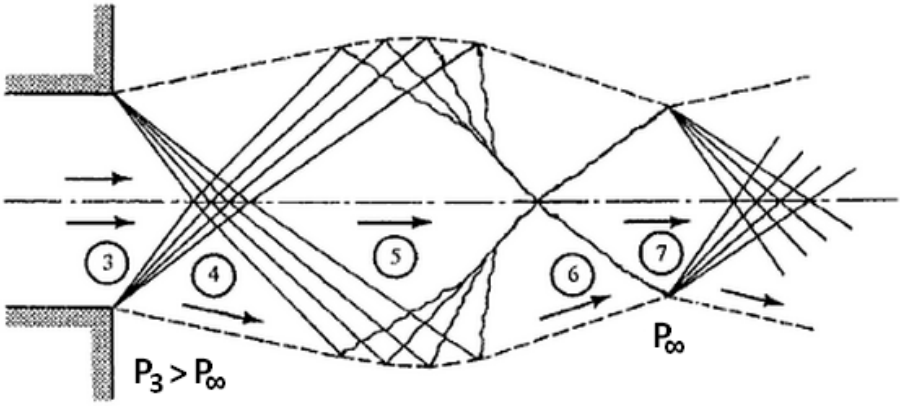


b) Schematic of the underexpanded jet flow structure.

Figure 9 Underexpanded jet (Zucker & Biblarz, 2002).

### 1.2.3.2 Lateral jet in supersonic crossflow

The lateral jet interaction is highly complex 3D flow structure (Figure 10) which is not easily predicted. A two-dimensional representation of the interaction is shown in Figure 11. The lateral jet expands through a Prandtl-Meyer fan at the lip of the orifice into the jet plume which is enclosed in a barrel shock and mach disc. The jet it acts as an obstacle to the flow similar to a bluff body. This obstacle causes a bow shock to form upstream of the jet. The pressure gradient across the bow shock induces separation of the incoming boundary layer, which in turn creates a separation shock. This separated region depends on the Reynolds number and the incoming boundary layer. A reflected shock impinges the surface behind jet causing a secondary shock and the boundary layer to thicken. In area of recirculation behind the barrel shock there is an area of low surface pressure.

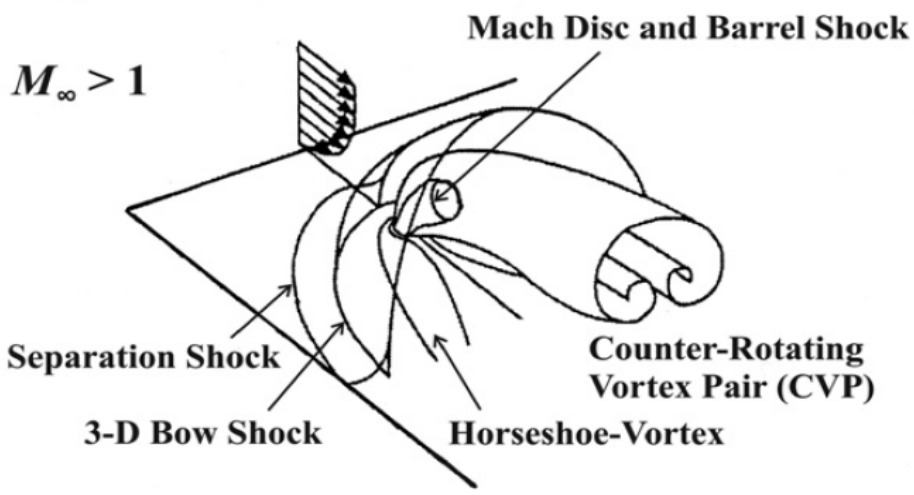


Figure 10 Three-dimensional schematic of the lateral jet in supersonic crossflow interaction (Ben-Yakar et al, 2006).

A pair of counter rotating vortices are created in the upstream separation region. The upstream vortex of this pair is shed sideways and wraps around the interaction forming the horseshoe vortices (Figure 10). Downstream of the jet the flowfield is dominated by vertical structures which enhance jet and freestream mixing.

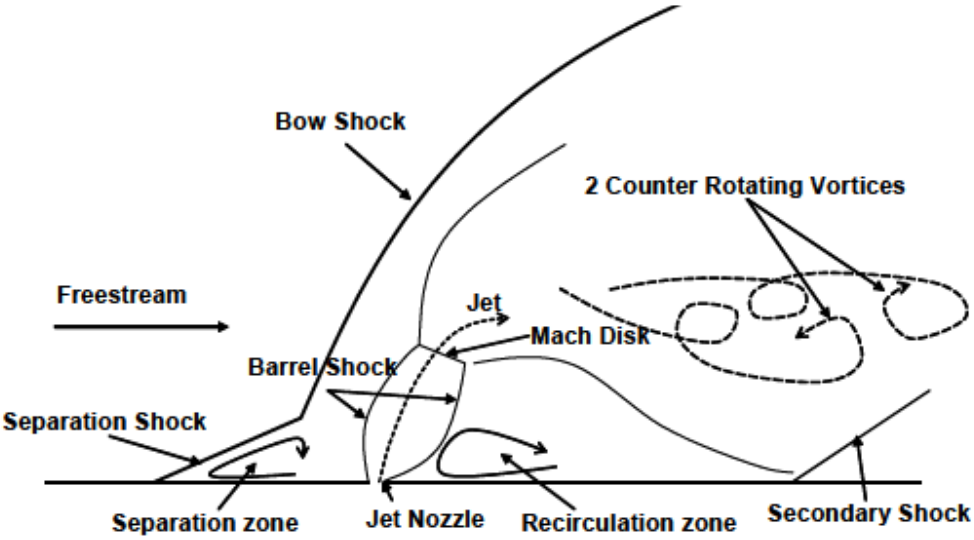


Figure 11 Two-dimensional schematic of the lateral jet in supersonic crossflow interaction (Lee et al., 2004).

The parameter most commonly used to characterise the jet in crossflow interaction is the pressure ratio (PR), defined in Equation 6:

$$PR = \frac{P_{0j}}{P_{\infty}} \qquad \text{Equation 6}$$

Where $P_{0j}$ is the jet total pressure and $P_{\infty}$ is the freestream static pressure.

When the jet and freestream gases differ the momentum parameter ratio (MPR) is a more appropriate parameter to describe the interaction (Equation 7):

$$MPR = \frac{(\gamma \cdot P \cdot A)_j}{(\gamma \cdot P \cdot A)_{\infty}} \qquad \text{Equation 7}$$

In this thesis all jet interactions investigated are air to air interactions and PR is used to characterise that interaction.

### 1.2.4 Unsteady aspects

The unsteady nature of the lateral jet in crossflow interaction has been noted by several authors. For a jet in subsonic crossflow Fric & Roshko (2006) found two sets of vortices that were unsteady in nature (shear layer vortices and wake vortices. Papamoschou and Hubbard (1993) carried out a schlieren visualization of a lateral jet in supersonic crossflow and the flow was found to be highly unsteady. VanLerberghe et al. (1994) visualised the interaction using oil flow visualization, shadowgraphy, planar Mie scattering from ethanol droplets and planar laser induce fluorescence (PLIF) from acetone droplets. The flowfield appeared to be “extremely steady”. Gruber et al. 1995 investigated a sonic jet in a Mach 2 freestream using planar Mie scattering. It was found that the bow shock was unsteady and that the unsteadiness of the bow shock near the jet exit arises from the intermittent nature of the large scale eddies formed on the windward jet side. The oscillation of the bow shock was also noted by Schafer et al. 2001. Despite all this evidence of unsteadiness in the lateral jet in crossflow interaction as far as the author is aware no quantitative measurement of this unsteadiness has been carried out.

## *1.3 Literature Review*

This literature review is not exhaustive as there has been an abundance of lateral jet interaction studies. The literature review has been divided into experimental and numerical studies for ease of reading.

### 1.3.1 Experimental Studies

In 1952 Morkovin et al. investigated the flow and pressure fields generated by a jet in supersonic crossflow. They subjected a supersonic jet to a Mach 1.9 crossflow in the Michigan Supersonic Wind Tunnel. The interaction was studied at various pressure ratios, angle of attacks and with different nozzle geometries. This definition of pressure ratio, the ratio between the total pressure of the jet and the static freestream pressure is regularly used in more modern literature.

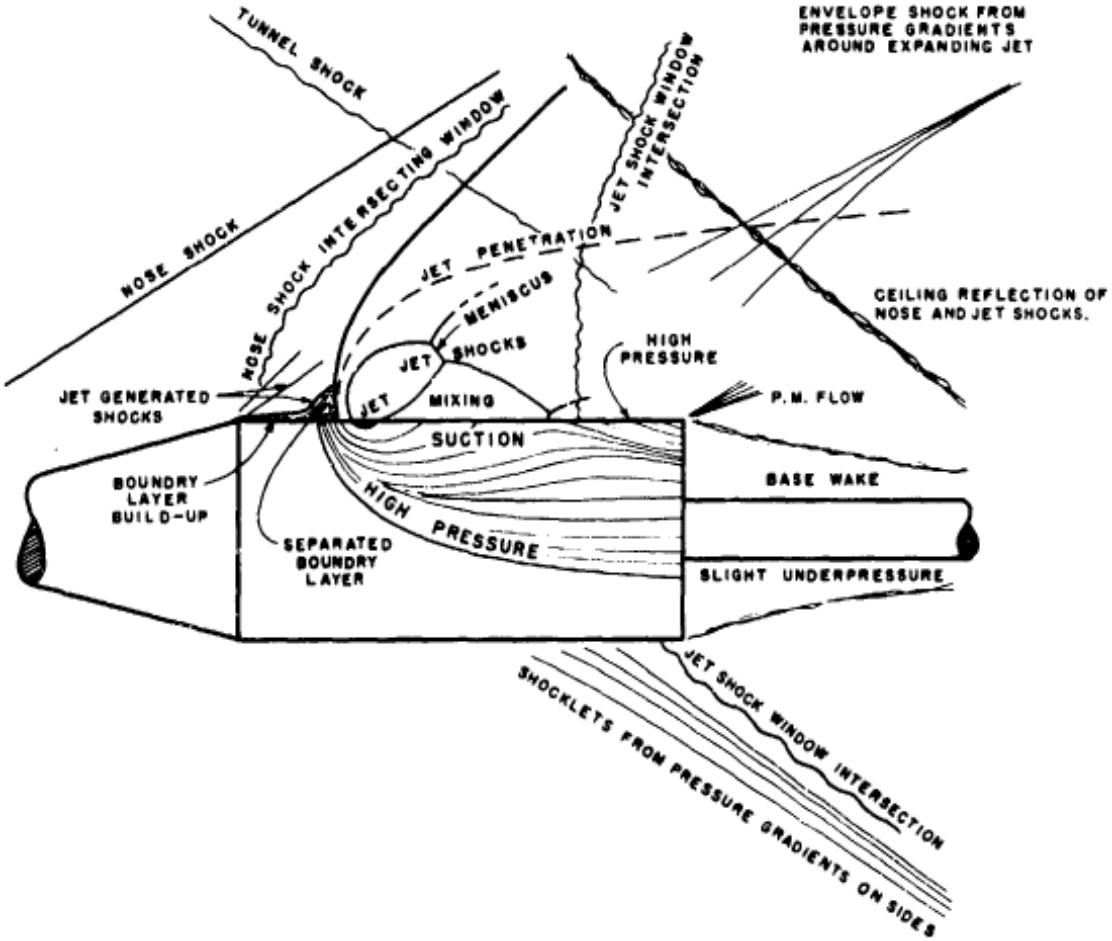


Figure 12 Flow and pressure regions, from flow visualization techniques. (Morkovin, 1952)

Using various flow visualization techniques Morkovin et al. (1952) were able to build up a qualitative picture of the interaction. The bow shock and the associated boundary layer separation in front of it were identified along with the barrel shock and Mach disk. Figure 12 shows their understanding of the flowfield.

A more in depth study was carried out by Cubbison et al. in 1961. They investigated a flat plate and an arrow wing reentry vehicle with a sonic jet near the leading edge. They measured the influence of pressure ratio, freestream Reynolds number and freestream Mach number on the centerline pressure distribution. Their results showed that the pressure ratio had a considerable effect on the pressure distribution while the freestream Mach number had a considerable effect on the pressure level. However the effect of Reynolds number was small in comparison. Schlieren photography was taken to try and explain the 3d flowfield which results in the pressure distribution. The separation of the boundary layer upstream of the interaction was shown in both the Schlieren photography and the pressure distributions, however the recompression system downstream of the interaction was seen only in the pressure distributions. Figure 13 shows a schematic of the near flowfield inferred from the schlieren photography.

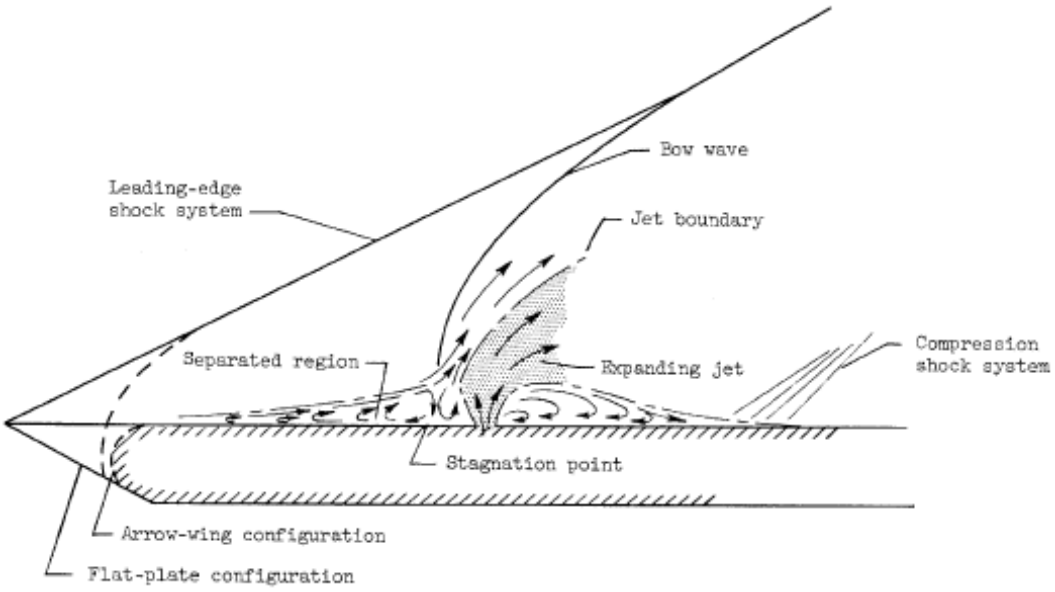


Figure 13 Schematic of the near flowfield (Cubbison et al. 1961)

While carrying out the Schlieren photography Cubbison et al. (2006) noted an oscillation of the bow shock and concluded that this was linked to the unstable characteristics of the boundary layer separation.

The effectiveness of using sonic and supersonic jets for lateral reaction control thrusters was examined by Letko (1963). Various pressure ratios were tested in a Mach 4.5 freestream and coefficients of pressure were reported along the centerline of the interaction. Total force was measured on the test plate and was divided into the thrust force generated by the jet alone and the force from the pressure distribution on the plate caused by the interaction of the jet with the freestream. This was done by calculating the reaction force of an isolated fully expanded jet with mass flow equal to that of the test jet and comparing it to the measured force. From these measurements they then concluded that a supersonic jet was more efficient than a sonic one as a reaction control thruster. They also noted that if it was possible to eliminate the area of low pressure in the region behind the interaction then the efficiency of the reaction could be increased by 12%.

Most experimental work in 1970's and 80's had focused on the effect that various parameters had on the pressure distribution and little progress had been made in understanding the intricacies of the near flowfield since Morkovin et al. (1952) and Cubbison et al. (1961). Fric & Roshko (1994) looked to describe the flow structures resulting from a lateral jet interaction using flow visualization and hot-wire anemometry. Up until this time it was assumed that the flowfield behind a lateral jet bore strong similarities to the flowfield behind a cylinder in crossflow. This assumption had been supported by the finding of periodic fluctuations in the wake similar to those found behind a bluff body. Fric & Roshko (1994), however, concluded that this was not a valid assumption and that there is no analogous shedding of vorticity from the lateral jet interaction. Instead for the first time the boundary layer on the wall from which the jet issues was identified as the source of the vertical structures in the wake of a lateral jet.

Fric & Roshko (1994) identified four distinct types of vertical structure in the lateral jet interaction (Figure 14). The shear layer vortices and the wake vortices were found to be

unsteady while the horseshoe vortices and vortex pair were shown to be essentially steady in nature but may also contain an unsteady component.

The lateral jets studied by Fric and Roshko (1994) were subjected to subsonic crossflow only and the flowfield of a lateral jet subjected to a supersonic flowfield is fundamentally different.

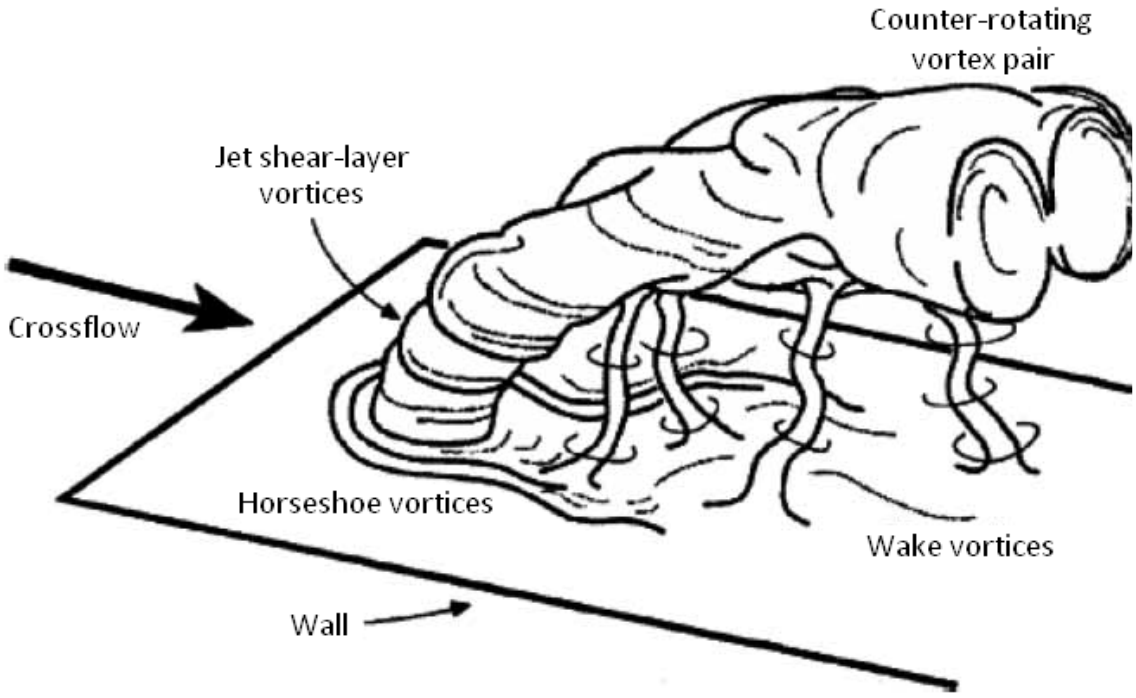


Figure 14 The four types of vertical structure associated with the lateral jet near field (Fric & Roshko 1994)

Papamoschou and Hubbard (1993) looked to answer a question which had not been addressed in previous work, how the relevant flow parameters such as Mach number, pressure ratio, density ratio momentum flux ratio and jet exit Mach number individually affect the penetration height. They defined the penetration height as the maximum height of the jet trajectory based on their schlieren visualizations (Figure 15). It was found that the trajectory reached a maximum height after six jet exit diameters downstream. They concluded that the penetration height was strongly dependent on the momentum flux ratio, weakly dependent on the freestream Mach number and practically independent of pressure ratio, density ratio and jet exit Mach number. The flow was found to be highly unsteady and they noted the need to account for this in computational models.

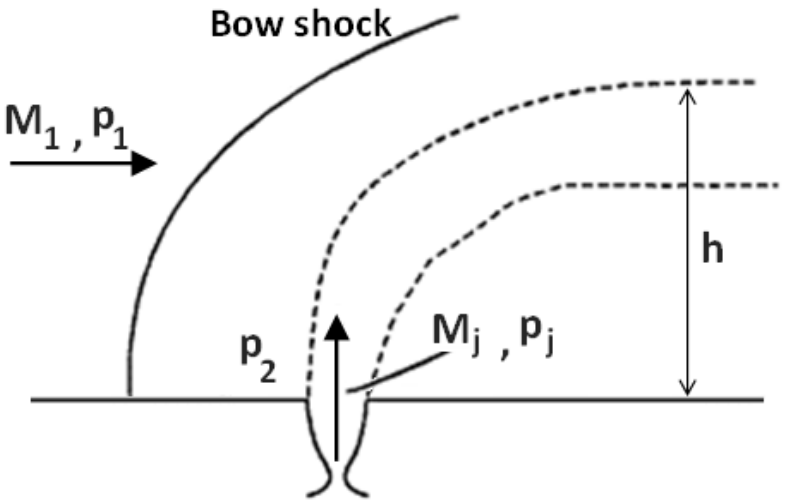


Figure 15 Schematic view of transverse jet and definition of penetration height. Papamoschou et al. (1993)

VanLerberghe et al. (1994) examined the flow structure of the jet in crossflow using oil flow visualization, shadowgraph, planar Mie scattering from ethanol droplets and planar laser induce fluorescence (PLIF) from acetone droplets. The shadowgraph visualization showed that the jet penetration height and hence bow shock strength increased with increasing momentum flux ratio. Repeating the test with helium instead of air but with the same momentum flux ratio yielded the same results showing that molecular weight has no effect. The flowfield appeared to be “extremely steady” and this was at odds with previous work (Papamoschou and Hubbard, 1993) which found substantial unsteadiness.

Primary and secondary separation was shown using oil flow visualization which also revealed a horseshoe vortex. Eddies along the jet-crossflow interface were found using Mie scattering and PLIF. The eddies were shown to be rotating in such a way that the jet fluid was moving faster than the crossflow fluid at their interface. These structures penetrated far into the crossflow.

In the mid nineteen nineties there was a lack of work on mean velocity and turbulence measurements in the lateral jet interaction. This was addressed by McCann & Bowersox (1996) and Santiago & Dutton (1997).

Three-dimensional, compressible turbulence and mean flow measurements were carried out by McCann & Bowersox (1996) across the plume of a low angled supersonic injection into a Mach 2.9 freestream. A kidney shaped Mach number distribution was found in jet plume. This distribution results from vorticity in the plume similar to the counter rotating vortices found by Fric and Roshko (1994) previously discussed. McCann & Bowersox (1996) present several mechanisms which could have been responsible for generating these vortices. Firstly, the induction of rotation by the cossflow wrapping around the jet and causing a lower pressure expansion along its downstream surface. Secondly, the turning of the jet adds energy to the rotation in the same way as the turning of flow in a curved duct. Finally, non-uniform shearing around the edge of the jet would contribute to its rotation. Turbulent kinetic energy measurements found two peak values that were co-located with the centers of the crossflow vortices.

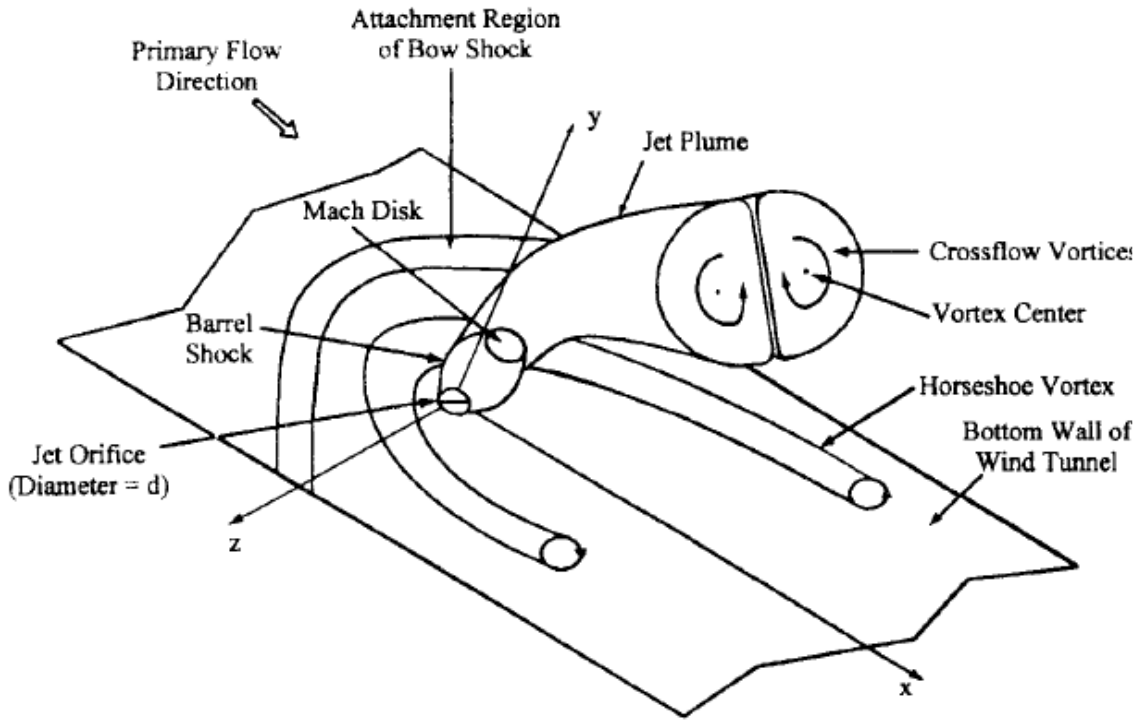


Figure 16 Schematic view of transverse jet flowfield as proposed by Santiago and Dutton (1997).

Santiago and Dutton also carried out work on mean velocity and turbulence measurements with their 1997 paper “Crossflow vortices of a jet injected into a supersonic crossflow”. They showed that the velocity field downstream of the jet interaction was dominated by the counter rotating crossflow vortices. They questioned the application of simple vortex models usually used for subsonic jets to supersonic jet interaction problems because of their highly three-dimensional and compressible nature.

All the literature discussed so far dealt with the lateral jet interaction taking place on an idealized flat plate. Schäfer et al. (2001) studied the interaction of a lateral jet issuing from a generic missile body into a supersonic freestream. The missile body consisted of a cone cylinder flare with the jet orifice located on the cylindrical mid-section. Laser Doppler Velocimetry (LDV) was carried out in the jet centre plane. The LDV system was limited to two component velocity measurements and the time resolution was not small enough to investigate the unsteady aspects of the interaction. Despite this a flow structure consistent with previous work and pressure measurements along the jet centerline was presented.

Stahl et al. (2008) carried out a comprehensive experimental campaign investigating the influence of the relevant parameters in the lateral jet interaction on a body of revolution. A generic missile was used, almost identical to that used by Schäfer et al. (2001). 148 static pressure taps were arranged in four longitudinal lines on the body surface. The effect of angle of incidence, pressure ratio, Reynolds number and multiple circumferential jets on the surface pressure distribution were investigated. As expected, at zero degrees angle of attack increasing the pressure ratio increased the pressure immediately in front of the bow shock however for angle of attacks ≥±5° it had a negligible effect. The upstream and downstream separation lengths were increased with increasing pressure ratio. Reynolds number was found to have a strong influence on upstream separation length. The lower pressure associated with a lower Reynolds number causes the separated region to grow considerably. Adding a second jet at the same axial position but offset circumferentially by 30° increased both the upstream and downstream separation lengths however adding a third had no effect on the downstream pressure distribution.

Stahl et al. (2008) dealt only with cold jets and there was a need for experimental data using hot jets for CFD validation. Stahl et al. (2009) addressed this need. Surface pressure measurements were carried out on a body of revolution, (same geometry as their 2008 paper) from which both hot and cold jets flowed into a supersonic crossflow. Using a hot jet as opposed to a cold one increased the upstream separation area but decreased the downstream separation region. The increase in upstream separation extended circumferentially as well as axially. As the area of high pressure in front of the jet reinforces the jet thrust and the area of low pressure behind the jet decreases the jets efficiency, the efficiency of the hot jet was found to greater than that of the cold jet. This effect was found to become more pronounced with increasing pressure ratio. These conclusions were inferred from the surface pressure distributions; however as no force measurements were made on the body no quantitative statements can be made.

### 1.3.2 Numerical Studies

This section deals with representative example of numerical work carried out on the lateral jet in crossflow interaction. The relevant properties including Mach number, Reynolds number and pressure ratio for each simulation are outlined in Table 3. Margasson (1993) conducted a review into the state of jet in crossflow research. He concluded that numerical simulations of the jet in crossflow interaction were inadequate. Specifically the near jet flowfield and the downstream surface had not been adequately resolved. More refined grids and more appropriate turbulence models were highlighted as two areas of improvement.

Qin and Foster (1995) simulated a supersonic lateral jet exhausting onto a supersonic crossflow. The major features of the interaction were captured including the bow shock, separation shock, horseshoe vortices, the pair of trailing jet vortices and the recompression shock downstream of the jet. Reasonable agreement was found with experimental data.

An assessment of the ability of turbulence models to predict the flowfield surrounding a supersonic jet exhausting into subsonic crossflow was undertaken by Payne (2001). At this time no consensus existed as to which turbulence model was most appropriate for this type of interaction. Often turbulence models were only accurate for certain kinds of flows (e.g. attached boundary layers). Payne (2001) compared the Spalart-Allmaras (SA) model, a low Reynolds number k-ε model and Wilcox's k-ω turbulence model. The SA model compared well to experimental total pressure and vorticity data downstream of the jet but gave poor results in the near jet region. The accuracy of the SA model in predicting total pressure downstream of the jet is illustrated in Figure 17. The converse was true of the other turbulence models. The k-ε and k-ω models performed well in the near jet region but over predicted the vorticity in the jet induced vortex pair as they were transported downstream. This highlighted the fact that because the lateral jet interaction contains flow features which could be reasonable predicted by current turbulence models but that no current RANS based turbulence model could adequately predict the complete flowfield. Payne noted that the degree of unsteadiness in the flowfield warranted further investigation.

| Author | Geometry | $M_\infty$ | $M_j$ | Re $m^{-1}$ | PR | αa | Medium | Turb Model | Experimental Comparison |
|---|---|---|---|---|---|---|---|---|---|
| Qin & Foster (1996) | BoR | 2 | Supersonic | $1.36x10^7$ | 14, 28 | 0, 10, 20 | Air | Baldwin-Lomax | ONERA total pressure dataset |
| Payne (2001) | Flat plate | 0.75 | 2.5 | $4.67x10^6$ | 25.7 | 0 | Air | SA, K-e, K-w | surface static pressure and flowfield total pressure |
| Gnemmi & Schafer (2005) | BoR | 3 | 1 | $3.16x10^7$ | 50, 70, 97 | 0 | Air | k-e/k-w SST | Simultaneous experiment |
| Kovar & Schuelin (2006) | Flat plate | 5 | 1 | $3.78x10^7$ | 100 | 0 | Air | modified SA | Centre-line surface pressure distribution |
| Dennis et al (2007) | BoR | 3 | 1 | $4.85x10^7$ | 5.8 | 0 | Air | SST | surface static pressure and flowfield total pressure |
| Lu & Dickman (2008) | Flat plate | 2 - 4.5 | 1.15 | $6.56x10^6$ | 5 - 2000 | 0 | Air | k-kl | - |
| Viti (2009) | Flat plate | 4 | 1 | $1.26x10^7$ | 532 | 0 | Air | k-w | - |

Table 3 Summary of numerical simulation properties

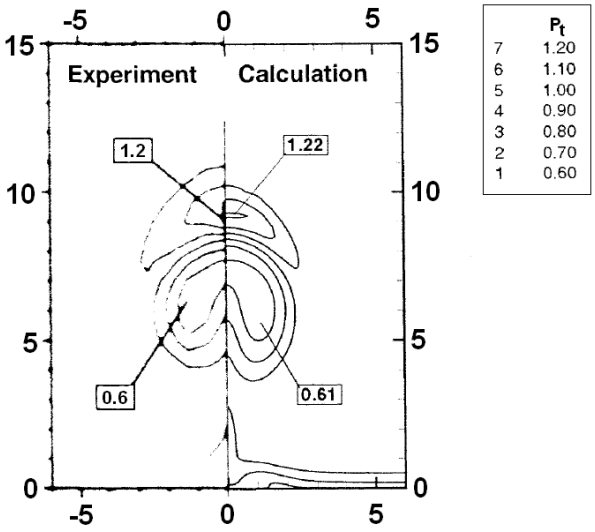


Figure 17 Comparison of experimental data with data predicted using the SA turbulence model. Contours of $P_t$ x$10^{-5}$ on a cross flow plane at x/d=10 downstream of the jet. (Payne 2001)

Gnemmi and Schäfer (2005) used Menter's (1994) shear stress transport turbulence model to simulate the flowfield around a sonic jet exhausted from a body of revolution into a Mach 3 freestream. The numerical model was validated using experimentally measured pressure distributions. The confidence in the predicted results was such that a study of the forces and moments on the body of revolution could be carried out. This allowed a study of the jet efficiency to be carried out. The numerical model was only validated using pressure distributions along the body symmetry plane and around the circumference of the body at the jet location. The forces and moments on the body are a result of the pressure distribution on the whole body. Further experimental work including force and moment measurements are necessary to validate the numerical model if it is to be used in this way. That being said the method shows promise as a design tool.

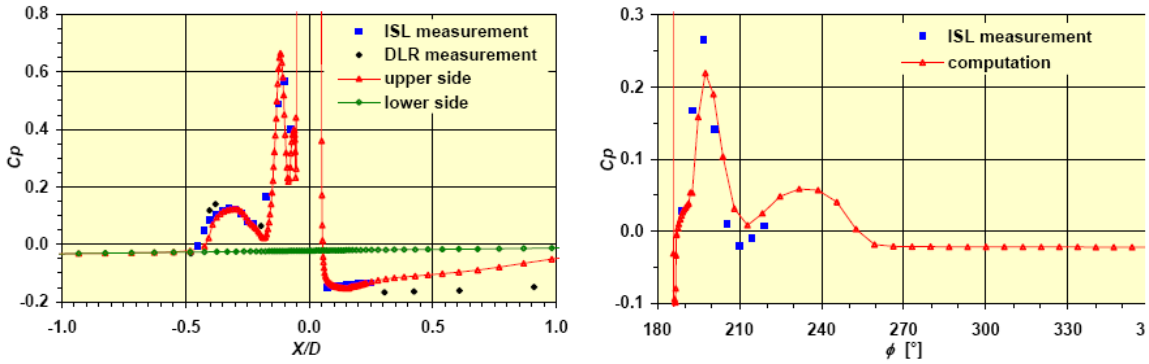


a) longitudinal direction b) circumferential direction

Figure 18 Measured and computed pressure coefficient on the body of revolution surface, PR=50, α=0˚, Gnemmi and Schäfer (2005).

A modified SA turbulence model was used by Kovar and Schuelin (2006) to investigate the lateral jet exhausting from a flat plate into a supersonic crossflow. The test matrix consisted of a single jet in crossflow, four jets in line and four jets side by side. The numerical model was compared to experimental data consisting of normalised pressure distributions both longitudinal and lateral at several axial stations. A fair agreement was found in the overall pressure distribution. However the size of the upstream separation zone was over predicted. It was concluded that this discrepancy was a result of the inadequate prediction of properties in the inner boundary layer. This was assumed to be the source of any discrepancies in the pressure distribution in the general flow field.

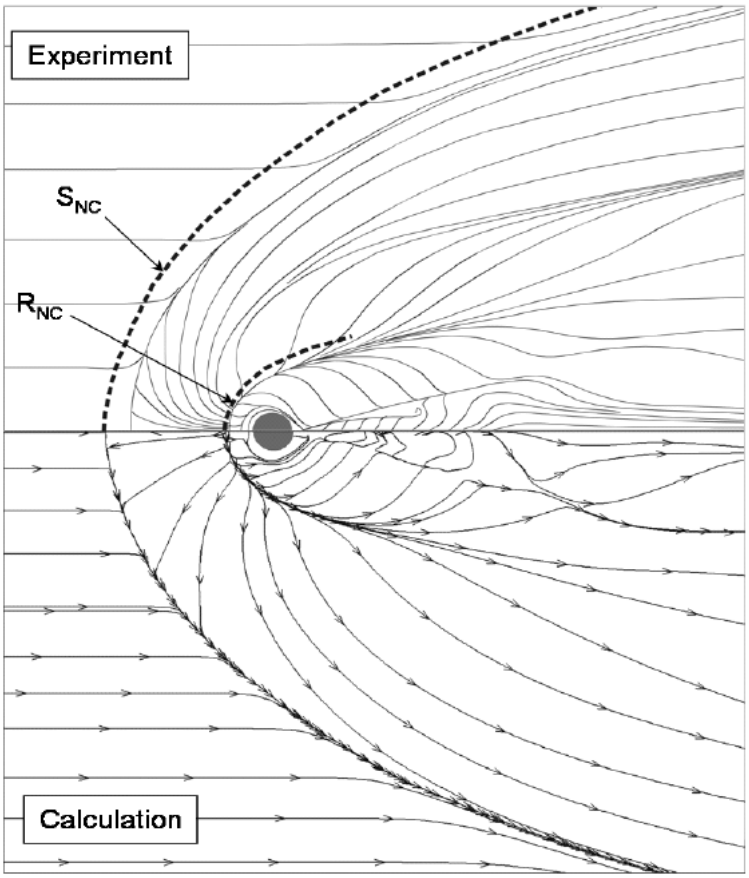


Figure 19 Representation of experimental (upper part) and numerical (lower part) wall streamline patterns for a single jet case. $S_{NC}$ and $R_{NC}$ denote numerical separation and reattachment linesfor comnparison (Kovar and Schuelin, 2006).

Dennis et al. (2007) used Menter's SST turbulence model when investigating the flowfield around a sonic jet issued from a body of revolution into a Mach 3 freestream. The pressure field and the interaction of the sonic jet with the freestream compared well to experimental data. Predicted surface pressures were compared to surface pressures measured using pressure sensitive paint and found to be in good agreement. However the horseshoe vortices could not be distinguished in the computed contours. The discrepancies between predicted and measured flow features were blamed on to inadequate grid refinement and the turbulence model employed.

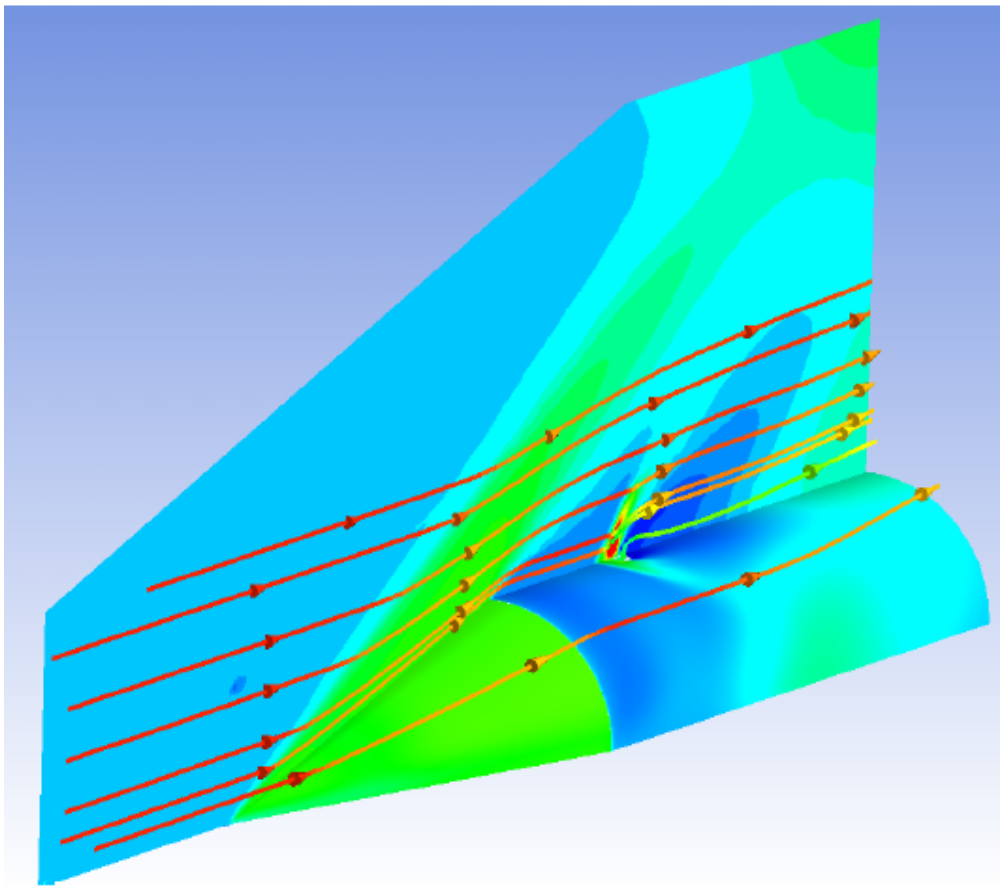

Figure 20 Computed pressure contours on symmetry plane and body of revolution with streamlines (Dennis at al 2007)

Lu and Dickman (2008) performed a detailed study of the flow field surrounding a supersonic jet issued from a flat plate into a supersonic freestream. Using the *k-kl* turbulence model (Smith, 1990) the surface topology was revealed using skin friction lines. Over a large range of pressure ratios (5≤PR≤2000) the upstream surface topology stayed the same but further spread out. Downstream of the jet the surface topology changed distinct differences were found as the pressure ratio increased (the rear pair of saddle points is pushed further downstream and an attachment node is observed). The main vortical structures present in the interaction were then investigated using streamlines. The results of this study agreed well with the accepted lateral jet in crossflow model. In addition to the accepted vortical structures a secondary horseshoe vortex and a pair of horn vortices just downstream of the orifice which were both engulfed by the jet vortices were found.

In 2009 Viti et al. also conducted an investigation into the flowfield surrounding a supersonic jet in crossflow. Unlike Lu and Dickman (2008) who used the *k-kl* turbulence model Viti et al. (2009) used Wilcox's (1998) k-ω turbulence model. Three primary shock formations were observed: a barrel shock, a bow shock, and a separation-induced shock wave. Six primary vortices were identified: the horseshoe vortex, an upper trailing vortex, two trailing vortices formed in the separation region and, aft of the bow shock wave, two more trailing vortices that eventually merge together into one single rotational motion.

# 2 Experimental methodology

The lateral jet interaction was investigated in a supersonic wind tunnel. Time averaged and high bandwidth pressure measurements were carried out. This chapter provides a description of all the relevant experimental apparatus and techniques used in the experimental campaign.

## *2.1 Experimental apparatus*

### 2.1.1 Wind tunnel

#### 2.1.1.1 Wind tunnel description

Cranfield University's 2 ½" x 2 ½" supersonic wind tunnel () is of a suck down, open return design. The settling chamber is open to the atmosphere and the diffuser is connected to a 40m$^3$ vacuum tank. Two valves isolate the test section from the vacuum tank a quick release valve and an adjustable valve which can be used to set transonic mach numbers. The settling chamber is open to the School of Engineering hangar. Before entering the settling chamber air passes through an alumina drying bed. There is a contraction of 144:1 from the settling chamber to the test section.

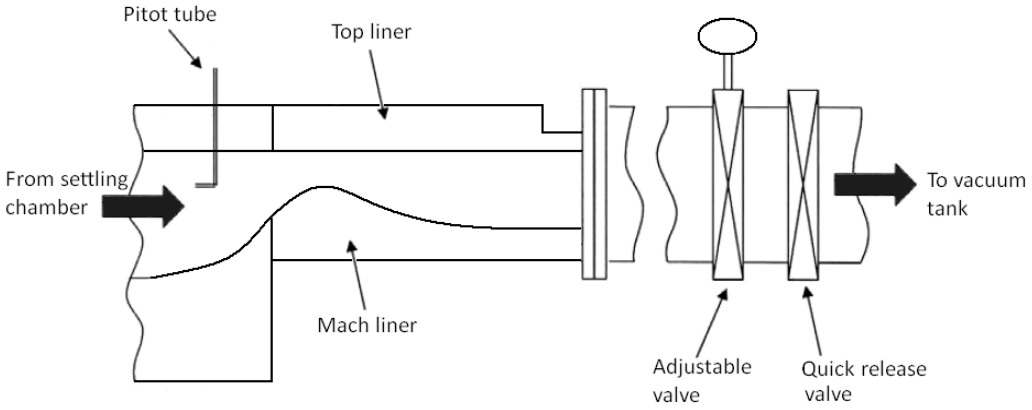


Figure 21 Schematic of the 2 ½" x 2 ½" supersonic wind tunnel

Liners can be fitted to the top and bottom of the test section. For supersonic tests a "Mach liner" is fixed in the bottom of the test section. The Mach liner creates a contraction which accelerates the subsonic air from the test section to Mach 1 at its throat and then an expanding section which acts as a supersonic nozzle accelerating the flow to a set Mach number. The Mach number in the test section is set by the geometry Mach liner. Using

different Mach liners a Mach numbers from 1.8 to 3.2 can be achieved (with corresponding unit Reynolds numbers of $1.14 \times 10^7$ to $7.14 \times 10^6$).

### 2.1.1.2 Mach number measurement

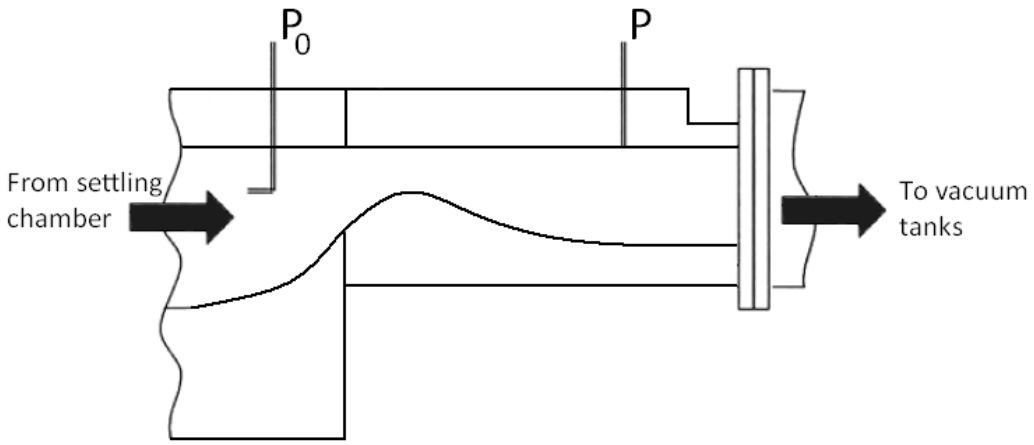


Figure 22 Schematic of the Mach number measurement setup in the 2 ½" x 2 ½" supersonic wind tunnel

Total pressure and static pressure are measured in the settling chamber and test section respectively. Doran (2006) measured the difference in total pressure between the settling chamber and test section and found the difference to be negligible. It is therefore assumed that total pressure in the test section equals that in the test section. The Mach number in the test section can then be calculated from the isentropic pressure relationship Equation 8.

$$\frac{P_{t1}}{P_1} = \left(1 + \frac{\gamma - 1}{2} M_1^2\right)^{\frac{\gamma}{\gamma - 1}} \qquad \text{Equation 8}$$

### 2.1.1.3 Background noise assessment

Before aerodynamic testing began an investigation was undertaken to identify electrical noise within the measurement chain. This was carried out by acquiring pressure data but with both the tunnel and the jet off. This effectively measured the ambient, still background noise and electrical noise levels. Figure 23 shows the FFT for this case. At low frequencies the signal is dominated by pressure peaks at multiples of 50Hz. This indicates electrical interference from the mains which runs at 50Hz and its harmonics. However the amplitude of these peaks is below the nominal resolution of the system (9.2Pa). Efforts to identify the sources of electrical noise were made by turning off and isolating from the power supply any electrical items in the vicinity. This made no difference except that a frequency peak at 32.5KHz (not shown here) was removed by replacing a CRT monitor with an LCD monitor.

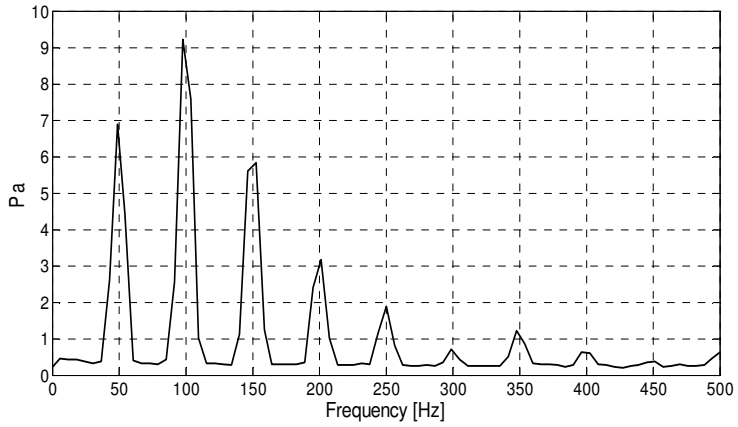


Figure 23 FFT of acquired signal, jet off, tunnel off.

The background noise of the tunnel working section under supersonic flow conditions was evaluated by acquiring pressure data with the tunnel on but the jet off. The FFT of this case is shown in **Error! Reference source not found.** An increase in the amplitude of frequencies from 0 to 1500Hz can be seen but these values are small and are mostly below the nominal resolution of the system and are dominated by electrical noise.

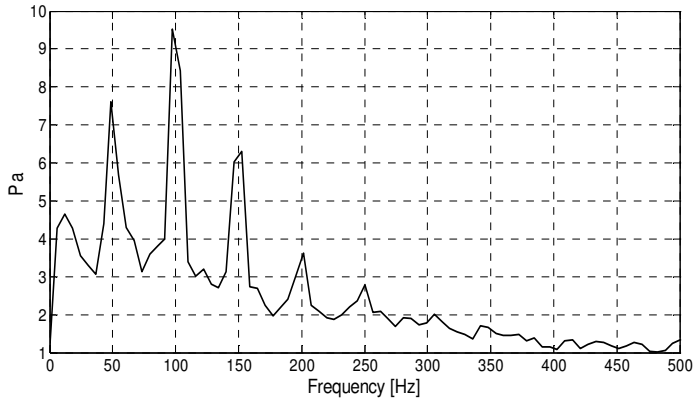


Figure 24 FFT of acquired signal, jet off, tunnel on.

The influence of filters and the sampling rates were also investigated and these results are presented in Appendices A and B respectively. Increasing the sampling rate made little difference to the signal. The OASPL stayed the same, however some peaks were removed specifically at 35kHz and around 43kHz. However the focus of the investigation was on frequencies of a couple of hundred to a few thousand hertz and it did not affect the OASPL it made no significant difference. Filtering removed some spectral content. This was probably due to aliasing of higher frequency content which was removed by the filters.
The OASPL was reduced from 131.71 to 121 84 by filtering.

### 2.1.2 Instrumentation

#### 2.1.2.1 Data acquisition system

The voltage output from the micro-Kulite transducers was amplified using a Fylde M14DS amplifier with a gain of 20 and then passed through a Fylde 301 SF low pass filter with a nominal cut-off frequency of 50kHz before being acquired by National Instruments USB-6295 DAQ card (Figure 25). LABVIEW, a virtual instrumentation workbench, was used to control the sampling rate and number of samples recorded. These values along with freestream total temperature and pressure and plenum total pressure were then written to a delimited text file. A screenshot of the Labview program front end is shown in Appendix C. In all cases $2^{18}$ (262144) samples were recorded at a rate of 100kHz.

The USB-6295 is a 16 bit DAQ card and was measuring a voltage range of 20V (±10V). This means the voltage resolution equates to 0.305mV (Equation 9) or roughly 9Pa when converted into pressure (Table 1).

$$\frac{V_{range}}{2^{16}} = V_{resolution} \qquad \text{Equation 9}$$

| Kulite # | 1 | 2 | 3 | 4 | 5 |
|---|---|---|---|---|---|
| Calibration constant | 30767 | 30938 | 30114 | -30815 | -30712 |
| Pressure resolution | 9.4Pa | 9.4Pa | 9.2Pa | 9.4Pa | 9.4Pa |

Table 4 Pressure resolution for each micro-Kulite pressure transducer.

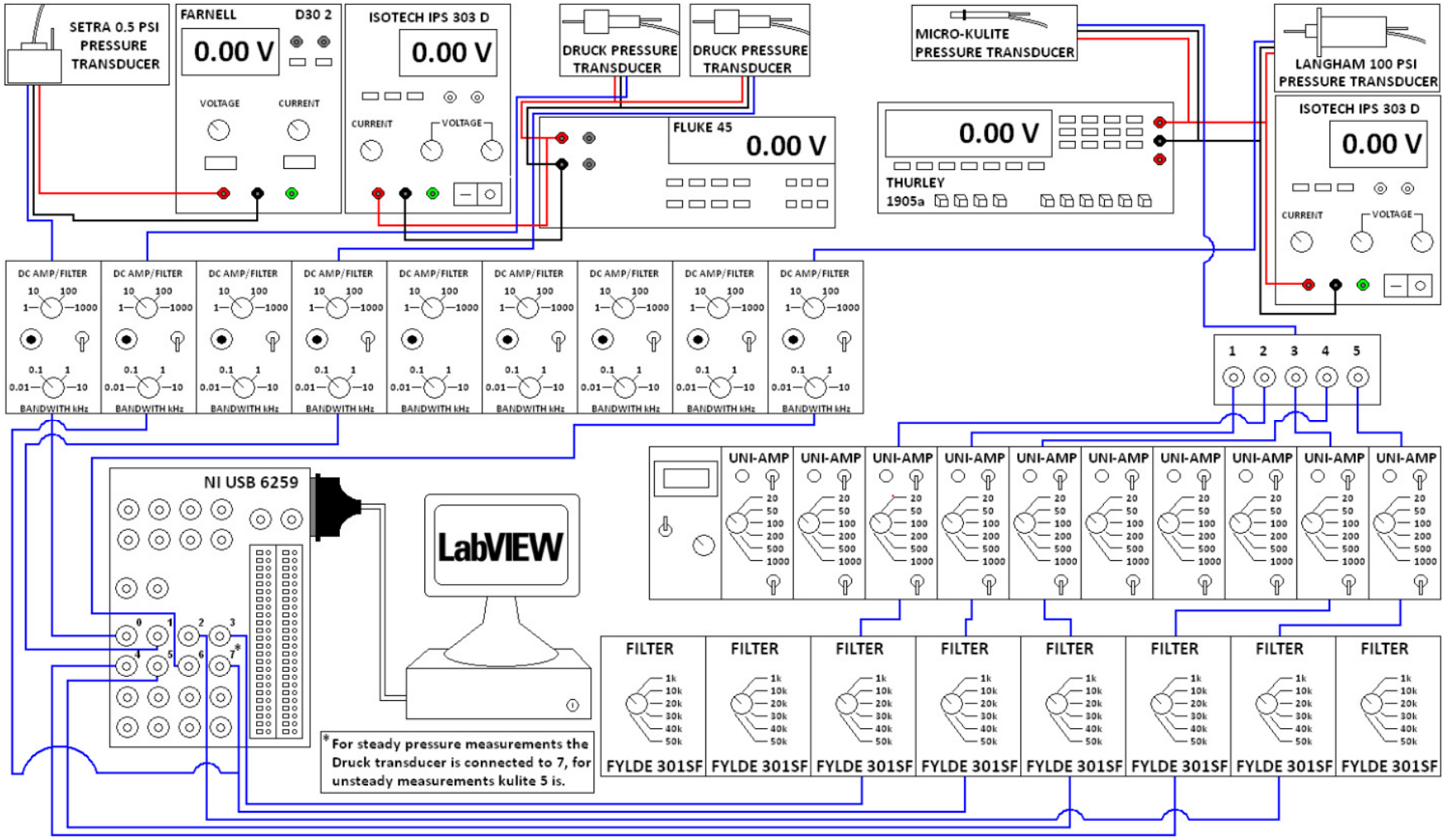


Figure 25 Schematic of the data acquisition system.

### 2.1.2.2 Uncertainty analysis

The uncertainties in the presented measurements are comprised of a combination of sources including the model location, pressure transducers, random errors, data acquisition system. These sources of error have been assessed and total uncertainties calculated using the method by Taylor (1997). Full details of the uncertainty analysis are presented in Appendix D, the results of which are summarized below.

The uncertainty in Mach number and coefficient of pressure ($C_p$) were found to be ±0.02 ±0.01 respectively. Uncertainty in pressure ratio measurement varied with pressure ratio and freestream Mach number from ±0.5 (PR=50, M=2.4) to ±9 (PR=200, M=3.1), (Table 5). Uncertainty in OASPL varied slightly between the high bandwidth pressure transducers due to them having slightly different calibration constants. These results are presented in Table 6.

| | M=2.4 | M=3.2 |
|---|---|---|
| PR | ±PR | ±PR |
| 200 | 1.6 | 9.0 |
| 150 | 1.2 | 6.8 |
| 110 | 0.9 | 5.1 |
| 97 | 0.8 | 4.5 |
| 70 | 0.6 | 3.3 |
| 55 | 0.5 | 2.6 |
| 50 | 0.5 | 2.4 |

Table 5 Uncertainty in pressure ratio

| Kulite | Quoted uncertainty | Data acquisition card uncertainty | Uncertainty from repeatability study | Total uncertainty |
|---|---|---|---|---|
| 1 | ±0.13 dB | ±6.27E-03 dB | ±0.29 dB | ±0.32 dB |
| 2 | ±0.13 dB | ±6.31E-03 dB | ±0.20 dB | ±0.24 dB |
| 3 | ±0.13 dB | ±6.14E-03 dB | ±0.58 dB | ±0.59 dB |
| 5 | ±0.13 dB | ±6.26E-03 dB | ±0.27 dB | ±0.30 dB |

Table 6 Total uncertainties for the high bandwidth pressure transducers.

### 2.1.3 Schlieren visualization

Schlieren visualisation is an optical system which allows the visualisation of inhomogeneous media. Light travelling through homogenous media travels uniformly, however light rays travelling through an inhomogeneous media are deflected proportional to the gradient of refractive index in that media. The refractive index of a gas depends upon its temperature, density and composition. This allows the visualisation of flow features in a compressible flowfield due to density gradients. Features such as shockwaves and boundary layers can be visualised, for example Figure 26 shows a schlieren visualisation of flow over a body of revolution with a jet of air issuing into the freestream.

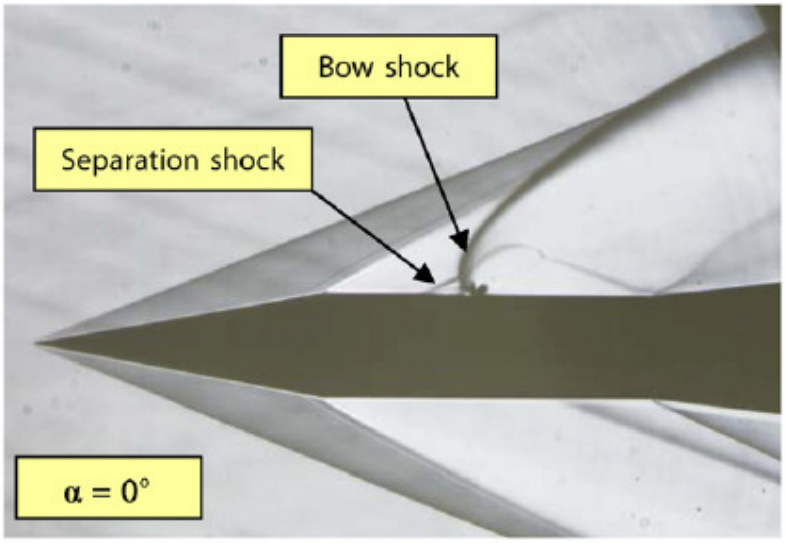


Figure 26 Schlieren Visualisation of flow over a body of revolution with a lateral jet injected into the crossflow (Stahl et al. 2008)

The most common schlieren set up is the z-type two mirror schlieren system (Settles 2001). This consists of a light source which shines on a parabolic mirror which reflects the parallel light rays through the test section. Density or temperature gradients in the flow in the test section cause gradients of refractive index which deflect the light rays. These light rays then fall on another parabolic mirror which focuses the image onto the knife edge. The purpose of the knife edge is to block part of the image which has the result of selecting only horizontal or vertical gradients

(depending on the orientation of the knife edge). A lens then focuses the image onto a CCD camera which captures the image.

The schlieren set up in 2 ½ " x 2 ½ " wind tunnel in Cranfield University is of the z-type two mirror type however it goes further than the system described above in that it uses a high speed CCD camera (Photron APX) to capture the temporal evolution of the flow. This system is shown in Figure 27. This high speed camera can capture images at up to 120,000 frames per second, though this is limited by the resolution of the image being captured. This limitation is due to the time limit on processing images between taking frames, the higher the resolution of the image the longer it takes to process slowing the frame rate. A summary of the high speed cameras capabilities is shown in Table 7.

.

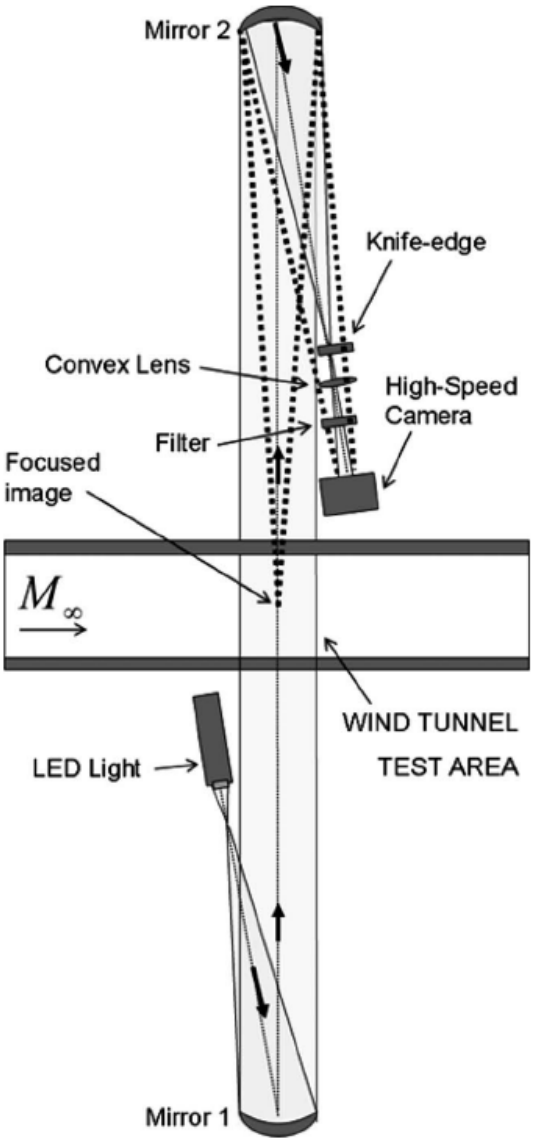


Figure 27 Schlieren set up in Cranfield University (Estruch et al. 2008)

| Frames per second | Max. Resolution |
|---|---|
| 1000 | 1024x1024 |
| 2000 | 1024x768 |
| 3000 | 512x1024 |
| 4000 | 1024x512 |
| 6000 | 512x512 |
| 8000 | 1024x256 |
| 10000 | 512x256 |

Table 7 Capabilities of the Photron APX high speed camera

## *2.2 Experimental Design*

### 2.2.1 Scaling of the experiment

The main constraint in the design stage of the experiment was the size of the wind tunnel test section. The experiment had to be scaled to minimize the interference effect of the test section walls. This required the extents of the jet interaction to be estimated. The penetration height and jet trajectory were estimated using a method outlined in Portz & Segal 2006. Penetration height is a function of nozzle diameter. The experiment also had to be scaled so that the horseshoe vortices would not impact the test section side walls and alter the flowfield downstream of the nozzle. The lateral spread of the horseshoe vortices is a function of the pressure ratio. A nozzle of diameter 1.5mm was selected due to these constraints based on a parametric study of other experiments/simulations and a CFD prediction of the experiment.

The plenum contraction was initially designed using a fourth-order polynomial from wind tunnel contraction section guidelines. However this resulted in not being able to place pressure sensors close to the jet nozzle. The plenum wall was machined to the minimum wall thickness allowed to allow pressure transducers to be placed as close as possible to the nozzle.

### 2.2.2 Jet delivery system

Compressed air from the School of Engineering compressed airline is passed though a Sealey in-line water trap/filter to a PRG501 precision pressure regulator. A plenum with an internal diameter of 30mm is connected to the outflow port of the pressure regulator. The pressure regulator is used to set the total pressure in the plenum. The plenum has four static pressure ports equally spaced around its circumference. The Mach number in the plenum is low enough due to a low mass flow rate that static pressure can be assumed equal to total pressure. Total temperature can be measured in the plenum by inserting an insertion thermocouple through a compression fitting. When not in use this port is sealed with compressed PTFE tape. The plenum has a converging section which accelerates the flow to Mach 1 at its 1.5mm diameter exit (Figure 28). A lug on the outside of the converging section is used to connect the plenum to a plate which fits into the top liner of the tunnel. An aluminum support rail spans and is clamped to the top of the wind tunnel. The plenum is fixed to this rail by a bolt through a support lug on its side (Figure 29).

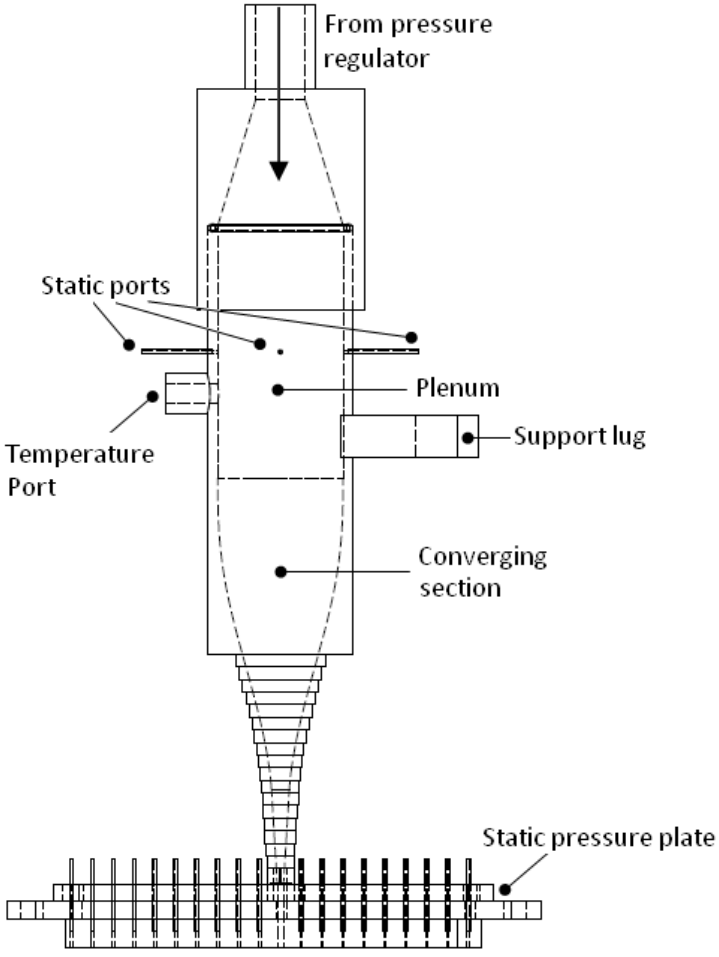


Figure 28 Schematic of the jet plenum and it's converging section

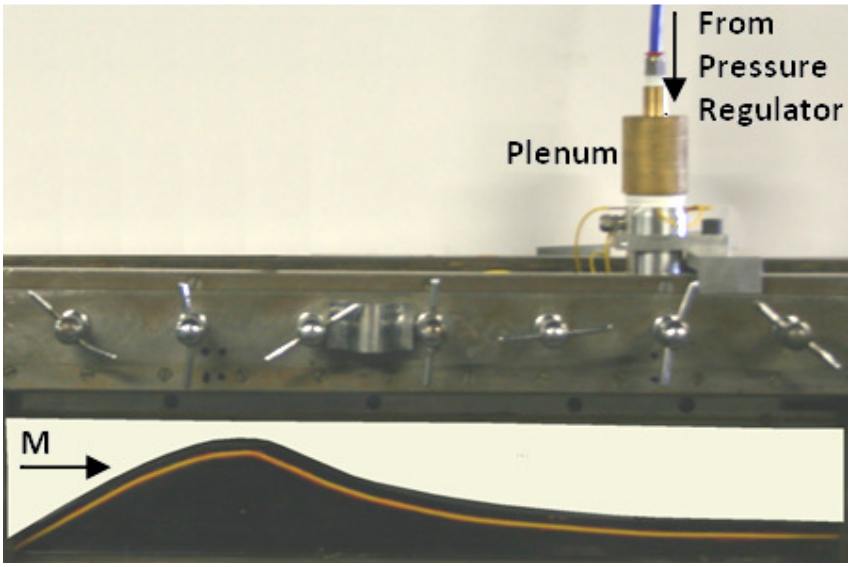


Figure 29 Jet delivery system assembled in the 2 ½" x 2 ½" supersonic wind tunnel.

### 2.2.3 Liner inserts

A lug on the end of the plenum converging section fits one of two liner inserts; a pressure tapping insert and a micro-Kulite retention insert Figure 30. The bottom surface of the inserts (shaded in Figure 30) fits flush to test section ceiling and allows a time-averaged pressure survey using the pressure tapping insert or high bandwidth pressure measurements using the micro-Kulite retention insert to be made along the jet interaction centerline.

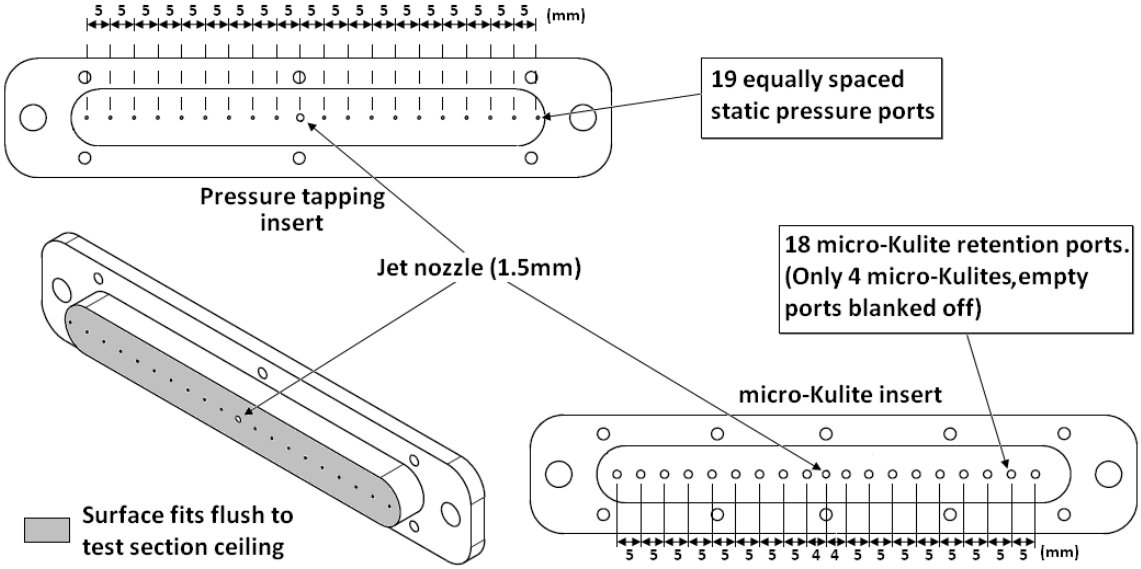


Figure 30 Liner inserts. Top left: Static pressure tapping plate. Bottom right: Micro-Kulite retention plate.

## *2.3 Oil flow visualization*

Photography

To allow repeatable oil flow photographs to be taken a formal procedure was set up. The bottom liner was removed and a mirror placed at an angle in the tunnel section (Figure 31). The position of this mirror was marked on the test section floor, so it could be placed in the same position at the same angle repeatedly. The camera was setup on a tripod and fixed so that it could not move. The position of the tripod legs were then marked on the floor. The same settings on the Canon EOS 300D camera were used each time.

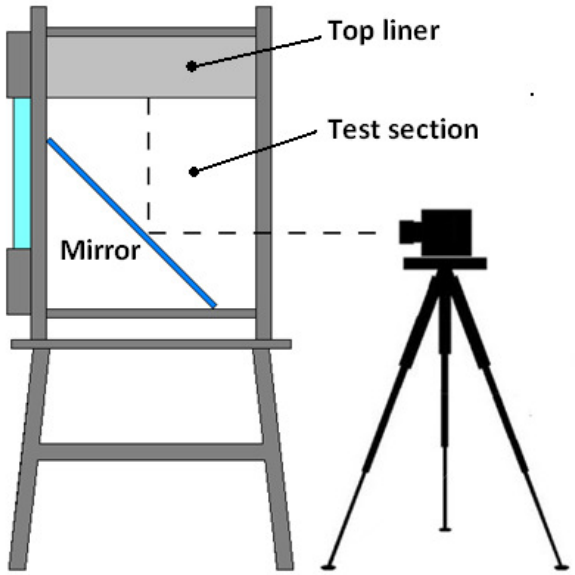


Figure 31 Schematic showing the method by which oil flow visualization photographs were taken.

## 2.4 Characterisation of the incoming boundary layer

Factors which determine the character of the incoming boundary layer include displacement thickness, momentum thickness and shape factor. The displacement thickness ($\delta^*$) is the small, but finite displacement of the outer streamlines by the boundary layer (Figure 32) and is defined by Equation 10.

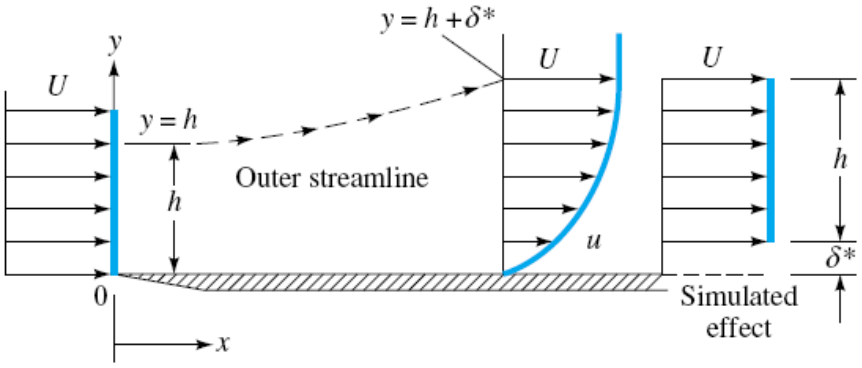


Figure 32 Displacement effect of a boundary layer (White, 1999)

$$\delta^* = \int_0^{\delta} \left(1 - \frac{\rho U}{\rho U_e}\right) \partial y \qquad \text{Equation 10}$$

The momentum thickness (θ) is the thickness of layer which, at zero velocity, has the same momentum defect, relative to the outer flow as the actual boundary layer (Currie 1993).

$$\theta = \int_0^{\delta} \frac{\rho U}{\rho U_e}\left(1 - \frac{U}{U_e}\right) \partial y \qquad \text{Equation 11}$$

The ratio between displacement thickness and momentum thickness is known as the shape factor (H).

$$H = \frac{\delta^*}{\theta} \qquad \text{Equation 12}$$

H is a good indicator of the pressure gradient on the boundary layer. The higher H, the stronger the adverse gradient (White, 1999). Separation occurs approximately at:

$$H_{sep} = \begin{cases} 3.5\ laminar\ flow \\ 2.4\ turbulent\ flow \end{cases}$$ Equation 13

In order to calculate the displacement thickness, momentum thickness and shape factor the velocity and density profiles throughout the boundary layer must be known. A pitot probe (Figure 33) was placed in the flow in the same streamwise location as a static port (Figure 34). When the probe is in the supersonic section of the boundary layer a shockwave forms in front of the tip. Assuming that the shock is normal close to the tip the normal shock wave relations can be used. Conditions upstream and downstream of the shockwave are denoted by the subscripts 1 and 2 respectively.

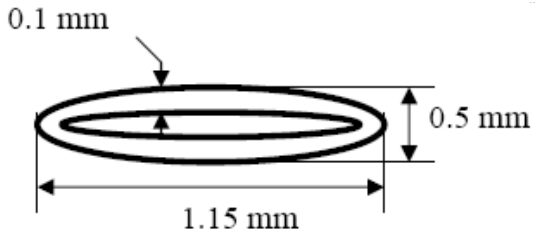


Figure 33 Pitot probe tip dimensions

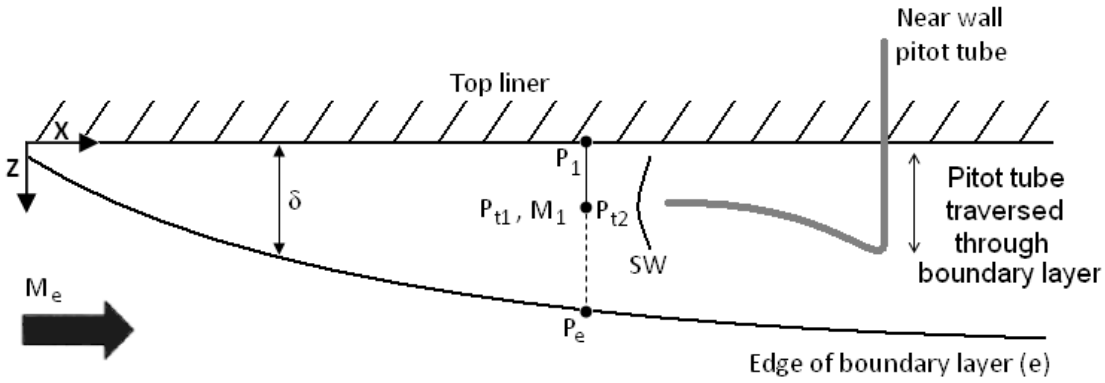


Figure 34 Schematic of the boundary layer measurement setup in the Cranfield University 2 ½" x 2 ½" wind tunnel

It is assumed total pressure is lost throughout the boundary layer while static pressure remains constant in the direction normal to the wall.

$$P_{t1} \neq P_{t\infty} = P_{te}$$ Equation 14

$$\frac{\partial P}{\partial y} = 0 \rightarrow P = P(x) \rightarrow P_1 = P_e \qquad \text{Equation 15}$$

Using the perfect gas law the density profile can be expressed as:

$$\frac{\rho}{\rho_e} = \frac{PRT_e}{P_e RT} = \frac{PT_e}{P_e T} \qquad \text{Equation 16}$$

But from Equation 15, $P_1 = P_e$, therefore:

$$\frac{\rho}{\rho_e} \approx \frac{T_e}{T} \qquad \text{Equation 17}$$

The temperature distribution depends on the Prandtl number (Schlichting, 2000). It is the ratio of viscous diffusivity and thermal diffusivity (Equation 18).

$$Pr = \frac{\mu c_p}{k} = \frac{Viscous\ diffusivity}{Thermal\ diffusivity} \qquad \text{Equation 18}$$

The Prandtl number can be viewed as the ratio between the velocity boundary layer and the thermal boundary layer. When Pr=1 the two boundary layers coincide. The Prandtl number depends solely on the material in question and for air Pr=0.72. When Pr ≠ 1 there is an imbalance between frictional heating and conduction and the adiabatic wall temperature is not equal to the freestream total temperature. The recovery factor, r, is a measure of this difference (Equation 19).

$$r = \frac{T_{aw} - T_e}{T_{te} - T_e} = f(Pr) \qquad \text{Equation 19}$$

The recovery factor is purely a function of Pr. For turbulent flows r can be represented by Equation 20 (Benedict 1984).

$$r = Pr^{1/3} \qquad \text{Equation 20}$$

For air r=0.896.

The velocity profile can be calculated from the Mach number profile and the temperature profile using:

$$U(y) = M_1(y) \cdot \sqrt{\gamma R T(y)} \qquad \text{Equation 21}$$

In the supersonic layer of the boundary layer $P_{t2}$ and $P_1$ need to be known in order to calculate the Mach number:

$$\frac{P_{t2}}{P_1} = \frac{P_{t2}}{P_2} \cdot \frac{P_2}{P_1} = f(M_1) \qquad \text{Equation 22}$$

Using the isentropic pressure relationship:

$$\frac{P_{t2}}{P_2} = \left(1 + \frac{\gamma - 1}{2} M_2^2\right)^{\frac{\gamma}{\gamma - 1}} \qquad \text{Equation 23}$$

And the shock relationships:

$$M_2^2 = \frac{1 + \frac{\gamma - 1}{2} M_1^2}{\gamma M_1^2 - \frac{\gamma - 1}{2}} \qquad \text{Equation 24}$$

$$\frac{P_{t1}}{P_1} = \left(1 + \frac{\gamma - 1}{2} M_1^2\right)^{\frac{\gamma}{\gamma - 1}} \qquad \text{Equation 25}$$

The Rayleigh Pitot equation can be derived:

$$\frac{P_{t2}}{P_1} = \left[\frac{(\gamma + 1)^2 M_1^2}{4\gamma M_1^2 - 2(\gamma - 1)}\right]^{\frac{\gamma}{\gamma - 1}} \cdot \left[\frac{2\gamma M_1^2 - (\gamma - 1)}{\gamma + 1}\right] \qquad \text{Equation 26}$$

$P_{t2}$ and $P_1$ are measured and allow the calculation of the Mach number profile.

In the subsonic layer of the boundary layer there is no shock in front of the pitot tube and the Crocco-Busemann relation (Equation 27) relates the temperature distribution to the velocity distribution. This relation is exact for Pr=1 and is an acceptable approximation for flows with Pr≅1 (White, 1999).

$$T \cong T_w + (T_{aw} + T_w)\frac{U}{U_e} - r\frac{U^2}{2c_p} \qquad \text{Equation 27}$$

Using the Crocco-Busemann relation there are two approaches for solving for the temperature profile either assuming a recovery factor of 1 or assuming a constant recovery factor throughout the boundary layer.

Assuming r=1 the total temperature remains constant throughout the boundary layer:

$$T_{aw} = T_e + \frac{U_e^2}{2c_p} = T_{te} = T_{t\infty} \qquad \text{Equation 28}$$

and reduces Equation 27 to:

$$T(y) = \frac{T_{t\infty}}{\left(1 + \frac{M(y)_1^2 \gamma R}{2c_p}\right)} \qquad \text{Equation 29}$$

Now the temperature profile can be calculated from the Mach number profile.
Assuming a constant recovery factor, r=0.896, from Equation 20 the adiabatic wall temperature can be calculated from:

$$T_{aw} = T_e + r\frac{U_e^2}{2c_p} \qquad \text{Equation 30}$$

Assuming that $T_w = T_{t\infty} = T_{te}$and substituting $U = M_1\sqrt{\gamma R T_1}$ into the Crocco-Busemann relation gives:

$$T(y) = T_{0e} + (T_{aw} - T_{0e})\frac{M_1\sqrt{\delta RT}}{U_e} - r\frac{M_1^2\gamma RT}{2c_p}$$ Equation 31

Equation 31 can be rearranged into a quadratic equation in the form:

$$AT(y)^2 + BT(y) + C = 0$$ Equation 32

Where

$$A = \left(1 + r\frac{M_1^2\gamma R}{2c_p}\right)^2$$ Equation 33

$$B = -\left[2\left(1 + r\frac{M_1^2\gamma R}{2c_p}\right)T_{te} + \left((T_{aw} - T_{te})\frac{M_1^2\sqrt{\gamma R}}{U_e}\right)\right]$$ Equation 34

and

$$C = T_{te}^2$$ Equation 35

A, B and C are all known from the Mach number distribution and the temperature profile can then be calculated.

The presence of a pitot tube in a shear layer alters the nature of the flow (Grosser, 1997). This alteration can be broken down into three effects. At low Reynolds numbers d=based on the probe diameter the Reynolds number effect becomes important. When the probe is within two probe diameters of a solid surface the wall proximity effect becomes significant. In high speed flow the dominating effect however is the velocity gradient/centerline displacement effect Figure 35.

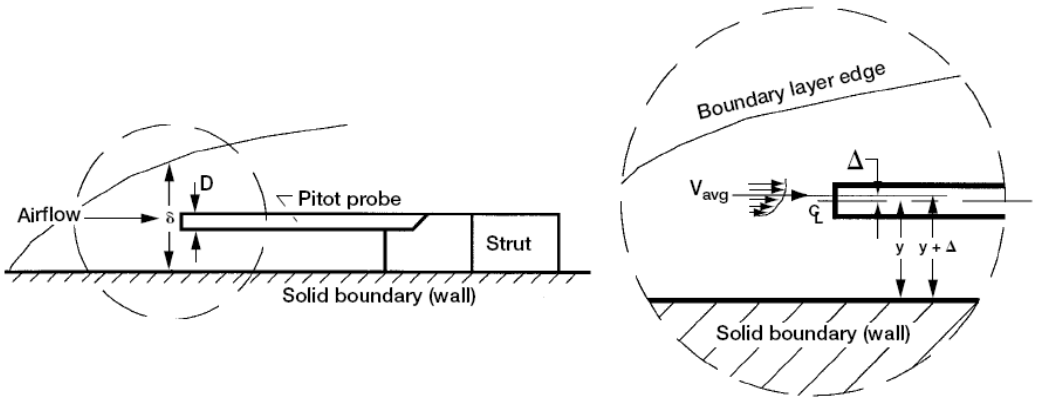


Figure 35 Illustration of centerline displacement effect (Grosser 1997).

MacMillan (1957) performed a series of experiments to determine the centerline offset error and the wall effect error. These errors where then combined into one function (Figure 36). This correction was applied to the velocity profile measured in the 2 ½" x 2 ½" wind tunnel.

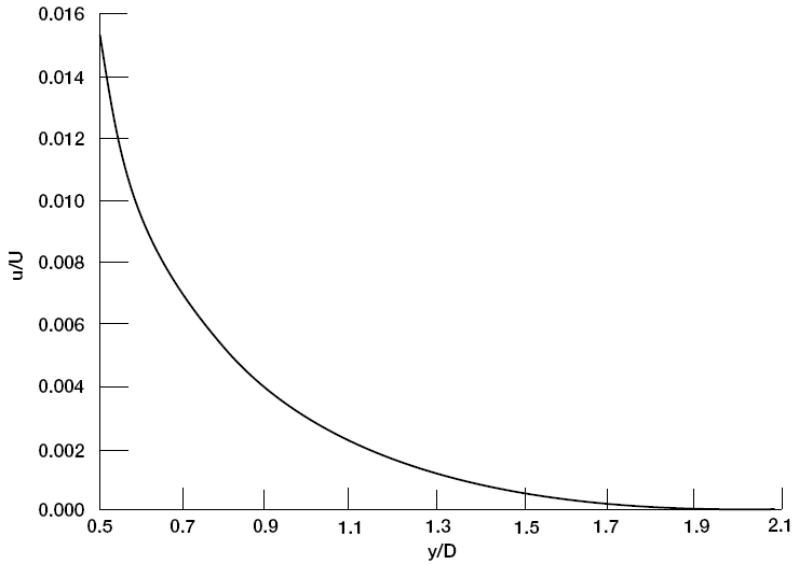


Figure 36 MacMillan's wall effect expressed as a function of y/D (Grosser 1997)

## 2.5 Data Processing

The delimited text files outputted by Labview were imported into Matlab for signal processing. The Fast Fourirer transform (FFT) output , power spectral density (PSD) and sound pressure level (SPL) were calculated for each case using the m-file in Appendix E. The unsteady pressure signal can be divided into two parts, the steady and unsteady components (Equation 36) illustrated in Figure 37.

$$P = P_{av} + P' \qquad \text{Equation 36}$$

Where $P_{av}$ is the average pressure and P' is the fluctuating pressure.

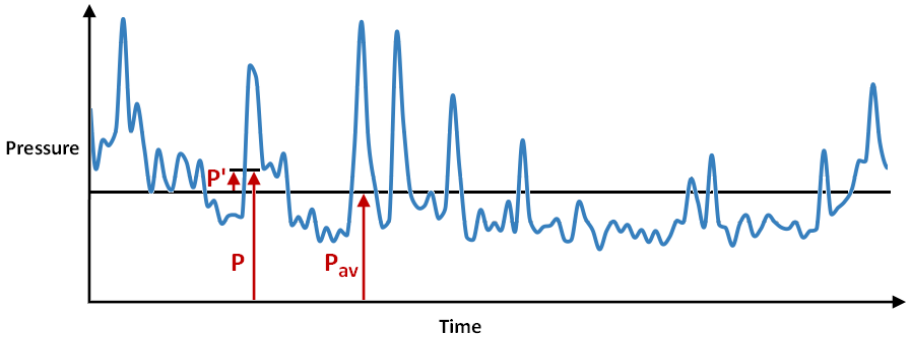


Figure 37 Steady and fluctuating components of an unsteady signal.

Using a Fourier transform converts the function from the time domain to the frequency domain. In order to minimize leakage into other frequencies the data was windowed with a Hanning function window (Equation 37) before being processed (Figure 38). This however reduces the amplitude of the function in the frequency domain and amplitude and power correction factors have to be applied (2 and 8/3 respectively) to make up for this loss.

$$w(n) = 0.5\left(1 - \cos\left(2\pi\frac{n}{N}\right)\right), 0 \leq n \leq N \qquad \text{Equation 37}$$

Where N is equal to the window length, L minus one (Oppenheim & Schafer, 1989).

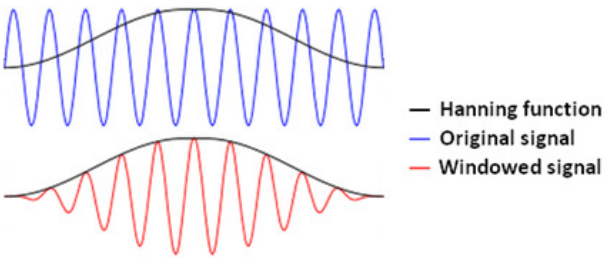


Figure 38 The Hanning function.

The PSD was calculated using Equation 38:

$$PSD = \frac{|P|^2}{N \cdot \Delta f} \qquad \text{Equation 38}$$

Where P is the pressure signal in the frequency domain transformed using a Fourier transform of p.

SPL (Equation 39) is a common way of presenting acoustic data. It is the deviation of the local pressure from the ambient pressure caused by a sound wave and is measured in decibels (dB).

$$SPL = \frac{20 \log P_{fluc}}{P_{ref}} \qquad \text{Equation 39}$$

Where $p_{fluc}$ is the unsteady component of p and $p_{ref}$ is a reference pressure, in this case 2 x$10^{-5}$, the threshold of human hearing.

Finally the OASPL can be calculated from Equation 40:

$$OASPL = \frac{20 \log P_{rms}}{P_{ref}} \qquad \text{Equation 40}$$

Where $p_{rms}$ is the root mean square of p.

Ensemble averaging was used in the signal processing with a block length of 16384 samples with a 50% overlap. This meant that the frequency resolution was 6.1Hz (Equation 41).

$$\Delta f = \frac{f_s}{N_{s/block}} = \frac{100{,}000Hz}{16384} = 6.1Hz \qquad \text{Equation 41}$$

# 3 Numerical methodology

## 3.1 Gridding approach

All grids were constructed using the commercial grid generation software Gridgen (version 15.11). A structured, multi block approach was used. Grid cells were refined near solid walls to provide adequate boundary layer resolution. This was achieved by adjusting the near wall grid refinement until a non-dimensional wall distance $y^+$ (Equation 42) of approximately 1 was achieved.

$$y_1 = 2_{y^+} \frac{L}{\sqrt{0.039} Re_L^{0.9}} \qquad \text{Equation 42}$$

Where L is the characteristic length (Gülich, 2010).

Further details of the gridding approach for each numerical configuration are give in §4.1.1, §4.2.1 and §4.3.1

## 3.2 Averaging the Navier-Stokes equations

Turbulent flow is characterised by a broad range of spatial and temporal scales. Resolving these scales by solving the instantaneous Navier-Stokes equations is a difficult and expensive computing problem. The usual approach is to average the equations, to remove the small scales Cebeci et al. (2005). This is achieved by decomposing all variables into their mean and fluctuating components and to time average the equations. The averaged equations now contain additional unknown variables such as the Reynolds stresses. Turbulence models are used to determine these unknown variables in terms of known quantities. Traditionally for incompressible flows the Navier-Stokes equations are time averaged using Reynolds averaging (leading to the Reynolds averaged Navier-Stokes (RANS) equations). However for compressible flows where density gradients become significant Reynolds averaging leads to complex correlations between variables. The problem can be dramatically simplified by using a density-weighted averaging procedure suggested by Favre (1965).

## 3.3 Solver

All numerical simulations were carried out using the commercial code Cobalt. Cobalt is a hybrid Navier-Stokes solver. It solves neither the instantaneous Navier-Stokes nor the Favre-averaged Navier-Stokes equations. In Cobalt the Favre averaged Reynolds stress tensor and all the terms containing *k* are neglected. Cobalt solves a discretized form (second order) of the instantaneous Navier-Stokes equations with the averaging process entering indirectly through the turbulence model when the eddy viscosity is calculated (Haas, 2009). Haas (2009) deals with the practical implications of this approach concluding that it is possible that some terms containing *k* would balance each other. However in some cases, particularly at hypersonic velocities, the turbulent kinetic energy and Reynolds stresses may not be small enough to be neglected. An extensive programme of simulations comparing Cobalt to a traditional Farve-averaged code is necessary to fully understand the implications of this approach.

## 3.4 Turbulence models

The flowfield surrounding a lateral jet in supersonic crossflow is highly complex involving multiple instances of flow separation and reattachment. Many different turbulence models have been used to simulate the jet in crossflow interaction with no consensus existing on the most appropriate model to use. For each configuration (flat plate, body of revolution, body of revolution at incidence) an investigation into the most appropriate turbulence model was carried out. The four RANS based turbulence models available in Cobalt (Spalart-Allmaras, Spalart- Allmaras with rotation correction, k-ω and Menter's shear-stress transport) were used in this investigation.

A brief description of the turbulence models considered is provided in the following section.

### 3.4.1 Spalart-Allmaras

The Spalart-Allmaras turbulence model was developed in 1992 (Spalart & Allmaras, 1992). It is a based on a single equation which solves a transport equation for a variable which is identical to the turbulent viscosity, except in near wall viscous boundary layers. SA was

designed for aerodynamic flows such as transonic flow over airfoils, including boundary layer separation (Pope, 2000). SA has often been used to simulate the lateral jet in supersonic crossflow interaction due to its stability and relatively rapid computation time (Lee et al, 2004, Min et al, 2006, Kovar & Schülein, 2006 and Dessaint, 2008). However reservations exist as to its effectiveness in predicting the lateral jet in supersonic crossflow interaction. Payne (2001) compared various turbulence models for a supersonic jet in subsonic crossflow and concluded that SA gave poor results in the near jet region but showed excellent agreement with downstream pressure and vorticity data. SA can over predict the rate of the plane jet spreading by almost 40% (Pope, 2000) and is quite in accurate for flows with shock-induced separation at Mach numbers greater than 3 (Wilcox, 2006).

### 3.4.2 SA with rotation correction (SARC)

SARC is a modification to the original SA model to account for the effect of system rotation and/or streamline curvature. This is achieved by modifying the production term to take into account both the rate of strain and vorticity. Shur et al. (2000) assessed the SARC turbulence model using a range of rotating and curved channel flows. SARC was shown to be much more accurate than the original SA model for these flows. When applied to a two-dimensional flow U-turn, SARC models the flow upstream of separation well. Downstream of separation skin friction and pressure coefficients are also predicted well, however the length of the recirculation zone is overestimated and too slow a recovery after reattachment predicted. Shur et al. (2000) concluded that this discrepancy was probably caused by the original SA model and was not a problem with the modifications. When applied to a three-dimensional flows one global iteration was found to use 20% CPU time but the convergence rate was faster. SARC has also been used to model forebody vortices at high angles of attack (Champigny et al. 2006) to get a better description of the vortical flow.

### 3.4.3 k-ω model

The k-ω model is a two equation turbulence model solving for two transported variables k, the turbulent kinetic energy and ω the specific dissipation. The k- ω turbulence model was adapted from the k-ε model. Wilcox (1998) replaced the dissipation rate equation with an

equation for specific dissipation. The version of the k-ω model modeled the behavior of attached adverse pressure gradients more accurately than the k-ε model (Bardina et al., 1997). This model performed poorly in predicting shear flows over predicting the spreading of a round jet. In Wilcox's 1998 version of the k-ω model, the model used by Cobalt, Wilcox modified closure coefficients to become functions of the flow variables (Morgans et al., 1999). This model is as accurate for attached boundary layers, backward-facing steps, and mildly separated incompressible flows.

### 3.4.4 Shear-stress transport model (SST)

The shear-stress *k-ω* model (SST) was developed by Menter (1994). It was developed to address the need to accurately predict aerodynamic flows with strong adverse pressure gradients and separation. The k-ε model failed to predict the proper behaviour of turbulent boundary layers up to separation, while the *k-ω* model performed well in the near wall regions for moderate pressure gradient it fails for pressure induced separation. The SST model blends these two models together selecting combing the robustness of *k-ω* turbulence model near walls with capabilities of the k-ε model away from the walls. The definition of the turbulent viscosity is modified to account for the transport of the principal turbulent shear stress. These modifications make the SST model applicable to a large range of flows (e.g. pressure induced separation, complete aircraft configurations). Dennis et al. (2007) used the SST model to simulate a sonic jet in supersonic jet and found that the pressure distribution and flowfield features were well captured.

## *3.5 Error and uncertainty in CFD calculations*

Error in CFD calculations is defined as a deficiency in the CFD model that is not due to lack of knowledge while uncertainty is defined as a potential deficiency in the model caused by lack of knowledge. (Versteeg and Malalasekera, 2007)

| | | |
|---|---|---|
| **Error:** | *Numerical errors* | Roundoff errors, iterative convergence errors, discretisation errors |
| | *Coding errors* | Mistakes or bugs in the software |
| | *User errors* | Human error through the incorrect usage of the software |
| **Uncertainty:** | *Input uncertainty* | Inaccuracies due to limited information, geometry approximation, |
| | *Physical model uncertainty* | Discrepancies due to simplifications (e.g. steady flow), turbulence model etc. |

(Versteeg and Malalasekera, 2007)

A discussion of the iterative convergence and discretisation error is give below. Discrepancies due to the turbulence model are discussed for each numerical configuration §4.1.2.2, §4.2.2.2 and §4.3.2.2. All other sources of error and uncertainty including round off error and programming errors were considered negligible.

### 3.5.1 Iterative convergence

The iterative convergence error was evaluated by monitoring the solution residuals and forces and moments on the body as the solution progressed.

### 3.5.2 Grid convergence

A grid convergence investigation was carried out for each configuration to assess the sensitivity of the solution to spatial resolution. The method by which this was achieved is outlined below. The results of these investigations are presented in §4.1.2.1, §4.2.2.1 and §4.3.2.1.

The normal force coefficient $C_Z$, axial force coefficient $C_X$ and pitching moment coefficient $C_m$ calculated from the different grids are analysed to check for grid independence. The ratio

of grid refinement r is defined in terms of the grids sizes (Ng) across two levels of refinement (Ng1, Ng2) (Equation 1):

$$r = \frac{N_{g=1}}{N_{g=2}} \qquad \text{Equation 43}$$

For all cases the ratio of grid refinement was r=2.

$$p_{con} = \ln\left(\frac{C_{X,g=4} - C_{X,g=2}}{C_{X,g=2} - C_{X,g=1}}\right) / \ln r \qquad \text{Equation 44}$$

Richardson's Extrapolation (Roache, 1998) is used to estimate the value of the coefficient in question for a grid with a spacing of zero (g=0).

$$C_{X,g=0} \cong C_{X,g=1} + \frac{C_{X,g=1} - C_{X,g=2}}{r^{p_{con}} - 1} \qquad \text{Equation 45}$$

The grid convergence indexes are then calculated using Equation 46 (Roache, 1998). A factor of safety of $F_S$=1.25 is used as three levels of grid refinement are considered (Roache, 1998).

$$GCI_{g=1,2} = \frac{F_S \left|\frac{C_{X,g=1} - C_{X,g=2}}{C_{X,g=1}}\right|}{r^{p_{con}} - 1} \qquad \text{Equation 46}$$

$$GCI_{g=2,4} = \frac{F_S \left|\frac{C_{X,g=2} - C_{X,g=4}}{C_{X,g=2}}\right|}{r^{p_{con}} - 1} \qquad \text{Equation 47}$$

The grid convergence indexes can then be used to check whether the solutions lie in the asymptotic range and hence satisfy Equation 48:

$$AR \cong \frac{GCI_{g=2,4}}{GCI_{g=1,2}\, r^{p_{con}}} \cong 1 \qquad \text{Equation 48}$$

# 4 Numerical campaign

## *4.1 Numerical Investigation of a jet in crossflow interaction on an idealised flat plate*

The lateral jet in supersonic crossflow interaction was idealised with the body surface modelled as a flat plate. This was done to remove interference from surface geometry and reduce the complexity of the problem. Boundary conditions were chosen to match that of Kovar & Schülein (2006) to allow the accuracy of the CFD method to be investigated. This allowed a comparison between existing experimental data and numerical solutions found using CFX-TASCflow.

### 4.1.1 Grid & boundary conditions

To assess the ability of the CFD method (Cobalt ref) to predict the jet in crossflow interaction, a flat plate was modelled with the same geometry as the flat plate investigated numerically and experimentally by DLR (Kovar & Schülein, 2006). This is an idealised test case as it removes some of the more complex flow interactions and uses a simple geometry which enables a useful level of measurement instrumentation. The flat plate measures 660mm in length (x-direction) and 400mm in width (y-direction). A 6mm sonic nozzle is located at x=360mm and y=200mm (Figure 39).

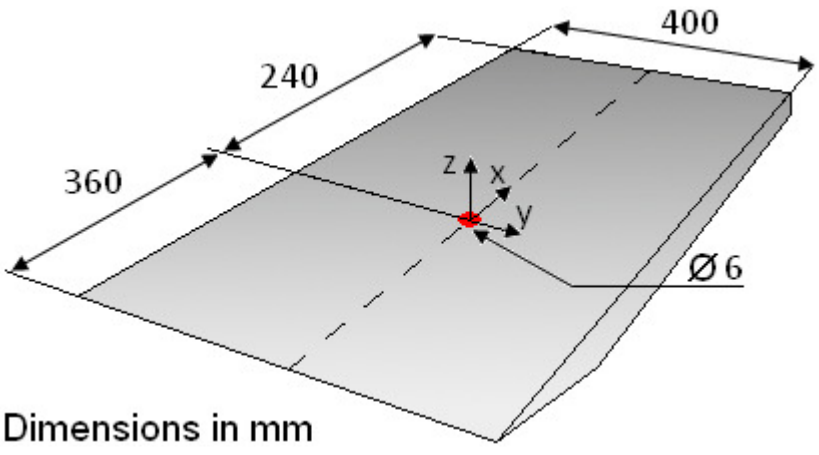


Figure 39 Schematic of the DLR flat plate.

The interaction was assumed to be symmetric about the centreline (y=0mm) and as such it was possible to reduce to computational load by modelling half of the computational domain. The structured hexahedral grid was refined in the region of the jet (Figure 40). Cell sizes in the direction normal to the plate were adjusted until a $y^+$ (Equation 42) of 1 was achieved. The jet nozzle was modelled as a cylinder with a height of 24mm this allowed the build up of a realistic boundary layer (Figure 41). Initially a coarse grid with 599,821 cells was created. This was then further refined until grid independence was shown (§ 4.1.2.1).

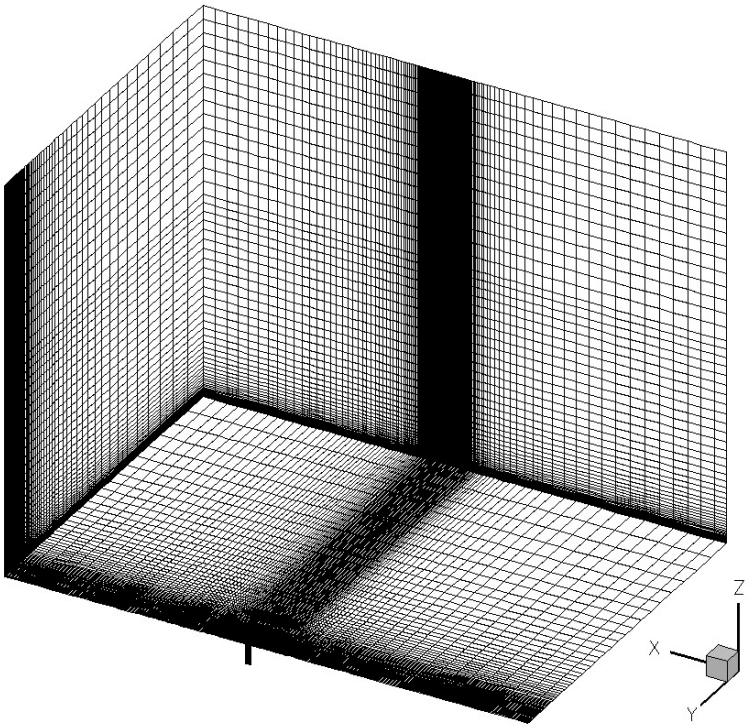


Figure 40 Computational grid for idealised flat plate.

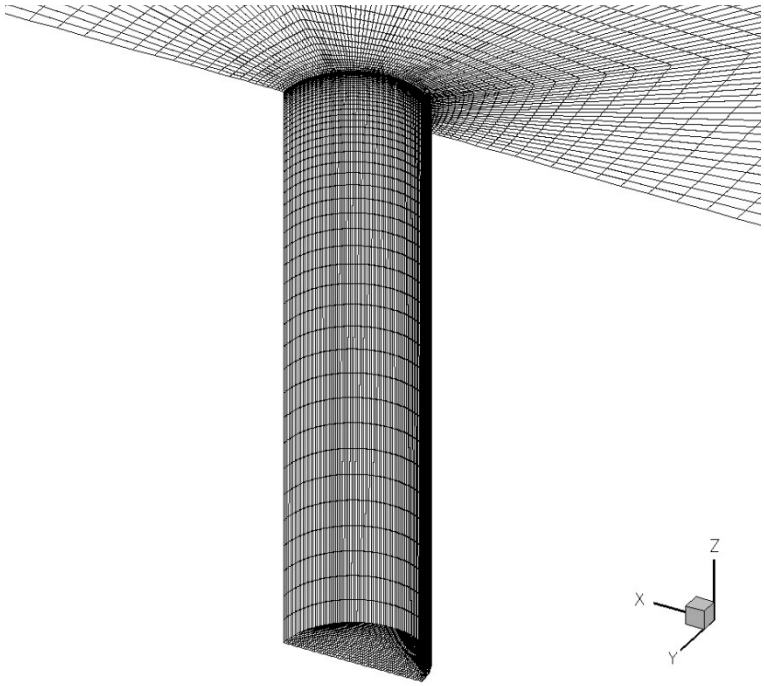


Figure 41 Close-up of the jet nozzle geometry in the computational grid for idealised flat plate.

The flat plate and the nozzle wall were modelled by a solid adiabatic wall with the no slip condition specified. A farfield boundary condition was set for the inlet, outlet and exterior using the Modified Riemann Invariants method with the inlet total temperature and total pressures specified. The jet source was modelled using a source boundary condition with specified total temperature and total pressure (Table 8).

Table 8 Summary of crossflow and jet conditions

| | |
|---|---|
| Freestream Mach number | 5 |
| Reynolds number | $Re_L = 25 \times 10^6$ |
| Jet pressure ratio | $P_{0j}/P_\infty$=100 |
| Jet gas | Air |
| Jet total temperature | $T_{0j}$=295 K |
| Freestream static temperature | $T_\infty$=68 K |
| Jet diameter | d=6 mm |
| Flat plate length | L=660 mm |

### 4.1.2 Validation

#### 4.1.2.1 Grid Independence

The initial grid consisted of 599,821 cells. This grid was then refined three times with an approximate refinement factor of two, resulting in four grids with the cell count outlined in Table 9.

Table 9 Number of cells in each mesh.

| Mesh #: | # Cells: | Description |
|---|---|---|
| 1 | 599,821 | Coarse |
| 2 | 1,208,440 | Medium |
| 3 | 2,438,760 | Fine |
| 4 | 4,893,516 | Extra-fine |

The symmetric nature of the interaction and the fact that the plate is not yawed meant that the plate was not subject to any net force in the y direction or net yawing or rolling moment. Normal force coefficient $C_Z$, axial force coefficient $C_X$ and pitching moment coefficient $C_m$ were therefore chosen as the criteria used to check for grid independence as described in Chapter 3.5. Initially solutions for meshes 1, 2 and 3 were obtained. The grid convergence for these meshes is given in Table 10. The three coefficients are all converged within acceptable limits, with the biggest percentage difference between coefficients calculated for the different grids being 1.83% for the axial force coefficient. It should be noted that these force and moment coefficients are small (in relation to a flat plate) and as such these small percentage differences equate to very small differences in forces and moments.

Table 10 Grid convergence for the DLR idealised flat plate meshes 1, 2 and 3.

| | coarse (g=1) | medium (g=2) | fine (g=3) | zero (g=0) | $GCI_{3,2}$ | AR | $p_{con}$ | %diff3,2 |
|---|---|---|---|---|---|---|---|---|
| $C_Z$ | -2.41E-03 | -2.36E-03 | -2.33E-03 | -2.27E-03 | 3.32% | 0.99 | 0.60 | 1.39% |
| $C_X$ | 8.46E-04 | 8.32E-04 | 8.17E-04 | 1.21E-03 | 0.74% | 0.23 | 2.00 | 1.83% |
| $C_m$ | 1.02E-03 | 1.02E-03 | 1.03E-03 | Non-monotonic | Non-monotonic | Non-monotonic | Non-monotonic | 1.09% |

There was a difference of 1.09% for the pitching moment coefficient which was deemed acceptable. The grid convergence index for this coefficient could not be calculated as the solutions for the pitching moment coefficient from the three grids were non-monotonic. It was then decided to solve mesh 4 (the “extra-fine” grid with 4,893,516 cells) to see if any improvement in grid convergence could be achieved. The grid convergence for the finest three meshes is shown in

Table **11**. The percentage difference between the finer grids (3 &4) reduced for the normal force coefficient and the pitching moment coefficient but increased for the axial force coefficient. The solutions for the pitching moment coefficient remained non-monotonic. Further refining the grid was not an option due to computational restraints. However, overall the changes in coefficient values between the finest grids was small and the solution was considered independent of further spatial refinement. As a results of the of grid independence

assessment Mesh 3 (2,438,760 cells) was selected. Mesh 4 (4,893,516 cells) offered little improvement in grid convergence

Table 11 Grid convergence for the DLR idealised flat plate meshes 2, 3 and 4.

| | medium (g=2) | fine (g=3) | extra-fine (g=4) | zero (g=0) | $GCI_{4,3}$ | AR | $p_{con}$ | %diff4,3 |
|---|---|---|---|---|---|---|---|---|
| $C_Z$ | -2.36E-03 | -2.33E-03 | -2.29E-03 | -3.01E-03 | 0.61% | 0.23 | 2.00 | 1.48% |
| $C_X$ | 8.32E-04 | 8.17E-04 | 8.08E-04 | 7.96E-04 | 1.95% | 0.99 | 0.76 | 1.09% |
| Cm | 1.02E-03 | 1.03E-03 | 1.02E-03 | Non-monotonic | Non-monotonic | Non-monotonic | Non-monotonic | 0.29% |

The accuracy of the solution was assessed by comparing the normalised wall pressure distribution along the interaction centreline to experimental data measured by DLR (Kovar & Schülein 2006). This was a qualitative assessment but showed whether the solution was converging on the correct one (as determined experimentally). This comparison is presented in Figure 42 with two areas of interest, the secondary upstream pressure peak associated with the flow attachment upstream of the jet and the downstream pressure peak associated with flow reattachment highlighted (Detail A and B respectively). It is in these two areas that the largest disagreement between grids is found. The upstream and downstream pressure peaks both increase with increases in grid refinement. This trend leads predictions of the downstream peak being less accurate with increases in mesh refinement. The spatial resolution of the experimental pressure values is not high enough to define accurately the upstream pressure peak. Meshes two and three (1,208,440 and 2,438,760 cells) provide the closest fit to the experimental pressure values in the upstream pressure peak (Detail A).

The over prediction of the downstream pressure peak was an area of concern. Efforts were made to improve the solution in this area by carrying out a local mesh refinement. Mesh three was adapted increasing the number of cells in the area downstream of the jet taking the cell count from 2,438,760 to 4,995,540. This however did not improve the prediction and efforts in this direction were abandoned.

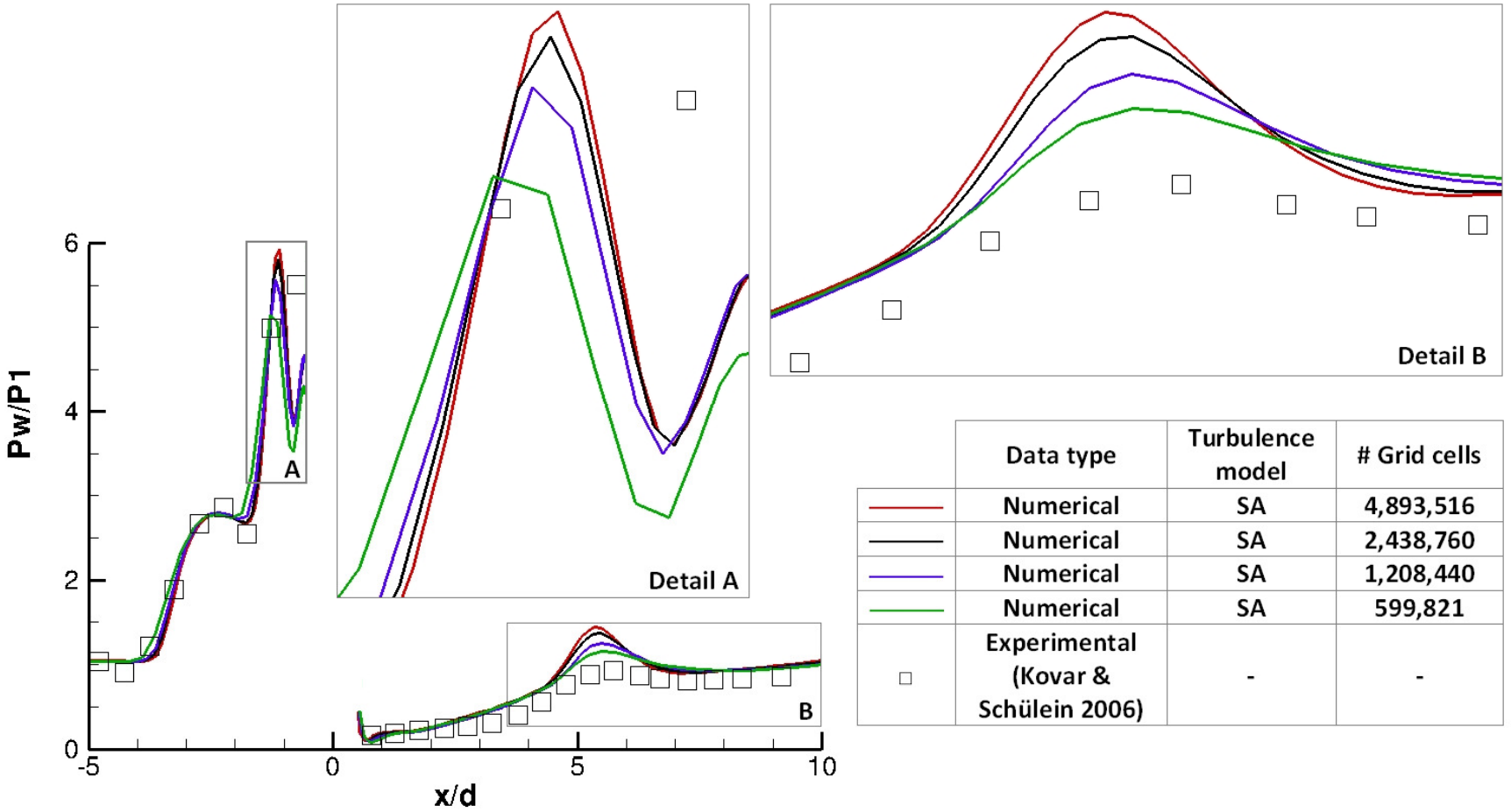


Figure 42 Comparison of normalized wall pressure distribution for the DLR idealised flat plate meshes 1, 2 and 3, PR=100.

### 4.1.2.2 Turbulence model study

Four turbulence models, Spalart-Allmaras (SA), Menter's Shear Stress Transport (SST), Spalart-Allmaras with Rotation Correction (SARC) and Wilcox's 1998 k-ω model were trialled (described in more detail in Chapter 3.3). These solutions were calculated using Mesh 3 (2,438,760 cells) as selected in the grid independence study (Chapter 4.1.2.1).

The normalized wall pressure distribution for the different turbulence models was compared to experimental data (Figure 43). SST and k-ω failed to predict upstream separation and the pressure plateau associated with it. These models also over predicted the second pressure peak associated with upstream flow reattachment. Downstream these two turbulence models performed well agreeing with the experimental data except in the region of higher pressure caused by flow reattachment where pressure was over predicted substantially. Due to their poor performance in the upstream region both SST and k-ω were discounted. Both SA and SARC performed better in the upstream region with SA the better of the two predicting separation and the initial pressure plateau. Downstream both SA and SARC over predicted the pressure in the reattachment region. Kovar & Schülein 2006 presents representative experimental wall streamlines for the DLR flat plate. Figure 44 shows the comparison between these experimental results and the computed wall skin friction lines from Cobalt for each turbulence model. These results underline SA as the candidate which gives the best agreement for the upstream separation and reattachment regions. The overall predicted flow field was in good agreement with the experimental streamlines.

The normalized wall pressure and representative wall streamline comparisons lead to the selection of SA as the turbulence model that best predicts the lateral jet in crossflow issued from an idealized flat plate.

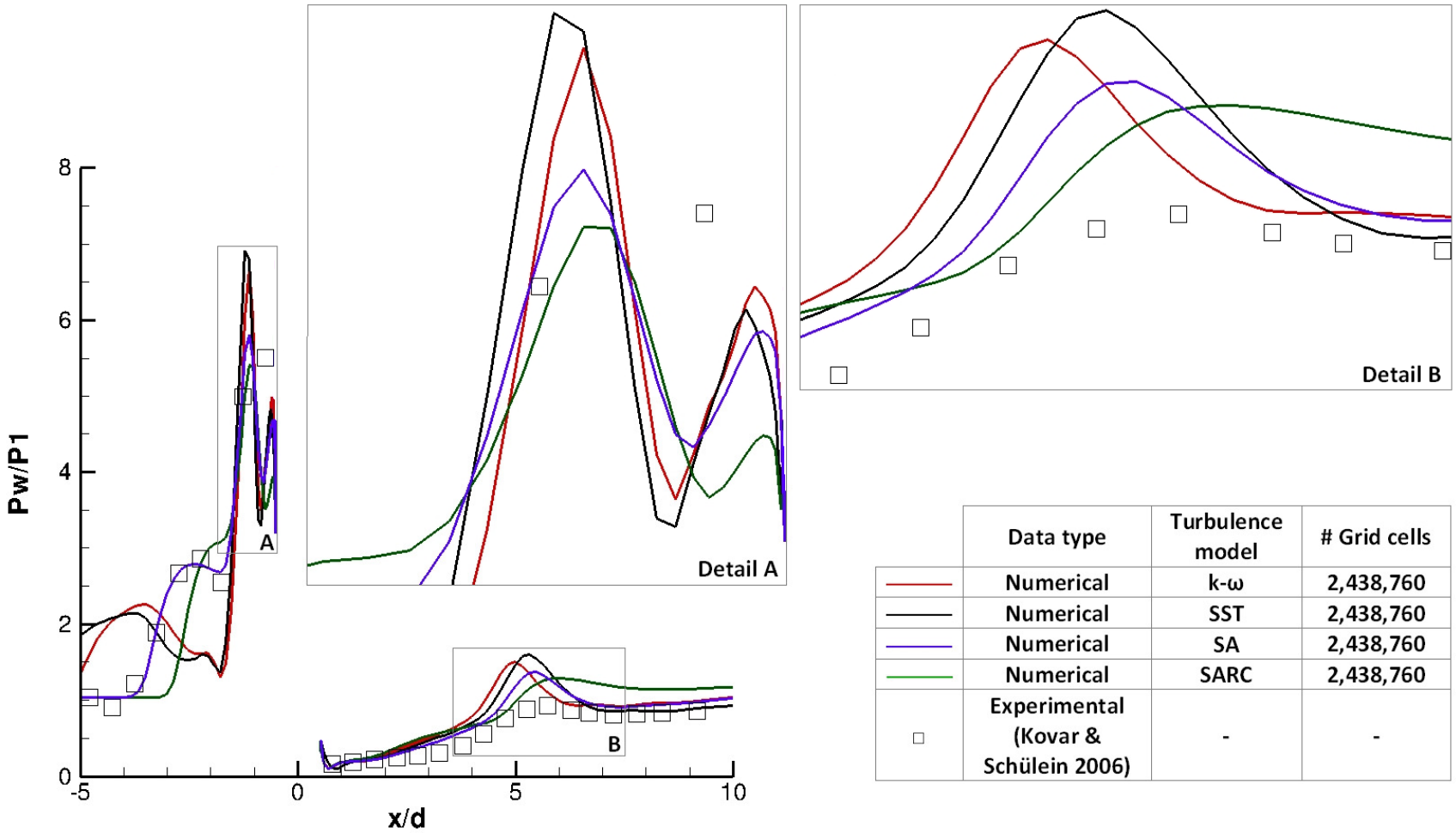


Figure 43 Comparison of normalized wall pressure distribution for the different turbulence models trialed, PR=100.

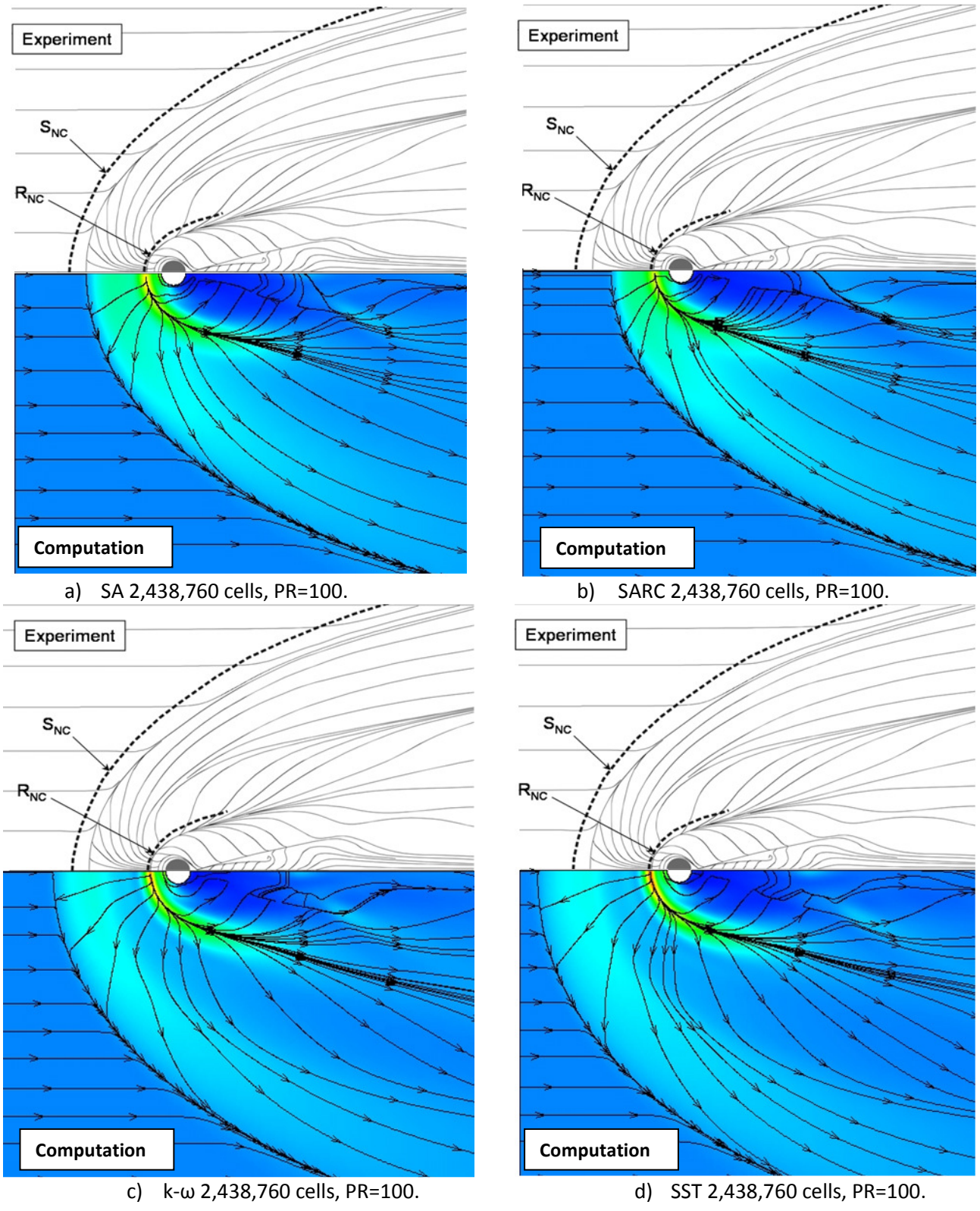


a) SA 2,438,760 cells, PR=100.

b) SARC 2,438,760 cells, PR=100.

c) k-ω 2,438,760 cells, PR=100.

d) SST 2,438,760 cells, PR=100.

Figure 44 Top: Representation of experimental wall streamline patterns. $S_{NC}$ and $R_{NC}$ denote numerical separation and reattachment lines from DLR Tau code.
Bottom: Contours of wall pressure and skin friction streamlines from Cobalt with specified turbulence model.

The reattachment area downstream of the jet was investigated using streamlines. The region (3.67≤x/d≤7) was seeded with 100 streamlines. Streamlines were calculated upstream and downstream of the seed point. These streamlines were then extracted for each turbulence model and combined into one plot where they were coloured by turbulence model (Figure 45). In the comparison of normalized wall pressure distribution (Figure 43), the best prediction of the upstream region was found using the one equation turbulence models (SA & SARC). In Figure 45 streamlines for SA and SARC both consist of jet fluid only, which is through the Mach disk shed sideways and as it moves downstream moves towards the area of low pressure behind the Mach disk. The streamlines predicted by the k- ω turbulence model consist only of freestream fluid while those predicted by the SST turbulence model consist both of jet and freestream fluid. As the streamlines that reattach downstream of the jet can be traced back to the region in front of the jet it can be seen that accurate prediction of the downstream region requires the upstream region to be accurately predicted as well. Any discrepancies in the upstream region will be transported downstream and effect the prediction there. From the comparison of normalized wall pressure distribution (Figure 43) k-w and SST over predict the upstream separation length with SA & SARC providing a much better fit to the experimental data. This effect can be seen downstream reattachment region where the discrepancies between the numerical and experimental data are greatest for k-w and SST

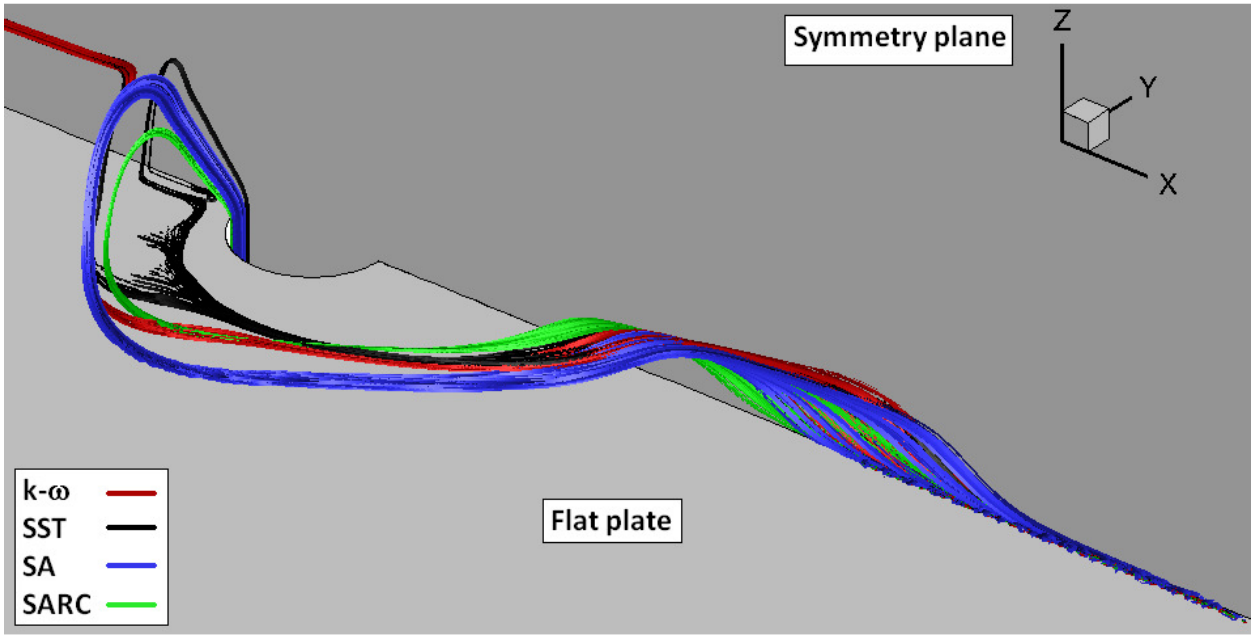


Figure 45 Reattachment streamlines comparing the four turbulence models trialed.

### 4.1.3 Results and Discussion

#### 4.1.3.1 Comparison of experimental and numerical data

Figure 46 compares numerical results using Cobalt with the SA turbulence model and a grid of 2.4 million cells with computational and experimental results from DLR (Kovar & Schülein 2006). The DLR computations were performed using the Tau code. Cobalt provides a better prediction of the upstream separation than the DLR Tau code. Both numerical codes captured the pressure plateau associated with the separated region well. There is not enough spatial resolution in the experimental results to definitively define the pressure peak associated with the bow shock. The DLR Tau code predicts a much larger pressure peak than Cobalt ($P_w/P_1$=7.9 as opposed to $P_w/P_1$=5.8). In the downstream region up until x/d=4 Cobalt better predicts the pressure distribution. The over prediction of the pressure peak associated with the reattachment of the flow downstream of the jet by is not unique to Cobalt. The DLR Tau Code makes the same over prediction. Downstream of the interaction and the reattachment region (x/d>8) the pressure distribution predicted by the DLR Tau code better matches the experimental results with Cobalt slightly over predicting the pressure (e.g $\Delta P_w/P_1 \approx 0.2$ at x/d=11).

In the previous section, (§ 4.1.2.2), a comparison between representative experimental wall streamlines and numerical coefficient of skin friction streamlines was made. This comparison (Figure 44) also included the upstream separation and reattachment lines predicted by the DLR Tau code. Figure 44a) gives this comparison for the Cobalt case under discussion here (SA, 2,438,760 cells). Here it can be seen that both Cobalt and the DLR Tau code accurately predict the upstream reattachment lines while only Cobalt captures the upstream separation line. This agrees with the pressure distributions in Figure 46.

In addition to the experimental longitudinal pressure distribution, along the interaction centreline, Kovar & Schülein 2006 also presents experimental and numerical lateral pressure distributions in three positions (x=0mm, x=50mm and x=100mm). Comparisons between Cobalt and these results are presented in Figure 47, Figure 48 and Figure 49 respectively.

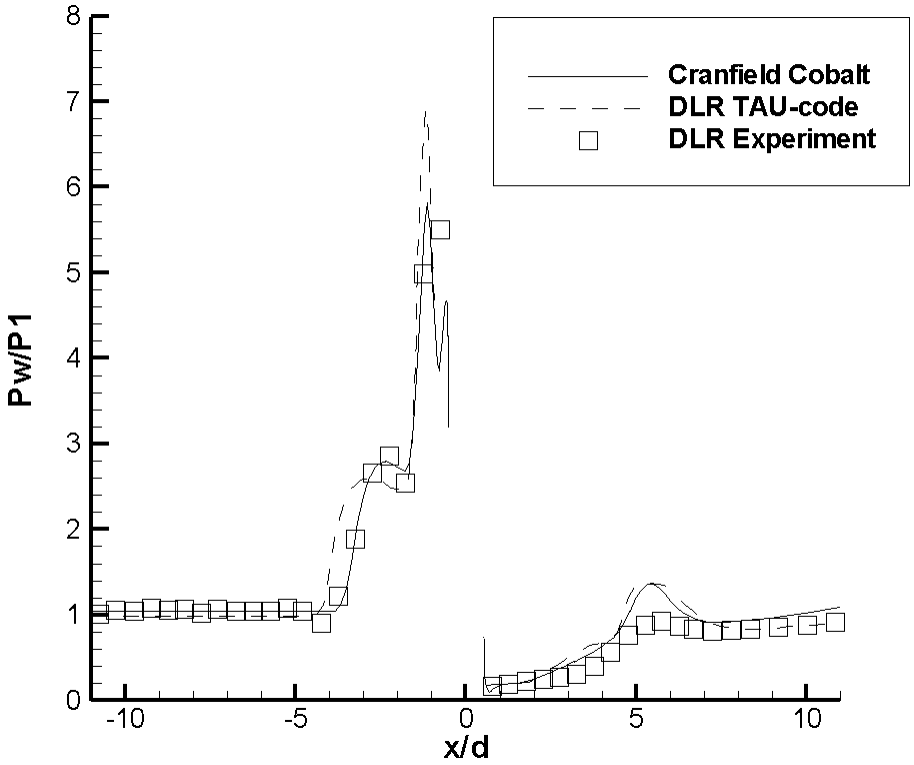


Figure 46 Normalised wall pressure in the x direction at y/d=0, PR=100.

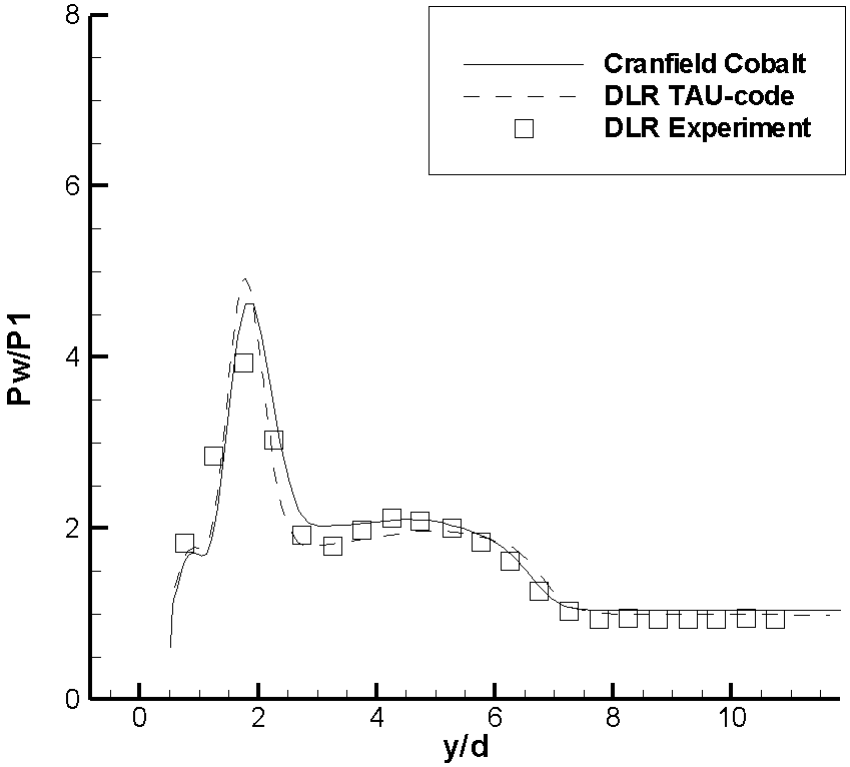


Figure 47 Normalised wall pressure in the y direction at x/d=0, PR=100.

At x/d=0 (Figure 47), both Cobalt and the DLR Tau code both have a good overall agreement with the experimental data, however in the region of x/d=0 and 2<y/d<4 the DLR Tau code performs better. Both Cobalt and the DLR Tau code over predict the pressure peak y/d≈2 with the DLR Tau code having the larger overestimation. Figure 48 shows the normalised wall pressure distribution for the lateral plane at x/d=8.33. Here the influence of the jet is still evident however it has decreased. Both Cobalt and the DLR Tau code agree well with the experimental results with and the DLR Tau code performing marginally better. The influence of the jet has also disappeared at x/d-16.67 with the pressure being almost equalised. Cobalt and DLR Tau code agree with each other but slightly over predict the normalised pressure.

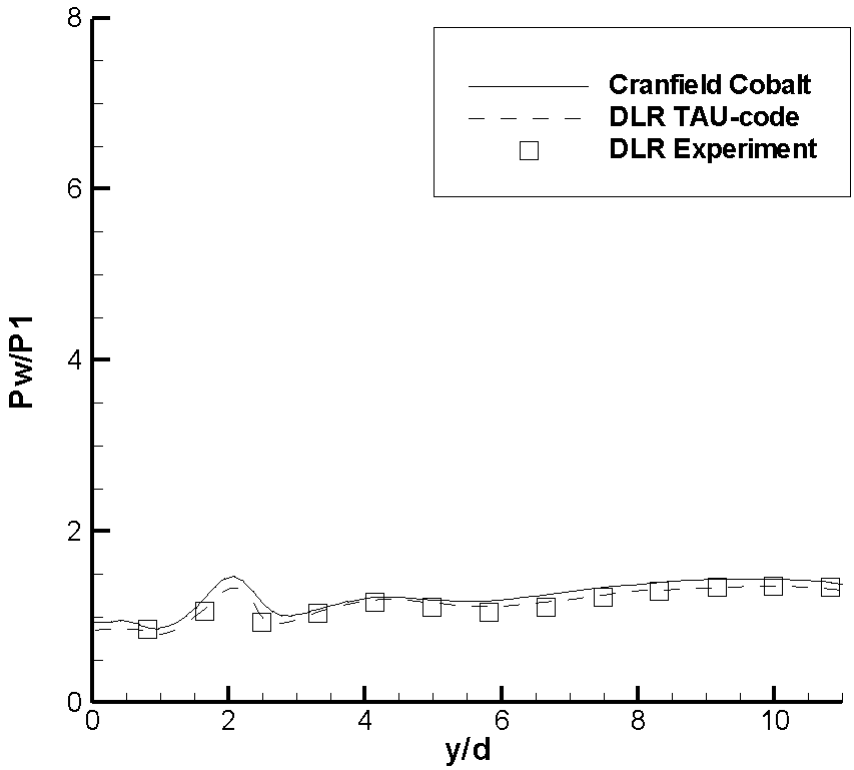


Figure 48 Normalised wall pressure in the y direction at x/d=8.33, PR=100.

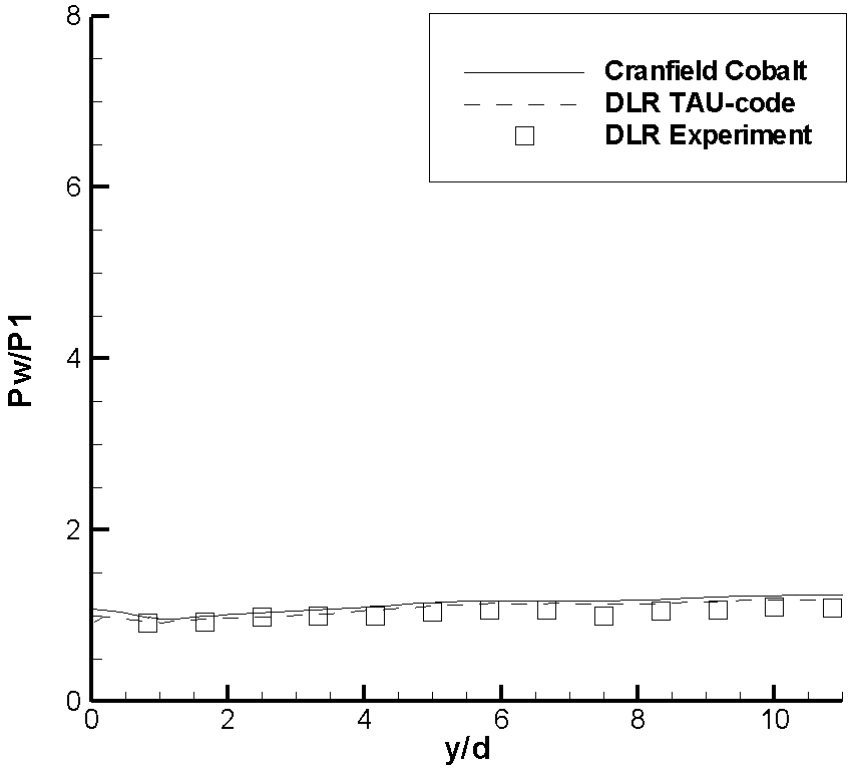


Figure 49 Normalised wall pressure in the y direction at x/d=16.67., PR=100.

### 4.1.4 Conclusions

An acceptable level of grid convergence was achieved with a grid consisting of 2,438,760 cells. Of the four turbulence models trialed Salart-Allmaras performed most accurately in the prediction of the lateral jet in supersonic flow issued from an idealized flat plate interaction. An area of concern however, is the over prediction of the pressure peak associated with the reattachment of flow downstream of the jet. Efforts were made to improve the solution in this area by adapting the existing structured grid. These efforts were unsuccessful. A new approach with an unstructured grid may yield better results in this area.

Cobalt using SA and the grid selected in the grid independence study was shown to more accurately predict the upstream separation line than the DLR Tau code. Comparing results from Cobalt and the DLR Tau code to experimental pressure distributions showed that both codes perform very well with each out-performing slightly the other in some areas. Cobalt can be used to perform a reasonably accurate prediction of the lateral jet in supersonic flow issued

from an idealized flat plate interaction. A more substantial experimental campaign incorporating pressure sensitive paint visualization would allow a more in depth assessment of the numerical codes.

## *4.2 Numerical Investigation of ajet in crossflow interaction on a body of revolution*

In the previous chapter the CFD method was shown to provide a reasonable prediction of the lateral jet issued from a flat plate into a supersonic crossflow. This model however is not representative of real world applications. A generic missile body provides a more realistic lateral jet in crossflow scenario. Gnemmi & Schäfer (2005) performed an experimental and numerical investigation of a generic missile body using CFX TASCflow. Using the same geometry and appropriate boundary conditions for the current CFD method allowed its accuracy to be tested using the experimental data and its performance compared to that of CFX TASCflow.

### 4.2.1 Grid & boundary conditions

The test model reported by Gnemmi & Schäfer (2005) is of a cone, cylinder, flare construction and is representative of a simple high-speed missile configuration (Figure 50). A 4mm diameter, circular, sonic jet is located on the cylindrical section of the body at x/D=4.2.

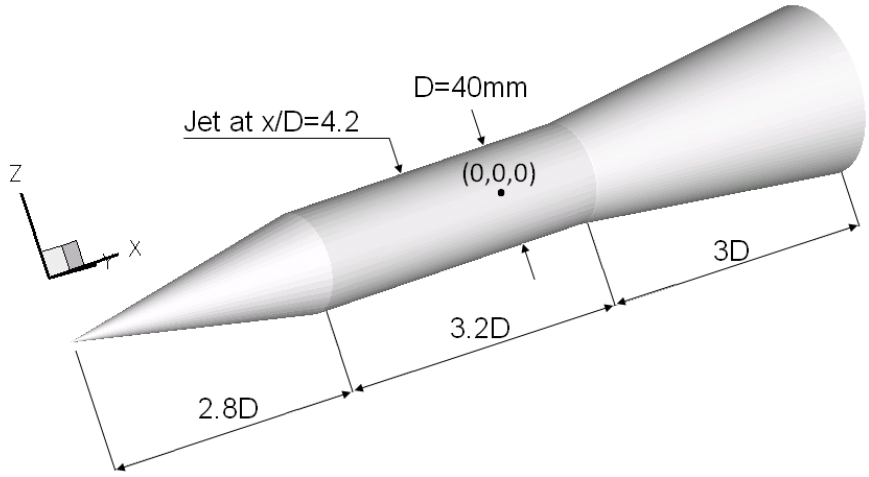


Figure 50 ISL body of revolution based on Gnemmi & Schäfer 2005

Due to the symmetrical nature of the problem it was possible to reduce the computational load by halving the computational domain. A structured, quad, multi-block, grid was constructed. Additional grid refinement was applied in the region which the jet plume was expected (Figure 51 & Figure 52) .The near wall cell sizes were adjusted until a $Y^+$ approximately equal to one was

achieved. A coarse grid consisting of 882,217 was initially constructed. This was then refined until satisfactory grid convergence had been achieved.

The jet nozzle was modelled as a cylinder 12mm in length. This was to allow a boundary layer to grow and for the flow in the jet exit plane to be calculated rather than imposed. The body wall and nozzle wall were modelled as solid, adiabatic walls with the no slip condition specified. A farfield boundary condition was set for the inlet, outlet and exterior using the Modified Riemann Invariants method with the inlet total temperature and total pressures specified. The jet source was modelled using a source boundary condition with specified total temperature and total pressure (Table 8).

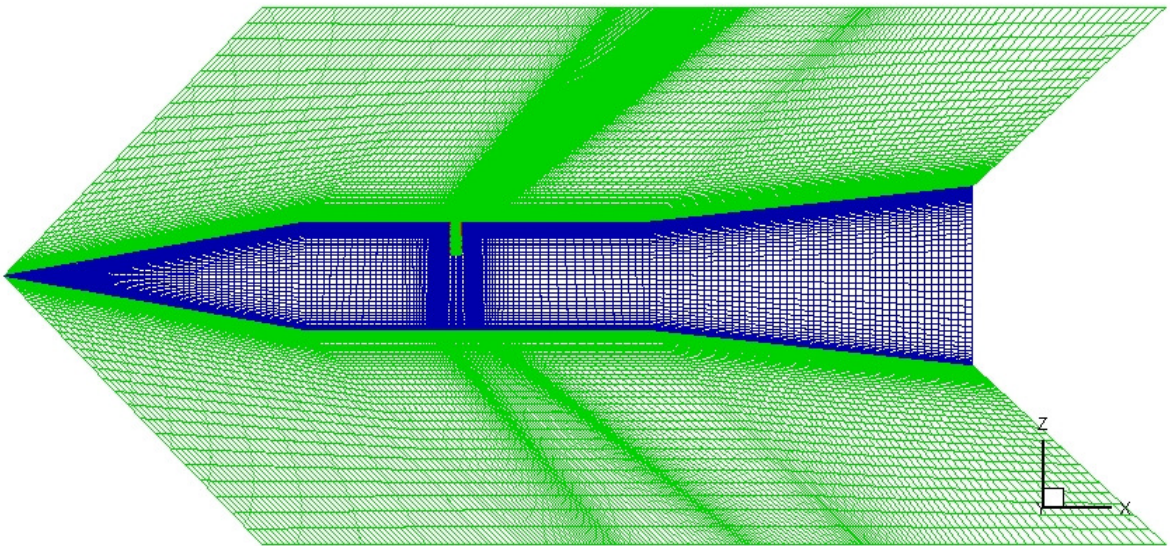

Figure 51 ISL body of revolution computational domain, symmetry plane.

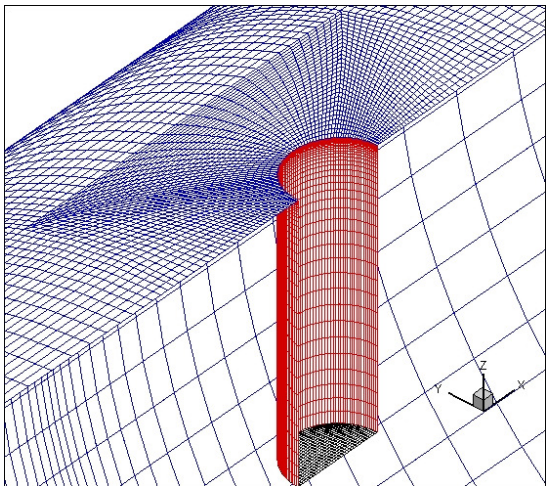

Figure 52 ISL body of revolution computational domain, close up of jet exit.

Table 12 Summary of crossflow and jet condition

| | |
|---|---|
| Freestream Mach number | 3 |
| Reynolds number | $Re_D = 2.1 \times 10^6$ |
| Jet pressure ratio | $P_{0j}/P_\infty$=50, 70, 97 |
| Jet gas | Air |
| Jet static temperature | $T_j$=223 K |
| Freestream static temperature | T=103.2 |
| Freestream static pressure | $P_\infty = 0.195 \times 10^5$ |
| Jet diameter | d=4 mm |
| Body diameter | D=40 mm |

## 4.2.2 Validation

### 4.2.2.1 Grid Independence

The initially constructed, coarse grid was refined twice with an approximate refinement ratio of two, resulting in three grids (Table 13). Each constituent block was refined by the same ratio and the cells adjacent to the body wall were kept the same height to maintain a $Y^+$ of one.

| Mesh #: | # Cells: | Description |
|---|---|---|
| 4 | 882,217 | Coarse |
| 2 | 1,740,316 | Medium |
| 1 | 3,468,528 | Fine |

Table 13 Number of cells in each mesh developed for the ISL body of revolution.

Normal force coefficient $C_Z$, axial force coefficient $C_X$ and pitching moment coefficient $C_m$ were calculated for the different grids and these criteria were used to check for grid independence as described in Chapter 3.5. Table 14 outlines the results from this grid convergence study. The Richardson's extrapolation method (Roache, 1998) was only utilised for the coefficient of axial force. This was due to the fact that solutions for normal force and pitching moment coefficients were non-monotonic. This was taken to be due to the inaccuracy of the coarse mesh as the percentage difference between solutions from the fine and medium grids was small (0.90% for $C_Z$ and 0.54% for $C_m$.

| | coarse (g=4) | medium (g=2) | fine (g=1) | zero (g=0) | $GCI_{1,2}$ | AR | $p_{con}$ | %diff1,2 |
|---|---|---|---|---|---|---|---|---|
| $C_Z$ | 1.01E-01 | 1.01E-01 | 9.97E-02 | non-monotonic | non-monotonic | non-monotonic | non-monotonic | 0.90% |
| $C_X$ | 2.40E-01 | 2.40E-01 | 2.39E-01 | 2.40E-01 | 0.12% | 0.09 | 2.00 | 0.29% |
| $C_m$ | -7.70E-01 | -7.75E-01 | -7.71E-01 | non-monotonic | non-monotonic | non-monotonic | non-monotonic | 0.54% |

Table 14 Grid convergence for the ISL body of revolution meshes 1, 2 and 4.

The accuracy of the solution was assessed qualitatively by comparing the distribution of coefficient of pressure along the interaction centreline found numerically to that found by ISL experimentally (Gnemmi & Schäfer, 2005). This comparison is presented in Figure 53 with two areas of interest highlighted. Detail A highlights the pressure rise and subsequent pressure plateau associated with upstream separation while Detail B shows the pressure peak associated with flow reattachment in greater detail. All three grids predict upstream separation at the same point ($x/d \approx -4.3$). The exact point of separation found experimentally is not known exactly

but inferring its location from the nearest experimental data point suggests that it is slightly further upstream, (x/d≈-4.5), than predicted numerically. The rise in coefficient of pressure associated with upstream separation is equally predicted by all three grids, ($C_p$=0.13). This is a slight over prediction when compared to the experimental vale of $C_p$=0.123. The peak pressure due to the upstream flow reattachment was calculated to be the same value, ($C_p$=0.58), from the medium and fine grids. The spatial resolution of experimental data points is not enough in this region to definitively define the experimental pressure peak. Downstream of the interaction limited experimental values are available. In the region they are available good agreement is found with the numerical results. Identical results are found in this region for all grids. No experimental data is available for the area in which the pressure rise associated with downstream flow reattachment occurs. This was an area of concern in the DLR idealised flat plate study (Chapter 4.1). Unlike the DLR idealised flat plate study the peak pressure in this region does not increase monotonically with further grid refinement. In fact it reduces in magnitude from the coarse grid to the medium grid, with the same peak value also calculated from the fine grid. This might suggest that the solution is converging in this region.

Values of upstream separation length, pressure rise due to the upstream separation, peak pressure due to flow reattachment and the minimum downstream Cp in the area of recirculation are equally calculated by meshes 1 and 2. On the basis of the assessment of grid independence Mesh 2 (1,740,316 cells) was selected.

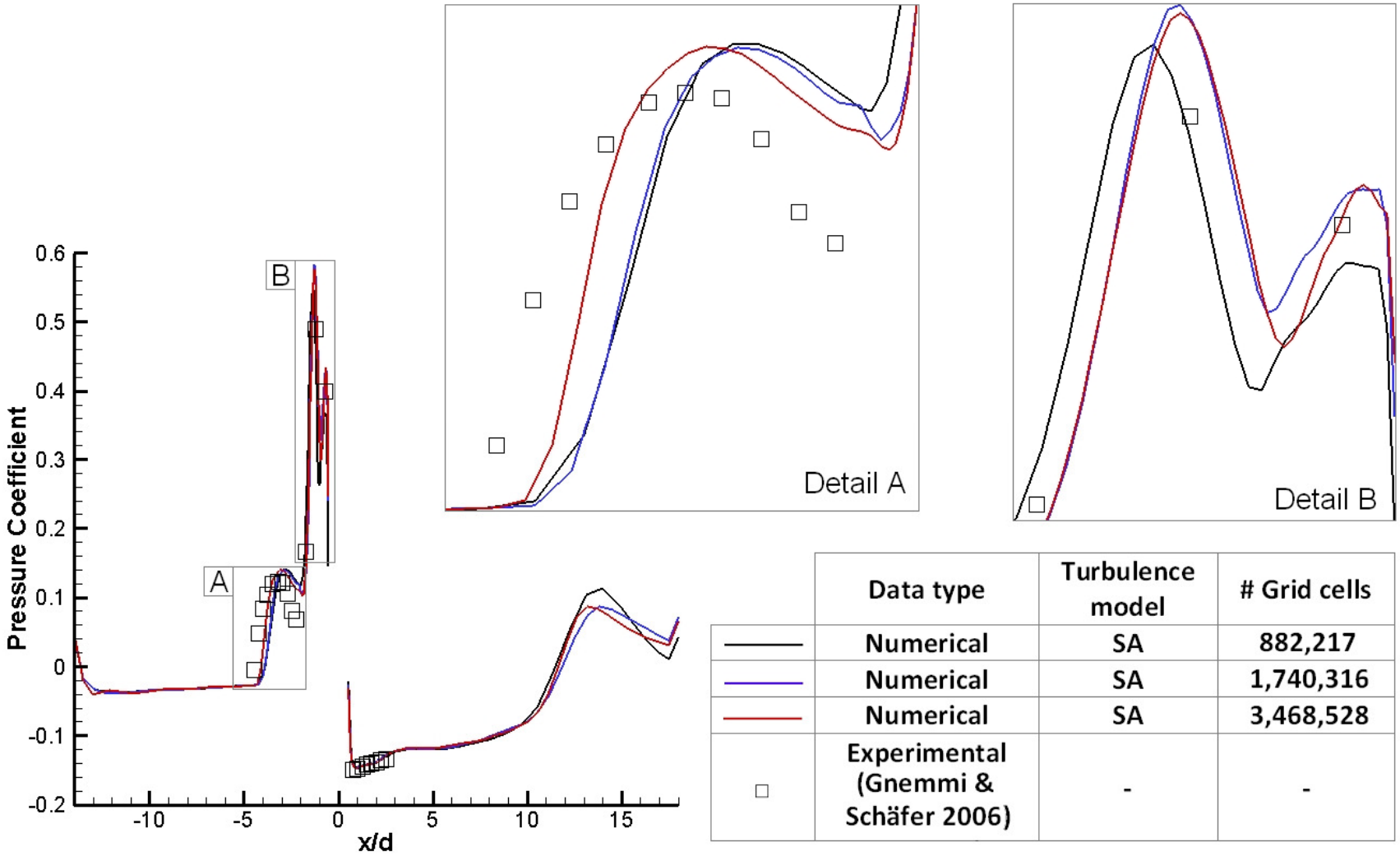


Figure 53 Comparison of coefficient of pressure distribution for the ISL body of revolution meshes 1, 2 and 4, PR=97.

### 4.2.2.2 Turbulence model study

The same four turbulence models trialled in the DLR idealised flat plate study, (SA, SST, SARC & k-ω), were once again trialled for the ISL body of revolution. These solutions were calculated using Mesh 2 (1.7 million cells (Table 9)) as selected in the grid independence study (Chapter 4.2.2.1). The distribution of coefficient of pressure along the interaction centreline was calculated for each turbulence model (Figure 54). In Detail A, the region in which the pressure rise caused by upstream flow separation occurs, very different pressure distributions are calculated by the different turbulence models. SARC does not capture the separation point well and over estimates the pressure rise. The pressure rise is under predicted by SST. The most accurate estimation of pressure rise is calculated from k-ω. SA also provides a reasonable estimation though not as close to the experimental data as k-ω. k-ω and SA predict the same separation point. The measured separation lies halfway between that predicted by SST and that predicted by k-ω and SA. In the region of peak pressure associated with upstream flow reattachment, (Figure 54, Detail B), SARC and SA best fit the experimental data points. Both SST and k-ω predict much higher pressure peaks than SARC and SA in this region. Downstream of the jet in the area of recirculation almost identical coefficient of pressure profiles are predicted which fit well with the experimental data. Based on this qualitative assessment SA was selected as the turbulence model which best predicts the lateral jet in crossflow issued from a body of revolution interaction.

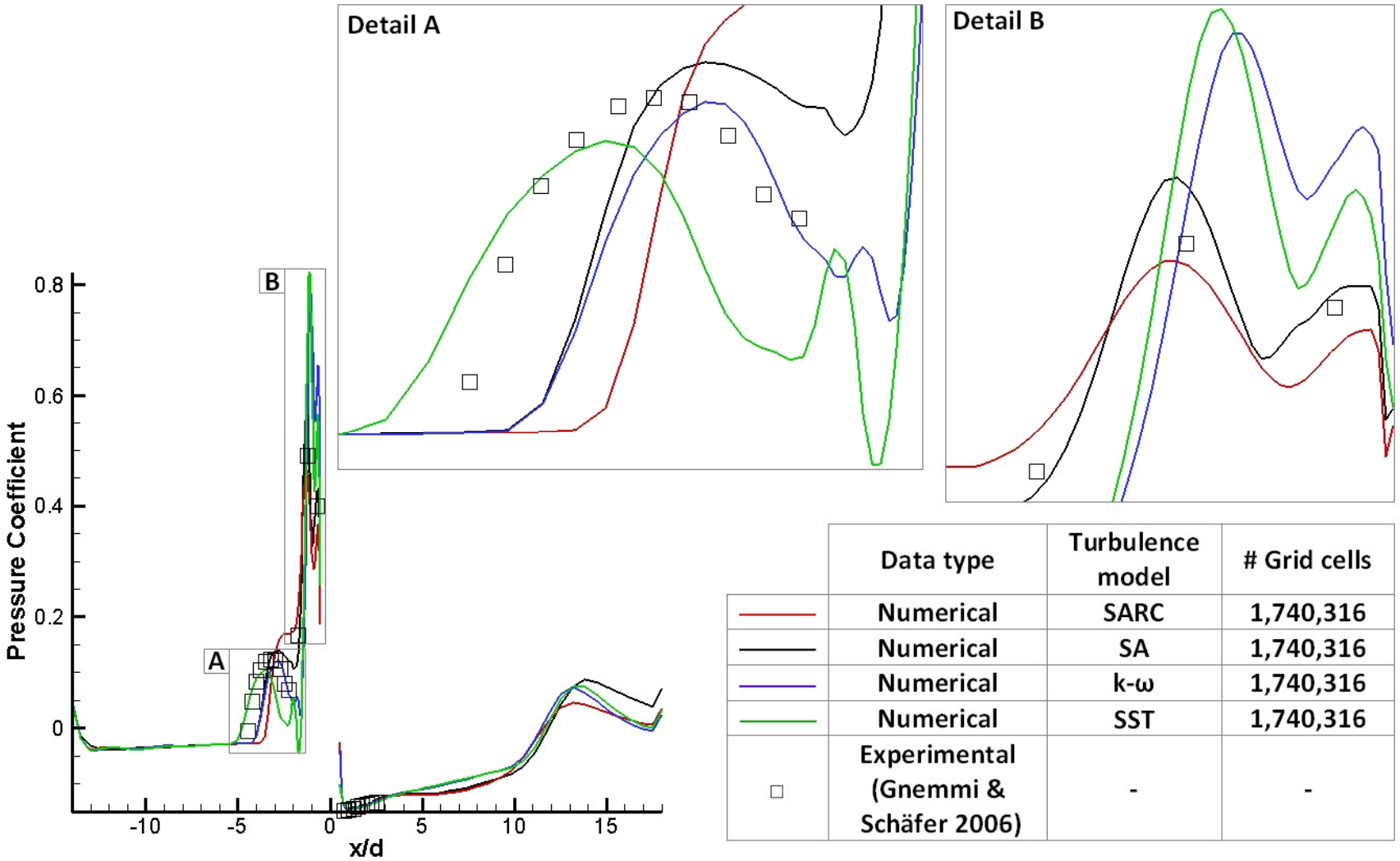


| | Data type | Turbulence model | # Grid cells |
|---|---|---|---|
| | Numerical | SARC | 1,740,316 |
| | Numerical | SA | 1,740,316 |
| | Numerical | k-ω | 1,740,316 |
| | Numerical | SST | 1,740,316 |
| □ | Experimental (Gnemmi & Schäfer 2006) | - | - |

Figure 54 Comparison of coefficient of pressure distribution for the ISL body of revolution for the turbulence trialed, PR=100.

### 4.2.3 Results and Discussion

#### 4.2.3.1 Comparison of experimental & numerical data

Gnemmi & Schäfer 2005 present numerical and experimental data for three body of revolution configurations. Three pressure ratios are investigated (PR=50, 70 & 97) at 0° angle of attack. The ISL experiment reported coefficients of pressure along the interaction centreline (longitudinal direction) and in the circumferential direction at x/d=0.

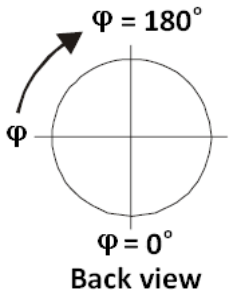


Figure 55 Circumferential coordinate system.

Figure 56 presents measured (ISL experiment) and numerical (Cranfield, Cobalt & ISL CFX TASCflow) pressure coefficient distributions. Upstream separation is predicted by both numerical codes. Cobalt over predicted the initial pressure rise (12%) and subsequent pressure plateau caused by the flow separation while CFX TASCflow under predicted this rise (9%). The ISL experiment measured a decrease in pressure coefficient between the upstream separation line and the flow reattachment (x/d≈-1.75). This decrease in pressure is not predicted well by Cobalt but captured by CFX TASCflow. The area of under-pressure in the recirculation region downstream of the interaction is well predicted by both codes with Cobalt performing slightly better.

The pressure distribution around the circumference of the body at x/d=0 is presented in Figure 57. The effect of the jet interaction is felt up to ϕ=110°. The pressure distribution measured experimental is well predicted by the numerical codes with the biggest discrepancy being at ϕ≈155 ($\Delta C_p$=0.013 & $\Delta C_p$=0.019 for Cobalt and CFX TASCflow respectively). The spatial resolution of the pressure transducers is not fine enough to accurately measure the pressure peak at ϕ≈165. An experimental data point at this location gives a pressure coefficient value greater (8%) than the maximum presented by CFX TASCflow. Cobalt predicts a much higher pressure peak but it is impossible to tell whether this is a more accurate prediction.

Overall the pressure coefficient distribution was well predicted by Cobalt. Numerical results and their comparisons to equivalent experimental results for all pressure ratios investigated (PR=50, 70 & 97) are presented in Appendix F.

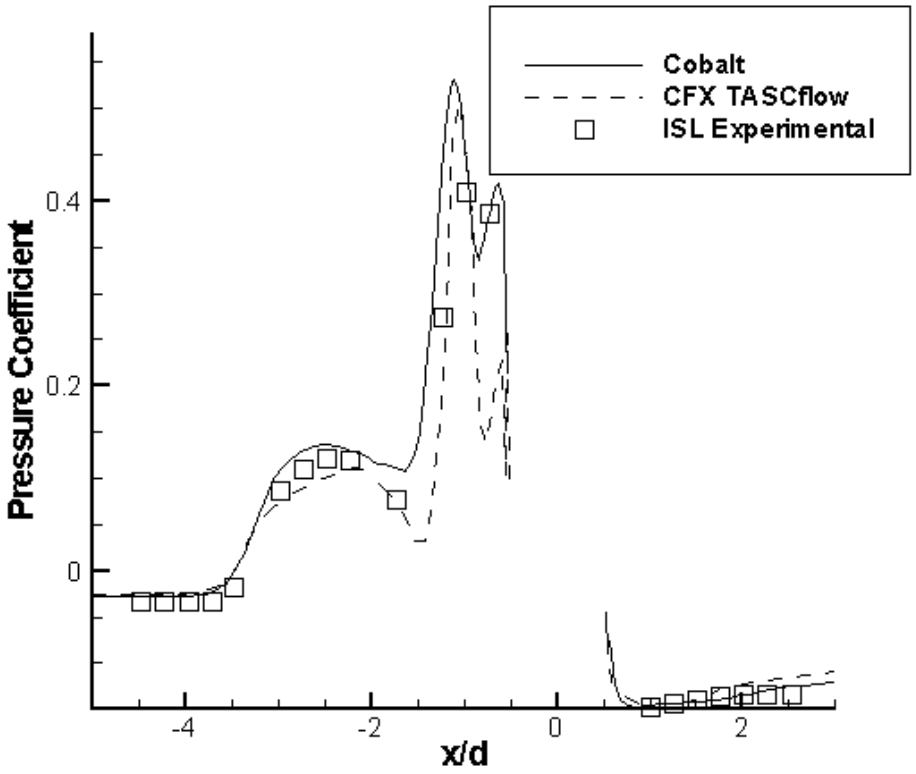


Figure 56 Coefficient of pressure in the longitudinal direction for the ISL BoR, PR=50.

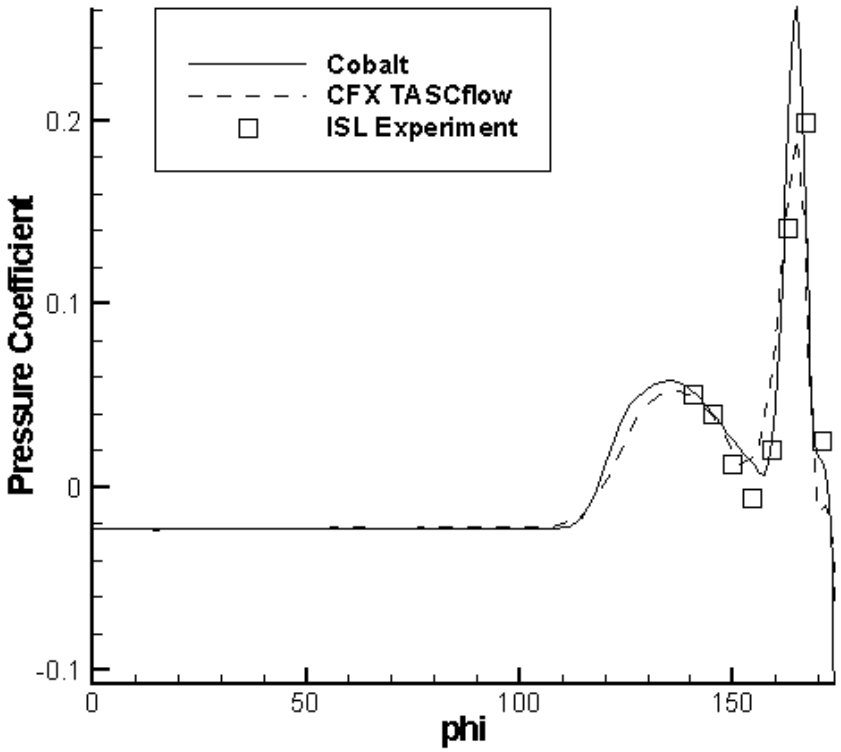


Figure 57 Coefficient of pressure in the circumferential direction for the ISL BoR, PR=50.

### 4.2.4 Conclusions

It was considered that a sufficient level of grid independence was achieved with a mesh consisting of 1.7 million cells. Using this mesh a turbulence model study was undertaken. Of the turbulence models trialled SA provided the best prediction for a lateral jet in supersonic crossflow issued from a body of revolution. Cobalt can be used to perform a reasonably accurate prediction of the lateral jet in supersonic flow issued from a body of revolution. Experimentally measured force and moments would allow a more in depth assessment of the numerical codes for this configuration.

## *4.3 Numerical Investigation of a jet in crossflow on a body of revolution at incidence*

In §4.2 the current CFD method was shown to give a reasonable prediction of the lateral jet issued from a body of revolution into a supersonic crossflow. In real world applications a body of revolution is subjected to different angles of attack. At different angles of attack the flowfield around a lateral jet in supersonic crossflow is substantially different. To test the CFD method for different angles of attack the DLR generic body of revolution was modelled. Experimental data for this model exists over an angle of attack range from -10° to 15°. This experimental data consisting of coefficient of pressure distributions along the interaction centreline was used to test the accuracy of the CFD method. The influence of angle of attack, pressure ratio and Reynolds number on the interaction was then investigated.

### 4.3.1 Grid & boundary conditions

The test model used by DLR in Stahl et al. (2008) (Figure 58) is almost identical to the model used by ISL in Gnemmi & Schäfer 2005. Both bodies are of a cone, cylinder, flare construction. The only difference is the location of the jet. In the ISL model the jet nozzle was located at 4.2 diameters downstream of the nose tip, whereas the jet nozzle is located at 4.3 diameters downstream for the DLR model. This difference means direct comparisons cannot be made between the two. This was not an issue as the no cases were carried out with a common pressure ratio. If numerical cases were to be run with the only difference being the nozzle location the differences are expected to be minor except perhaps in the region where the body transitions to the flare afterbody as this is close to the flow reattachment point for some some configurations.

A structured, multi-block, “C” shaped mesh was generated around the missile body using Gridgen. The mesh was refined in the near wall regions and in the jet exit plane (Figure 59). Cells adjacent to solid boundaries were adjusted until a $y^+ \approx 1$ was achieved. It was assumed that the interaction was symmetrical along the X-Z plane which allowed the computational domain to be reduced by one half. The jet nozzle was modeled as a cylinder of 12mm in length (Figure 60). This was to allow the build of a boundary layer in the nozzle and to enable the flow at the exit plane to be predicted and not simply imposed i.e. the cross flow will affect the exit flow of the duct. In Stahl et al. (2008) the jet nozzle was described as cylindrical with sonic flow at its exit. No description of the boundary layer in the nozzle is given.

The inlet, outlet and exterior boundaries were modeled using modified Riemann Invariants as a farfield boundary condition. The jet source was modelled using a source boundary condition with specified total temperature and total pressure (Table 8).

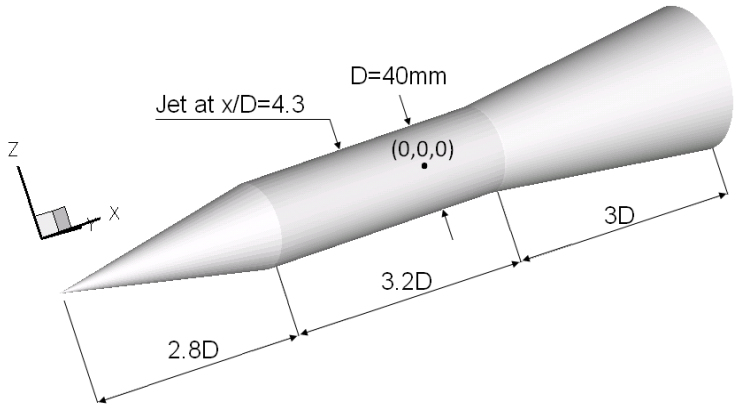


Figure 58 DLR wind tunnel test model, adapted from Stahl et al. 2008.

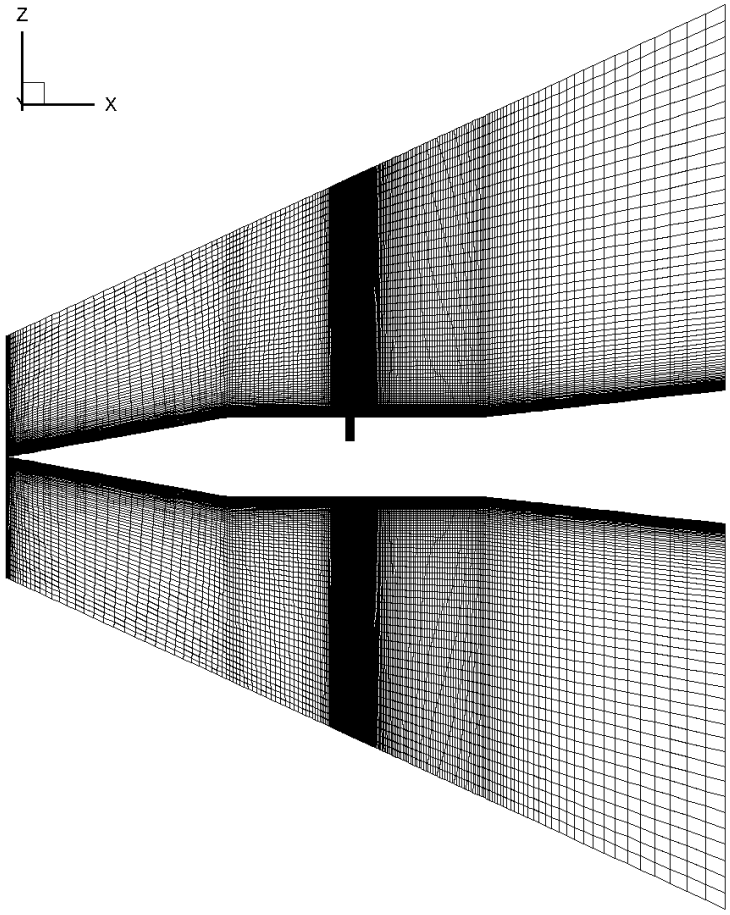


Figure 59 DLR body of revolution computational domain, symmetry plane.

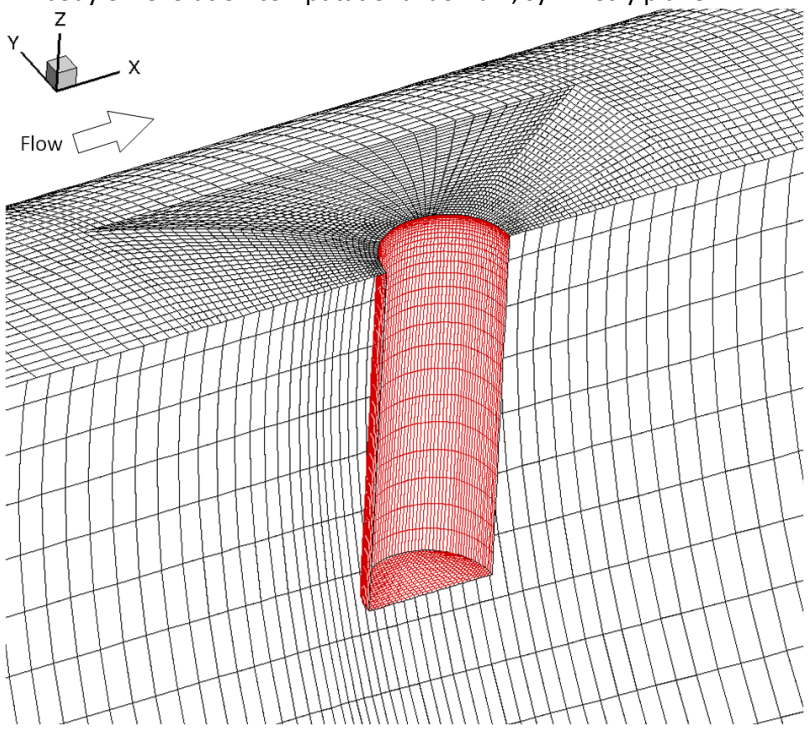


Figure 60 DLR body of revolution computational domain, close up of jet exit.

| | |
|---|---|
| Freestream Mach number | 2.8, 3.0 |
| Reynolds number | $Re_D = 1.9 \times 10^6$, $0.5 \times 10^6$ |
| Jet pressure ratio | $55 \leq P_{0j}/P_\infty \leq 300$ |
| Angle of incidence | $-10° \leq \alpha \leq 15°$ |
| Jet gas | Air |
| Jet total temperature | $T_{0j}$=280 K |
| Freestream total temperature | $T_\infty$=280 K |
| Jet diameter | d=4 mm |
| Body diameter | L=40 mm |

Table 15 Summary of crossflow and jet conditions

### 4.3.2 Validation

#### 4.3.2.1 Grid Independence

The first mesh generated consisted of 1,460,369 cells using the test conditions in Table 8 with a pressure ratio of 150. This pressure ratio was chosen as it was the highest pressure ratio for the cases with the body at incidence. This mesh was then refined twice using a refinement ratio approximately equal to 2. This resulted in three grids as shown in Table 16.

| Mesh #: | # Cells: | Description |
|---|---|---|
| 4 | 1,460,369 | Coarse |
| 2 | 2,939,664 | Medium |
| 1 | 5,865,598 | Fine |

Table 16 Number of cells in meshes generated for the DLR body of revolution.

Grid convergence was assessed using the method outlined in § 3.5. The results of this assessment are presented in Table 17. For increasing grid refinement, calculated values of normal force, axial force and pitching moments were monotonic. This allowed the Richardson's Extrapolation method (Roache, 1998) to be utilized. The axial force coefficient can be considered to be converged with a grid convergence index (GCI) of 0.13% and a difference in $C_X$ of 0.31% between the fine and medium

grid. Larger differences were found for the normal force and pitching moment coefficients (1.51% and 2.17% respectively).

As an additional assessment of grid convergence the coefficient of pressure distribution along the interaction centerline (ϕ=180° as defined in Figure 61) was plotted for each mesh (Figure 62). This allowed the areas in which the solutions differed to be highlighted.

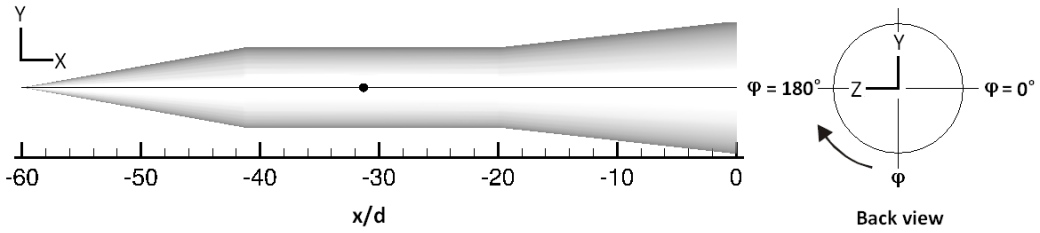


Figure 61 Definition of circumferential location ϕ.

The predicted coefficient of pressure distribution upstream of the jet injection predicted by the three meshes is almost identical, with the same separation line, pressure plateau and pressure peaks. Moving downstream of the jet this trend continues with solutions from all three meshes agreeing until the region of increasing pressure due to flow reattachment on the body is encountered (16≤x/d≤19). The peak pressure coefficient predicted in this area decreases monotonically with increases in grid refinement with the $C_p$ value differing by 0.012 between the fine and medium grids and by 0.007 between the medium and coarse grids.

| | **coarse (g=4)** | **medium (g=2)** | **fine (g=1)** | **zero (g=0)** | **$GCI_{1,2}$** | **AR** | **$p_{con}$** | **%diff1,2** |
|---|---|---|---|---|---|---|---|---|
| $C_Z$ | 1.24E-01 | 1.25E-01 | 1.27E-01 | 1.24E-01 | 0.63% | 0.07 | 2.00 | 1.51% |
| $C_X$ | 2.35E-01 | 2.35E-01 | 2.36E-01 | 2.35E-01 | 0.13% | 0.13 | 2.00 | 0.31% |
| Cm | -9.64E-01 | -9.69E-01 | -9.91E-01 | -9.62E-01 | 0.91% | 0.06 | 2.00 | 2.17% |

Table 17 Grid convergence for the DLR body of revolution at 0° aoa, PR=150, meshes 1, 2 and 4, see § 3.5 definitions and method.

Based on the grid convergence assessment above and the comparison of pressure distributions for the fine mesh the solution was considered to be grid independent for an angle of attack of 0°.

The grid constructed to model the DLR body of revolution was done so with the purpose of investigating the body at various angles of attack. Changing the angle of attack changes the flowfield. It therefore cannot be assumed that because a solution was considered grid independent for one angle of attack that this is the case at another angle of attack. This observation led to grid convergence being assessed at the angle of attack extremes (aoa=-10° and 15°). The results of the grid convergence assessment for aoa=15 are presented in Table 18. For all criteria ($C_Z$, $C_X$ and $C_m$) the solutions were considered independent of further spatial refinement with the highest GCI for the normal force coefficient (0.04%) and the largest discrepancy between grids presented by the axial force coefficient (0.07%).

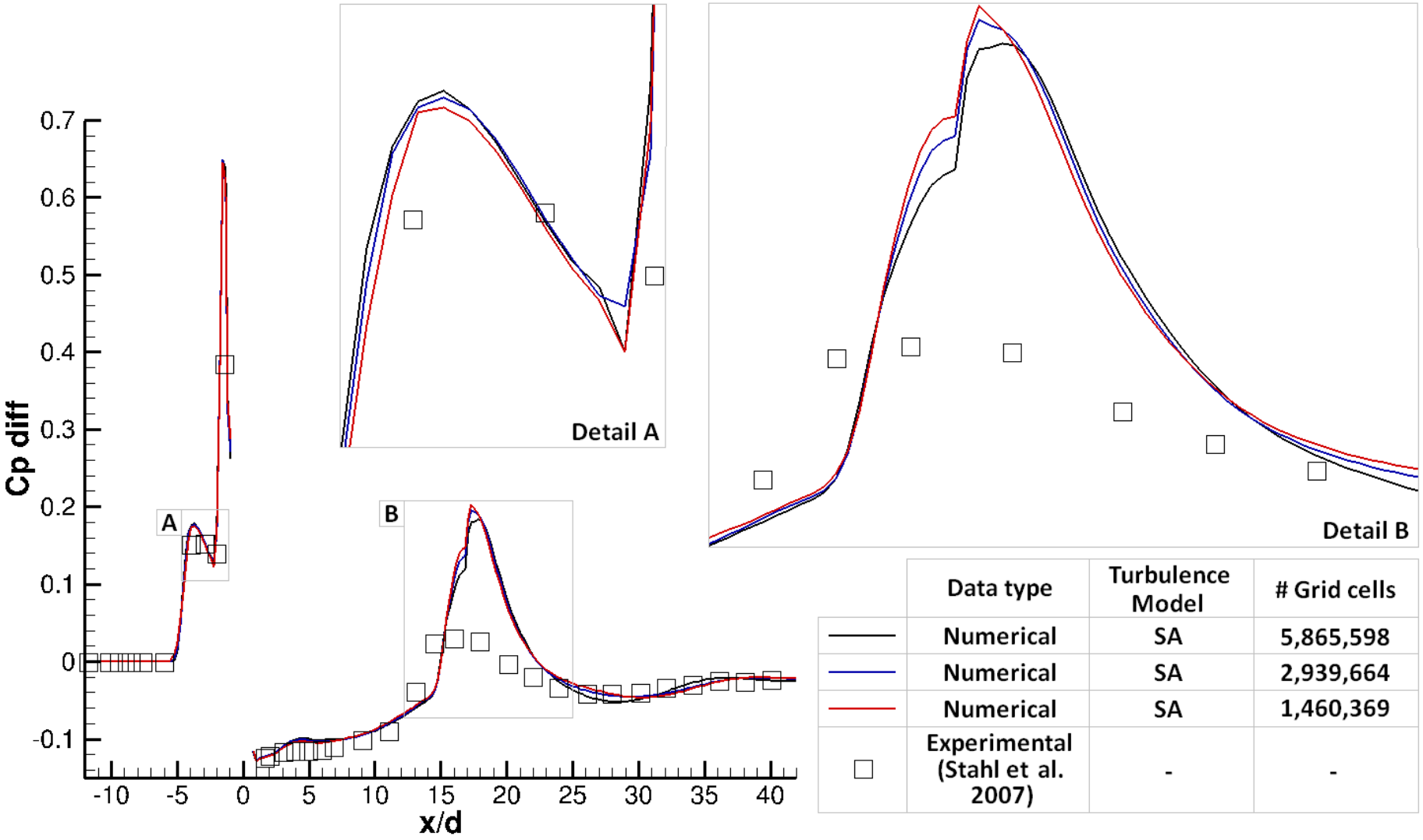


Figure 62 Comparison of coefficient of pressure distribution for the DLR body of revolution meshes 1, 2 and 4, PR=150, 0° aoa, ϕ=180°.

| | coarse (g=4) | medium (g=2) | fine (g=1) | zero (g=0) | $GCI_{1,2}$ | AR | $p_{con}$ | %diff1,2 |
|---|---|---|---|---|---|---|---|---|
| $C_Z$ | 2.08E+00 | 2.08E+00 | 2.08E+00 | 2.08E+00 | 0.04% | 1.00 | 1.09 | 0.04% |
| $C_X$ | 7.96E-01 | 7.96E-01 | 7.97E-01 | 7.96E-01 | 0.03% | 0.08 | 2.00 | 0.07% |
| $C_m$ | -1.20E+01 | -1.20E+01 | -1.20E+01 | -1.20E+01 | 0.01% | 0.08 | 2.00 | 0.02% |

Table 18 Grid convergence for the DLR body of revolution at 15° aoa, meshes 1, 2 and 4

The pressure coefficient distributions predicted by the three meshes along the centreline of the interaction are compared in Figure 63. As was the case for the body at 0°, agreement in the upstream region is good with the largest discrepancies found in the region of peak pressure associated with flow reattachment downstream of the jet. Based on the results presented in Table 17 and the comparisons of pressure distributions the solutions for the fine grid were considered to be reasonably independent of further spatial refinement at this angle of attack.

A solution for the body at -10° angle of attack was only calculated using the medium and fine grids. Because only two levels of refinement were used the Richardson's Extrapolation method could not be used. The convergence at this angle of attack was assessed only by comparing the distribution of the pressure coefficient along the interaction centerline. This comparison is presented in Figure 64. Overall a similar pressure distribution is predicted by both grids with the largest disagreements found at local pressure peaks. The initial pressure rise associated with flow separation upstream of the interaction is predicted to be 2.7% larger by the fine mesh. The pressure peak caused flow reattachment in front of the interaction is also predicted a larger coefficient of pressure value (2.6% larger). Downstream of the interaction the pressure peak in the area of recirculation ($x/d \approx 13.4$) the fine grid predicts a pressure coefficient 9.8% larger than that predicted by the medium grid. The agreement between solutions for the coefficient of pressure distribution for the medium and the fine grid is comparable to the agreement for the body at 15° angle of attack. The fine grid was therefore considered to be reasonably independent of further spatial refinement for an angle of attack of -10°.

As the solutions were considered reasonably independent of the grids for -10°, 0° and 15° it was assumed that the solution was also reasonably independent of further spatial refinement when the body was at an angle of attack of 10°.

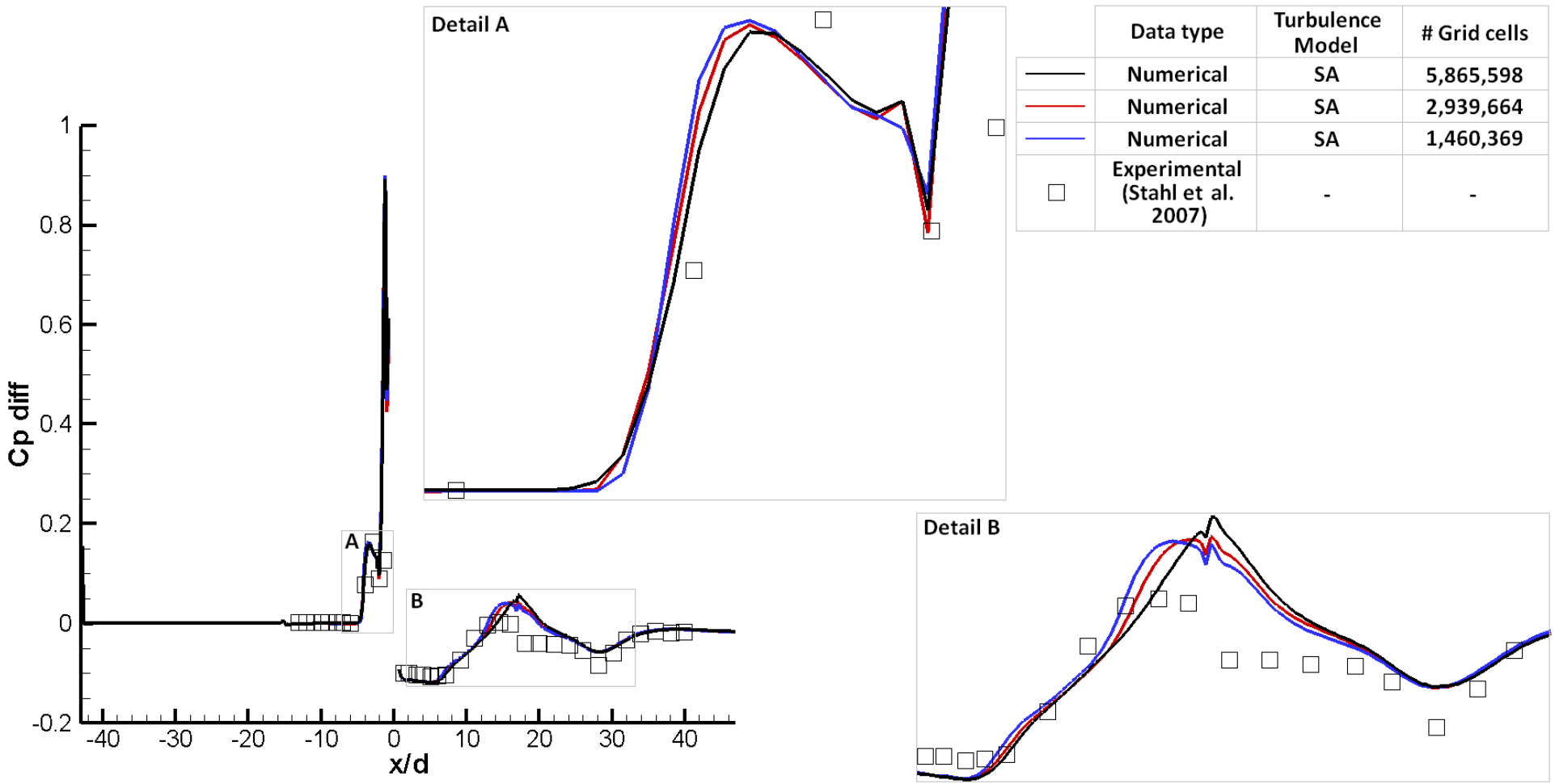


Figure 63 Comparison of coefficient of pressure distribution for the DLR body of revolution meshes 1, 2 and 4, PR=150, 15° aoa, ϕ=180°.

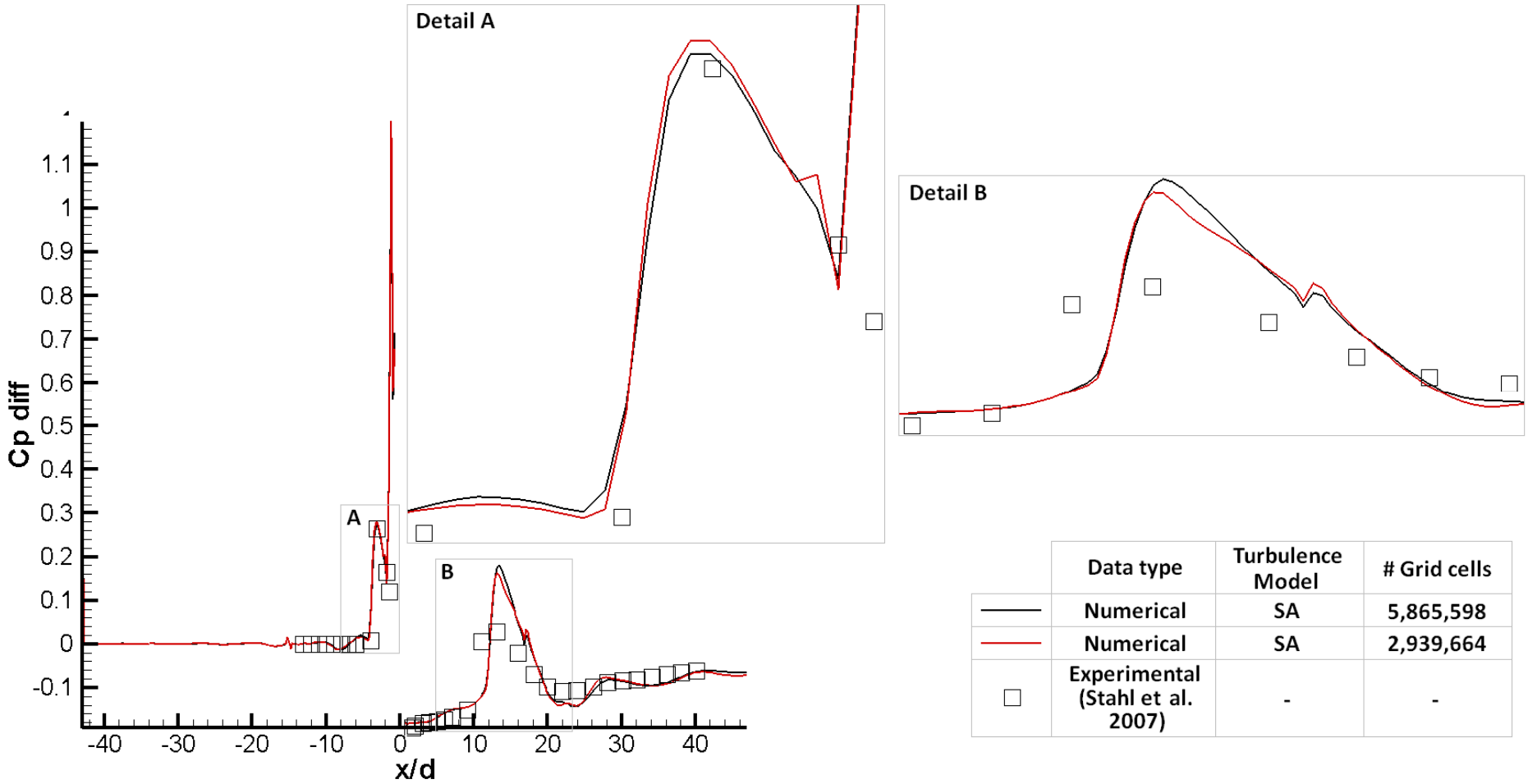


| | Data type | Turbulence Model | # Grid cells |
|---|---|---|---|
| ——— | Numerical | SA | 5,865,598 |
| ——— | Numerical | SA | 2,939,664 |
| □ | Experimental (Stahl et al. 2007) | - | - |

Figure 64 Comparison of coefficient of pressure distribution for the DLR body of revolution meshes 1, 2 and 4, PR=150, -10° aoa, ϕ=180°.

### 4.3.2.2 Turbulence model study

Four turbulence models were trialed (SA, SST, SARC and k-ω) at the same angles of attack investigated in the grid convergence assessment (-10°, 0° and 15°). The different turbulence models were then assessed by comparing the coefficient of pressure distribution along the interaction centerline with experimental data (Stahl et al. 2008). The results of this assessment carried out with the body at an angle of attack of 0° are presented in Figure 65. For this configuration each turbulence model predicts a different separation point. The spatial resolution of the experimental data points does not allow for an exact experimental separation line. However a range in which this separation line occurs can be defined (-5.95≤x/d≤-3.96). The separation line predicted by SST falls outside this range. SST most accurately predicts the pressure rise associated with separation (ΔCp=0.152). SARC over predicts this pressure rise by 36%. In the region of separated flow upstream of the bow shock the experimentally measured coefficient of pressure distribution plateaus. SA provided the best fit to the experimental data in this region and was considered to be the turbulence model which best predicted the pressure distribution upstream of the interaction.

The pressure distribution downstream of the jet is dominated by a pressure peak caused by flow reattachment (13≤x/d≤28). As was the case with a lateral jet issuing from a flat plate into a supersonic freestream (§4.1) the reattachment region is not well predicted by any of the turbulence models. The peak pressure coefficient in this region is over predicted by all turbulence models with the largest over prediction (ΔCp=0.155) by SA and the smallest by SARC ((ΔCp=0.053).

In the region of low pressure between the barrel shock and flow reattachment (4≤x/d≤13) agreement between the predicted and measured pressure distribution is closer. The distribution predicted by SA and SARC fits well to the experimental data while the distribution predicted by SST and k-ω over predicts the pressure coefficient by 0.027 at the point of maximum difference (x/d=6.9).

Downstream of the reattachment region x/d>28 the predicted pressure distribution fits the measured distribution well for all the turbulence models. In this region no turbulence can be said to perform better than the others.

Taking all the above into consideration SARC was considered to be the turbulence model that best predicted the pressure distribution downstream of the jet injection for this angle of attack. This conclusion, however, led to a conflict for in the selection of the best overall turbulence model to simulate the jet interaction. SA was considered to be the most accurate turbulence model, despite its obvious error in the region of flow reattachment downstream of injection. It is the best performing turbulence model in all other areas.

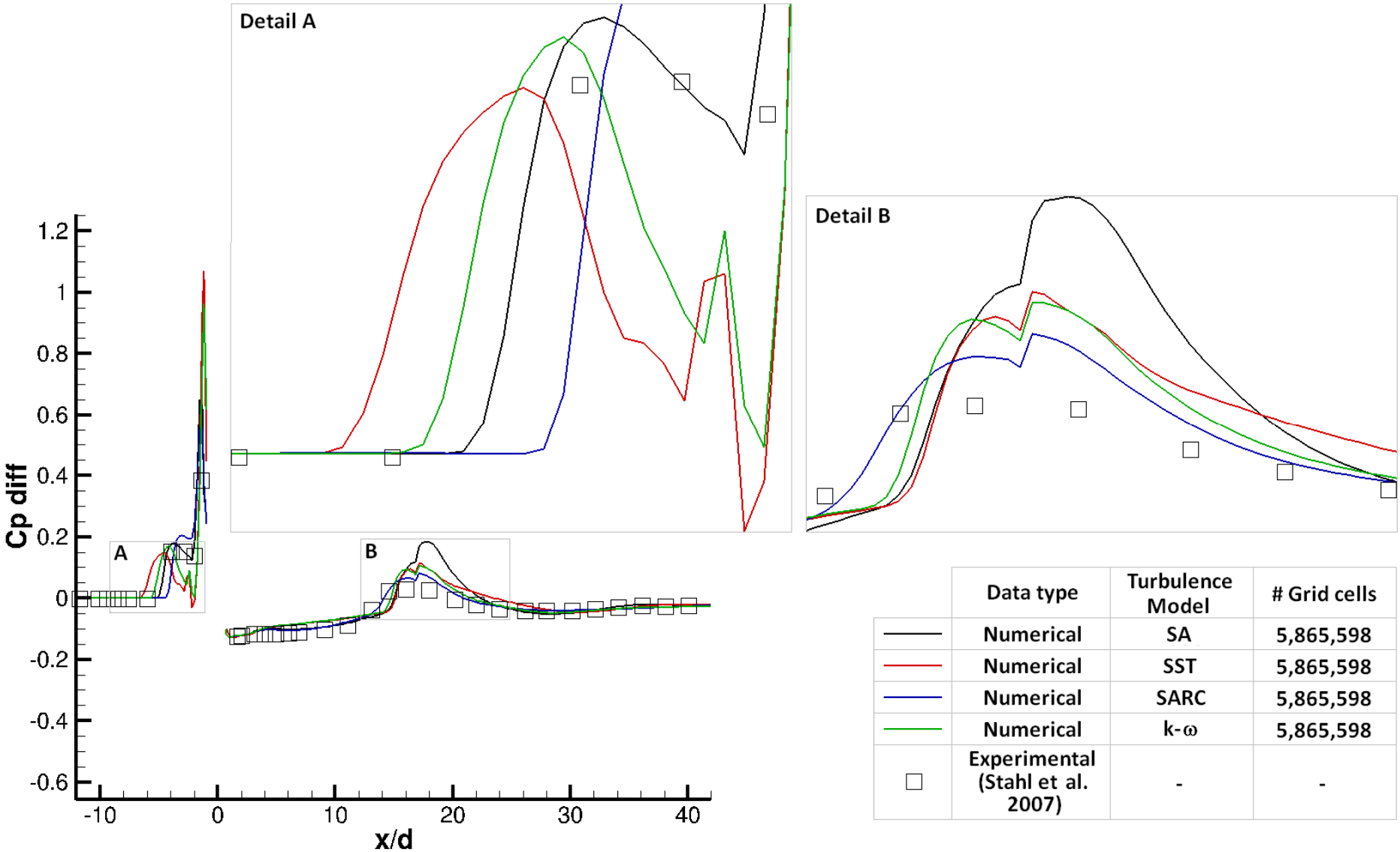


Figure 65 Comparison of coefficient of pressure distribution for the DLR body of revolution for candidate turbulence models, PR=150, 0° aoa, ϕ=180°.

The same assessment was carried out for the DLR body at -10° and 15° angle of attack. The results of these assessments are presented in Figure 66 and Figure 67 respectively. At both of these angles of attack SA was considered to best fit the experimental data points upstream of the jet interaction. In this region the agreement between the SA predictions and the experimental data was good for the -10° angle of attack case. For the 15° angle of attack case the choice of turbulence model is not so clear cut, but SA clearly best predicts the pressure rise associated with upstream flow separation. As was the case for the body at 0° incidence, SARC provides the best fit to experimental data in the downstream region when the body is at -10° angle of attack. When the body was at 15° angle of attack the turbulence model with the best fit to experimental data in the region downstream of the jet was not so clear cut. SST best predicts the drop in pressure coefficient at x/d≈17 and hence was selected as the best performing turbulence model in this region. The results of the turbulence model assessment for all angles of attack investigated are presented in Table 19.

| | **Upstream (x/d<0)** | | | | **Downstream (x/d>0)** | | | |
|---|---|---|---|---|---|---|---|---|
| **AOA** | **SA** | **SST** | **k-ω** | **SARC** | **SA** | **SST** | **k-ω** | **SARC** |
| 0° | ✓ | | | | | | | ✓ |
| -10° | ✓ | | | | | | | ✓ |
| 15° | ✓ | | | | | ✓ | | |

Table 19 Summary of turbulence models considered the best fit to experimental data.

For all angles of attack SA performed best in the upstream region. In the downstream regions SA performs well except in the region of flow reattachment. Overall SA was considered the turbulence model which best predicts the lateral jet in supersonic flow issued from a body of revolution at incidence interaction of the turbulence models trialed.

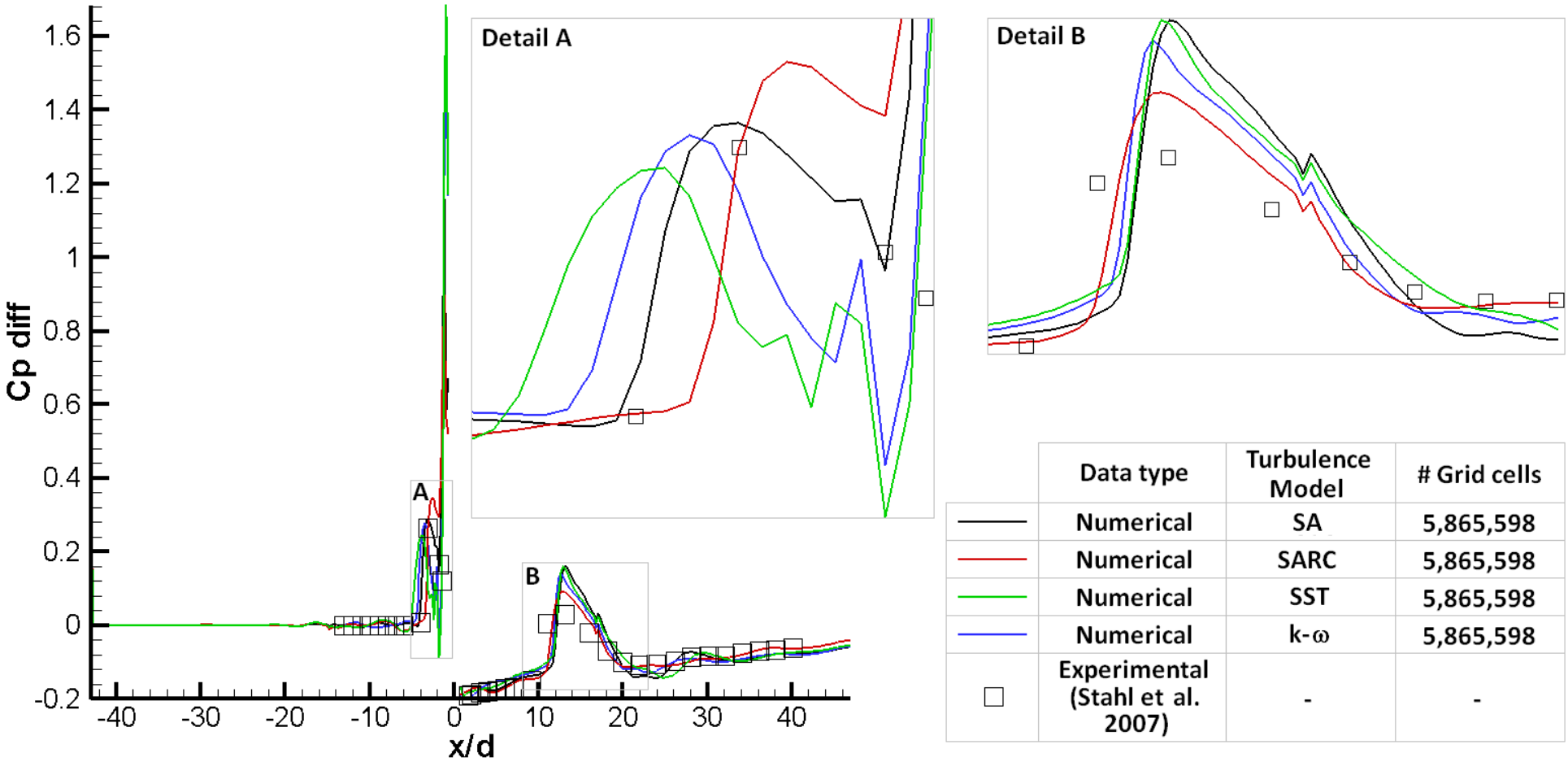


| | Data type | Turbulence Model | # Grid cells |
|---|---|---|---|
| | Numerical | SA | 5,865,598 |
| | Numerical | SARC | 5,865,598 |
| | Numerical | SST | 5,865,598 |
| | Numerical | k-ω | 5,865,598 |
| □ | Experimental (Stahl et al. 2007) | - | - |

Figure 66 Comparison of coefficient of pressure distribution for the DLR body of revolution for candidate turbulence models, PR=150, -10° aoa , ϕ=180°.

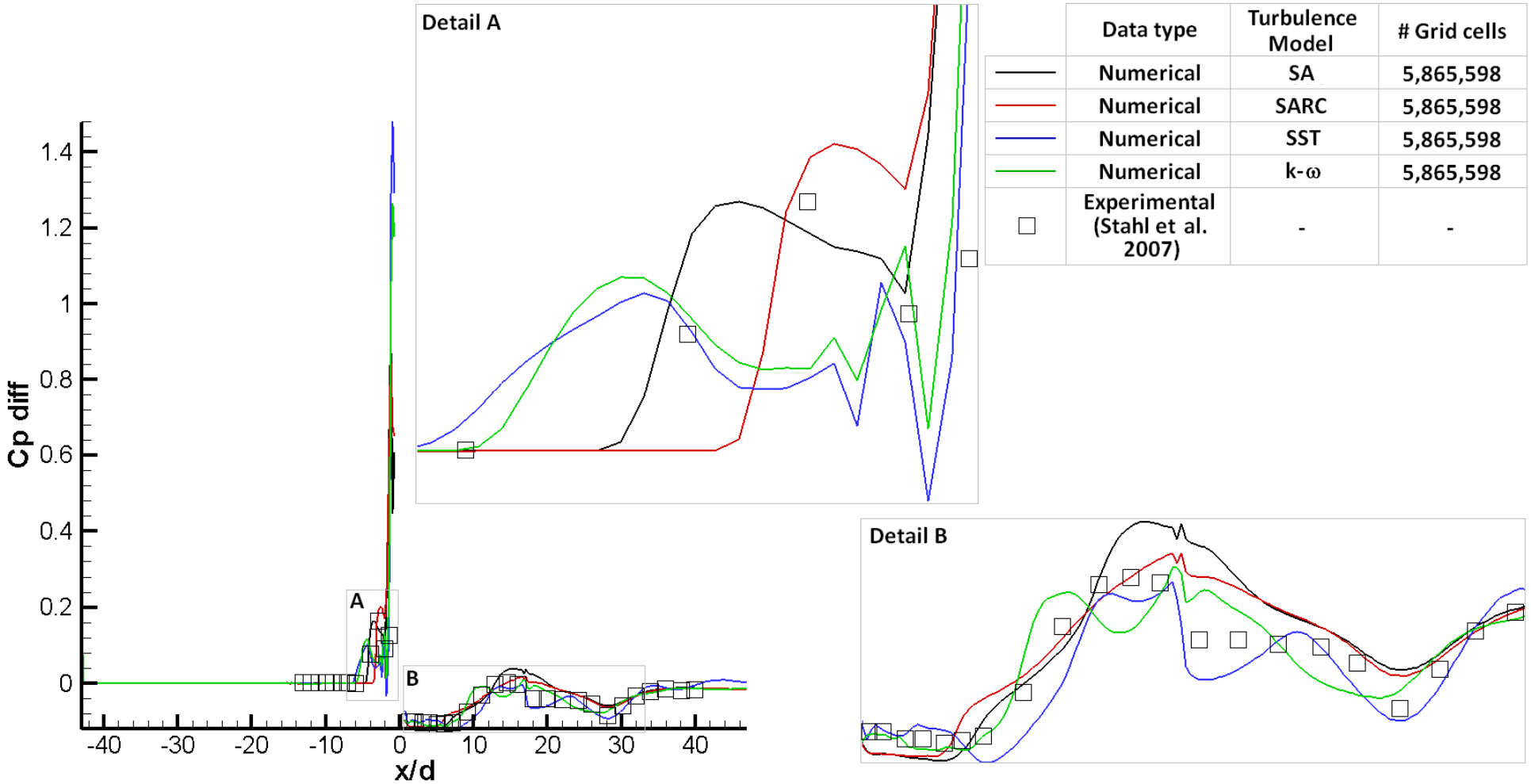


| | Data type | Turbulence Model | # Grid cells |
|---|---|---|---|
| | Numerical | SA | 5,865,598 |
| | Numerical | SARC | 5,865,598 |
| | Numerical | SST | 5,865,598 |
| | Numerical | k-ω | 5,865,598 |
| □ | Experimental (Stahl et al. 2007) | - | - |

Figure 67 Comparison of coefficient of pressure distribution for the DLR body of revolution for candidate turbulence models, PR=150, 15° aoa, ϕ=180°.

### 4.3.3 Results and Discussion

#### 4.3.3.1 Investigation of the parameters effecting the JICF on a body of revolution

Three parameters which influence the lateral jet in supersonic crossflow interaction have been investigated: namely, the pressure ratio, the body angle of attack and the freestream Reynolds number. The coefficient of pressure along the interaction centerline has been calculated for each case both with and without the jet. The pressure distributions were then subtracted and plotted as Cp diff (Equation 49). This was done to remove the influence of the body geometry and to isolate the influence of the jet.

$$C_{p\ diff} = C_{P_J} - C_{P_{NJ}} \qquad \text{Equation 49}$$

Where $C_{P_J}$ and $C_{P_{NJ}}$ are the coefficients of pressure with and without a side jet respectively.

***The influence of pressure ratio on the JICF on a body of revolution***

The pressure ratio was varied from 55 to 200 to investigate the influence of jet pressure on the wall pressure distribution. Pressure ratios were chosen to match those used by Stahl et al. 2008. Figure 68 shows $C_{p\ diff}$ plotted for the pressure ratios investigated (). Three areas of interest are highlighted. Firstly Detail A highlights the effect of upstream flow separation on the wall pressure distribution. Secondly Detail B presents a more in depth look at the pressure rise associated with the bow shock in front of the jet. Finally Detail C shows the region of flow reattachment downstream of the jet injection. From Detail A it can be seen that the upstream separation line ($L_u$ defined in Figure 69) moves further upstream as the pressure ratio increases. This relationship is almost linear (Figure 70). The pressure rise associated with the flow separation increases from $C_{p\_diff}$=0.167 to $C_{p\ diff}$=0.178 (an increase of 6.6%) as the pressure ratio is increased from 55 to 200. The peak pressure associated with the bow shock also increases (58%) with increases in pressure ratio. An increase in high surface pressure in front of the jet acts to augment the jet thrust. The downstream flow reattachment point moves downstream with increases in pressure ratio causing the area of

low pressure behind the barrel shock to extend further downstream. This low pressure region acts to diminish the jet thrust force and hence reduce the jet effectiveness. Increasing the pressure ratio both produces a net force upstream of the jet which augments the jet thrust and a net force downstream of the jet which counteracts the jet thrust. It is the balance between these net force changes that dictates whether increasing the pressure increases the efficiency of the jet. The total forces and moments on the body are investigated in Chapter 4.4.

From the definition of pressure ratio (Equation 6) it can be that an increase in pressure ratio with no change in freestream conditions is achieved by an increase in jet total pressure.

$$PR = \frac{P_{0j}}{P_\infty} \qquad \text{Equation 50}$$

When the jet total pressure is increased and the sonic jet exit condition maintained the ratio between static and total jet pressure remains constant due to the isentropic pressure relationship (Equation 51). Hence an increase in jet total pressure leads to an increase in jet static pressure.

$$\frac{P_j}{P_{0j}} = \left(1 + \frac{\gamma - 1}{2} \cdot {M_j}^2\right)^{\frac{\gamma-1}{\gamma}} \qquad \text{Equation 51}$$

Momentum is defined in Equation 52. Analyzing this equation it can be seen that an increase in jet static pressure while the other variables remain constant causes an increase in momentum.

$$Momentum = \rho_j A V_j = \frac{P_j}{RT_j} \cdot A \cdot M_j \cdot \sqrt{\gamma R T_j} \qquad \text{Equation 52}$$

As pressure ratio was increased and the sonic condition at the jet exit was maintained the momentum of the jet plume was increased. This carried the jet plume further into the freestream. This effect was shown by calculating the jet penetration height parameter which is defined as the vertical distance between the centre of the jet exit plane and the bow shock (Figure 69) for each pressure ratio (Figure 71).

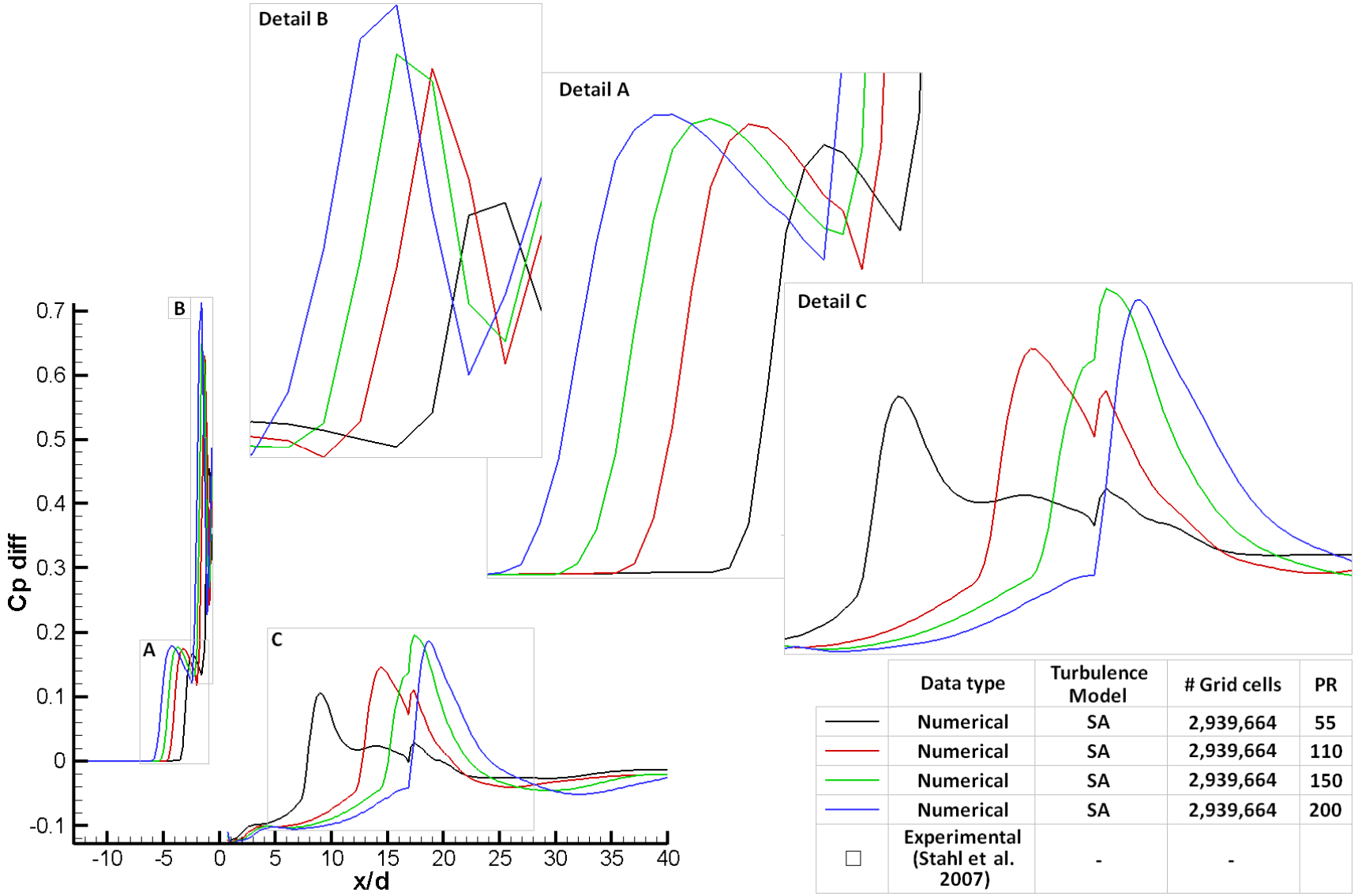


Figure 68 Variation in predicted centerline, differential pressure coefficient distribution on the DLR test body with change in pressure ratio.

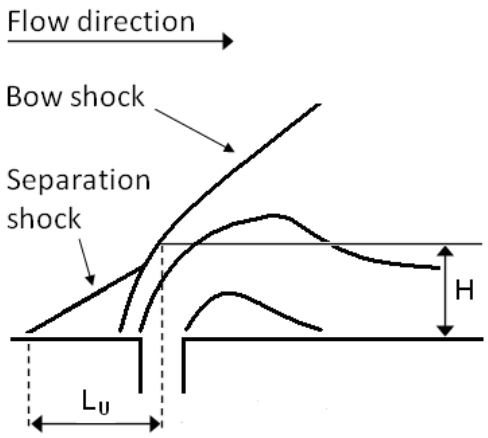


Figure 69 Definition of upstream separation length Lu and penetration height H.

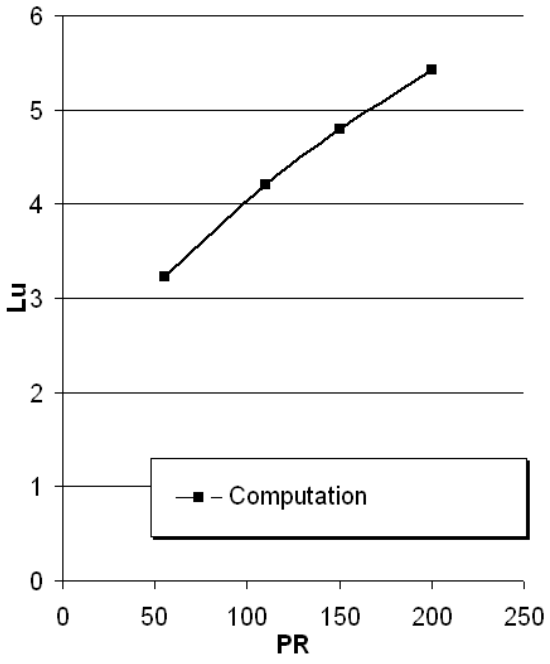


Figure 70 Variation in upstream separation length with changes in pressure ratio

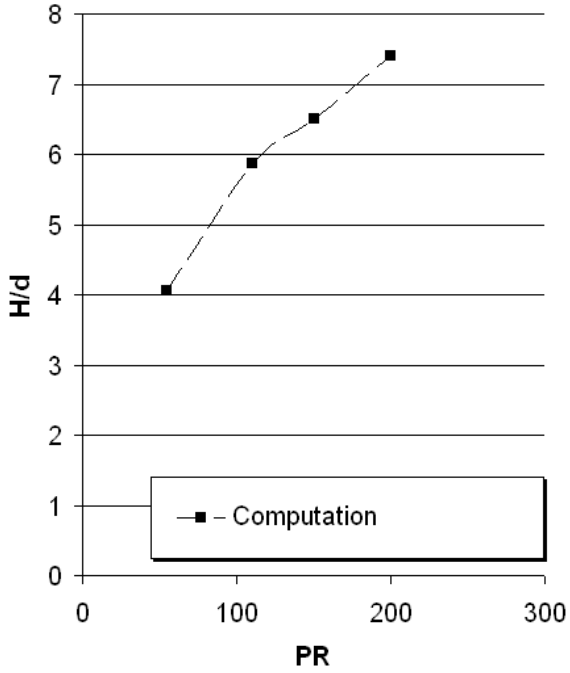


Figure 71 Variation of jet penetration height with changes in pressure ratio

***The influence of angle of attack on the JICF on a body of revolution***

Alpha was varied from -10° to 15°and the pressure coefficient along the centreline of the interaction for each angle of attack was calculated and compared in Figure 74.

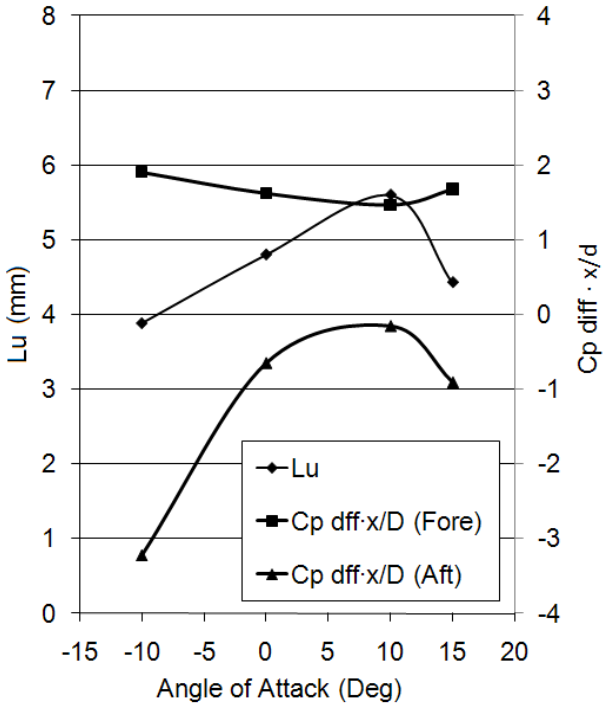


Figure 72 Variation in centreline upstream separation length Lu and $C_{p\ diff}\ \frac{x}{d}$ with angle of attack

Flow separation in front of the jet was investigated by plotting the surface streaklines based on the surface skin friction vectors and noting where these lines coalesced to form a separation line. The results of this study are presented in Figure 72. Within the -10° to 10° angle of attack range the relationship between separation length and angle of attack is approximately linear, with increases in angle of attack causing increases in separation length. Increasing the angle of attack further leads to a reduction in the upstream separation length. This is because a significant change occurs in the area of separation in front of the jet (Figure 73). The influence of the jet in the circumferential direction is seen further upstream when the body is at 15° angle of attack.

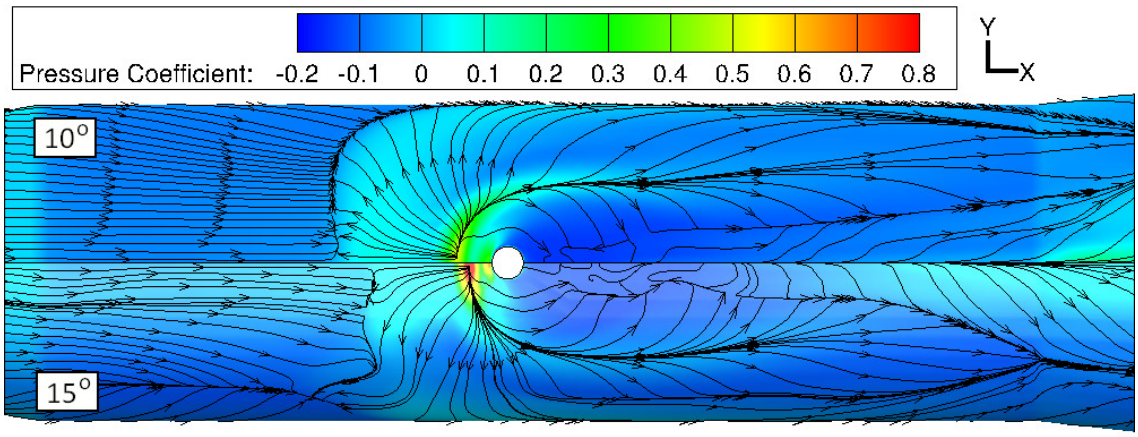


Figure 73 Contours of pressure coefficient mapped onto the body surface with superimposed surface streaklines. Top half: PR=150, aoa=10° Bottom half: PR=150, aoa=15°. Flow is from left to right.

This relationship between upstream separation length and pressure ratio can be seen in Figure 68. It can also be seen in Figure 68 that there is a decrease in the initial pressure rise due to separation when the pressure ratio is increased. So as the separation length increases with increasing pressure ratio the pressure rise due to separation decreases. To investigate the coupling between separation length and pressure rise, the coefficient of pressure was integrated along the body axis (x/d) in the region with upstream of the jet (Equation 53). This analysis is not meant as a force analysis on the body as it is carried out only along the interaction centreline and is not necessarily representative of the pressure distribution on the whole body.

$$C_{p\ diff\ \cdot \frac{x}{d}(fore)} = \int_{x/d_{tip}}^{-0.5} C_{p\ diff}\ \partial(\frac{x}{d}) \qquad \text{Equation 53}$$

$C_{p\ diff\ (fore)}$ is plotted in Figure 72 and shows that as separation length and pressure rise due to separation vary the area beneath the Cp curve does not change considerably.

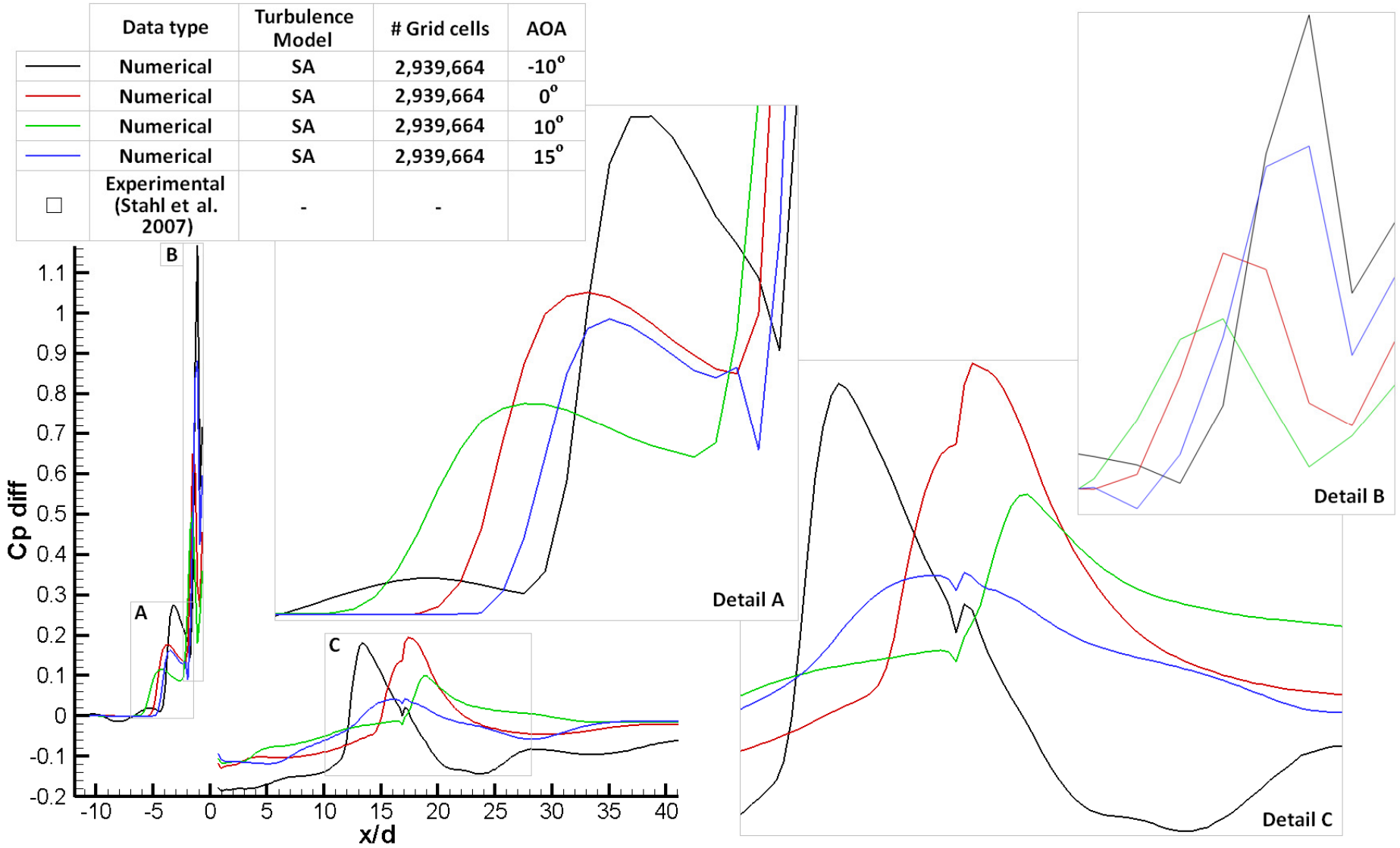


Figure 74 Variation in predicted centerline, differential pressure coefficient distribution on the DLR test body with change in angle of attack.

### 4.3.4 Conclusions

An acceptable level of grid convergence was achieved with a grid consisting of 5.9 million cells for the DLR body of revolution at an angle of attack of -10, 0° and 15°. Overall the Spalart-Allmaras turbulence model was assessed to most accurately predict the lateral jet in supersonic flow issued from a body of revolution interaction of the turbulence models trailed. The area of concern identified in the idealised flat plate study (the over prediction of the pressure peak associated with the reattachment of flow downstream of the jet) also exists when the lateral jet interaction problem utilised on a body of revolution. Cobalt can be used to perform a reasonably accurate prediction of the lateral jet in supersonic flow issued from an idealized flat plate interaction. Experimentally measured force and moments and surface flow visualisation would allow a more in depth assessment of the numerical codes.

## *4.4 Evaluating the efficiency of the jet interaction*

### 4.4.1 The effect of pressure ratio, angle of attack and Reynolds number on the forces and moments

#### 4.4.1.1 Pressure ratio

To evaluate the influence of pressure ratio, angle of attack and Reynolds number on the forces and moments induced by a lateral jet interaction, the normal, axial and pitching moment coefficients have been calculated. Coefficients are presented for cases with the jet on and for cases without a jet (Table 20, Table 21 and Table 22).

Figure 75a), Figure 75b) and Figure 75c) show the normal axial and pitching moment coefficients for the ISL body of revolution at 0° angle of attack. As expected of a body of revolution at 0° angle of attack and 0° yaw the normal force and pitching moments are zero and the axial force coefficient is constant for the no jet case. With the jet on a small positive normal force is induced which increases with pressure ratio from 0.07 to 0.1. The axial force coefficient is also increased by the jet interaction however its relationship to pressure ratio over the investigated range ($50 \leq PR \leq 97$) is weak. The axial force coefficient decreases from 0.25 to 0.24 when the pressure ratio increases from 50 to 97. The jet produces a negative (pitch down) moment which increases with pressure ratio. This moment is caused by the balance between the area of high surface pressure in front of the jet and the area of low surface pressure in its wake (Figure 76). As the pressure ratio increases the pressure in the bow shock region increases and the area of low pressure downstream increases leading to an increase in magnitude of the pitch down moment (Figure 76, Figure 77 & Figure 78).

The normal, axial and pitching moment coefficients are also compared to results calculated by the CFX-TASCflow code (Gnemmi & Schäfer, 2005). The magnitude of the coefficient under investigation was under predicted by Cobalt in comparison to CFX-TASCflow, however as no experimental values exist, little can be drawn from this, except that they follow the same trends. The difference ranges from 9.9% for the normal force coefficient with a pressure ratio of 55 to 12.6% for the pitching moment coefficient with a pressure ratio of 97.

| DLR BoR | | | ISL BoR | | |
|---|---|---|---|---|---|
| CN | CA | $Cm_{(0)}$ | CN | CA | $Cm_{(0)}$ |
| -0.0011 | 0.2549 | 0.0084 | -0.0001 | 0.2555 | 0.0003 |

Table 20 Aerodynamic coefficients of the BoR without the lateral jet.

ISL test body

| PR | $F_j$[N] | CA0 | $F_i$[N] | CN | Mj | $M_{i(0)}$ | $Cm_{(0)}$ | Mi | $X_{cp}/D$ | $X_{cg}/D$ | $X_{cp}$-$X_{cg}$ [m] |
|---|---|---|---|---|---|---|---|---|---|---|---|
| 50 | -15.2813 | 0.2452 | 11.1319 | 0.0721 | -0.6113 | -3.4628 | -0.5607 | -1.5926 | 7.78 | 4.2 | -0.14 |
| 70 | -21.4918 | 0.2423 | 13.0480 | 0.0845 | -0.8597 | -4.0284 | -0.6524 | -1.8363 | 7.72 | 4.2 | -0.14 |
| 97 | -29.8760 | 0.2396 | 15.4992 | 0.1004 | -1.1950 | -4.7804 | -0.7742 | -2.1766 | 7.71 | 4.2 | -0.14 |

Table 21 Variation of the aerodynamic forces and coefficients on the ISL test body with the lateral jet with variation in pressure ratio.

DLR test body

| PR | $F_j$[N] | CA0 | $F_i$[N] | CN | Mj | $M_{i(0)}$ | $Cm_{(0)}$ | Mi | $X_{cp}/D$ | $X_{cg}/D$ | $X_{cp}$-$X_{cg}$ [m] |
|---|---|---|---|---|---|---|---|---|---|---|---|
| 55 | -13.5627 | 0.2440 | 9.6770 | 0.0767 | -0.5425 | -3.0482 | -0.6046 | -1.3838 | 7.87 | 4.3 | -0.14 |
| 110 | -27.3228 | 0.2382 | 13.6841 | 0.1090 | -1.0929 | -4.2796 | -0.8522 | -1.9259 | 7.82 | 4.3 | -0.14 |
| 150 | -37.3301 | 0.2355 | 15.5613 | 0.1241 | -1.4932 | -4.8485 | -0.9666 | -2.1720 | 7.79 | 4.3 | -0.14 |
| 200 | -49.8393 | 0.2318 | 17.3900 | 0.1388 | -1.9936 | -5.3928 | -1.0761 | -2.4017 | 7.75 | 4.3 | -0.14 |

Table 22 Variation of the aerodynamic forces and coefficients on the DLR test body with the lateral jet with variation in pressure ratio.

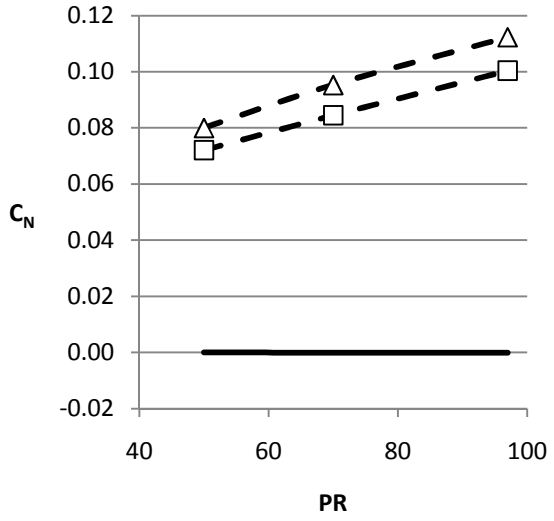


Figure 75a) Coefficient of normal force on the ISL BoR, α=0°. CFX-TASCflow results from Gnemmi & Schäfer (2005).

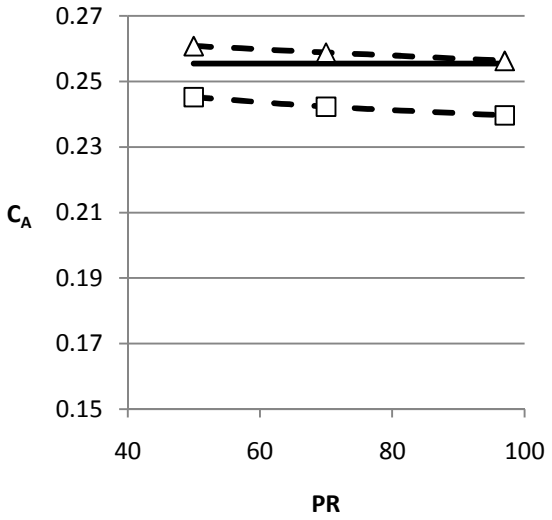


Figure 75b) Coefficient of axial force on the ISL BoR, α =0°., CFX-TASCflow results from Gnemmi & Schäfer (2005).

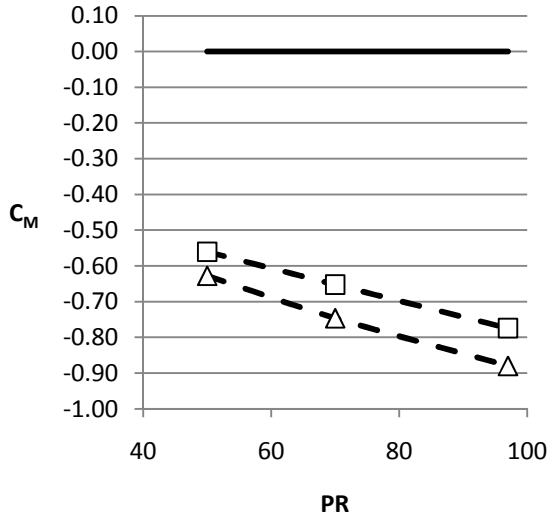


Figure 75c) Pitching moment coefficient on the ISL BoR evaluated at the nose tip, α =0°. CFX-TASCflow results from Gnemmi & Schäfer (2005).

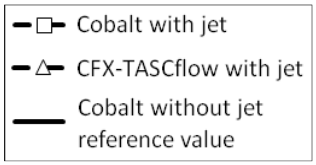


For a statically stable missile the centre of gravity should be located at least half a caliber ahead of the centre of pressure (Gnemmi & Schäfer (2005)). Here $X_{c.g.}$ is assumed to be coincident with the nozzle location. For the ISL body of revolution this is 4.2 calibers downstream of the nose tip. The centre of pressure was found to be located approximately at 7.7 calibers downstream of the nose tip (Table 21). An increase in pressure ratio from 50 to 97 moved the

centre of pressure downstream by 0.9%. The DLR nozzle and hence the assume c.g. was located at 4.3 calibers downstream of the nose tip. For this body the centre of pressure was found to vary from 7.87 to 7.75 (1.5% decrease) as the pressure ratio was increase from 55 to 200 (Table 22). This would suggest that if the c.g. location assumption was correct both bodies of revolution would be statically stable for the range of pressure ratios investigated. (50≤PR≤200).

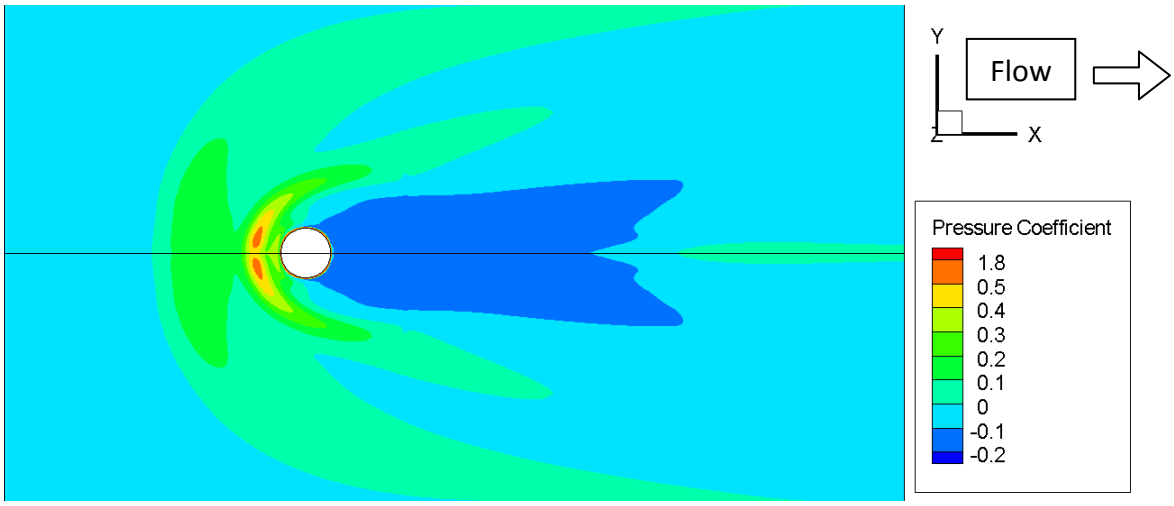


Figure 76 Contours of pressure coefficient mapped onto the ISL test body PR=50, α=0˚

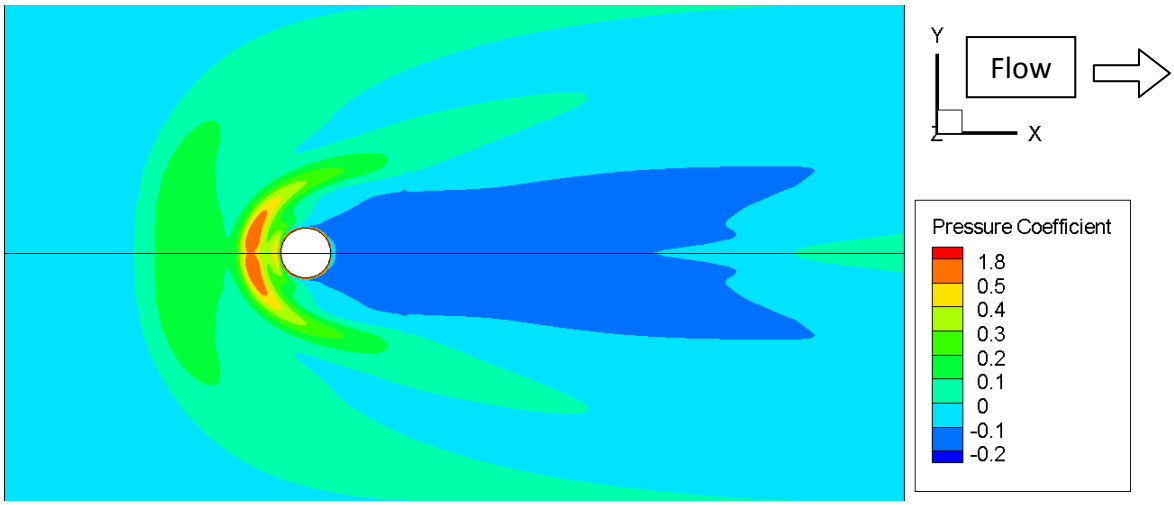


Figure 77 Contours of pressure coefficient mapped onto the ISL test body PR=70, α=0˚

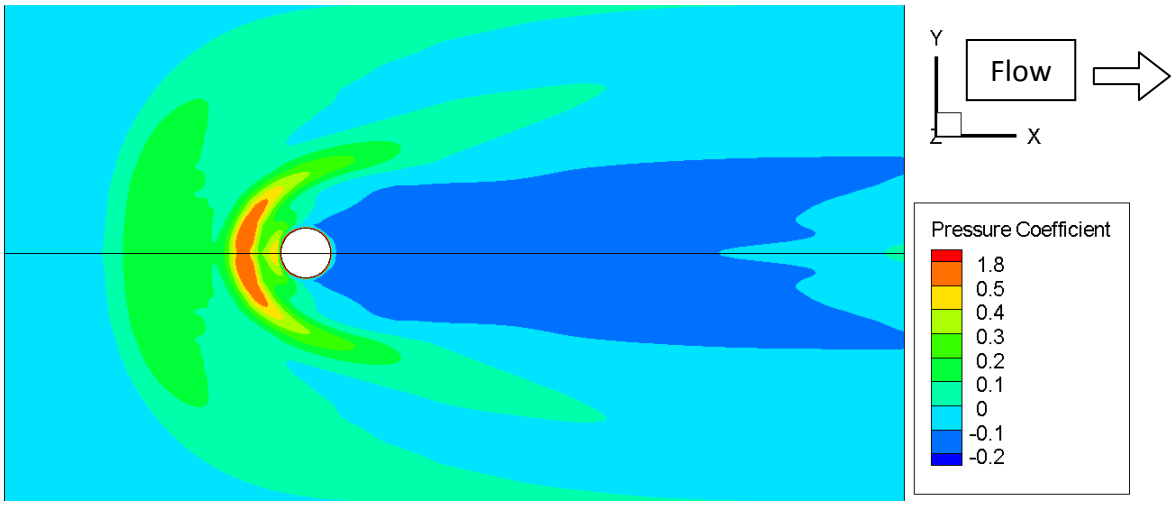


Figure 78 Contours of pressure coefficient mapped onto the ISL test body PR=97, α=0˚

The same three coefficients (Cm, Cx, Cz) were calculated for the DLR body of revolution. These are shown in Figure 79, Figure 80 and Figure 81. Here a larger range of pressure ratios were investigated (55≤PR≤200). The same trends were found i.e. increasing magnitude of normal force and pitching moment and decreasing axial force coefficients with increasing pressure ratio.

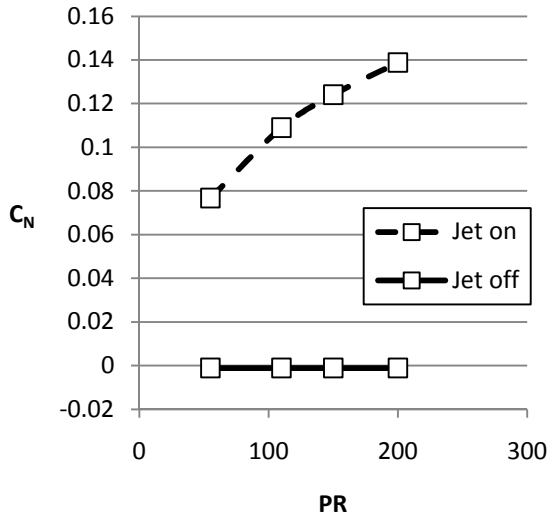


Figure 79 Coefficient of normal force on the DLR BoR, A=0°

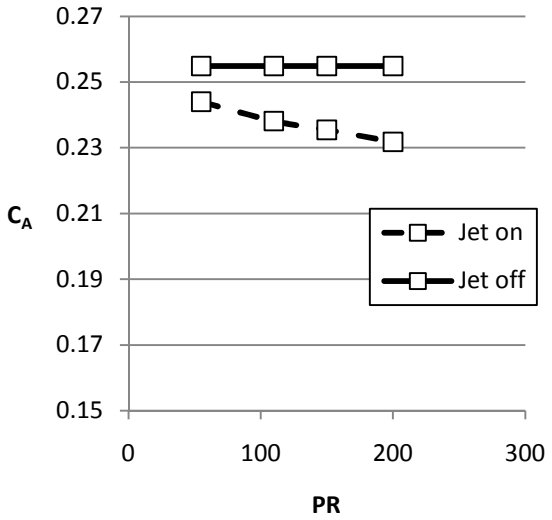


Figure 80 Coefficient of axial force on the DLR BoR, A=0°

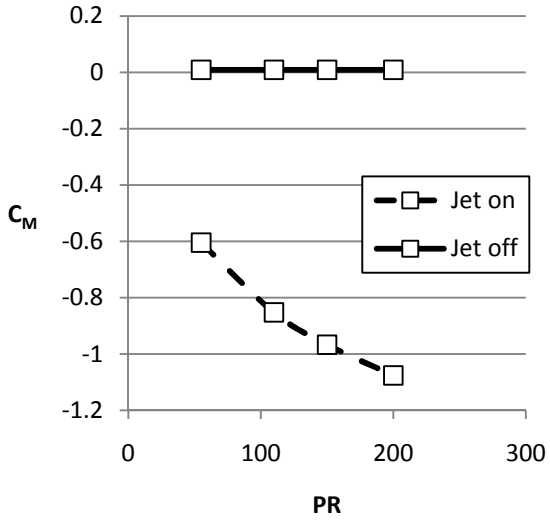


Figure 81 Pitching moment coefficient on the DLR BoR evaluated at the nose tip, A=0°

### 4.4.1.2 The Effect of Angle of attack

To investigate the influence of the angle of attack the normal, axial and pitching moment coefficients have been calculated for angles of attack of -10°, 0°, +10° and +15° (Table 23 & Table 24). For all cases the pressure ratio was equal to 150. Results are presented for the case with a jet and for the case without a jet. The angle of attack of the body has a greater influence on the normal force coefficient than the jet interaction. The coefficient of pressure distribution on the body surface is shown in Figure 83 to Figure 86. As α increases, the pressure on the body surface reduces leading to an increase in normal force. The surface pressure fore of the body c.g. (assumed to be coincident with jet nozzle ) goes from positive to negative as α goes from negative to positive (Figure 83 to Figure 86). This leads to a reduction in the moment coefficient (Figure 82c)).

The influence of the jet decreases as the angle of attack increases. At -10° the jet interaction decreases the magnitude of the negative normal force coefficient by 0.2 (17%) while at 0° and 10° the normal force coefficient is augmented by 0.13 and 0.04 (3%) respectively (Figure 82a). In the same way, the influence of the jet on the pitching moment coefficient decreases as the angle of attack increases (Figure 82c). As expected minimum axial force coefficient occurs at 0°, where the body presents the smallest wetted area to the freestream (Figure 82b). At this condition and at -10° the effect of the jet is to reduce the axial force coefficient by 0.02 and 0.06 respectively. The effect of the jet on the axial force coefficient is less significant at positive angles of attack.

| | DLR BoR | | |
|---|---|---|---|
| A | CN | CA | $Cm_{(0)}$ |
| -10 | -1.1453 | 0.4268 | 6.1976 |
| 0 | -0.0011 | 0.2549 | 0.0084 |
| 10 | 1.1454 | 0.4268 | -6.1983 |
| 15 | 2.1094 | 0.7998 | -12.0700 |

Table 23 Variation in the aerodynamic coefficients of the DLR test body without the lateral jet with variation in α.

| DLR test body | | | | | | | | | | | |
|---|---|---|---|---|---|---|---|---|---|---|---|
| α | $F_j$[N] | CA0 | $F_i$[N] | CN | Mj | $M_{i(0)}$ | $Cm_{(0)}$ | Mi | $X_{cp}/D$ | $X_{cg}/D$ | $X_{cp}$-$X_{cg}$ [m] |
| -10 | -37.3301 | 0.3647 | 24.7157 | -0.9465 | -1.4932 | -7.8032 | 4.6284 | -3.5521 | 7.89 | 4.3 | -0.14 |
| 0 | -37.3301 | 0.2355 | 15.5613 | 0.1241 | -1.4932 | -4.8485 | -0.9666 | -2.1720 | 7.79 | 4.3 | -0.14 |
| 10 | -37.3301 | 0.4369 | 4.9976 | 1.1856 | -1.4932 | -2.2581 | -6.6524 | -1.3985 | 11.30 | 4.3 | -0.28 |
| 15 | -37.3301 | 0.7961 | -3.3566 | 2.0824 | -1.4932 | 0.1442 | -12.0410 | 0.4331 | 1.07 | 4.3 | -0.13 |

Table 24 Variation of the aerodynamic forces and coefficients on the DLR test body with the lateral jet with variation in α.

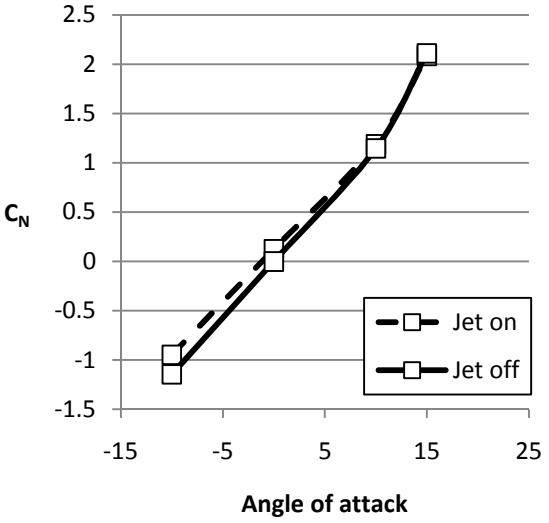


Figure 82a) Coefficient of normal force on the DLR BoR, PR=150

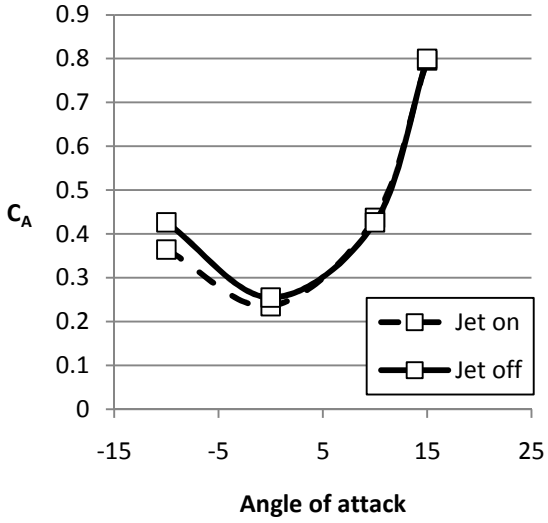


Figure 82b) Coefficient of axial force on the DLR BoR, PR=150

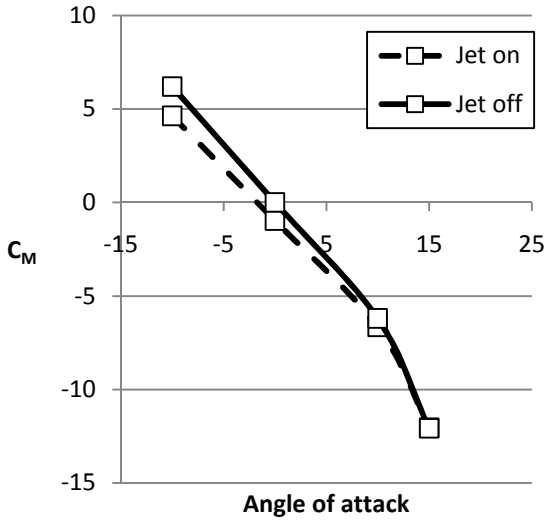


Figure 82c) Pitching moment coefficient on the DLR BoR, evaluated at the nose tip, PR=150

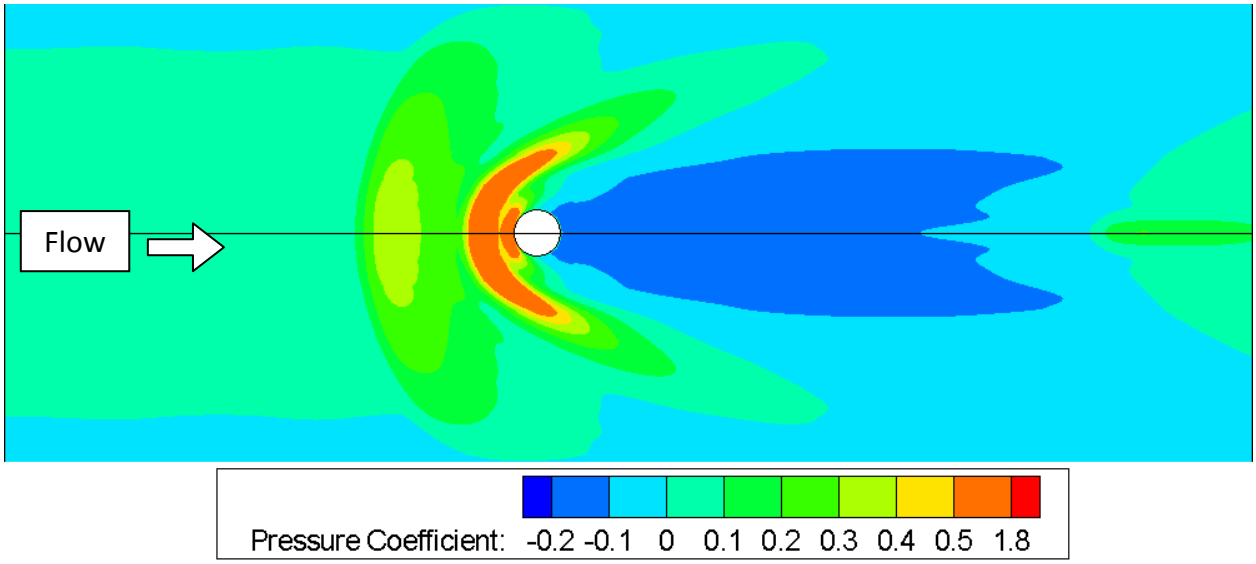


Figure 83 Contours of pressure coefficient mapped onto the DLR test body α=-10˚, PR=150.

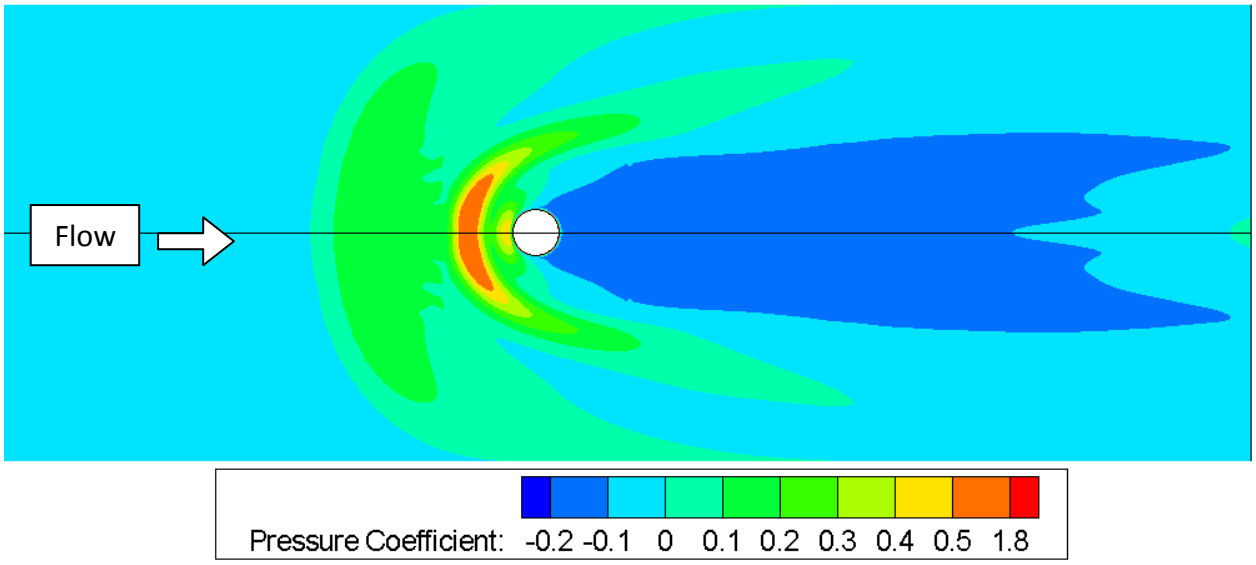


Figure 84 Contours of pressure coefficient mapped onto the DLR test body α=0, PR=150.

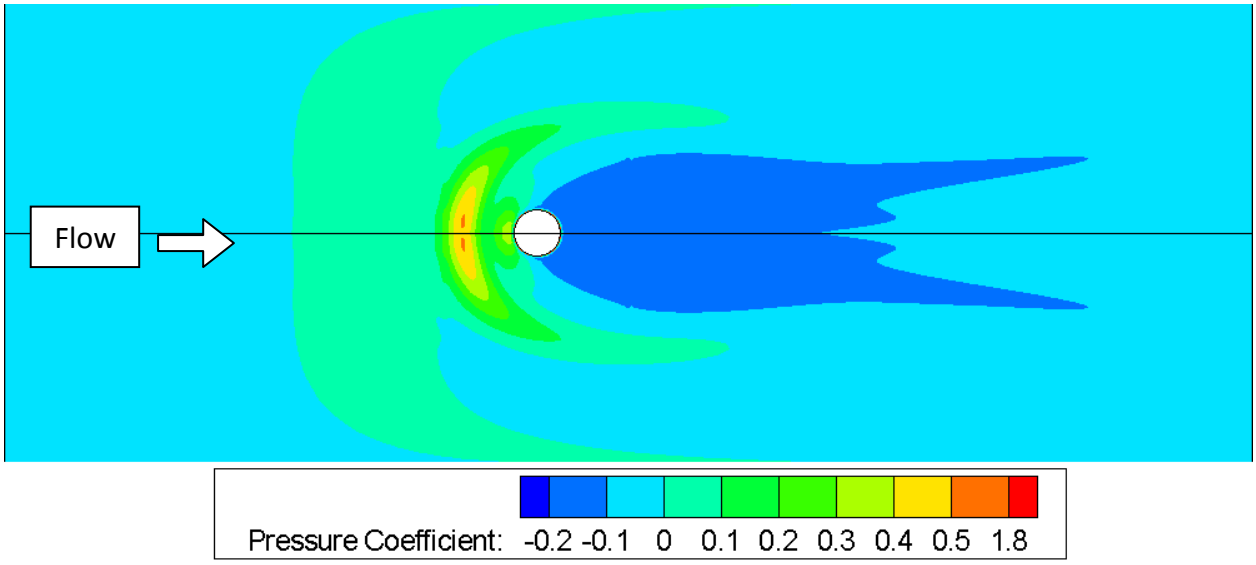


Figure 85 Contours of pressure coefficient mapped onto the DLR test body α=10˚, PR=150.

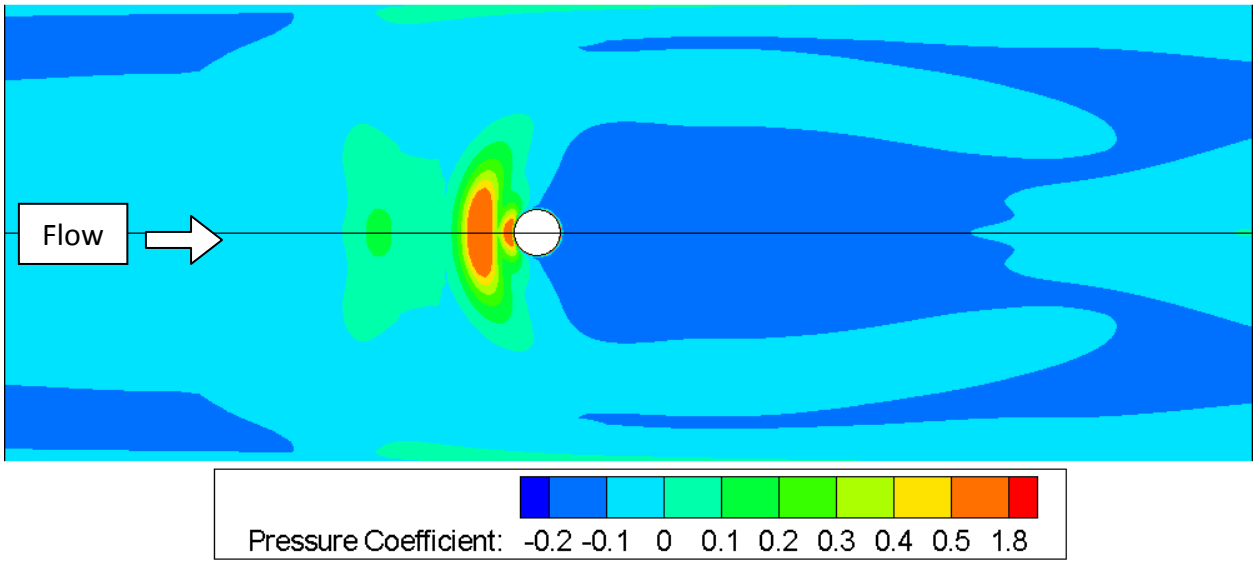


Figure 86 Contours of pressure coefficient mapped onto the DLR test body α=15˚, PR=150.

### 4.4.2 Force and moment amplification factors

The efficiency of the jet interaction has been assessed using the force and moment amplification factors $K_F$ and $K_M$ as described in Chapter 1.2.4. Figure 87 shows force and moment amplification factors for the ISL body of revolution calculated using Cobalt compared to CFX-TASCflow code (Gnemmi & Schäfer 2005). Similarly force and moment amplification factors have been calculated for the DLR body of revolution (also Figure 87).

For the pressure ratio under investigation here, ($55 \leq PR \leq 200$) the force amplification factor is below one (Figure 87). This means that the jet interaction force counteracts the jet thrust force. However the force amplification factor increases with pressure ratio and therefore the effect reduces. However the rate of change is reducing. For the DLR BoR an increase in pressure ratio from 55 to 110 lead to an increase in the force amplification factor of 0.21, but an increase in the pressure ratio from 110 to 200 only resulted in an increase of 0.15 in the force amplification factor. This is important to note as it suggests that at 0° angle of attack it may not be possible to keep increasing the pressure ratio to reach a force amplification factor greater than one. The force amplification factor may approach a value less than one.

The moment amplification factor is much larger, varying from 3.6 to a value of 2.8 as the pressure ratio is increased from 50 to 97. This is because the pressure distribution on the body with the area of high surface pressure upstream of the jet and area of low surface pressure downstream of the jet relative to the freestream pressure augments the nose down moment created by the jet thrust (Figure 76, Figure 77 & Figure 78).

In comparison to the amplification factors calculated using the CFX-TASCflow code (Gnemmi & Schäfer 2005) the force amplification factor is over predicted by an average of 28% while the moment amplification factor is under predicted by 8% (Figure 87). However as both data sets were calculated numerically and no experimental force and moment data exists for these configurations no conclusion can be drawn as to which is the more accurate.

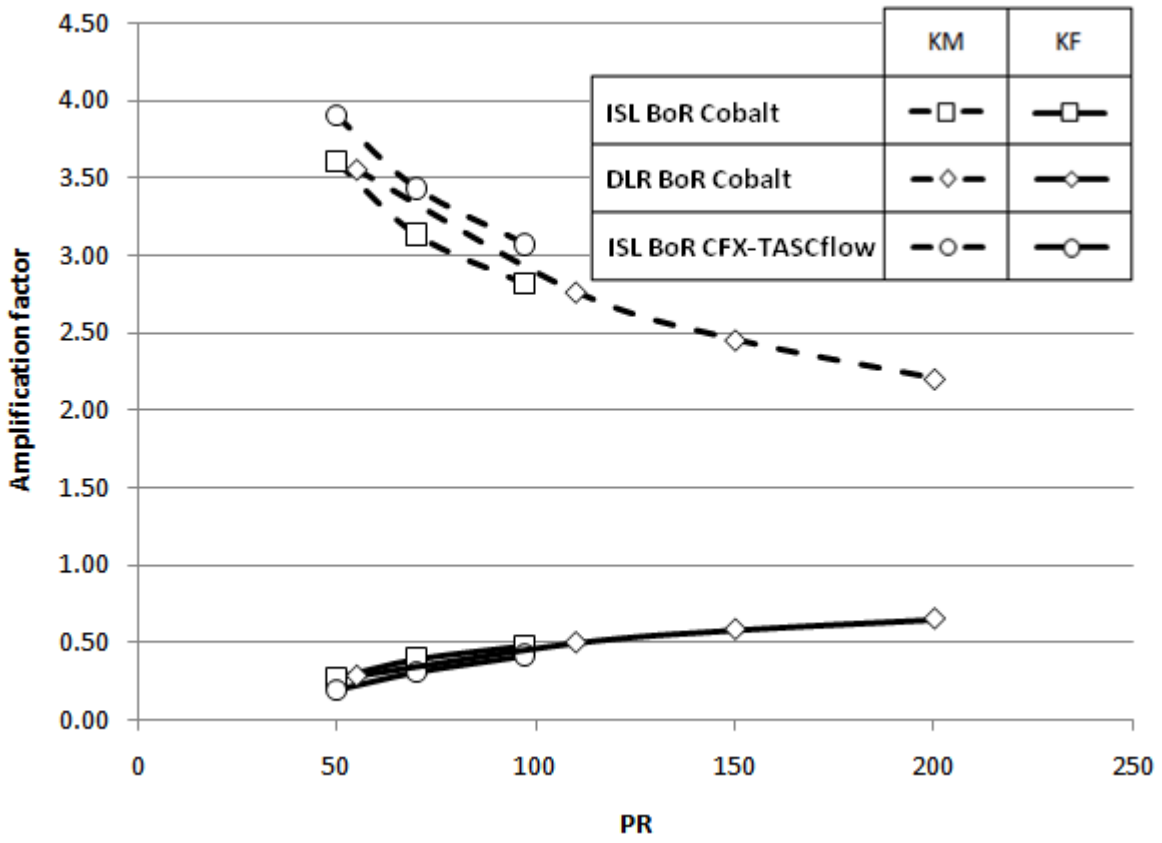


Figure 87 Predicted force and moment amplification factors $K_F$ and $K_M$ for the ISL BoR and DLR BoR, A=0°

The jet amplification factors at various angles of attack are presented in Figure 88. The force amplification factor increases as the angle of attack is increased. At =15° the force amplification factor is 1.09. At this angle of attack the jet interaction forces augment the jet thrust force. The pitching moment amplification factor decreases with increasing angle of attack. At α=15° the amplification factor is less than one. This means the interaction forces on the body counteract the desired moment. If this trend was to continue for higher angles of attack and KM became negative it would lead to control reversal. Here a moment opposing the intended moment would be induced.

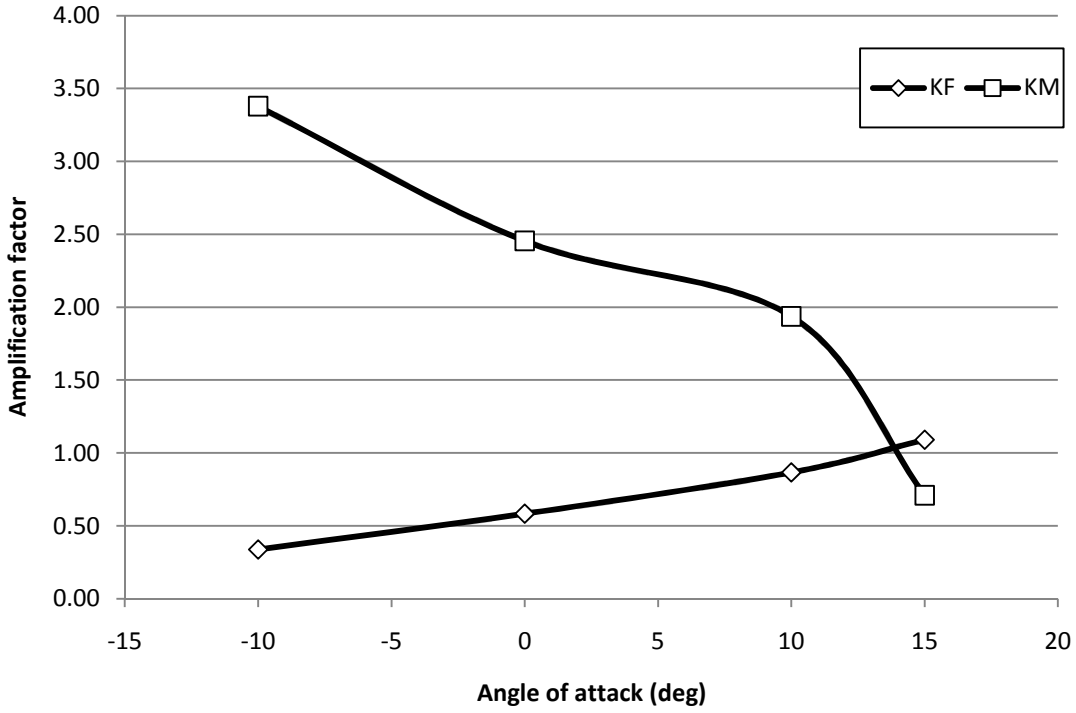


Figure 88 Force and moment amplification factors $K_F$ and $K_M$ for the DLR BoR, PR=150

These trends can be linked to the pressure distribution on the body. The centerline pressure distribution is given in Figure 89. Here pressure is given as $C_{P\ diff}$ which isolates the pressure distribution due to the presence of the jet. As α is increased the downstream pressure rise due to flow reattachment decreases. This counteracts the jet thrust force. However as α is increased the pressure peak just upstream of the jet increases substantially augmenting the jet thrust force and leading to an overall increase in KF. At a negative angle of attack the peak pressure in front of the jet is at its highest and the pressure trough downstream of the jet is at its lowest. This leads to a pitch down moment and high KM. Then as the angle of attack is increased the pressure rise just in front of the jet is reduced leading to a lower KM.

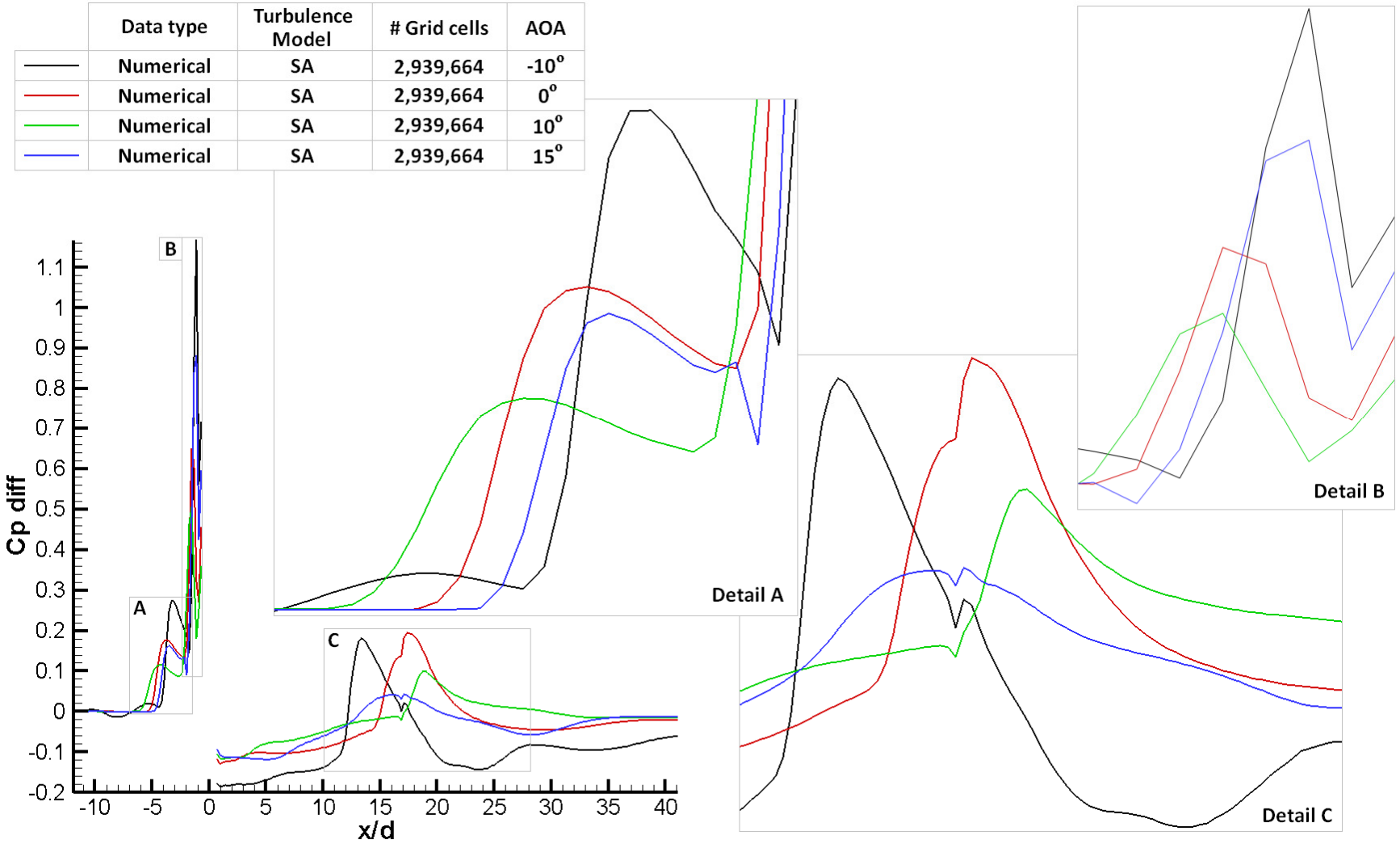


Figure 89 Variation in centreline differential pressure distribution for the DLR test body with variation in α, PR=150.

## 4.5 Detailed flowfield analysis of the JICF flowfield

Sections 4.1 to 4.4 dealt mostly with the forces moments and surface pressure distributions and how well they were predicted. These are a result of the complex 3d flowfield. In this section the flowfield is investigated by comparing identifiable features to the accepted flowfield model. For simplicity, and to eliminate the effects of surface geometry, the lateral sonic jet exhausted from an idealized flat plate into a Mach 5 freestream case is used for this analysis.

## 4.6 Main flow features of the supersonic jet interaction flowfield

Mapping local Mach number contours onto the interaction plane of symmetry reveals most of the features which characterize the lateral jet in supersonic crossflow interaction (Figure 90). The sonic jet was exhausted into the freestream at a right angle. The highly underexpanded jet underwent a Prandtl Mayer expansion and produces an inclined barrel shock terminating in a Mach disk. The Mach disk decelerates the supersonic flow passing through it to subsonic. The barrel shock acts as an obstruction to the flow inducing a detached bow shock upstream. The bow shock in turn creates an adverse pressure gradient in the incoming boundary layer causing it to separate. This separation bubble creates an interference shock. The barrel shock, Mach disk and reflected shock creates a triple point. The reflected shock then impinges upon the flat plate thickening the boundary layer downstream of the barrel shock. The lateral jet in supersonic cross flow creates a highly complex three-dimensional flow field consisting of shock and vortical structures. The main shock and vortical structures are identified and discussed in the following sections.

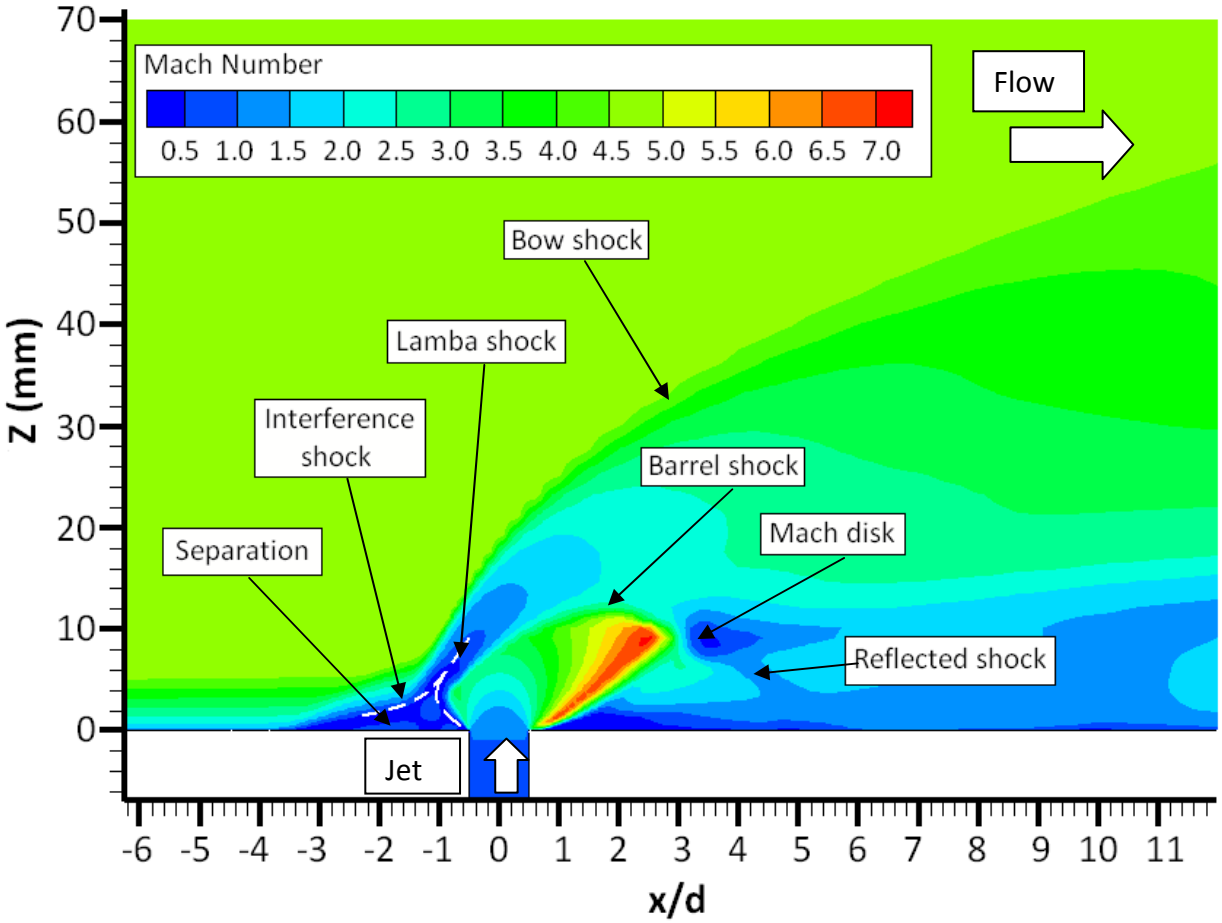


Figure 90 Contours of Mach number on the interaction plane of symmetry identifying recognizable flow patterns.

## *4.7 Shockwave structures in the lateral jet in supersonic flowfield*

As early as 1952 the main shock structures, including the bow shock and the inclined barrel shock, had been experimentally visualized (Morkovin, 1952). One method of visualizing the shock structures is schlieren visualization (Figure 91). This technique allows density gradients in the flowfield to be visualized.

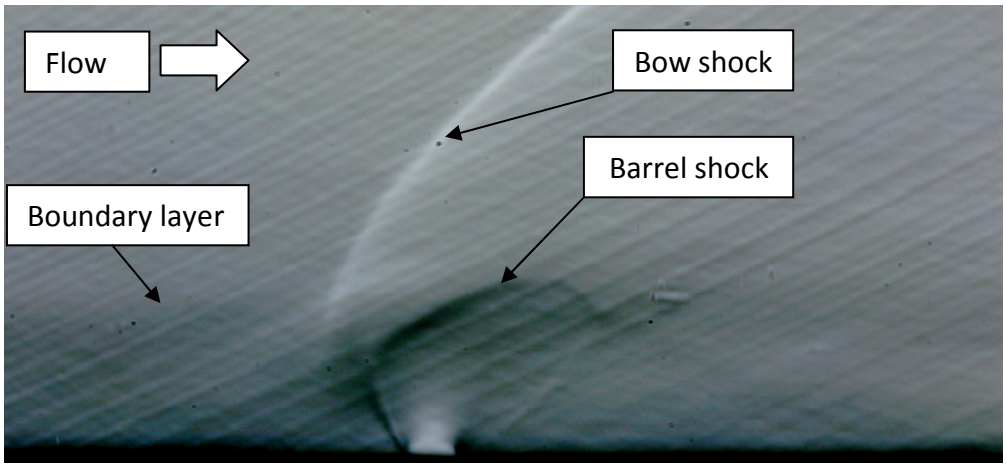


Figure 91 Schlieren visualization a lateral jet in supersonic crossflow interaction. (M=2.4, PR=70).

A similar result can be achieved numerically by plotting the density gradient magnitude on the interaction plane of symmetry (Figure 92). This differs slightly from schlieren visualization as it is a two-dimensional slice of the flowfield while schlieren is a two-dimensional representation of the three-dimensional flowfield. In Figure 92 the incoming boundary layer, bow shock and barrel shock are clearly visible as they were when contours of Mach number were mapped onto the symmetry plane (Figure 90). Contours of density gradient magnitude however provide a superior visualization of the reflected shock and its impingement on the flat plate surface. The reflected shock creates an adverse pressure gradient in the boundary layer downstream of the barrel shock ($x/d \approx 4.75$) causing it to thicken

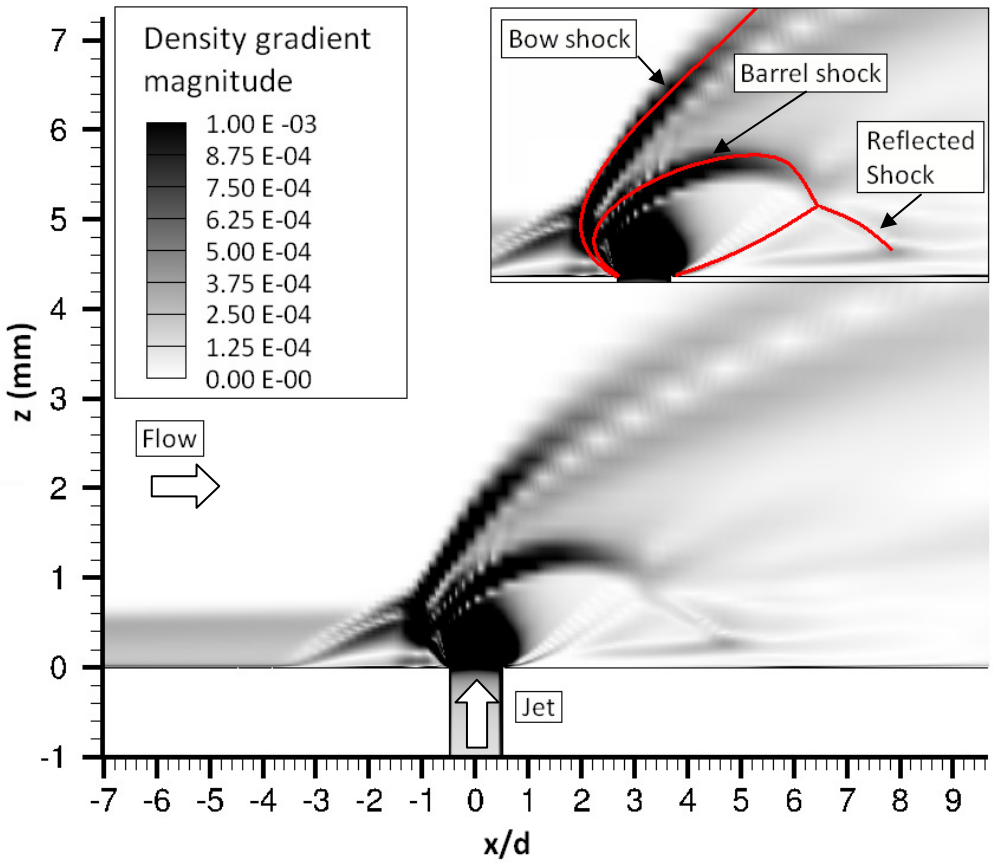


Figure 92 Density gradient magnitude mapped onto the interaction plane of symmetry.

An attempt to isolate the barrel shock was made using a Mach number iso-surface equal to the fully expanded jet Mach number. This approach works well for a jet exhausting into a quiescent medium. However when the jet is exhausted into a crossflow the static pressure around the ejector is not uniform. This leads to different fully expanded jet Mach numbers for the windward and leeward sides of the jet. A better approximation of the barrel shock structure was found using an entropy iso-surface (Figure 93). As the jet fluid is exhausted and expands in the plume entropy increases, the rate of this increase rises significantly through the boundary of the barrel shock allowing its structure to be extracted.

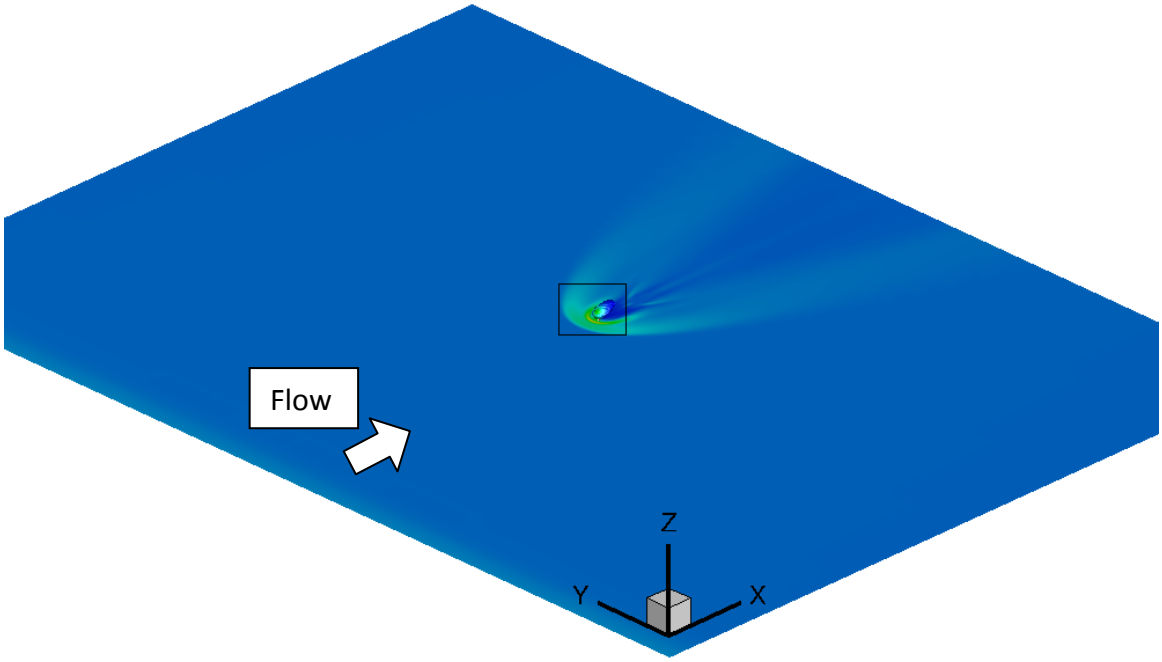


A) Overview of flat plate showing location of Figure 93b.

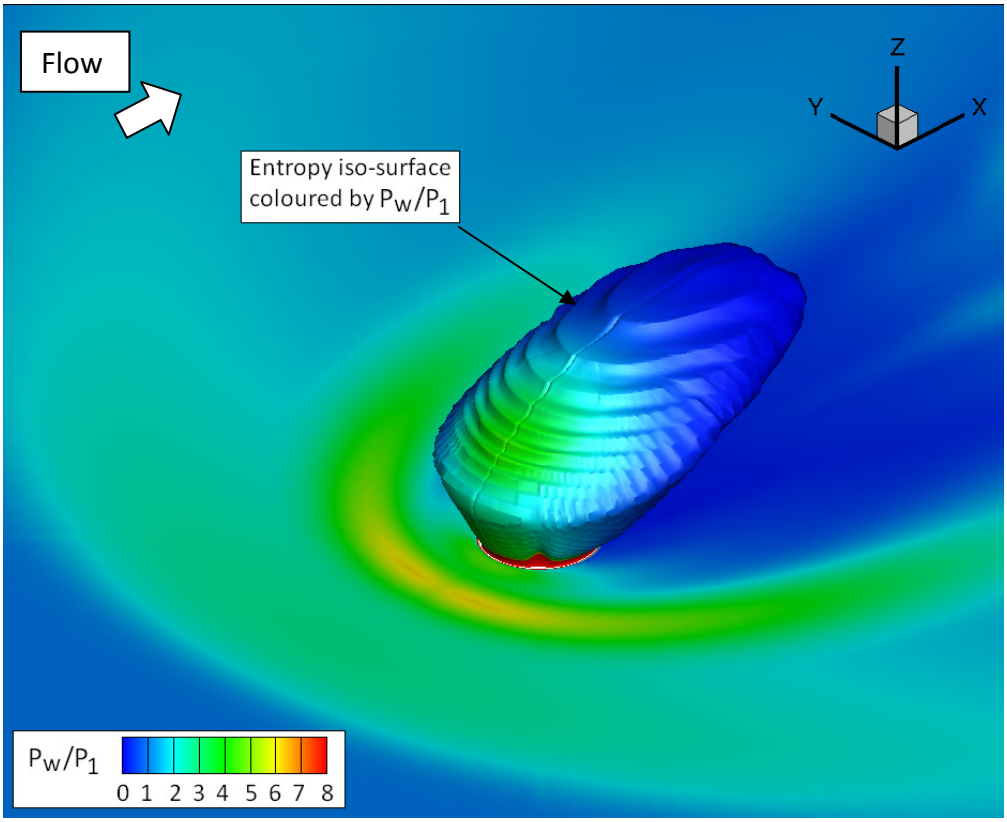


B) Close up of the barrel shock.

Figure 93 Isometric view of the barrel shock with contours of normalized pressure mapped on the flat plate.

The structure of the barrel shock in crossflow differs somewhat to that of a barrel shock in a quiescent medium. The higher local pressure on the windward side of the jet causes recompression to occur earlier than on the leeward side. This recompression shock is pushed downstream by the incoming flow folding the barrel shock in on itself and creating a reflection line. This reflection line is clearly visible in Figure 93 and Figure 94. Another feature unique to the jet in crossflow is the indentation on the downstream surface of the barrel shock. This is caused by the inclination of the barrel shock reducing the space available for the jet fluid to expand in the region immediately downstream of the jet. In this region the barrel shock reflects off the flat plate surface back into the barrel shock. Figure 94 shows this indentation on the leeward side of the barrel shock and the lines of inflection in the barrel shock curvature.

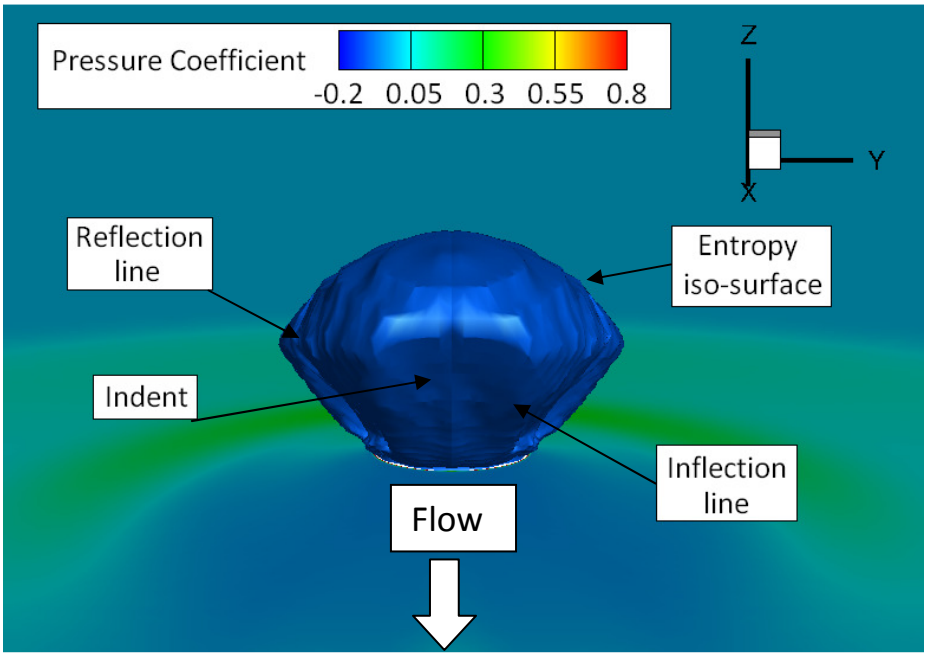


Figure 94 Downstream view of the barrel shock with contours of pressure coefficient mapped on the flat plate. Direction of flow is out of the page, aligned with the X axis.

## 4.8 *Vortical structures in the lateral jet in supersonic flow interaction*

The main vortical structures present in the lateral jet in supersonic interaction are captured in Figure 95. In this figure contours of Mach number are mapped onto the interaction plane of symmetry while contours of pressure coefficient are mapped onto the flat plate surface and contours of vorticity magnitude are mapped onto a crossflow plane aft of the Mach disk. Vortex paths are highlighted with volume ribbons and are coloured by source. The volume streamlines were created by first locating the vortex cores. This was done by projecting velocity vectors onto the crossflow plane. Volume streamlines were then seeded at these vortex cores.

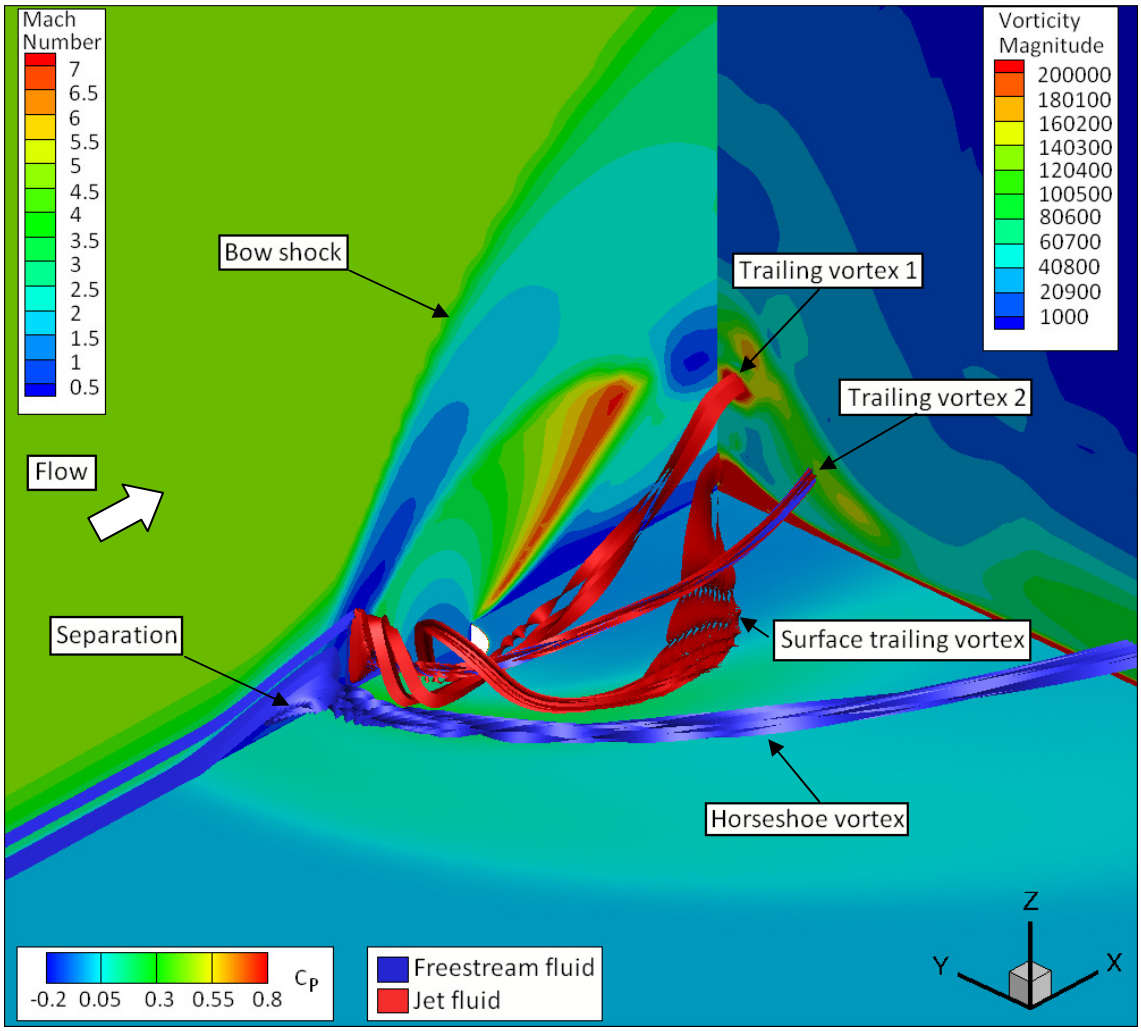


Figure 95 Isometric view of the flowfield around the injector. Streamlines coloured by source highlight the main vortical structures. Contours of Mach number are mapped onto the interaction plane of symmetry. Contours of pressure coefficient are mapped onto the flat plate surface and contours of vorticity magnitude are mapped onto a crossflow plane (x/d=4.43) aft of the Mach disk.

In the separated incoming boundary layer the vortex core (shown more clearly in Figure 96) which becomes the horseshoe vortex can clearly be seen. The horseshoe vortex is composed entirely of freestream fluid. As the horseshoe vortex progress downstream it continues to move further away from the x-z plane of symmetry.

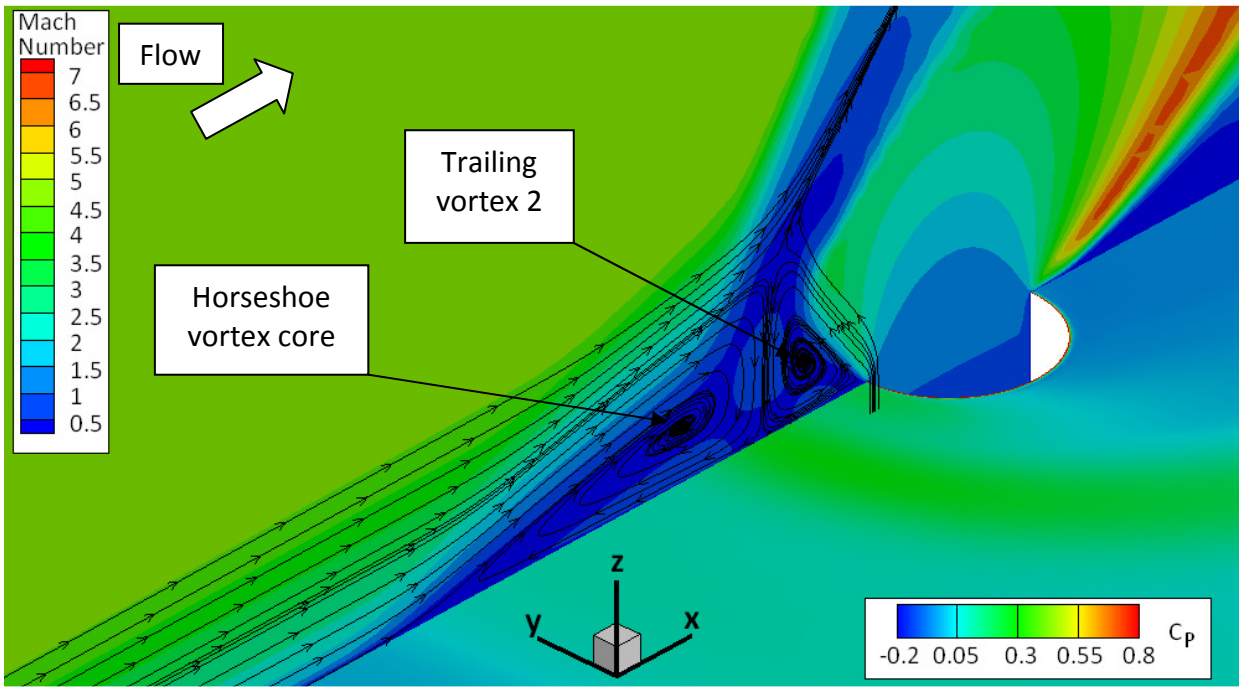


Figure 96 Close up view of the counter rotating vortex pair. Contours of Mach number mapped onto the interaction plane if symmetry. Contours of pressure coefficient mapped onto the flat plate.

There is another vortex present on the plane of symmetry between the horseshoe vortex core and the Mach disk. This vortex rotates in the opposite direction to the horseshoe vortex due to the shear layer between the created between the barrel shock and the separated flow. It is primarily made up of jet fluid entraining some fluid from the outer regions of the freestream boundary layer. The core of this vortex (Trailing vortex 2) is more clearly illustrated in Figure 96. In Viti et al. 2009 this counter rotating separation vortex generates several disparate vortical structures which were transported downstream. Specifically highlighted was the “Upper trailing vortex” which is transported close to the x-z plane of symmetry over the top of the barrel shock. No evidence was found for this vortex in this simulation. Similarly in Battisti’s (2010) numerical investigation into Cranfield University’s lateral jet experiments no upper trailing vortex was detected. This disparity may be explained by the difference in pressure ratio

between the cases. Viti et al. 2009 deals with a pressure ratio of 532 while Battisti (2010) investigates a pressure ratio of 50 and the flowfield analysis presented here describes a pressure ratio of 100. The inclination of the barrel shock is dependent on the pressure ratio. This alters the region in front the Mach disk i.e. the region where this upper trailing vortex is said to be formed. Support of this view is lent by Palekar et al. 2005 who did not detect the presence of this vortex when investing a lateral jet issued at a pressure ratio of 21.6 into a Mach 1.98 flow.

Fluid from the front of the barrel shock is convected sideways as the jet expands forming the surface trailing vortex. The impingement of this vortex on the flat plate can clearly be seen in the mappings of pressure coefficient on the flat plate (Figure 95). Moving downstream the surface trailing vortex moves towards the plane of symmetry into the low pressure region created as the barrel shock detaches from the surface of the flat plate.

Two more vortices were revealed by populating the crossflow plane at x/d=4.43 with surface streamlines of velocity and making the vorticity magnitude contour levels non linear (Figure 97). Trailing vortex 2 and the horseshoe vortex are not visible in the surface streamlines because their vorticity is normal to the crossflow plane. Trailing vortex 1 was already identified in Figure 95 and shown to consist of jet fluid. The source of the two new vortices (trailing vortex 3 and 4) is investigated in Figure 98. Trailing vortex 3 and 4 are both formed in shear layer regions between the slow moving jet fluid and the faster freestream flow. Trailing vortex 3 is formed in the region immediately downstream of the Mach disk while trailing vortex 4 is formed as fluid passes through the top of the barrel shock. Moving downstream trailing vortices 1, 3 and 4 merge creating a vortex referred to in the literature as the ‘kidney shaped vortex’ which dominates the flowfield.

Now that the main vortical structures have been identified they can be compared to Viti et al.’s (2009) model of vortex structures in the lateral jet interaction (Figure 100). As previously discussed the upper trailing vortex predicted by Viti et al. (2009) was not found. This was found to be the only discrepancy. The horseshoe vortex and trailing lower vortex (referred to here as

the surface trailing vortex) and the trailing longitudinal vortex (referred to here as trailing vortex 2) were all predicted as was the kidney shaped vortex.

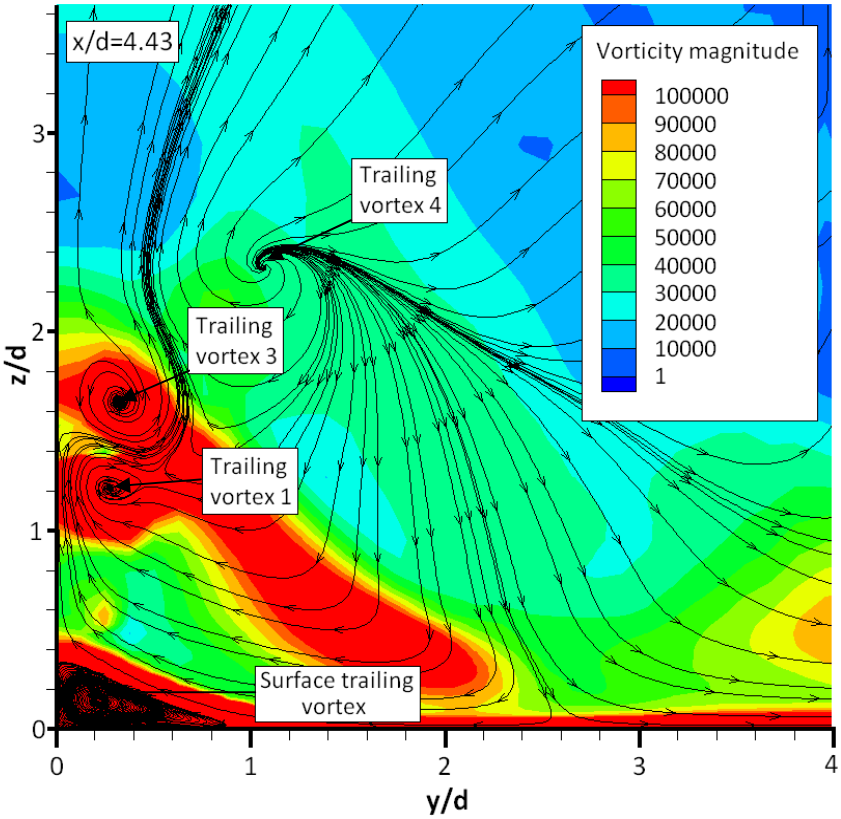


Figure 97 Contours of vorticity magnitude on a crossflow plane (x/d=4.43) with surface streamlines.

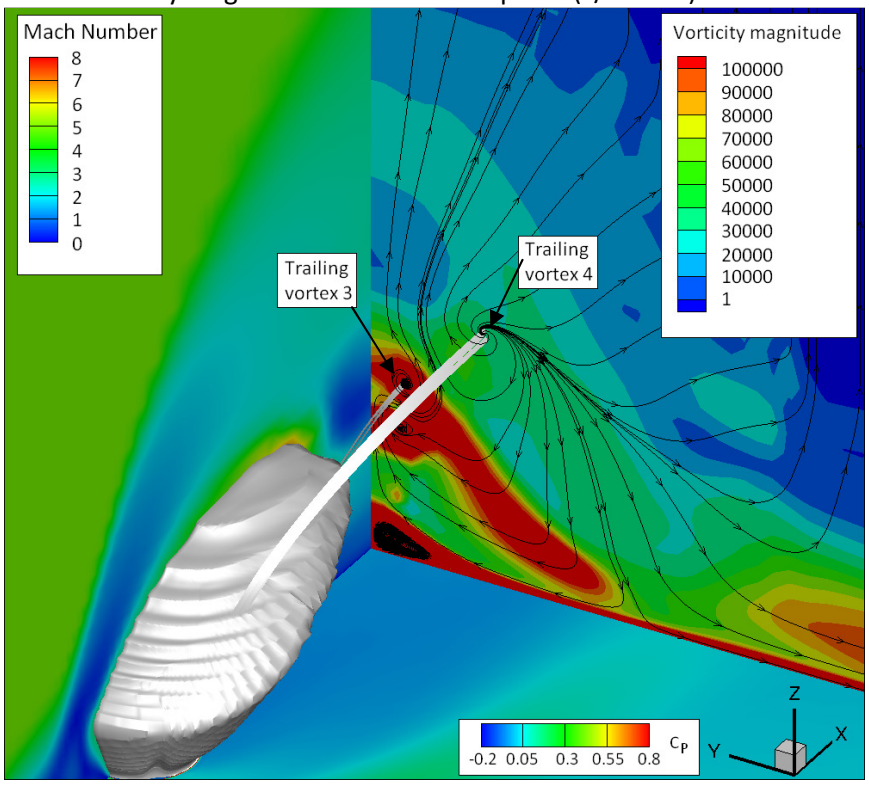


Figure 98 isometric view of the flowfield. Contours of Mach number are mapped onto the interaction plane of symmetry. Contours of pressure coefficient are mapped onto the flat plate surface and contours of voracity magnitude are mapped onto a crossflow plane (x/d=4.43) aft of the Mach disk

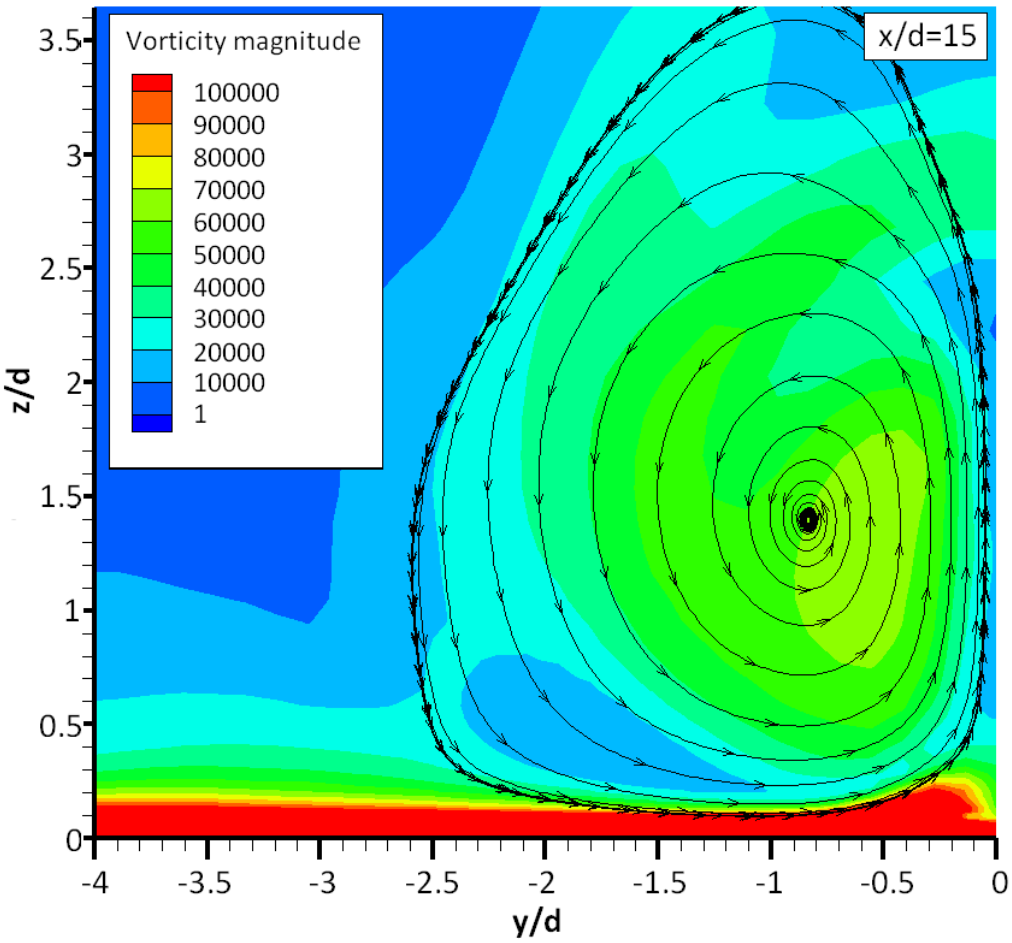


Figure 99 Contours of vorticity magnitude on a crossflow plane (x/d=15) with surface streamlines

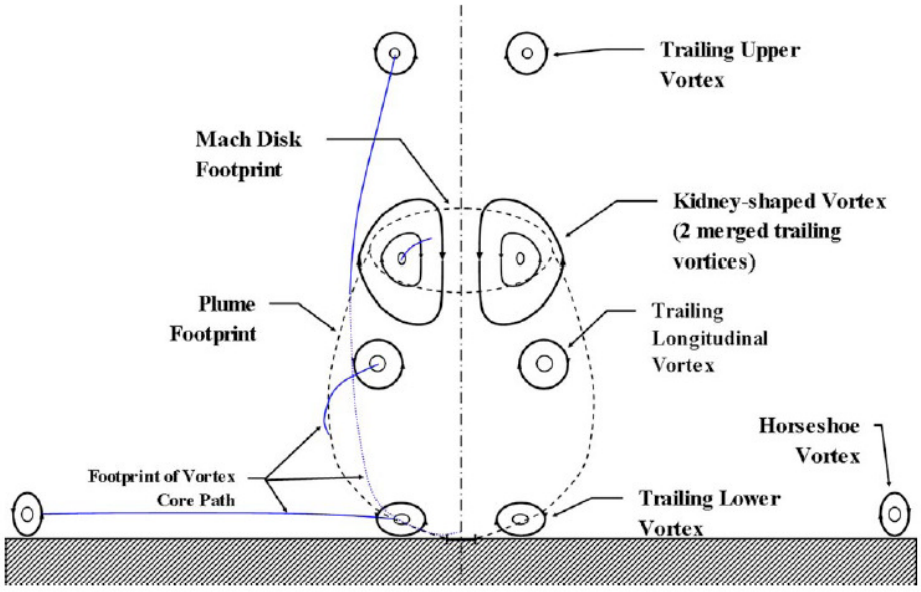


Figure 100 Viti et al.'s (2009) model of vortex structures at a crossflow plane aft of the barrel shock.

## *4.9 Surface pressure distribution*

An understanding of the three dimensional flow features can now be used to explain some features found in the surface pressure distribution. The non dimensionalised pressure distribution along the interaction centreline is shown alongside the distribution of the nondimensionalised pressure on the flat plate surface with superimposed skin friction streamlines in Figure 102. Nine areas of interest are marked (A to I). A marks the global separation line which corresponds to an increase in pressure along the interaction centreline. As discussed earlier the near wall region immediately upstream of the jet is dominated by a pair of counter rotating vortices (the horseshoe vortex & trailing vortex 2, see Figure 96). Region A to C corresponds to the horseshoe vortex core while region C to E corresponds to the core of trailing vortex 2. Point C marks the boundary between these two vortices and the attachment line that they create. The nondimensionalised pressure decreases from point B to C and from point D to C due to acceleration of the flow as it moves away from the attachment line. Downstream of jet nozzle the barrel shock remains attached to the flat plate surface for a short distance. Then as the barrel shock detaches from the surface (Region F to G) an area of low pressure is formed (Region G to H). The barrel shock, Mach disk and the reflected shock form a triple point (Figure 101). The reflected shock then impinges and thickens the boundary layer (see Figure 92) at x/d≈4.75. This impingement can clearly be seen as an increase in pressure from H to I in Figure 102. Downstream of point "I" pressure along the interaction centre line decreases to approximately the level of undisturbed flow.

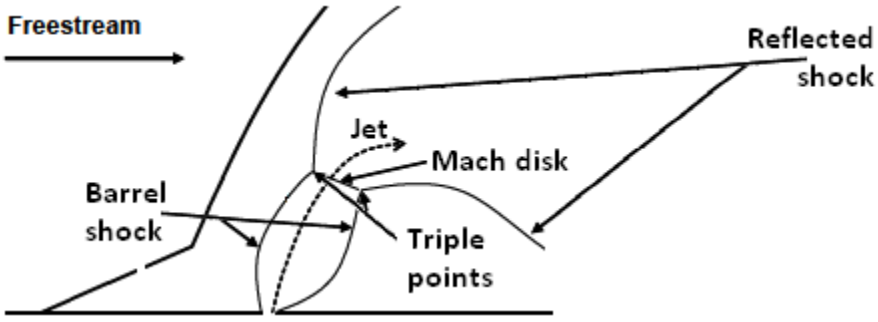


Figure 101 Schematic showing a 2-D representation of the flowfield which highlights the juncture of the barrel shock, Mach disk and reflected shock i.e. the triple point.

The flow topology on the surface of the flat plate is investigated in Figure 103 and compared to the findings of Lu & Dickmann (2008), (Figure 104). All the features described by Lu & Dickmann (2008) were found. The incoming flow separates at the global separation line with a saddle point on the interaction centreline. This is followed by the primary reattachment line and its attachment node. This attachment node marks the boundary between the two upstream counter rotating vortices. Secondary separation occurs just in front of the jet marked by a saddle point and separation line. This separation line wraps around the jet nozzle and terminates in a separation node downstream of the jet. Further downstream a pair of saddle

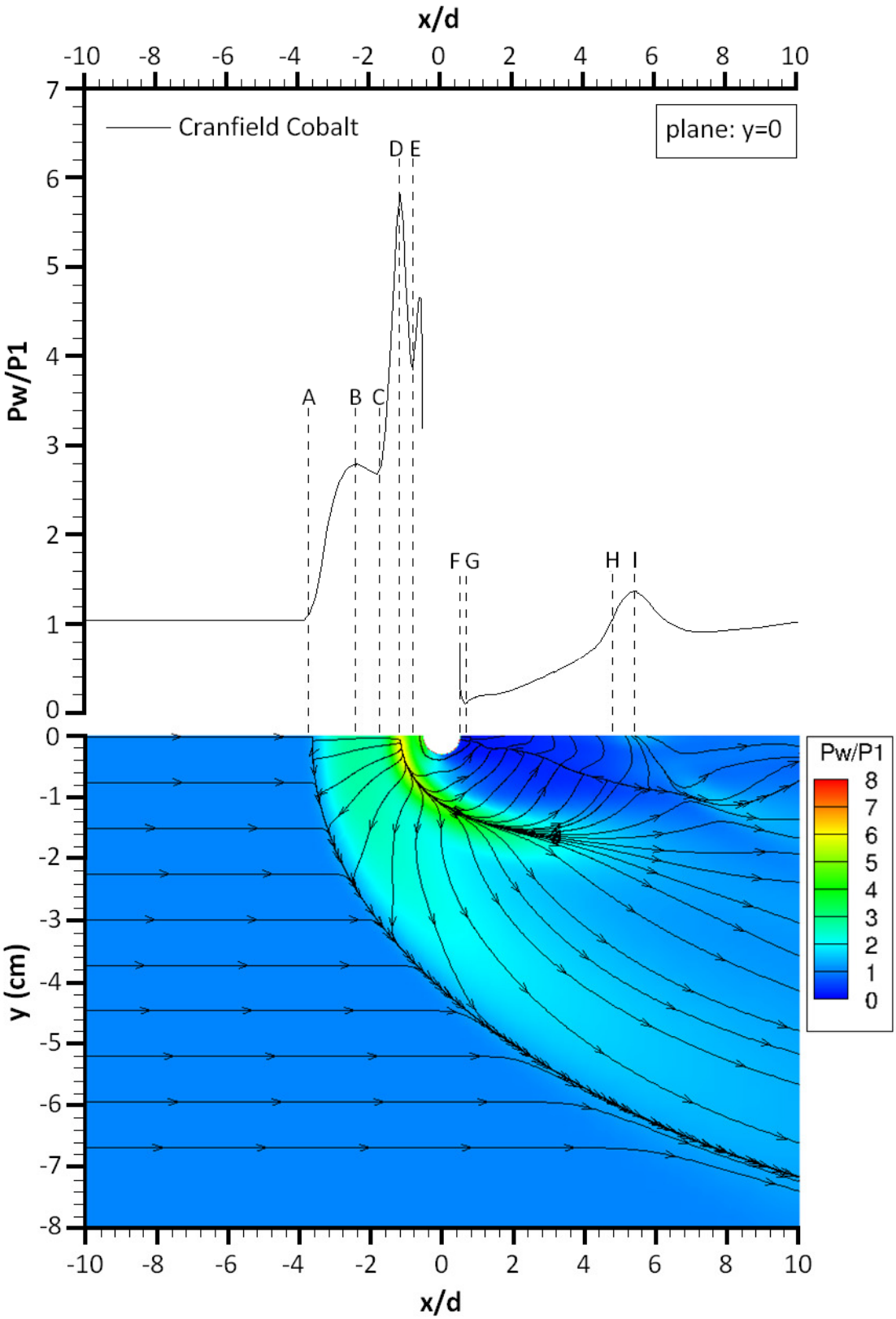


Figure 102 Top: Normalized wall pressure along the interaction plane of symmetry. Bottom: Contours of normalized wall pressure with superimposed streamlines of skin friction Where Pw is the wall pressure and P1 is the freestream pressure.

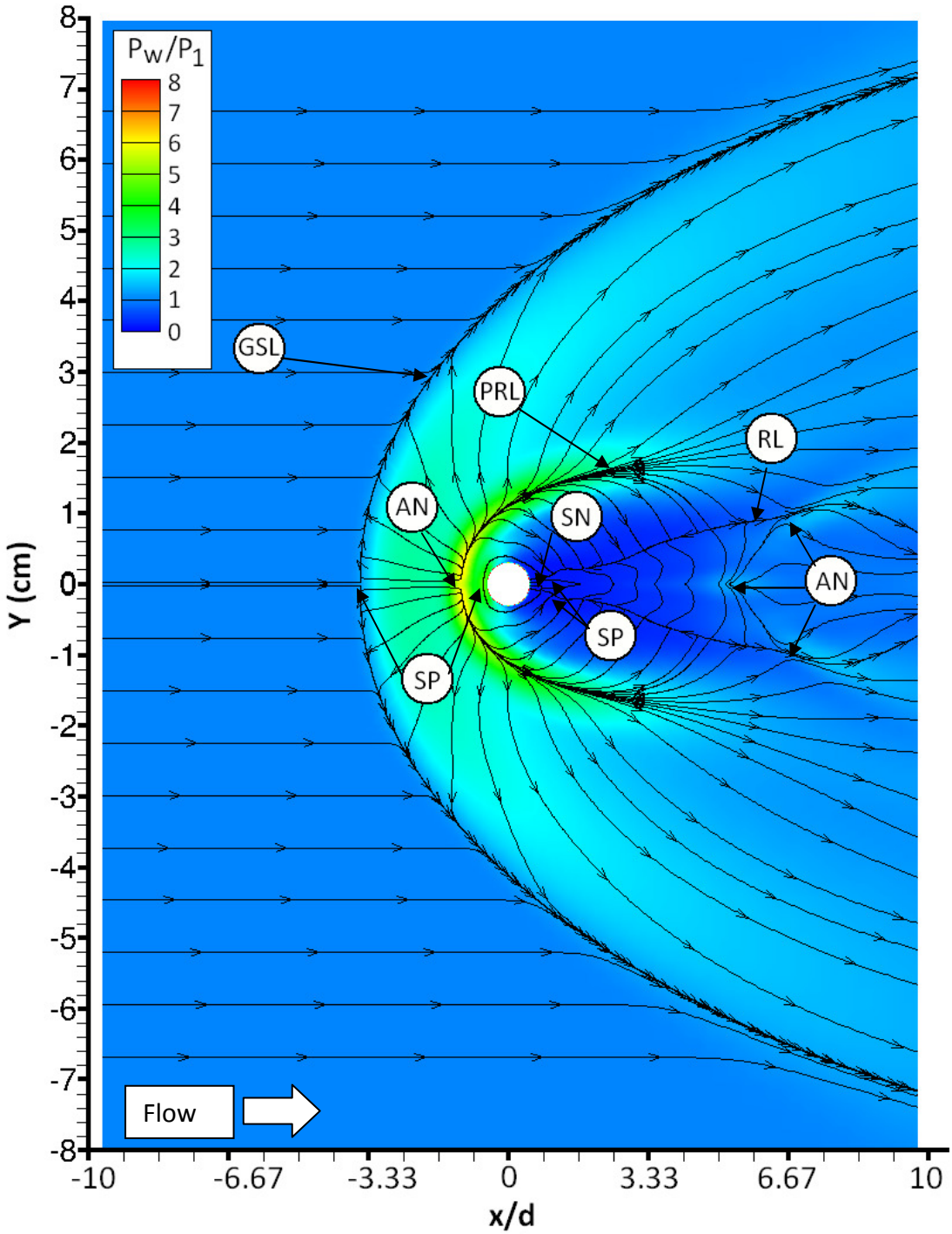


GSL: Global separation line
PRL: Primary reattachment line
RL: Reattachment line
AN: Attachment node
SN: Separation node
SP: Saddle point

Figure 103 Identification of flow topology features. Contours of normalized pressure mapped onto the flat plate surface with superimposed skin friction streamlines.

points are found with their separation lines. Finally a node of attachment where the reflected shock impinges upon the felt plate can be seen. In addition to the features described by Lu & Dickmann (2008) two extra nodes of attachment were found with corresponding attachment lines (at x/d≈6.67, y/d≈±1).

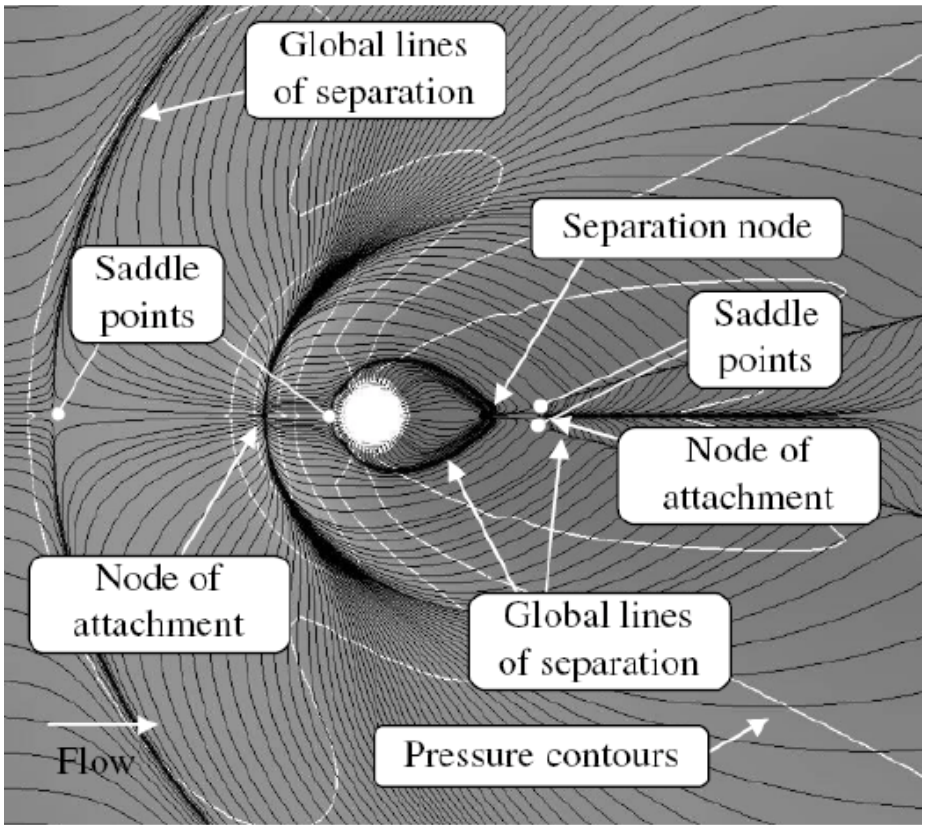


Figure 104 Lu & Dickman's (2008) Skin friction lines and flow topology, PR=100, M=2.

The flow attachment downstream of the jet is shown Figure 105. A marks the point where the reflected shock impinges on the plate. Jet fluid exhausted from the front of the barrel shock wraps around the barrel shock and reattaches at point A as well. B marks the location of the two nodes of attachment (mirrored about the interaction symmetry plane) which were not described by Lu & Dickmann (2008). These attachment nodes are also as a result of flow from the front of the barrel shock attaching to the surface.

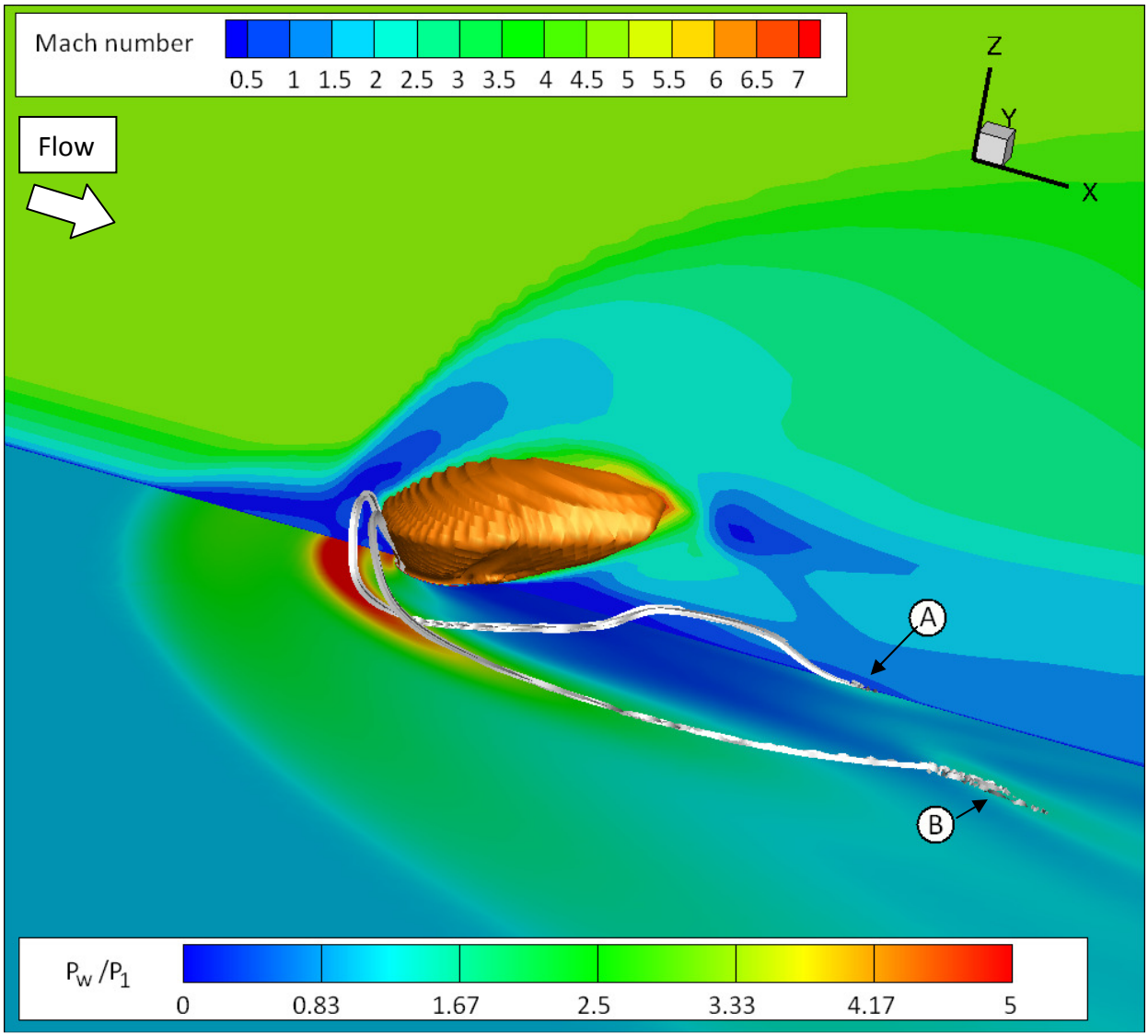


Figure 105 Isometric view of the flowfield with volume ribbons highlighting flow attachment downstream of the Mach disk. Mach disk surface approximated by entropy iso-surface. Contours of Mach number mapped onto the interaction plane of symmetry with contours of normalized surface pressure shown on the flat plate surface.

### 4.9.1 Body of revolution flowfield

Dennis (2007) states that the flowfield structure of a jet exhausted from a body of revolution is qualitatively the same as that over a flat plate. This premise is used to justify the use of a flat plate model as an idealised version of the problem (removing the influence of surface curvature). If the flowfield structures are qualitatively the same then the same shock and vortical structures should be present in both (though may differ in shape or trajectory). Similar flowfield analysis carried out above for the flat plate case was carried out for a body of revolution (DLR test model). All six vortical structures that were found in the flat plate analysis were found in the body of revolution analysis (Figure 106). No additional vortical structures were found. The main shock structures over the body of revolution were visualised by mapping contours of Mach number on the x-z plane of symmetry and by approximating the outline of the barrel shock with an entropy iso-surface. A similar shock structure was found to that over a flat plate with the separation, bow, barrel and reflection shocks highlighted in Figure 107. The Mach disk is shown in more detail in Figure 108. The indentation on the leeward side of the barrel shock and the lines of inflection in the barrel shock curvature due to the inclination of the barrel shock can once again be seen.

After investigating and extracting the main shock and vortical structures for a lateral jet interaction over a flat plate and a body of revolution it can be seen that the flowfields are qualitatively the same.

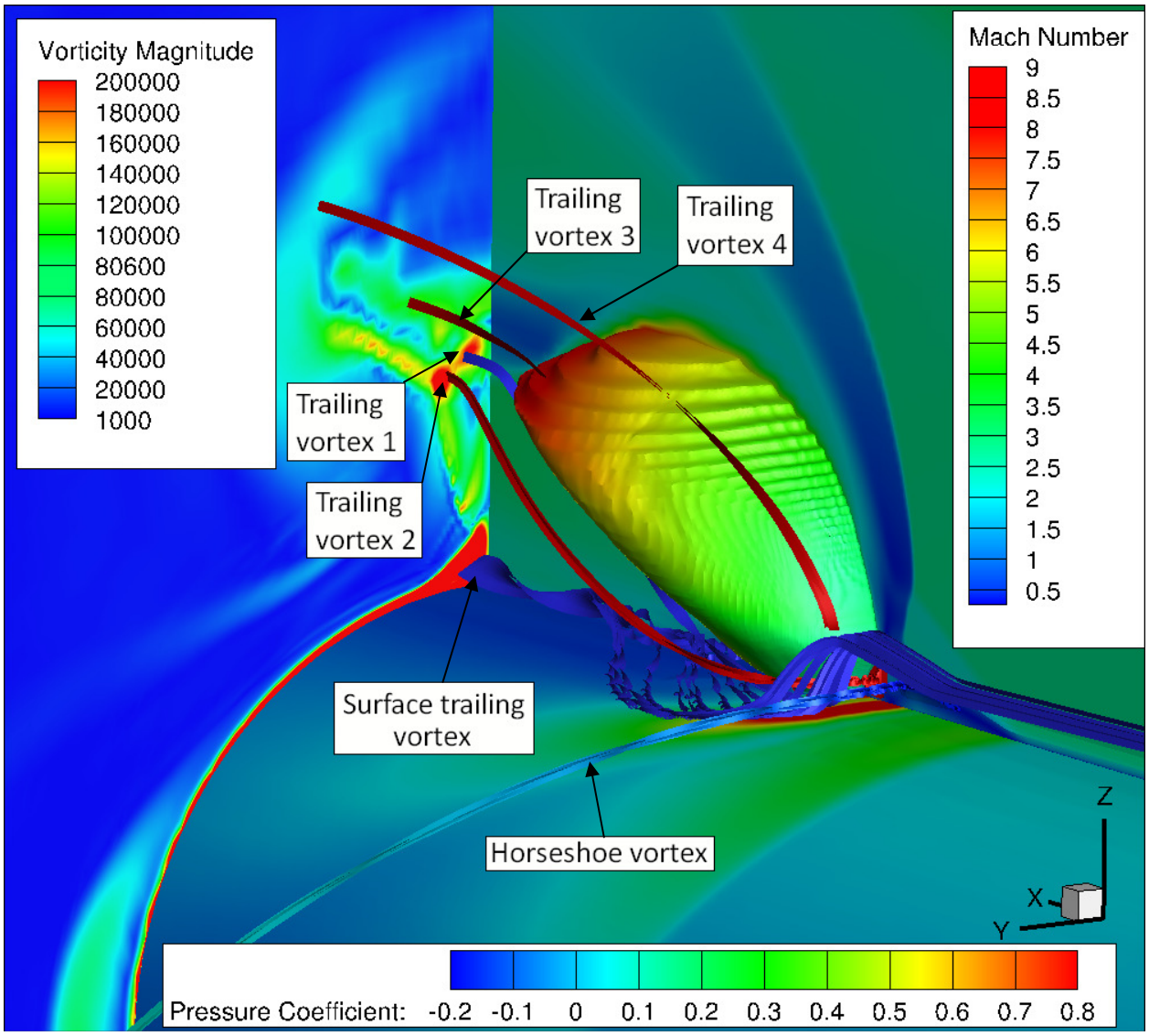


Figure 106 isometric view of the flowfield. Contours of Mach number are mapped onto the interaction plane of symmetry. Contours of pressure coefficient are mapped onto the body surface and contours of voracity magnitude are mapped onto a crossflow plane. Barrel shock is coloured by Mach number and streamlines are coloured by source (Red for jet fluid and blue for freestream fluid). DLR test body, aoa=0˚, PR=150.

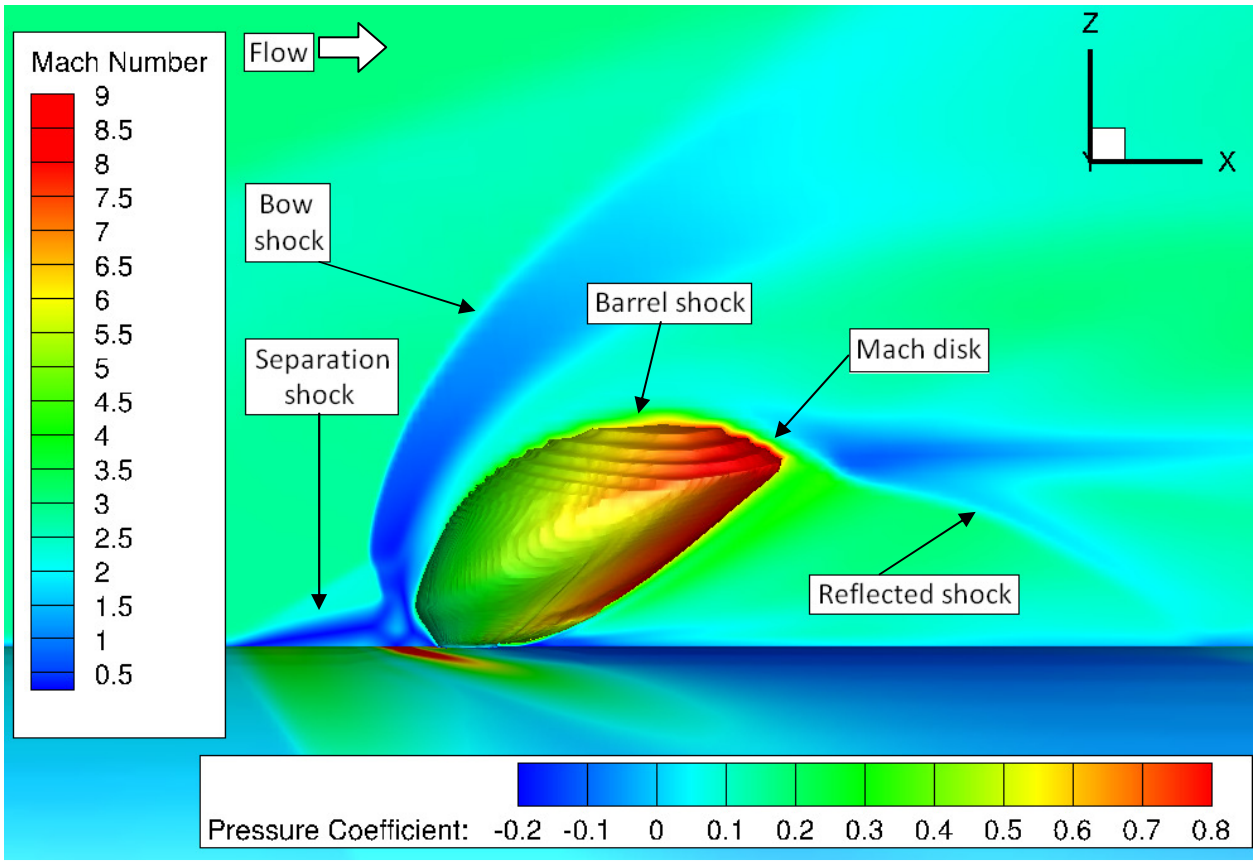


Figure 107 Contours of Mach number are mapped onto the interaction plane of symmetry. Contours of pressure coefficient are mapped onto the body surface. Barrel shock approximated by entropy iso-surface and coloured by Mach number. DLR test body, aoa=0˚, PR=150.

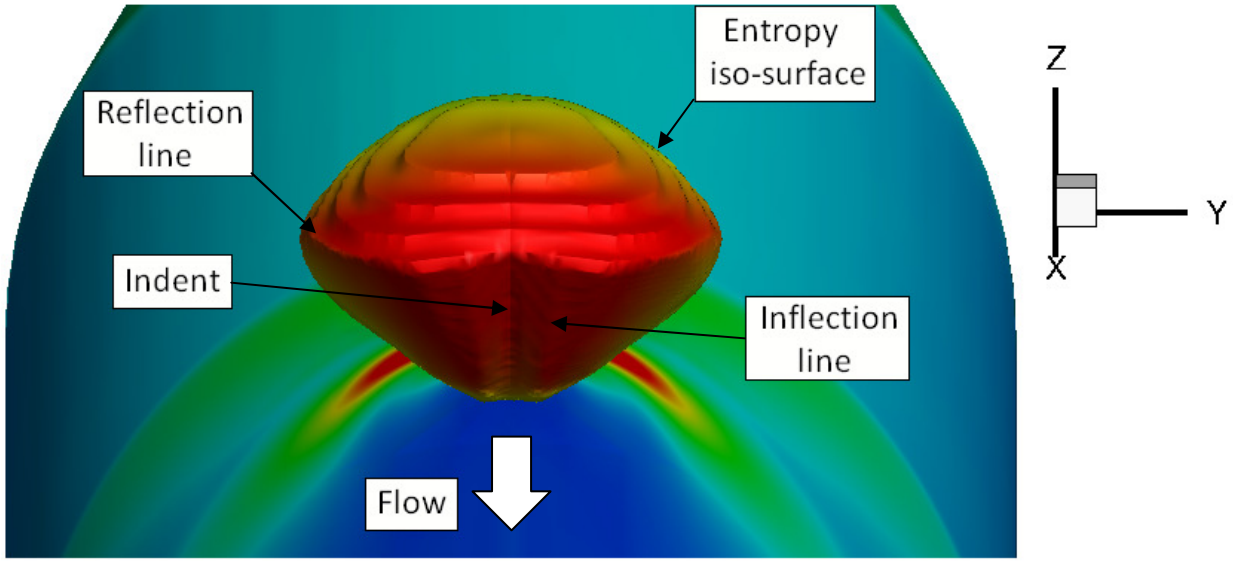


Figure 108 Contours of pressure coefficient are mapped onto the body surface. Barrel shock approximated by entropy iso-surface and coloured by Mach number. DLR test body, aoa=0˚, PR=150. Flow direction is out of page aligned with the x-axis.

## *4.10 Conclusions*

The main shock and vortical structures present in the lateral jet in supersonic crossflow interaction over a flat plate were identified and discussed. The vortical structures found compare well with Viti et al.'s (2009) model of vortex structures with the exception that no evidence for the upper trailing vortex was found. This may be due to the difference in pressure ratio. The approximate three-dimensional shape of the Mach disk was modelled as an entropy iso-surface. This allowed the reflection line and the leeward indentation in the barrel shock due to its reflection off the plate to be visualized. The flow topology was investigated using skin friction streamlines and was found to be in good agreement with Lu & Dickmann (2008). The flowfield for a lateral jet in supersonic crossflow interaction over a body of revolution was also investigated. The flowfields were found to be qualitatively the same.

# 5 Experimental campaign

The use of a RANS code to predict the lateral jet in supersonic crossflow is only valid if the problem contains no or negligible levels of unsteadiness. There is a gap in the literature in regards to measured levels of unsteadiness. Anecdotal evidence from flow visualisation techniques suggests that some aspects of the flowfield are unsteady. To address this issue the lateral jet in supersonic crossflow interaction was investigated in Cranfield University's 2 ½" by 2 ½" supersonic wind tunnel.

## *5.1 Characterisation of the incoming boundary layer*

The boundary layer on the ceiling of Cranfield University's 2 ½" x 2 1/2" supersonic wind tunnel was measured using the method outlined in §2.4. The boundary layer profile was measured for three Mach numbers (1.8, 2.4 and 3.1). For Mach 2.4 and 3.1 the boundary layer was also artificially thickened by placing a 3mm aluminum step upstream. These profiles are plotted in Figure 109 and compared to Prandtl's 1/7th power law for turbulent flow and a parabolic approximation of the Blasius equation for laminar flow. All five boundary layer profiles measured are similar to the Prandtl approximation and considered to be fully developed turbulent boundary layers.

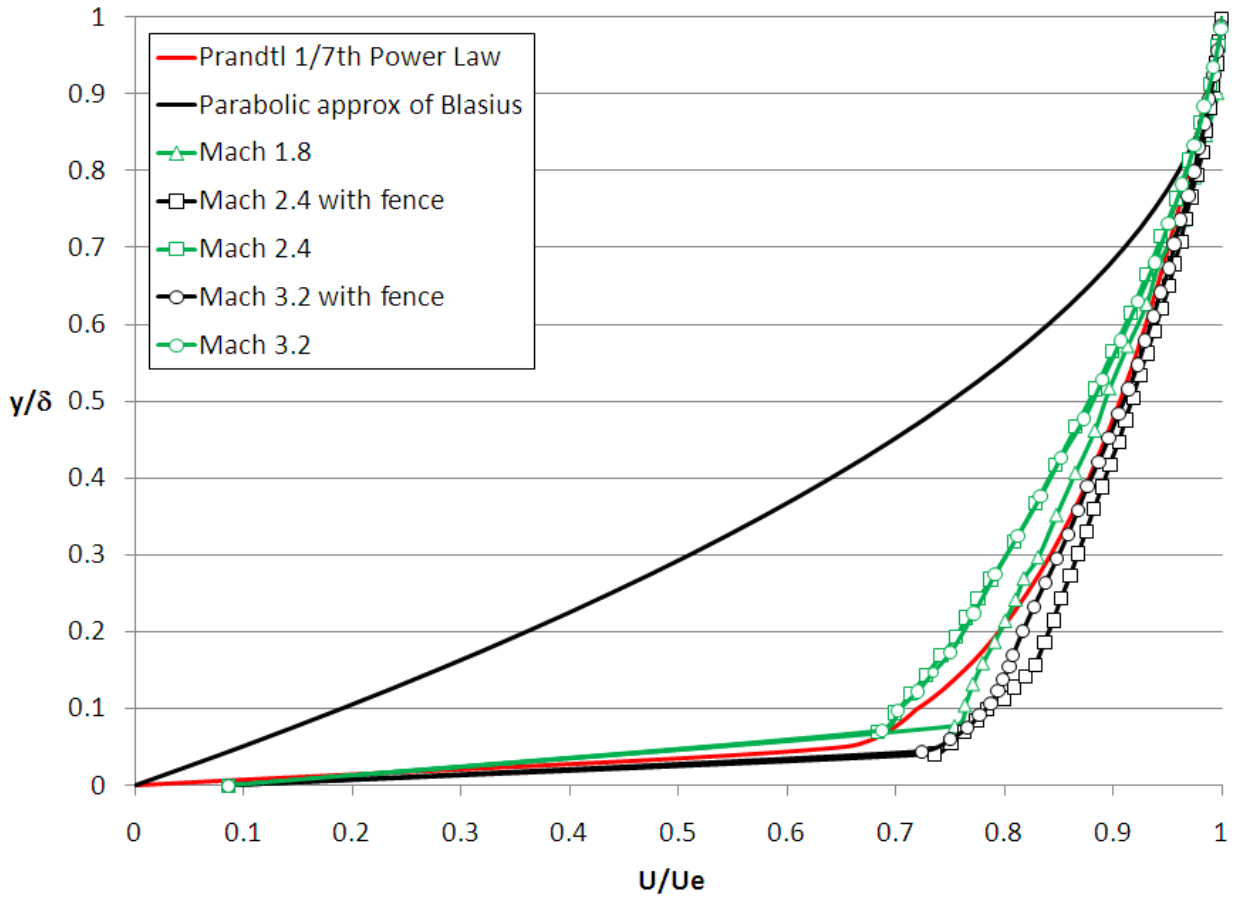


Figure 109 Comparison of measured and idealized boundary layer profiles.

Using the methods outlined in §2.4 the displacement momentum and energy displacements were calculated or each profile and are presented in Table 25.

| M | 1.8 | 2.4 | 2.4 | 3.1 | 3.1 |
|---|---|---|---|---|---|
| Fence | ✗ | ✓ | ✗ | ✓ | ✗ |
| $U_\infty$ (m/s) | 476.67 | 556.80 | 549.44 | 633.75 | 613.47 |
| $U_e$ (m/s) | 471.90 | 551.23 | 543.95 | 627.41 | 607.33 |
| $\delta$ (mm) | 4.55 | 8.63 | 5.04 | 7.95 | 4.93 |
| $T_e$ (K) | 178.65 | 138.07 | 142.06 | 93.18 | 105.57 |
| $\delta^*$ (mm) | 1.03 | 2.02 | 1.53 | 2.65 | 1.79 |
| $\theta$ (mm) | 0.62 | 1.27 | 0.84 | 1.42 | 0.88 |
| $\delta_3$ (mm) | 0.63 | 0.98 | 0.70 | 0.80 | 0.58 |
| H | 1.65 | 1.59 | 1.82 | 1.87 | 2.03 |

Table 25 Boundary layer parameters

## *5.2 Initial wind tunnel testing*

Before the high bandwidth measurements commenced the interaction was investigated to verify it was performing as expected. This consisted of a pressure survey along the interaction centreline and schlieren and oil flow visualisation.

### 5.2.1 Oil flow visualisation

The purpose of the oil flow visualisation was to see if the tunnel walls were affecting the interaction. Figure 110 shows an example oil flow visualisation of the lateral jet interaction.

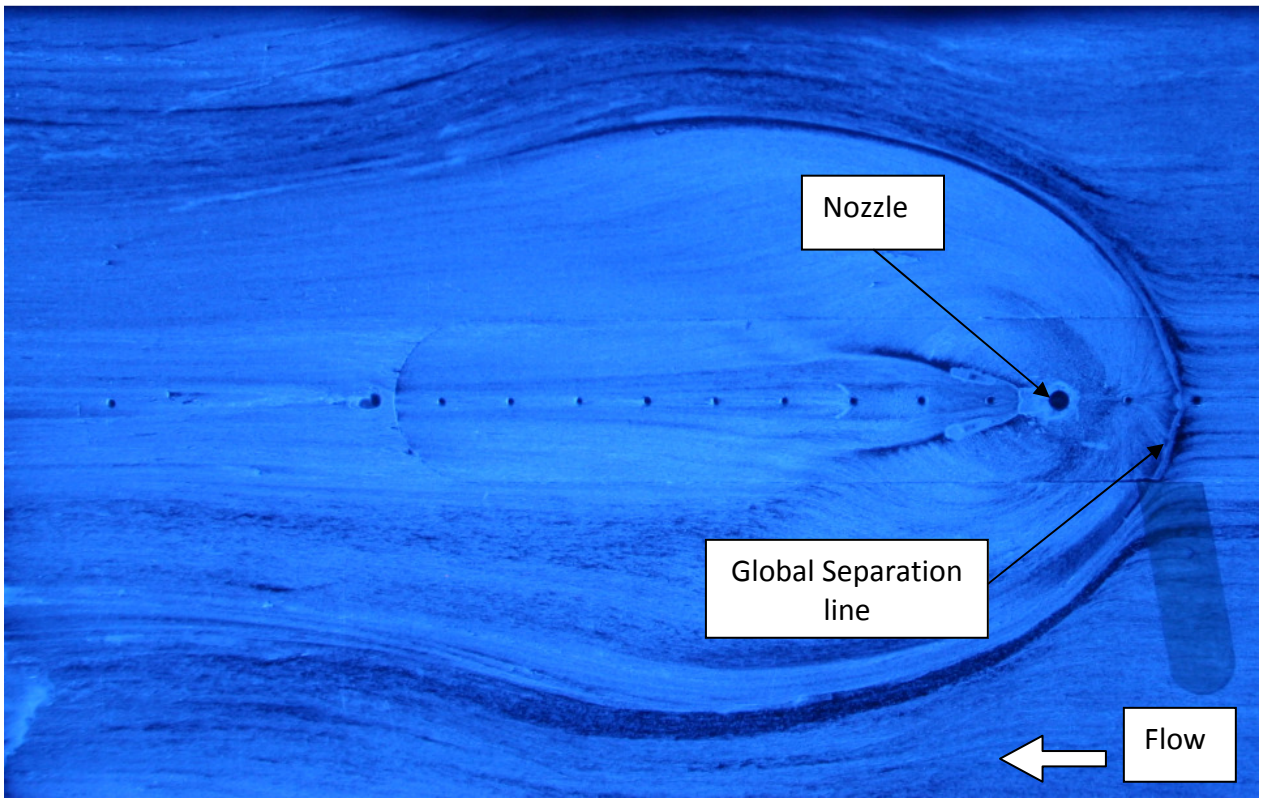


Figure 110 Oil flow visualisation of the lateral jet interaction M=2.4 PR=70.

Using the oil flow photographs and a numerical model of the experiment Battisti (2010) investigated the influence of the tunnel walls on the interaction. She concluded that at low

pressure ratios the influence of the tunnel walls was negligible. However as the pressure ratio was increased and hence the extent of the interaction increased the tunnel walls prevent a natural development of the flowfield. When the influence of the tunnel walls is felt it mostly in the downstream region.

### 5.2.2 Schlieren visualisation

Initial schlieren visualisations were carried out to make sure that the bow shock was not reflecting off the test section floor back into the region downstream of the jet. The incoming boundary layer and barrel shock in addition to the bow shock can clearly be seen in Figure 111. These initial schlieren visualisations were carried out for M=2.4 and M=3.1 for a range of pressure ratios (50≤PR≤200). The bow shock was not found to reflect off the test section floor in any of the tests.

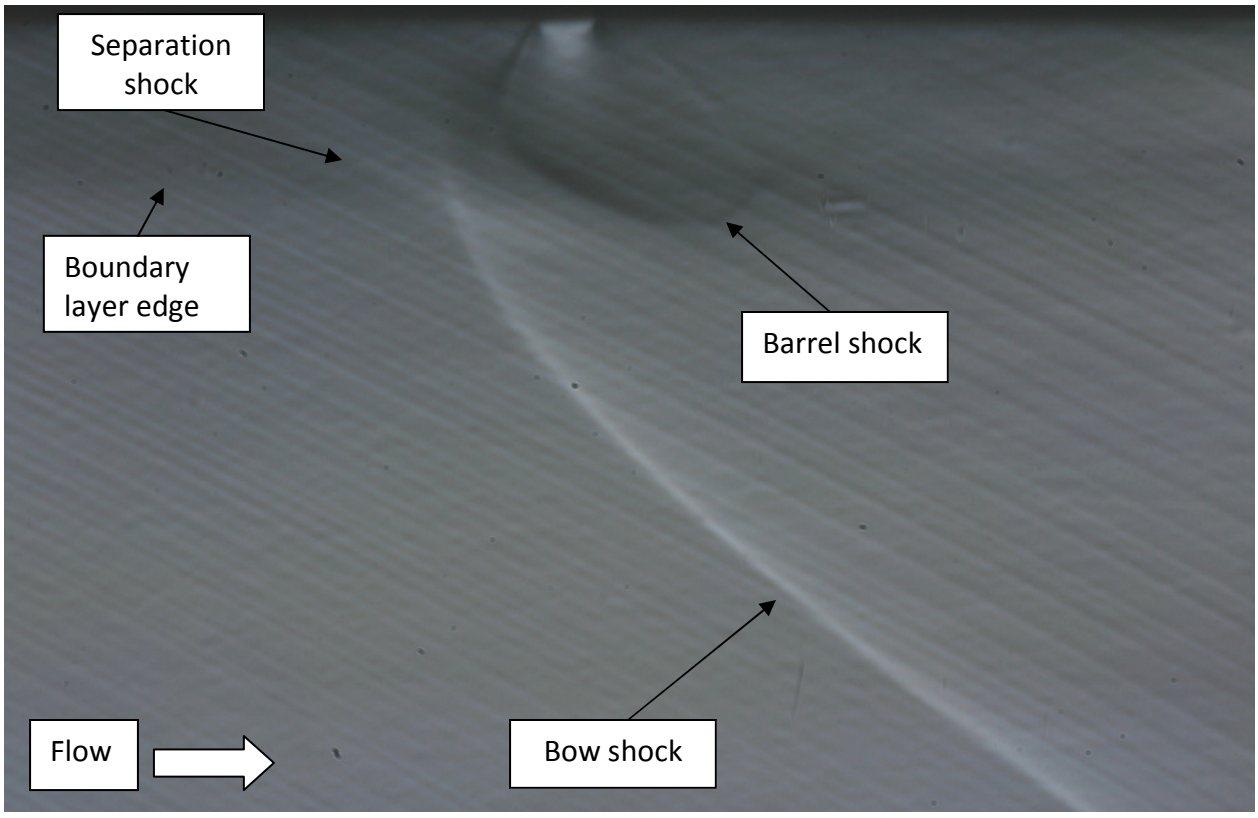


Figure 111 Time-averaged schlieren visualisation M=2.4 PR=70.

### 5.2.3 Pressure distribution along the interaction centreline

The pressure distribution along the interaction centreline was measured for all configurations (M=1.8, 2.4 & 3.1, 50≤PR200). A region of high pressure upstream and an area of low pressure downstream of the jet were found as expected. The spatial resolution of the measurements did not allow for the detailed pressure distribution immediately upstream of the jet to be captured. For the time-averaged pressure measurements the insert allowed the nearest measurement to be made 5mm from the jet, however for the micro-Kulite retention insert used in the high bandwidth pressure measurements allowed the nearest measurement to be made 4mm from the jet. Despite this slight improvement (Δx/d=0.67) this still limited the ability to resolve the pressure distribution in detail. Comparisons were made to the Battisti's (2010) prediction of the experiment (example comparison in Figure 112), which fitted the experimental data well both validating the numerical model and showing the experimental set up was performing as expected.

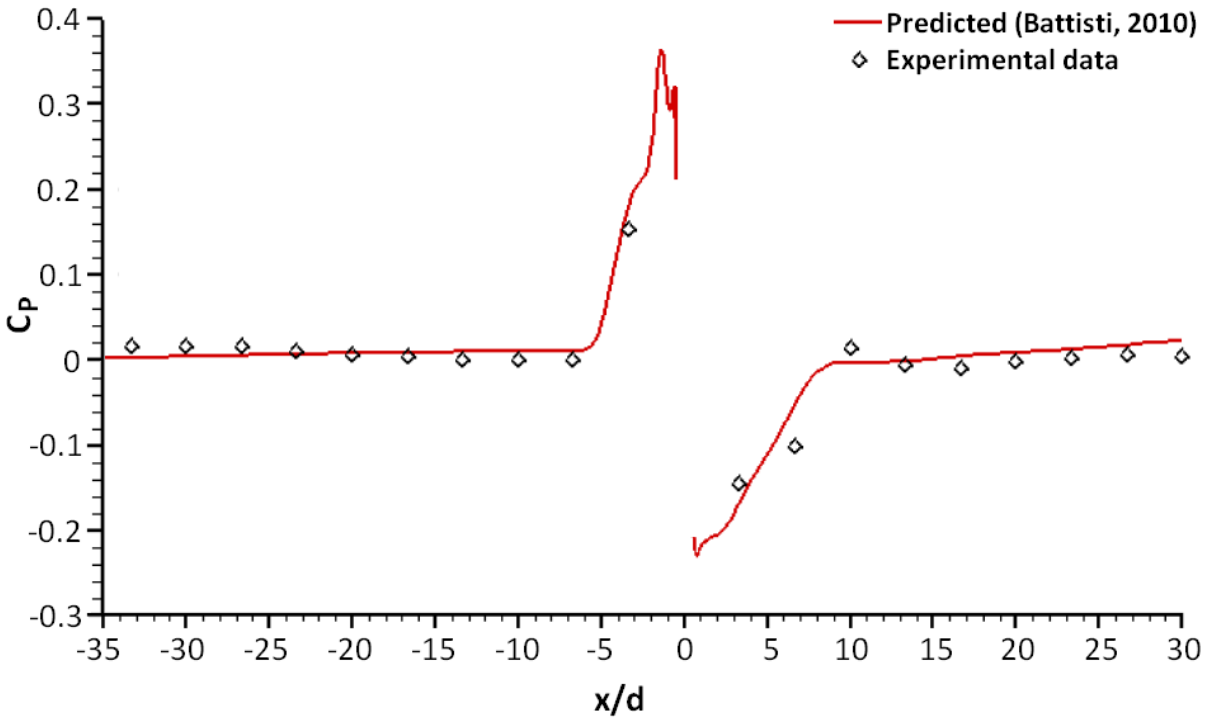


Figure 112 Coefficient of pressure centreline distribution, M=2.4 PR=50. Numerical data from Battisti (2010)

### 5.2.4 Conclusion

The experiment has been designed such that the test section floor and walls do not majorly effect the lateral jet interaction. Oil flow and schlieren visualisations conformed to the expected flowfield. Predicted coefficient of pressure data fitted the experimental data well. Pressure measurements are hampered spatial resolution.

## 5.3 High bandwidth pressure measurements

High bandwidth pressure measurements were acquired using four micro-Kulite (XCS-062-15D) high bandwidth pressure transducers. These differential pressure transducers have a range of 0-100kPa and a typical natural frequency of 200 kHz. Micro-Kulites were chosen because their small diameter (1.7mm) allowed a higher spatial resolution of measurements. Further details can be found in the micro-Kulite specification data sheet (Appendix G). These pressure transducers use a four arm Wheatstone bridge connected to a diaphragm. Deflection of the diaphragm, due to a change in pressure, results in a linearly proportional change in output voltage. By calibrating the pressure transducers against a series of known pressures the constant of linear proportionality can be found and voltages can be easily converted to pressures. These pressure transducers utilize a diaphragm of advanced design and its ability to deflect quickly is what allows them to measure high bandwidth pressure changes. The micro-Kulites were mounted in a sealed plenum connected to a Druck DPI 603 pressure calibrator and calibrated across their full range of 0 to 15 PSI (differential). The results of this calibration are presented in Appendix H.

## 5.4 Pressure transducer mounting location

The micro-Kulites were mounted in the top liner of the wind tunnel flush to the ceiling of the test section. They were retained using an o-ring and this limited the minimum spacing between transducers to 5mm (Figure 113). The pressure transducers were placed to maximize the chance of sensing the unsteadiness of the interaction. Figure 114 shows a schematic of the transducer placements. From preliminary oil flow visualization it was apparent that the foot of the upstream shock fell in the region between micro-Kulite 5 and the jet (Figure 114). Two sensors were placed up stream (at x/d=-2.67 & x/d=-3.33) to look for the movement of this shock and any unsteadiness associated with it or the separated region. Unsteadiness was also expected to be found downstream of the interaction in the area of low pressure. Micro-Kulite 1 was placed immediately downstream (x/d=2.67) for this reason. The final transducer, micro-

Kulite 3 was placed upstream of the interaction (x/d=-23.33) to find any pressure fluctuations associated with the incoming undisturbed flow.

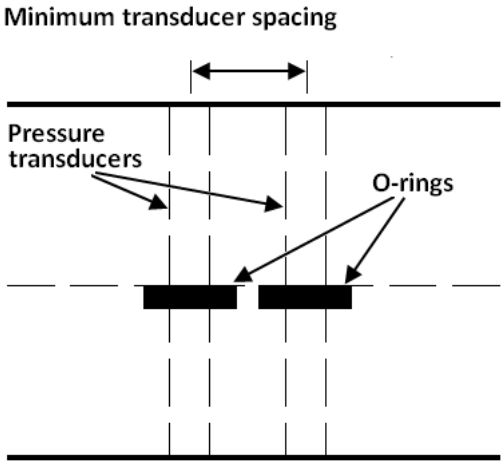


Figure 113 Pressure transducer retention method showing minimum spacing constraint.

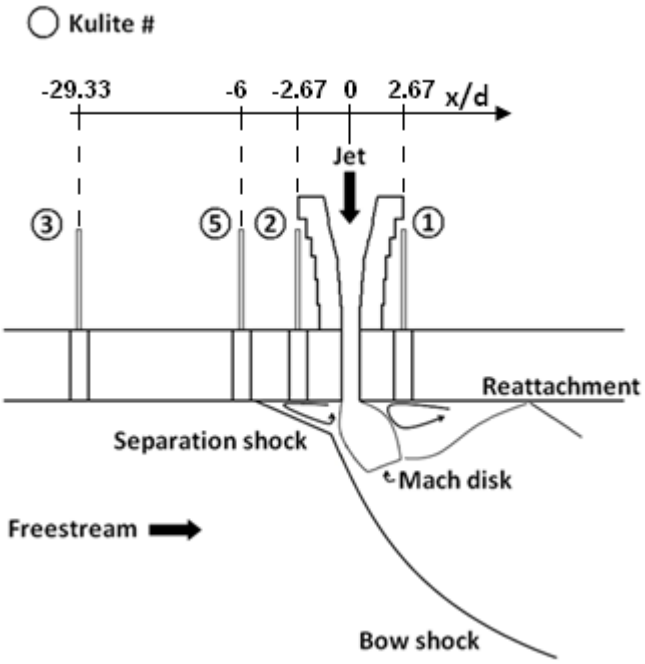


Figure 114 Schematic showing the placement of the micro-Kulite pressure transducers.

## 5.5 Operating conditions

Three Mach numbers were achieved in Cranfield University's 2 ½" x 2 ½" supersonic wind tunnel (M=1.8, 2.4, 3.1) by using different Mach liners. The corresponding freestream Reynolds number per unit length is given in (Table 26). The underexpanded, sonic jet had a measured total temperature of 18˚ which did not vary between tests. Pressure ratio is a function of jet total pressure and freestream Mach number. With a freestream Mach number of 1.8 it was not possible to achieve a pressure ratio of 50. Therefore MPR (defined in Equation 7) was also used as a characteristic parameter to allow a larger range of freestream Mach numbers to be investigated. This resulted in two series of tests; with constant PR and with constant MPR (Table 27 & Table 28 respectively).

| M | Re (1/m) |
|---|---|
| 1.8 | $1.4 \times 10^7$ |
| 2.4 | $1.1 \times 10^7$ |
| 3.1 | $7.6 \times 10^6$ |

Table 26 Freestream Reynolds number per unit length.

| δ/d | PR / M | 50 | 55 | 70 | 97 | 110 | 150 | 200 |
|---|---|---|---|---|---|---|---|---|
| 3.36 | 2.4 | ✔ | ✔ | ✔ | - | - | - | - |
| 3.29 | 3.1 | ✔ | ✔ | ✔ | ✔ | ✔ | ✔ | ✔ |
| 5.75 | 2.4 | ✔ | ✔ | ✔ | - | - | - | - |
| 5.30 | 3.1 | ✔ | ✔ | ✔ | ✔ | ✔ | ✔ | ✔ |

Table 27 Test conditions for constant pressure ratio (PR).

| δ/d | MPR / M | 2.7 | 3.0 | 3.8 | 5.3 | 5.9 | 8.1 | 10.8 |
|---|---|---|---|---|---|---|---|---|
| 3.03 | 1.8 | ✔ | ✔ | ✔ | - | - | - | - |
| 3.36 | 2.4 | ✔ | ✔ | ✔ | ✔ | ✔ | - | - |
| 3.29 | 3.1 | ✔ | ✔ | ✔ | ✔ | ✔ | ✔ | ✔ |

Table 28 Test conditions for constant momentum parameter ratio (MPR).

## *5.6 Results and Discussion*

Figure 115 shows the FFT output for each micro-Kulite transducer in a Mach 1.8 flow with the jet operating at MPR of 3.8 and a PR of 22. For this case there are increases in the amplitude of frequencies in the range 0Hz to 4kHz between micro-Kulite 3 upstream of the interaction and all the other pressure transducers which are influenced by the jet interaction. Of the two micro-kulites immediately upstream of the interaction, micro-Kulite 5 (x/d=-6, Figure 115) displays a larger increase in amplitude (maximum increase of ≈25Pa as opposed to ≈5Pa). This could be associated with the motion of the shockwave foot. Dupont *et al.* (2005) state that frequencies associated with the shock motion are in the region of a few hundred Hertz. In their experiments a SWTBL induced by a wedge shock generator in M=2.3 flow frequencies of the shock motion were 400Hz to 600Hz. The pressure transducer (micro-Kulite 2) immediately upstream, (x/D=-2.67), of the jet shows much lower amplitudes which are below the minimum resolution of the system (9.4Pa). micro-Kulite 1 at x/d=2.67 downstream of the jet in the area of recirculation measured higher amplitudes over a larger frequency range than the transducers upstream of the interactions. This was the case for every experimental configuration and for most cases there was no discernable unsteadiness measured upstream.

Figure 116 shows the FFT output for the pressure transducer placed in the freestream upstream of the interaction (micro-Kulite 3) in a M=3.2 flow for a range of pressure ratios (50≤PR≤200). Here all frequencies have an amplitude below the minimum resolution. These frequencies are the electrical noise in the system.This was also the case for the FFT output for micro-Kulite 5 (Figure 117). The downstream transducer (micro-Kulite 1) displays a clear trend with PR. As the pressure ratio increases the amplitude of pressure fluctuation increases in the low frequency range below 500Hz (Figure 118).

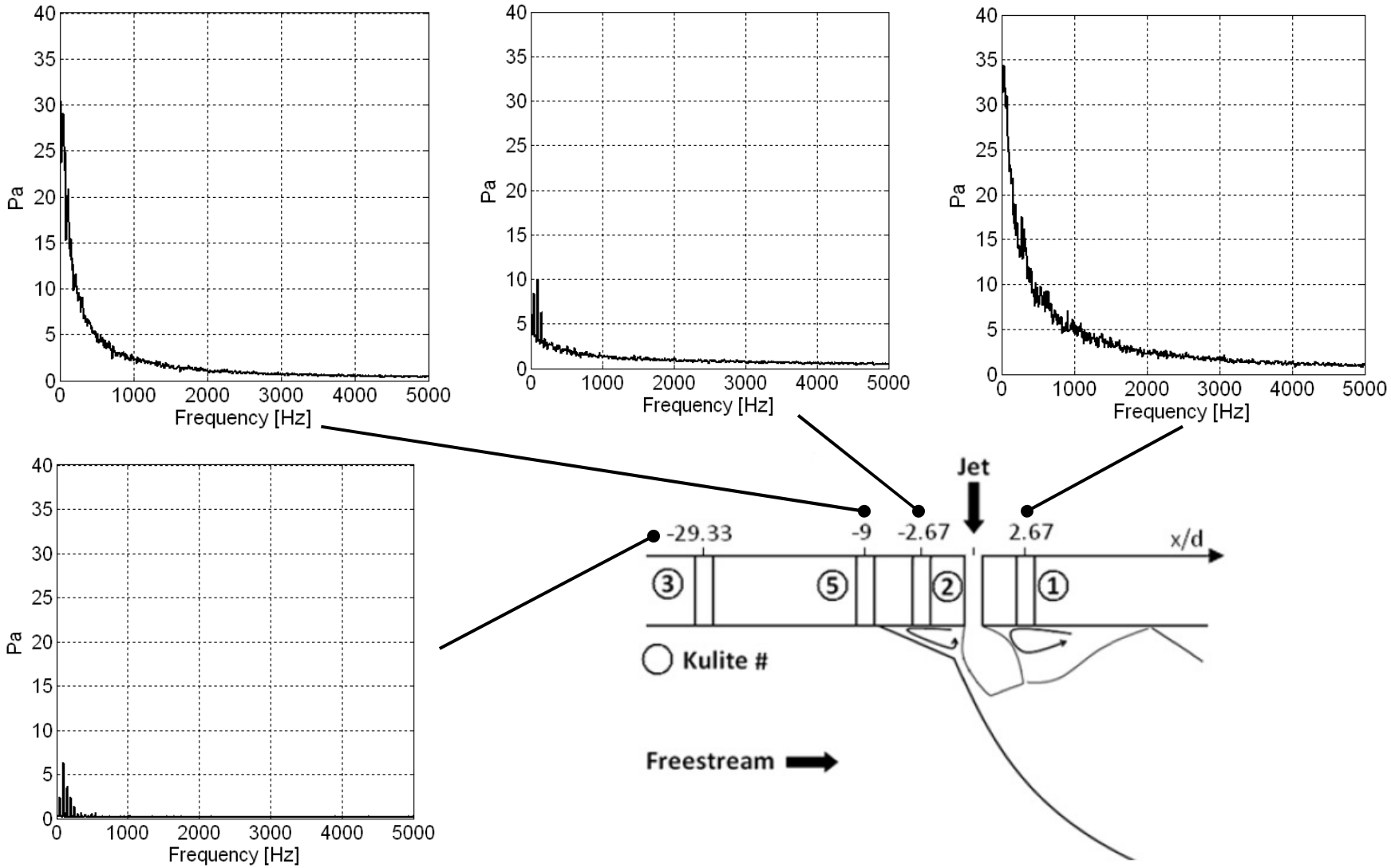


Figure 115 Pressure signal transformed into the frequency domain using a FFT, M=1.8, MPR=3.8.

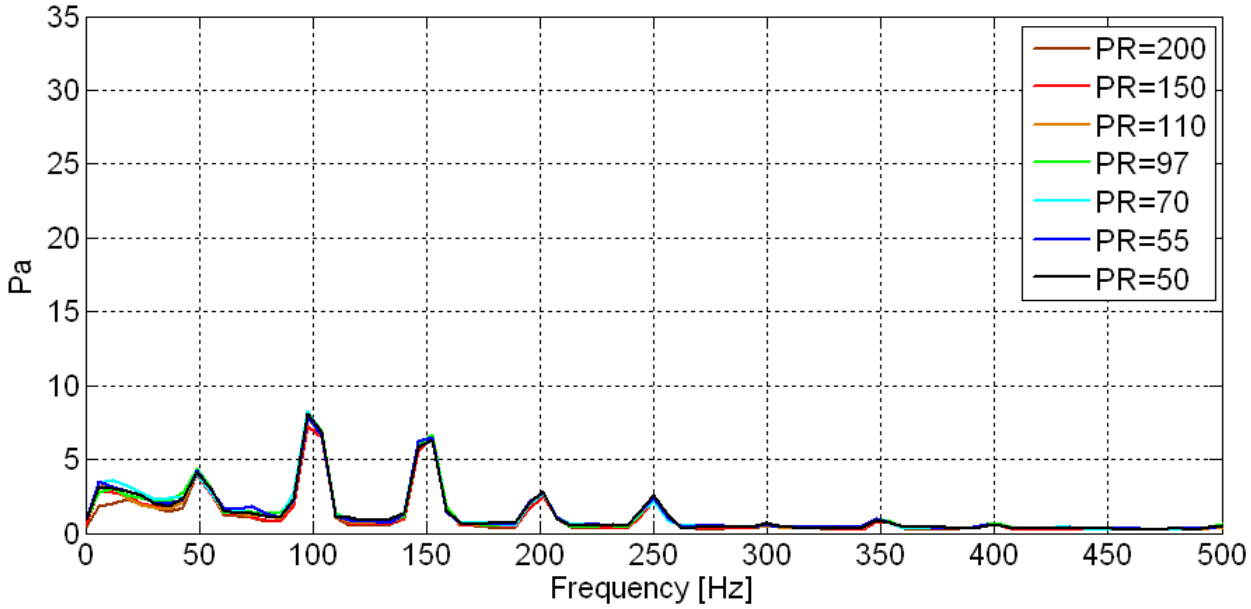


Figure 116 Effect of jet pressure ratio (PR) on pressure spectral distribution for a freestream of M=3.2. Data from micro-Kulite 3 which is far upstream of the jet (x/d=-29.33).

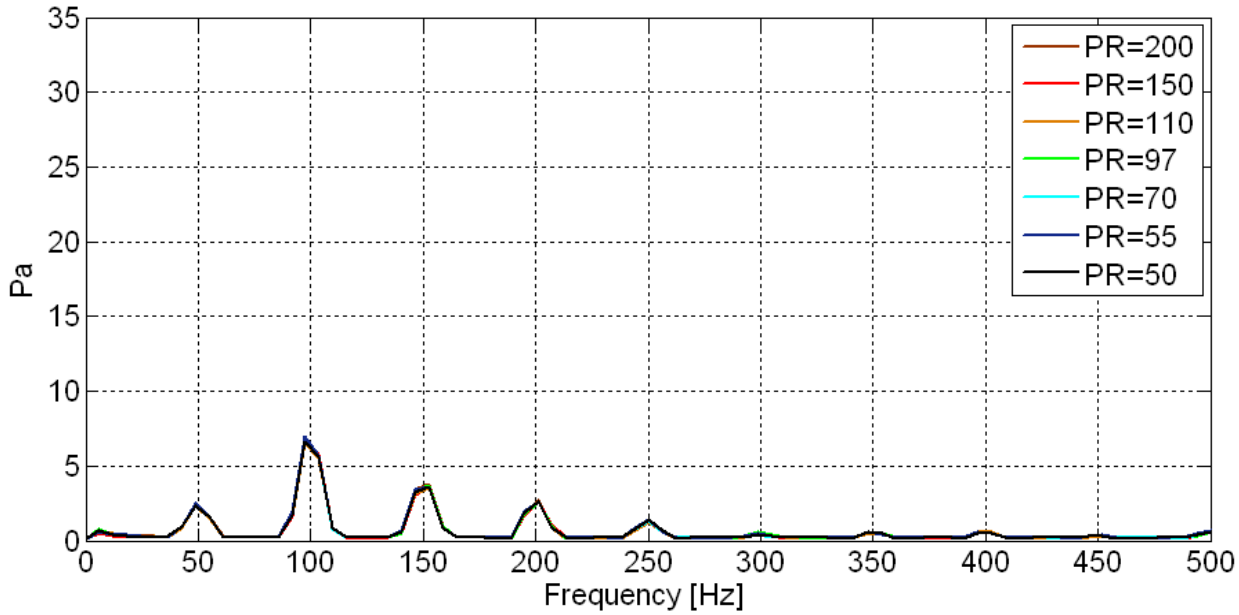


Figure 117 Effect of jet pressure ratio (PR) on pressure spectral distribution for a freestream of M=3.2. Data from micro-Kulite 5 which is upstream of the jet (x/d=-6).

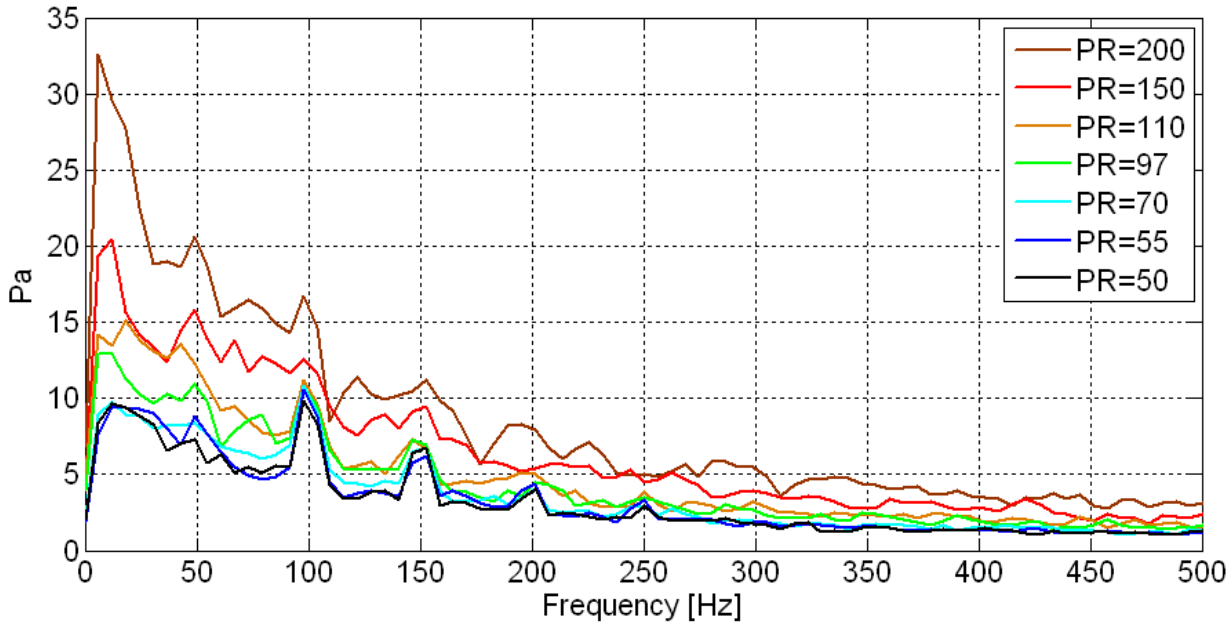


Figure 118 Effect of jet pressure ratio (PR) on pressure spectral distribution for a freestream of M=3.2. Data from micro-Kulite 1 which is downstream of the jet (x/d=2.67).

In an effort to quantify the level of unsteadiness and hence compare between cases the OASPL has been calculated for each case. Figure 119 shows the relationship between PR and OASPL for each pressure transducer. This shows that the relationship seen in Figure 118 for the downstream transducer is also true for the cases with a M=2.4 crossflow. OASPL increases roughly linearly with increases in PR. Conversely for this transducer (x/d=2.67, micro-Kulite 1) increasing the Mach number decreases the OASPL level. This is also seen for transducer 3 upstream of the interaction. This Mach number effect id due to decreases in static pressure as Mach number is increased. For the two transducers upstream of the jet there is no clear evidence that the PR has an effect on the level of unsteadiness.

Figure 120 shows the relationship between OASPL and MPR. In the area of recirculation (x/d=2.67, micro-Kulite 1) OASPL can be seen to increase with MPR and decrease with Mach number. Once again levels of OASPL upstream of the interaction (micro-Kulite 3) are seen to increase with decreasing Mach number but MPR does not have an effect. This scaling of OASPL with Mach number is seen at micro-Kulite 5 but the levels of OASPL have decreased and at micro-Kulite 2 no discernable trend is observed.

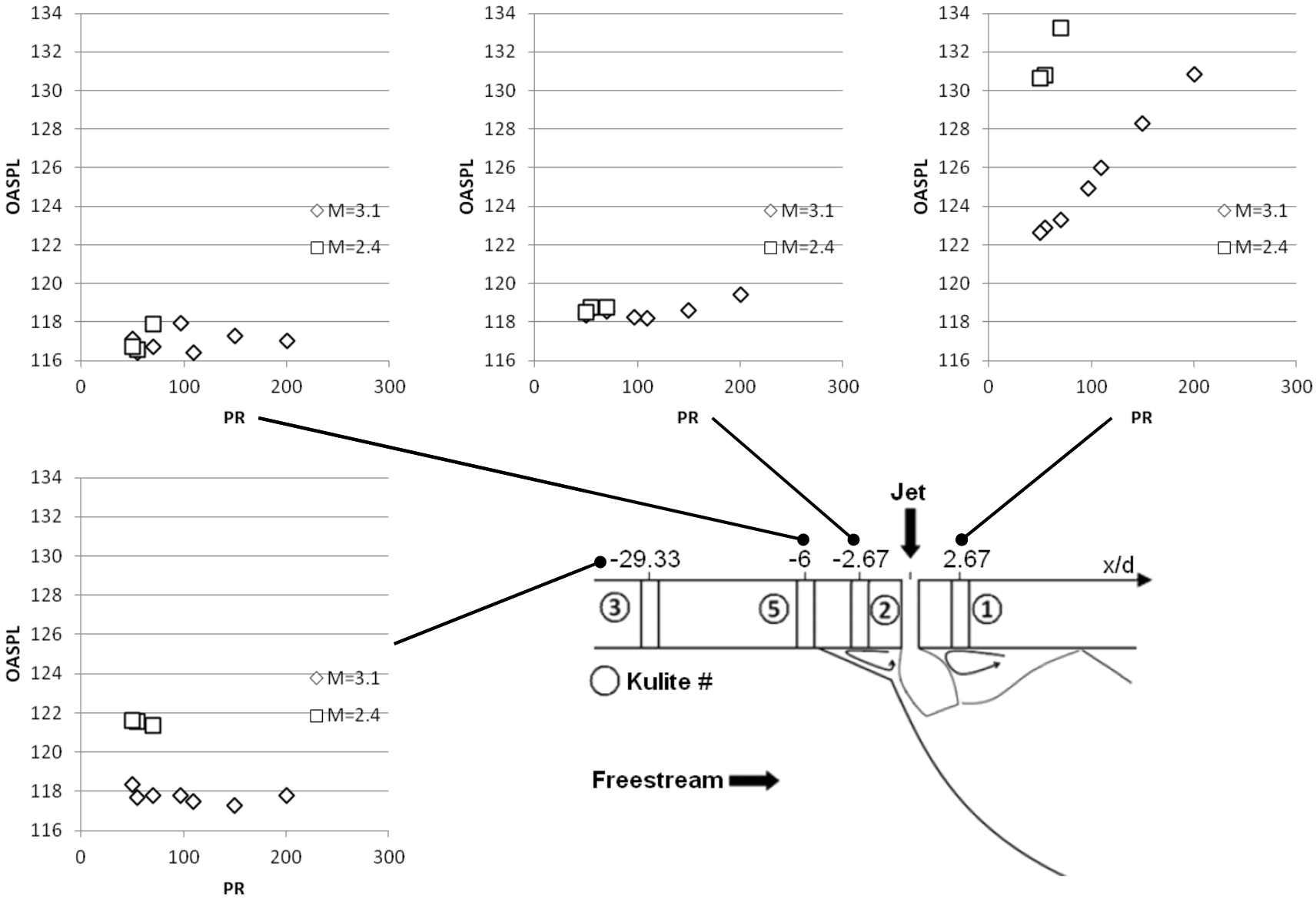


Figure 119 Relationship between OASPL and PR

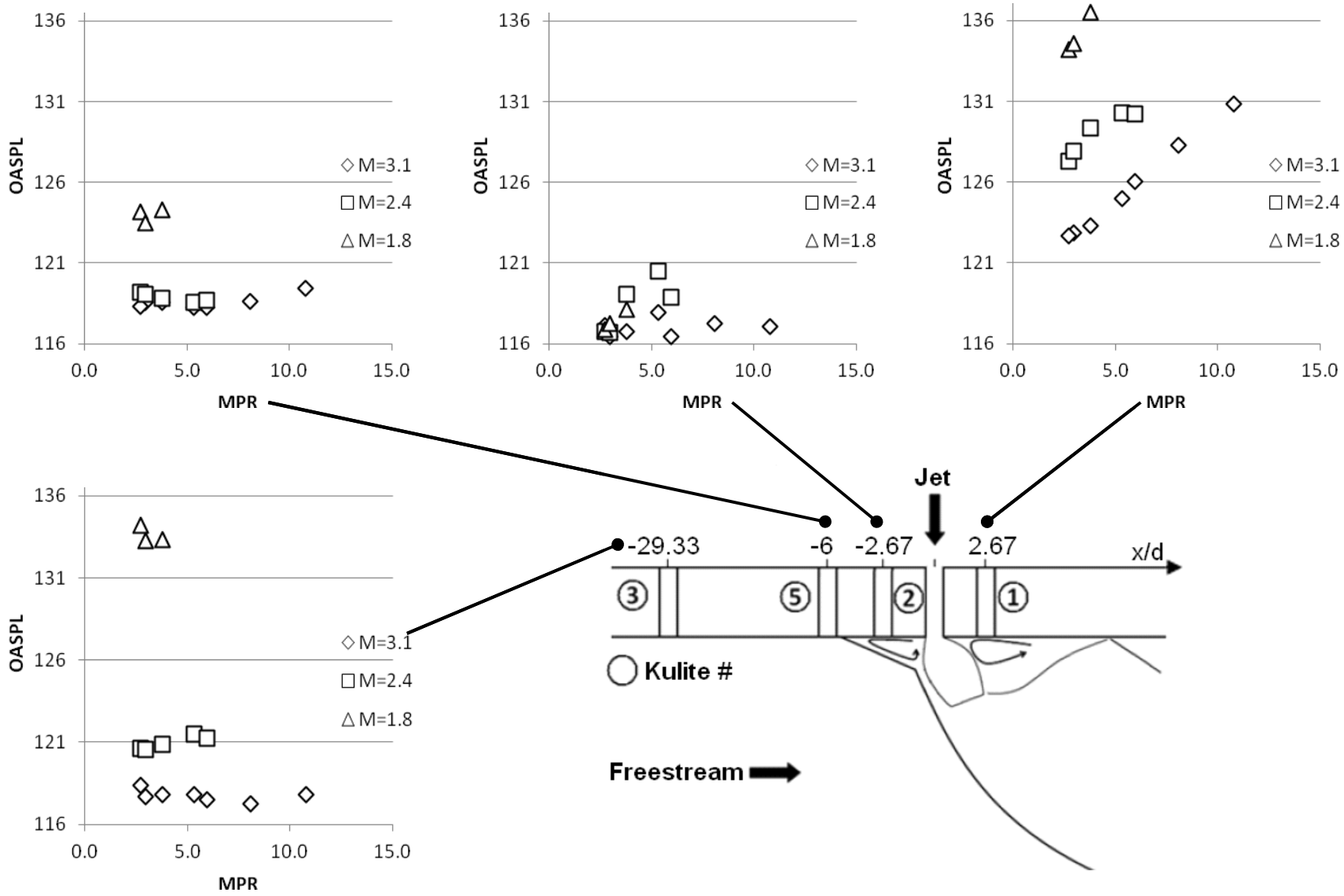


Figure 120 Relationship between OASPL and MPR

To investigate the influence of the approaching boundary layer, measurements were taken with a thicker boundary layer. The boundary layer was thickened using a 3mm fence. The approaching boundary layer and displacement thicknesses are presented in §5.1. Figure 121 shows the influence of the boundary layer on OASPL (the FFT output for each case is presented in Appendix I). Upstream of the interaction for both M=2.4 and M=3.2 flows the thicker boundary layer leads to higher levels of OASPL. For micro-Kulite 5 (x/D=-6) this effect is not seen however for micro-Kulite 2 which is just ahead of the jet (x/D=-2.67), the effect is very pronounced especially for the M=3.1 case with roughly an increase of 20 OASPL. Downstream this increase in OASPL is much less, roughly 3 OASPL and only occurs at lower PRs (50-110 for the M=3.1 case and 50-55 for M=2.4). This may possibly be explained by looking at the boundary layer profiles (Figure 109). The boundary layers which have been thickened have a larger $U/U_e$ in the near wall region and hence a larger velocity shear. Stronger shear levels lead to stronger levels of turbulence. The overall levels of unsteadiness are small. For example the case with the highest OASPL (M=3.1, PR=110, MPR=6, δ/d=5.3 & OASPL=143) non-dimensionalising the pressure signal amplitude with the total pressure gives a value of 0.15 (Equation 54).

$$\frac{|P|}{P_0} = 0.015 \qquad \text{Equation 54}$$

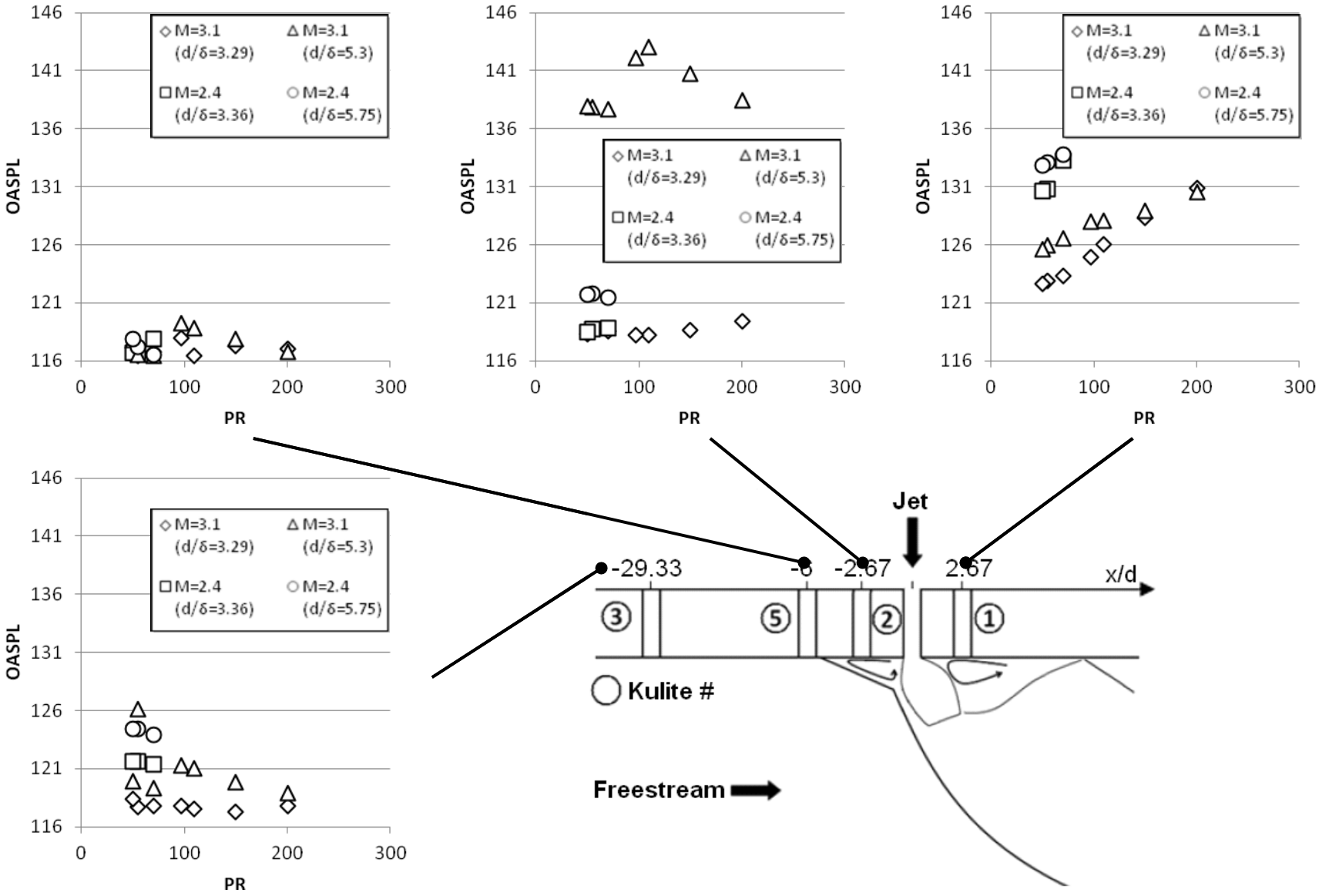


Figure 121 Influence of boundary layer thickness on OASPL.

Unsteadiness in the lateral jet interaction flowfield was investigated by Battisti (2010) using high-speed schlieren. Eight flowfield points were selected (Figure 122) and the fluctuating RGB values at these points were extracted from the recorded images. Each point was select to capture the behavior of a flow feature:

1. Freestream
2. Incoming boundary layer edge
3. Upstream separation shock
4. Bow shock foot
5. Bow shock,
   (adjusting to Mach angle)
6. Bow shock,
   (adjusted to approx Mach angle)
7. Barrel shock,
   (windward end of Mach disk)
8. Barrel shock,
   (leeward end of Mach disk)

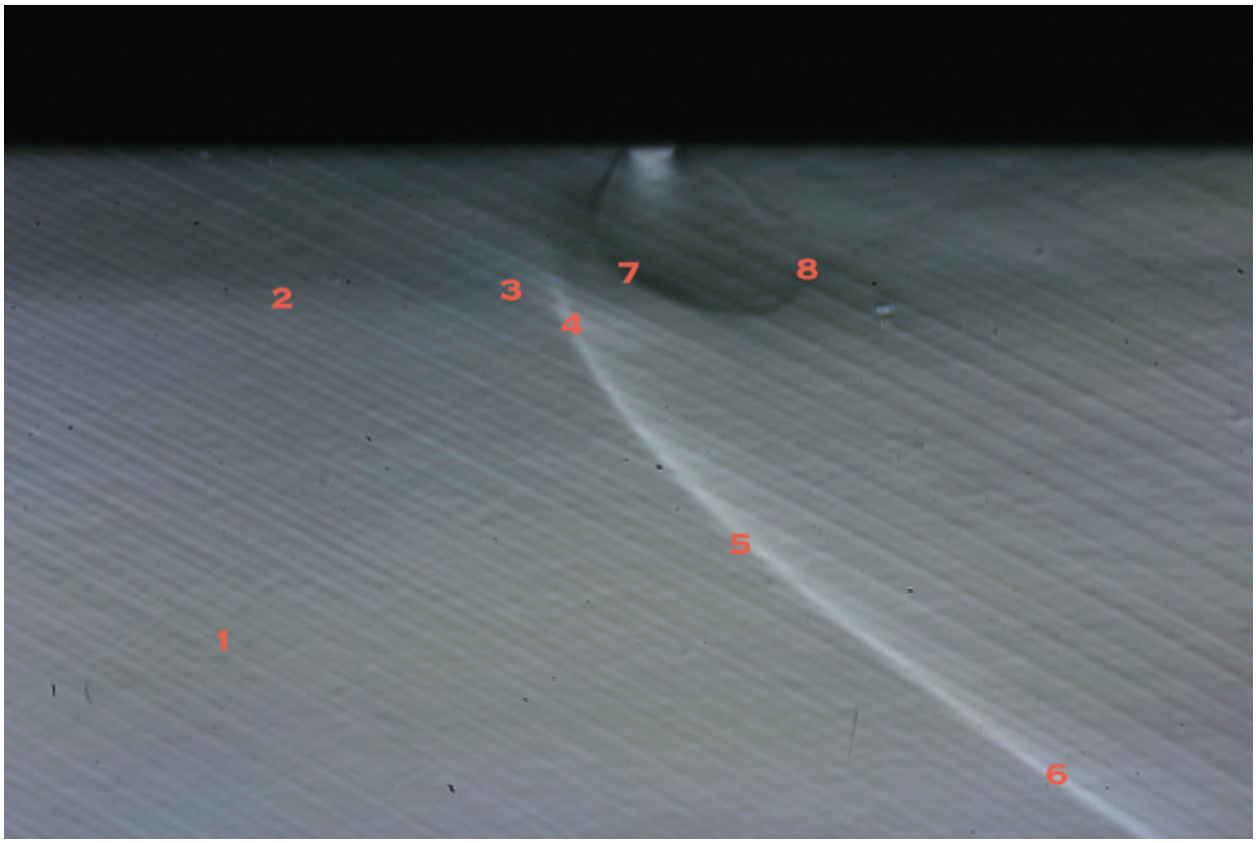


Figure 122 Time-averaged Schlieren image of the jet interaction (3072×2048 pixels), displaying the approximate locations where the flow was investigated (Battisti,2010).

At each point the extracted fluctuating RGB values were analyzed using a FFT to reveal the frequency spectrum (see Battisti (2010) for further details). The jet exhausted into a quiescent medium was also analyzed using high speed Schlieren. Battisti (2010) found that the jet in this configuration was very steady and was not a source of the unsteadiness observed in the crossflow interaction. Before discussing these results further it should be noted that the amplitudes recorded here were calculated from values of light intensity. Light intensity was dependent on the schlieren steup (knife edge cut-off, light source battery power etc.). This meant that comparisons in amplitudes could not be made between different tests. However in individual tests the light intensity across the whole image was considered uniform enough to allow comparisons between the amplitudes at different points in the image to be made.

Figure 123 shows the FFT output of a point in the freestream and a point on the edge of the incoming boundary layer. Low frequency pressure peaks were observed for both points. The similarity between spectrums for these points led Battisti (2010) to conclude that frequencies present in the freestream were dictated by low frequency fluctuations in the incoming boundary layer.

To identify the unsteadiness in the lateral jet interaction Battsisti (2010) subtracted the characteristic signal of the freestream from the signal measured on the bow shock and Mach disk. The FFT of these modified signals are presented in Figure 124. The highest levels of unsteadiness were on the leeward edge of the Mach disk. Battisti (2010) found that all frequencies at the foot of the bow shock near the jet exit (Point 4) were amplified suggesting a strong interaction between the bow shock and the jet.

Battsisti (2010) investigated the effect of boundary layer thickness, pressure ratio and Mach number on the levels of unsteadiness in the interaction by tracking bow shock movement. Using the amplitude of bow shock oscillation to quantify the level of unsteadiness it was found that levels of unsteadiness were increased by increasing the boundary layer thickness, pressure ratio or momentum parameter ratio. This is in agreement with the high-bandwidth wall

pressure measurements undertaken in the present study. However Battsisti (2010) found increased levels of unsteadiness with increased Mach numbers, the opposite trend to that found in the wall pressure measurements. This may be somewhat explained in the difference in measurement location. The high-speed schlieren images gave a measure of unsteadiness in the flowfield. Specifically the influence of Mach number investigation only measured the bow shock amplitude while the pressure transducers only measured the fluctuating wall pressure. Also a discernable trend in unsteadiness levels with variation of Mach number was not clear for micro-Kulite 2 (Figure 119) which was the pressure transducer closest to the bow shock. For this transducer OASPL was higher for some momentum parameter ratios at M=2.4 than at M=3.1 (Figure 120). This shows that the high-speed schlieren and high bandwidth wall pressure measurements are not necessarily incompatible and if a similar optical investigation of the downstream region was undertaken a different trend may be revealed.

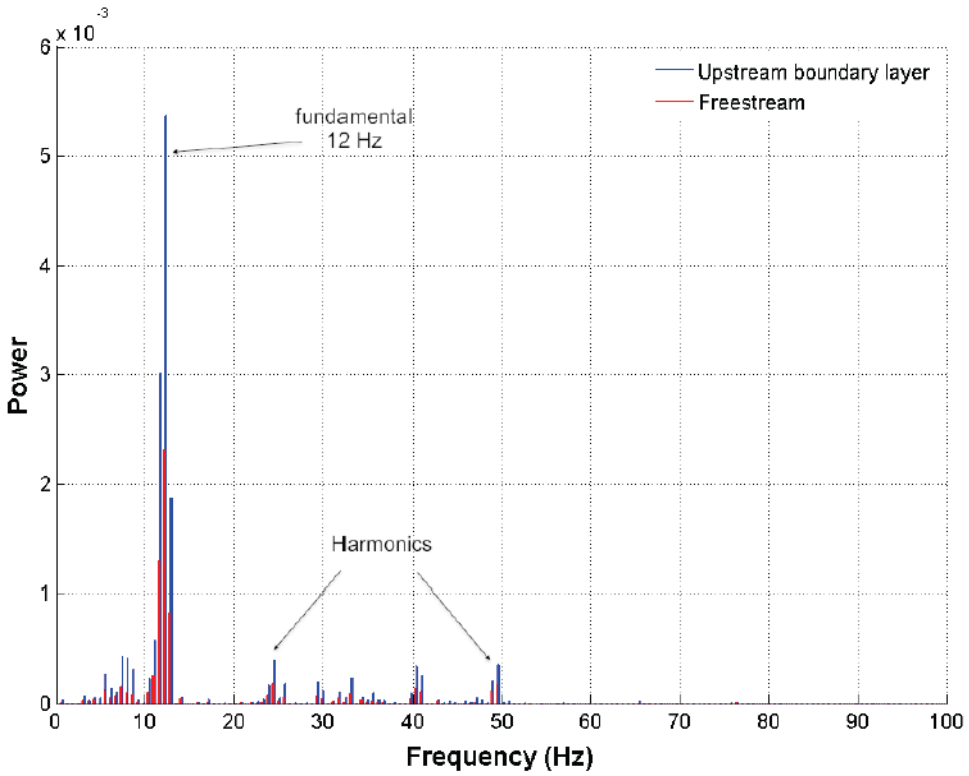


Figure 123 Frequency spectra of the freestream and the incoming boundary layer (Points 1 & 2 ), Δf = 1 Hz (Battisti 2010).

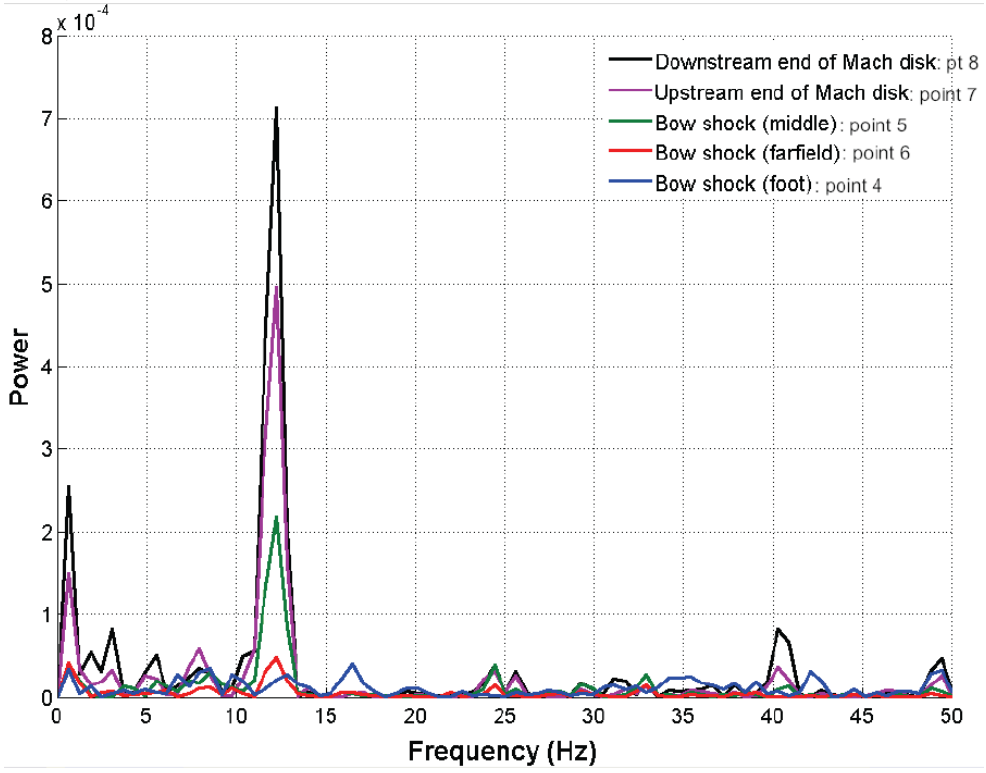


Figure 124 Frequency spectra of the Mach disk and the bow shock, Δf = 1 Hz (Battisti 2010).

Though there has been a lack of unsteadiness level measurements for the lateral jet in supersonic crossflow interaction the problem has similarities to other more studied problems. Upstream of the jet there is shock wave boundary layer interaction. This interaction has shown the same basic trends in the fluctuating pressure field hold for a range of interactions including those generated by blunt and sharp fins, ramps with sweep, and impinging shocks (Clemens & Narayanaswamy, 2009). A schematic of these configurations is given in Figure 125.

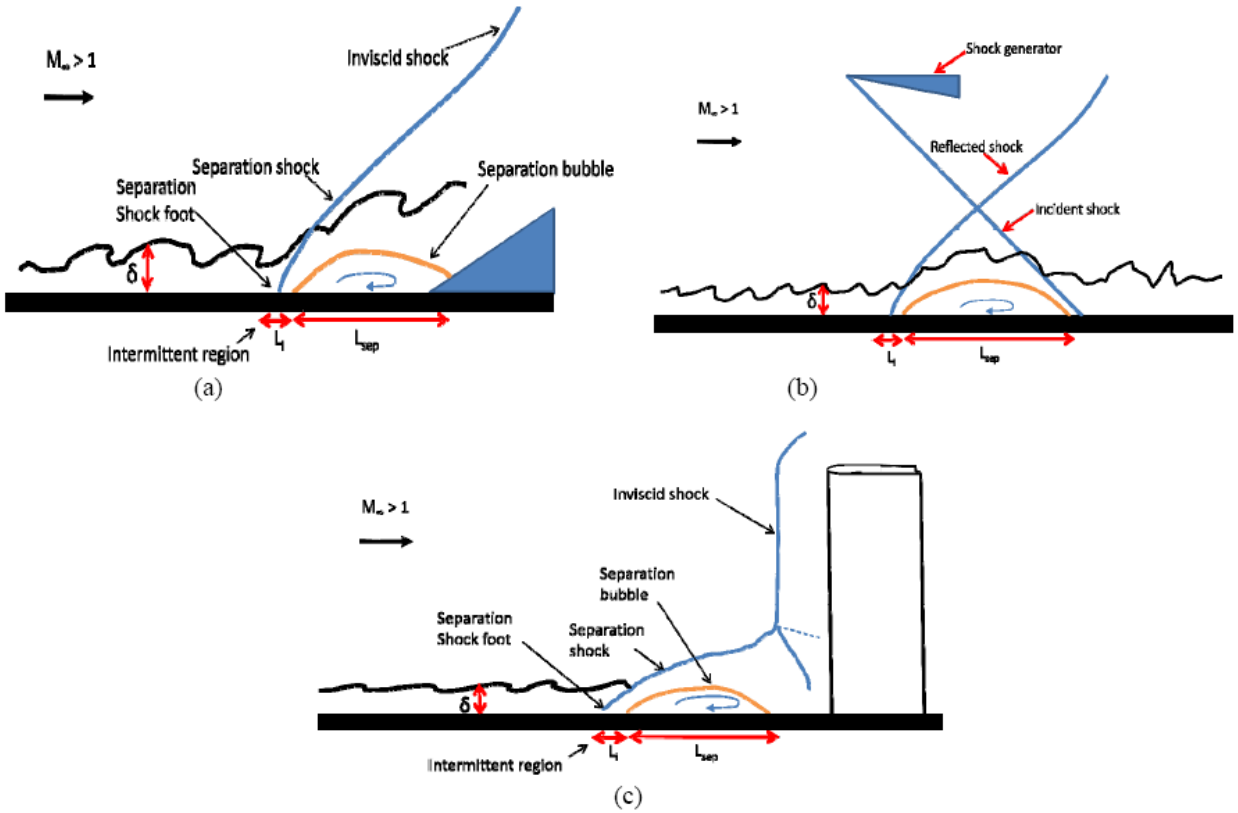


Figure 125 The three canonical shock wave / boundary layer interactions. (a) compression ramp, (b) impinging shock, and (c) blunt fin (Clemens & Narayanaswamy, 2009).

In previous work carried out in the Cranfield University 2 ½ " by 2 ½ " supersonic wind tunnel (Estruch et al., 2010), the interaction between an impinging shock created by a wedge shaped shock generator and a turbulent boundary layer in Mach 2.4 flow was studied experimentally. From high speed schlieren visualization a reflected shock frequency in the order of 100 Hz was found. Unsteady pressure measurements at the foot of the reflected shock were also dominated by low frequencies. Figure 126 and Figure 127 show the average of the frequency spectra upstream and downstream of a shock wave turbulent interaction. A similar low

frequency range (0-1.5kHz) dominates as in micro-Kulite 5 and micro-Kulite 1 (x/d=-6 & 2.67 respectively) in Figure 115. However a comparison of amplitudes is not possible because Figure 126 and Figure 127 are plotted with arbitrary units. What is of note however is the presence of distinguishable pressure peaks in the work by Estruch et al. (2010). Clear pressure peaks (apart from those caused by electrical interference) were not in found the present work either upstream or downstream of the interaction.

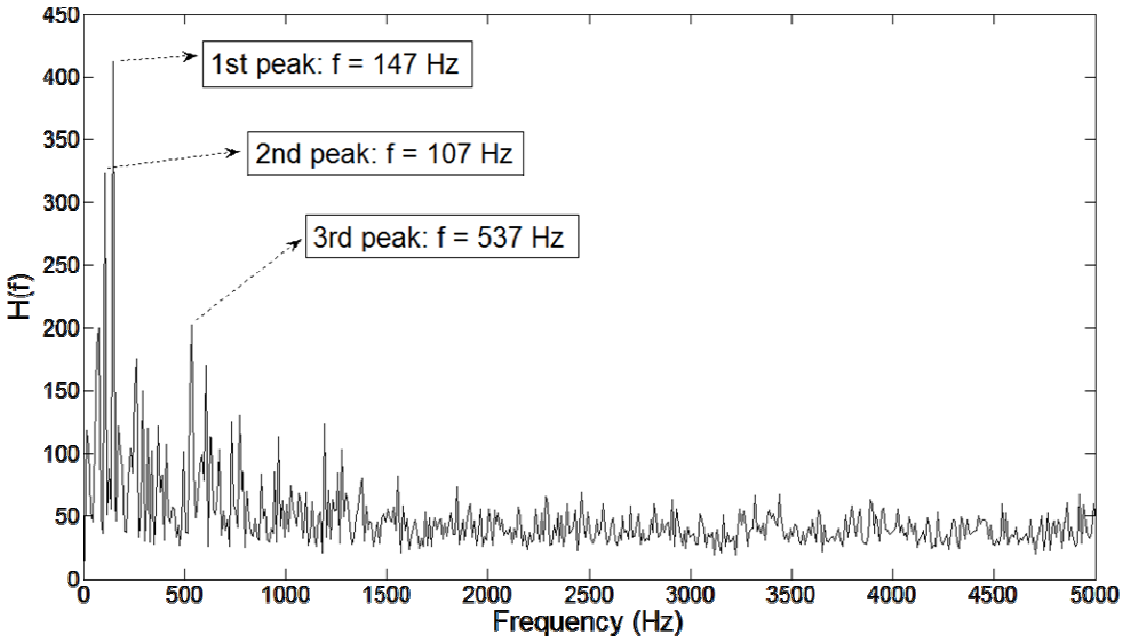


Figure 126 Average of the frequency spectra upstream of a shockwave turbulent boundary layer interaction with a shock generator deflected by 13° Estruch et al. (2010).

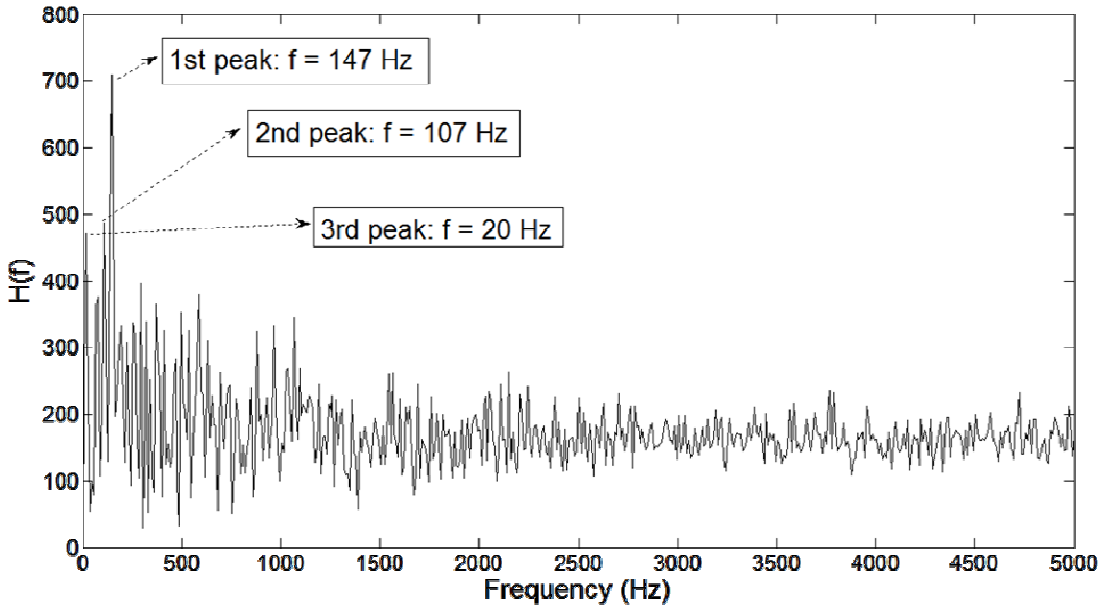


Figure 127 Average of the frequency spectra downstream of a shockwave turbulent boundary layer interaction with a shock generator deflected by 13° Estruch et al. (2010).

## *5.7 Conclusions*

For the lateral jet interaction at this scale the level of unsteadiness present was low (maximum $|P'|/P_\infty$=0.15) with the highest levels present in the region of recirculation downstream of the jet.

The amplitude of pressure fluctuations were in the same order as the minimum resolution of the measurement system. In some cases the amplitude of electrical interference was equal to or greater than pressure fluctuation in the flow.

In the area of recirculation downstream of the jet, OASPL was found to increase with increasing levels of PR or MPR and to decrease with increases of Mach number. Increasing the boundary layer thickness increased the OASPL immediately upstream of the jet. However in the downstream region only small increases were seen and only at lower pressure ratios.

# 6 Summary and conclusions

This final section summaries the work that has been carried out and presents the main conclusions.

## *6.1 Main accomplishments*

### 6.1.1 Numerical campaign

1. The lateral jet in supersonic crossflow interaction was investigated on a flat plate, a body of revolution and a body of revolution at incidence. These investigations encompassed a range of pressure ratios, Mach numbers and angles of attack.

2. Grid convergence and several RANS based turbulence models were studied extensively.

3. A detailed analysis of the flowfield surrounding the lateral jet in supersonic crossflow interaction over a flat plate and a body of revolution was completed.

4. The forces and moments on a body of revolution with a lateral jet were studied at a different pressure ratios and angles of attack.

### 6.1.2 Experimental campaign

1. The facility to study a lateral jet in supersonic crossflow experimentally in Cranfield University's 2 ½" x 2 ½" supersonic wind tunnel was designed, manufactured and utilised.

2. Time averaged pressure measurements, schlieren and oil flow visualisation were carried out to determine that the lateral jet system was in proper working order.

3. The unsteadiness present in the lateral jet in supersonic crossflow interaction was measured using high-bandwidth pressure transducers and post-processed using Matlab to reveal the spectral content. These measurements were carried out at varying Mach number pressure ratio and momentum parameter ratio.

## *6.2 Main conclusions*

### 6.2.1 Turbulence model study

None of the turbulence models trialled (SA, SARC, k-ω & SST) provided a good fit in all regions of the interaction. The main discrepancy between the predicted and measured centreline pressure distributions was in the over prediction of pressure at the point of downstream flow reattachment. All turbulence models suffered from this deficiency. The best fit to the experimental data was provided by the SA turbulence model. This model predicted the pressure distribution upstream of the jet well.

### 6.2.2 Flowfield analysis

The main shock and vortical structures identified in the flowfield analysis matched the accepted flowfield model. One discrepancy was the absence of an “upper trailing vortex” as found by Viti et al. however other authors (Palekar et al. 2005) have also failed to predict this feature and its absence might be due to the difference in pressure ratio. The flowfield for a lateral jet in supersonic crossflow interaction over a body of revolution was found to be qualitatively the same as that over a flat plate.

### 6.2.3 Force and moment analysis

The affect of pressure ratio and angle of attack on the body of revolution forces and moments was discussed. It was shown using force and moment amplification factors that aerodynamic interaction between the jet and the freestream could augment or counteract the jet thrust

force. Increasing either pressure ratio or angle of attack lead to increases in the force amplification factor and decreases in the moment amplification factor.

### 6.2.4 Unsteadiness assessment

The levels of unsteadiness measured were low with the highest levels of unsteadiness found in the area of recirculation between jet and downstream flow reattachment. The largest amplitudes were at low frequencies (0-5kHz). In the area of recirculation downstream of the jet, OASPL was found to increase with increasing levels of PR or MPR and to decrease with increases of Mach number. Increasing the boundary layer thickness increased the OASPL immediately upstream of the jet. However in the downstream region only small increases were seen and only at lower pressure ratios.

# References

BARDINA, J.E., HUANG, P.G. and COAKLEY, T.J., 1997. Turbulence modeling validation, testing, and development. NASA Technical Memorandum 110446.

BATTISTI, C., 2010. Sonic jets in supersonic crossflow. MSc thesis. Cranfield University, UK.

BENEDICT, R.P., 1984. Fundamentals of temperature, pressure, and flow measurements. 3rd ed. New York: John Wiley & Sons.

BEN-YAKAR, A., MUNGAL, G. M. & HANSON, R. K., 2006. Time evolution and mixing characteristics of hydrogen and ethylene transverse jets in supersonic crossflows. *Physics of Fluids*. Vol. 18, 026101.

BROWN, R., 2002. Missile Defense: Acquisition Innovation in Practice. 12th PEO / SYSCOM Commander's Conference Fort Belvoir, November 20-22.

CASSEL, L.A., 2003. Applying jet interaction technology. *Journal of Spacecraft and Rockets,* Vol. 4, No. 4, 523-537.

CEBECI, T., 2005. *Computational fluid dynamics for engineers: from panel to navier-stokes methods with computer programs.* Horizons Publishing, Long Beach.

CHAMPIGNY, P., DECK, S., DENIS, P. and MAGNIANT, S., 2006. Numerical Simulation of Forebody Vortices at High Angle of Attack and their Control Using Innovative Systems. Systems. *In Innovative Missile Systems (pp. 24-1 – 24-16). Meeting Proceedings RTO-MP-AVT-135, Paper 24*. Neuilly-sur-Seine, France: RTO.

CHAMPIGNY, P. and LACAU, R.G., 1994. Lateral jet control for tactical missiles. AGARD R-804, Special Course on Missile Aerodynamics.

CLEMENS, N.T. and NARAYANASWAMY, V., 2009. Shock/Turbulent Boundary Layer Interactions: Review of Recent Work on Sources of Unsteadiness. 39th AIAA Fluid Dynamics Conference 22 - 25 June 2009, San Antonio, Texas.

CUBBISON, R.W., ANDERSON, B.H. and WARD, J.J., 1961. Surface pressure distributions with a sonic jet normal to adjacent flat surfaces at Mach 2.92 to 6.4. NASA TN D-580 February 1961.

CURRIE, I., 1993. *Fundamental mechanics of fluids*. McGraw-Hill, New York.

DENNIS, K., SUZEN, Y.B. and MAHMUD, Z., 2007. Experimental and Computational Investigation of Sonic Reaction Control Jets into Supersonic Cross-flows. *37th AIAA Fluid Dynamics Conference and Exhibit, Miami, Florida.*

DESSAINT, R., 2008. Lateral jet control effectiveness at supersonic speeds, MSc Thesis, Cranfield University.

DORAN, D., 2006. Experimental investigation of transonic cavity flow control, MSc Thesis, Cranfield University, UK.

Dupont, P., Haddad, C., Ardissone, J. & Debiève, J.-F. 2005 Space and time organization of a shock wave/turbulent boundary layer interaction. *Aerospace Science and Technology*. Vol. 9, No.7,pp 561–572.

ESTRUCH, D., LAWSON, N.J., MACMANUS, D.G., GARRY, K.P. and STOLLERY, J.L., 2008. Measurement of shock wave unsteadiness using a high-speed schlieren system and digital image processing. *Review of Scientific Instruments,* Vol.79, No. 12, 126108.

ESTRUCH, D.; MACMANUS, D.G.; LAWSON, N.J.; GARRY, K.P., 2010 'Experimental study of unsteadininess in supersonic shockwave turbulent boundary-layer interactions with separation" *Aeronautical Journal*, Volume 114, Number 1155.

FAVRE, A., 1965. Equations des gaz turbulents compressibles. Parts I and II. *Journel de Mechanic,* 4, 361–421.

FLEEMAN, E.L., 2006. *Tactical missile design.* 2nd ed. AIAA Education Series.

FRIC, T.F. and ROSHKO, A., 2006. Vortical structure in the wake of a transverse jet. *Journal of Fluid Mechanics,* Vol.279, pp1-47.

GNEMMI, P. and SCHAFER, H.J., 2005. Experimental and Numerical Investigations of a Transverse Jet Interaction on a Missile Body, *43rd AIAA Aerospace Sciences Meeting and Exhibit,* Reno/NV, USA, January 10-13.

GROSSER, W.I., 1997. Factors influencing Pitot probe centerline displacement in a turbulent supersonic boundary layer. *NASA TM, 107341*, Lewis Research Center, Cleveland, OH.

GRUBER, M.R., NEJAD, A.S., CHEN, T.H. and DUTTON, J.C., 1995. Mixing and penetration studies of sonic jets in a Mach 2 freestream. *Journal of Propulsion and Power,* 11(2), 315-323.

Guelich J.F., 2010. *Centrifugal pumps/.*Springer Verlag, Berlin Heidelberg.

HASS, A., 2009. *Hypersonic heat transfer*, MSc Thesis, Cranfield University, UK.

KOVAR, A. and SCHULEIN, E., 2006. Comparison of experimental and numerical investigation on a jet in a supersonic cross-flow. *Aeronautical Journal,* 110(1108), 353-360.

LEE, J.W., MIN, B.Y., BYUN, Y.H. and LEE, C., 2004. Numerical Analysis and Design Optimization of Lateral Jet Controlled Missile, *21st International Congress of Theoretical and Applied Mechanics,* Aug.

LETKO, W., 1963. Loads induced on a flat plate at a Mach number of 4.5 with a sonic or supersonic jet exhausting normal to the surface. *NASA Technical note D-1935*.

LU, F.K. and DICKMANN, D.A., 2008. Topology of supersonic jet interaction flowfields at high pressure ratios. *ISFV13 - 13th International Symposium on Flow Visualization, FLUVISU12 - 12th French Congress on Visualization in Fluid Mechanics*, July 1-4, Nice, France

MACMLLLAN, F.A., 1957. Experiments on Pitot-tubes in shear flow. *R. & M. No. 3028, Brit. A.R.C.*.

MARGASON, R.J., 1993. Fifty years of jet in cross flow research, *AGARD, Computational and Experimental Assessment of Jets in Cross Flow,* AGARD 72nd FDP Meeting, Paper No. 1.

MCCANN G. J., BOWERSOX D.W., 1996. Experimental investigation of supersonic gaseous injection into a supersonic free-stream. *AIAA Paper 96-0197,* June.

MENTER, F.R., 1994. Two-equation eddy-viscosity turbulence models for engineering applications. *AIAA Journal,* 32(8), 1598-1605.

MIN, B.Y., LEE, J.W. and BYUN, Y.H., 2006. Numerical investigation of the shock interaction effect on the lateral jet controlled missile. *Aerospace Science and Technology,* 10(5), 385-393.

MORGANS, R., DALLY, B., NATHAN, G., LANSPEARY, P. and FLETCHER, D., 1999. Application of the revised Wilcox (1998) k-ω turbulence model to a jet in co-flow, *Second International Conference on CFD in the Mineral and Process Industries*, Melbourne, Australia.

MORKOVIN, M.V., PIERCE JR, C. and CRAVEN, C., 1952. Interaction of a side jet with a supersonic main stream. *Engineering Research Bulletin No. 35*, University of Michigan.

OPPENHEIM, A.V. and SCHAFER, R.W., 1989. *Discrete-Time Signal Processing*. Englewood Cliffs, NJ: Prentice Hall.

PALEKAR, A., TRUMAN, C.R. and VOROBIEFF, P., 2005. Prediction of Transverse Injection of a Sonic Jet in Supersonic Crossflow, *36th AIAA Plasmadynamics and Lasers Conference,* 2005, pp1-12.

PAPAMOSCHOU, D. and HUBBARD, D.G., 1993. Visual observations of supersonic transverse jets. *Experiments in Fluids,* 14(6), 468-476.

PAYNE, J.L., ROY, C.J. and BERESH, S.J., 2001. A comparison of turbulence models for a supersonic jet in transonic crossflow, *AIAA, Aerospace Sciences Meeting and Exhibit, 39th, Reno, NV*.

POPE, S.B. 2000. *Turbulent flows.* Cambridge: Cambridge University Press.

PORTZ, R. and SEGAL, C., 2006. Penetration of Gaseous Jets In Supersonic Flows. *AIAA Journal,* 44(10), 2426.

QIN, N. and FOSTER, G.W., 1995. Study of flow interactions due to a supersonic lateral jet using high resolution Navier-Stokes solutions, *AIAA, Fluid Dynamics Conference, 26th, San Diego, CA*.

ROACHE, P.J., 1998. *Verification and validation in computational science and engineering.* Hermosa Publishers Albuquerque, New Mexico.

SANTIAGO, J.G. and DUTTON, J.C., 1997. Crossflow vortices of a jet injected into a supersonic crossflow. *AIAA Journal,* Vol. 35 No. 5, pp 915-917, May.

SCHAFER, H., AUGENSTEIN, E., ESCH, H. and EDMUNDS, H., 2001. Experimental Investigation of Transverse Jet Interaction on a Missile Body Using Laser Velocimetry and Flow Visualization. *19th International Congress on Instrumentation in Aerospace Simulation Facilities,* Cleveland/OH, USA, August 27-30.

SCHLICHTING, H., GERSTEN, K. and GERSTEN, K., 2000. *Boundary-layer theory.* (Springer Verlag, Berlin), 8th edition.

SEILER, F., GNEMMI, P., ENDE, H., SCHWENZER, M. and MEUER, R., 2003. Jet interaction at supersonic cross flow conditions. *Shock Waves,* 13(1), 13-23.

SETTLES, G.S., 2001. *Schlieren and shadowgraph techniques: visualizing phenomena in transparent media.* Springer, Berlin Heidelberg New York.

SHUR, M.L., STRELETS, M.K. and TRAVIN, A.K., 2000. Turbulence modeling in rotating and curved channels: Assessing the Spalart-Shur correction. *AIAA Journal,* 38(5), 784-792.

SMITH, B., 1990. The k-kl turbulence model and wall layer model for compressible flows, *AIAA, Fluid Dynamics, Plasma Dynamics and Lasers Conference, 21 st,* Seattle, WA.

SPAID, F.W., CASSEL, L.A., WILSON, R.E. and DE L'ATLANTIQUE, O.D.T., 1973. Aerodynamic interference induced by reaction controls, AGARDograph No.173, Dec.

SPALART, P.R. and ALLMARAS, S.R., 1992. A one-equation turbulence model for aerodynamic flows, *AIAA, 30th Aerospace Sciences Meeting and Exhibit,* Reno.

STAHL, B., EMUNDS, H. and GÜLHAN, A., 2009. Experimental investigation of hot and cold side jet interaction with a supersonic cross-flow. *Aerospace Science and Technology,* 13(8), 488-496.

STAHL, B., ESCH, H. and GÜLHAN, A., 2008. Experimental investigation of side jet interaction with a supersonic cross flow. *Aerospace Science and Technology,* 12(4), 269-275.

TAYLOR, J.R., 1997. *An introduction to error analysis: the study of uncertainties in physical measurements.* Mill Valley, CA: Univ. Sci. Books.

VANLERBERGHE, W.M., DUTTON, J.C., LUCHT, R.P. and YUEN, L.S., 1994. Penetration and mixing studies of a sonic transverse jet injected into a Mach 1.6 crossflow, *AIAA, Fluid Dynamics Conference, 25th, Colorado Springs*.

VERSTEEG, H.K. and MALALASEKERA, W., 2007. *An introduction to computational fluid dynamics: the finite volume method.* Essex, UK: Longman.

VITI, V., NEEL, R. and SCHETZ, J.A., 2009. Detailed flow physics of the supersonic jet interaction flow field. *Physics of Fluids,* 21(4), 6101.

WHITE, F.M., 1999. *Fluid Mechanics,* 4th edn (Boston, MA: McGraw-Hill).

WILCOX, D.C., 2006. *Turbulence Modeling for CFD,* La Canada, CA: DCW Industries, Inc.

WILCOX, D.C., 1998. *Turbulence Modeling for CFD*, 2nd Ed, DCW Industries, INC. 5354 Palm Drive, La Cañada, CA 91011.

ZUCKER, R.D. and BIBLARZ, O. (eds), 2002. *Fundamentals of gas dynamics.*, second ed., Wiley, Hoboken.

# Appendix A

# *Influence of filtering on data aquisition*

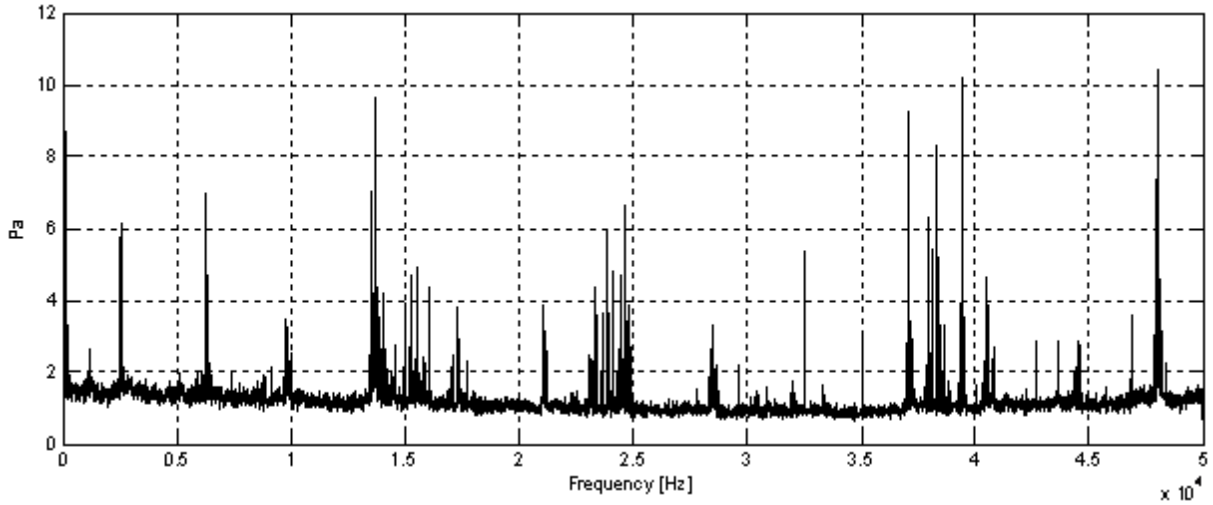


FFT of output acquired signal, sample rate 100kHz, tunnel off and no filters.

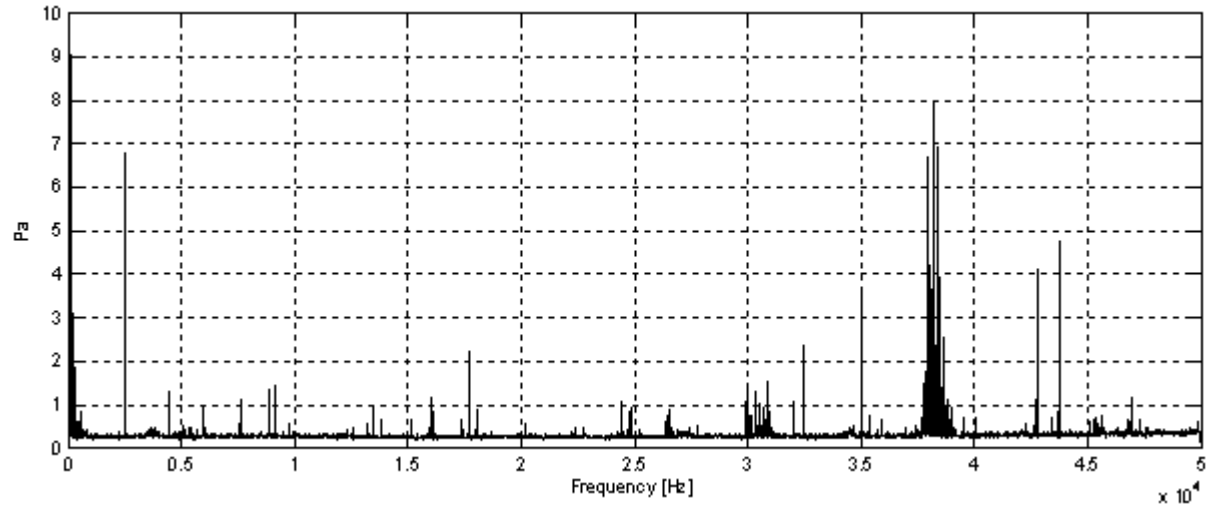


FFT output of acquired signal, sample rate 100kHz, tunnel off and filtered at 50kHz

Filtering removes some spectral content. This is probably due to aliasing of higher frequency content which is filtered out by the filters. The OASPL is reduced from 131.71 to 121 84 by filtering.

# Appendix B

# *Influence of sampling rate on data aquisition*

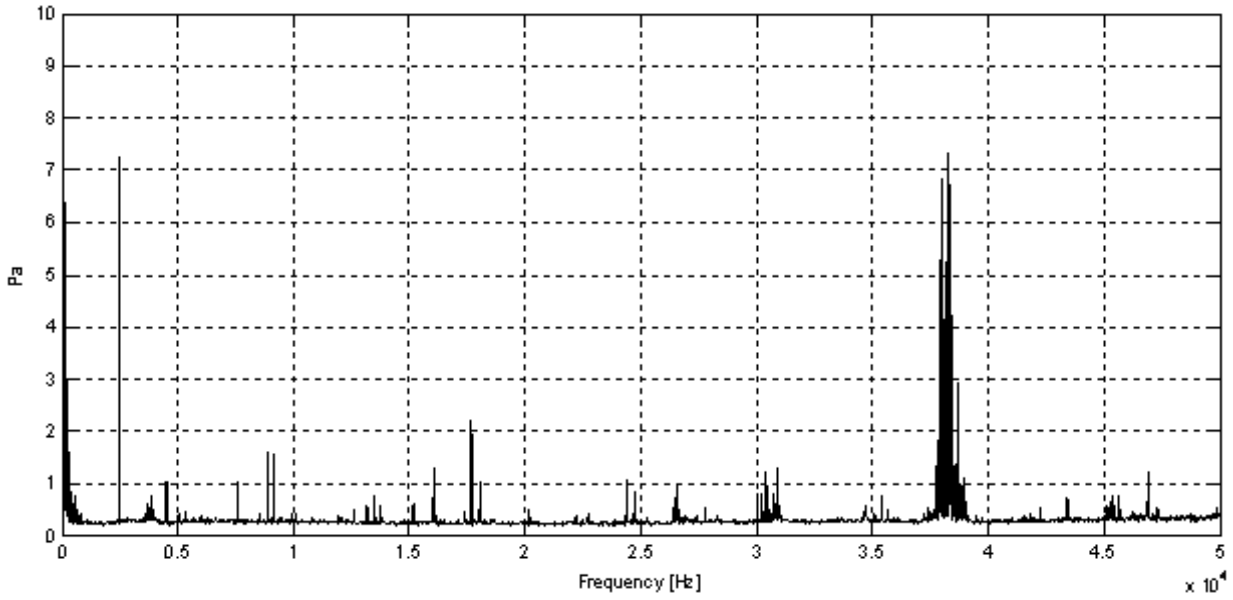


FFT output of acquired signal, sample rate 200kHz, tunnel off and filtered at 50kHz

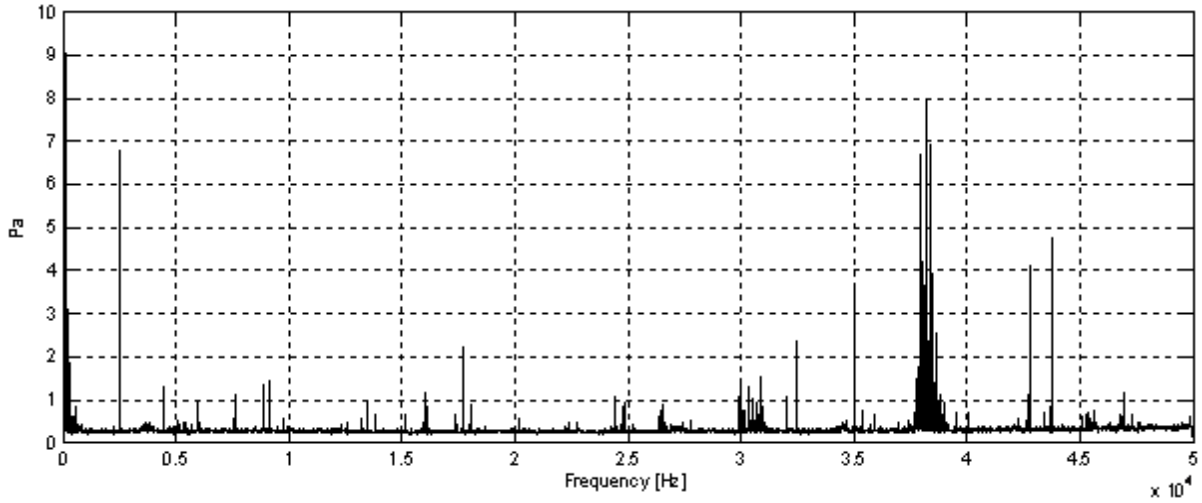


FFT output of acquired signal, sample rate 100kHz, tunnel off and filtered at 50kHz

Increasing the sampling rate makes little difference to the signal. The OASPL stays the same, however some peaks are not seen specifically at 35kHz and around 43kHz. However as we are interested in frequencies of a couple of hundred to a few thousand hertz and it does not affect the OASPL it makes no significant difference.

# Appendix C

## *Labview GUI screenshot*

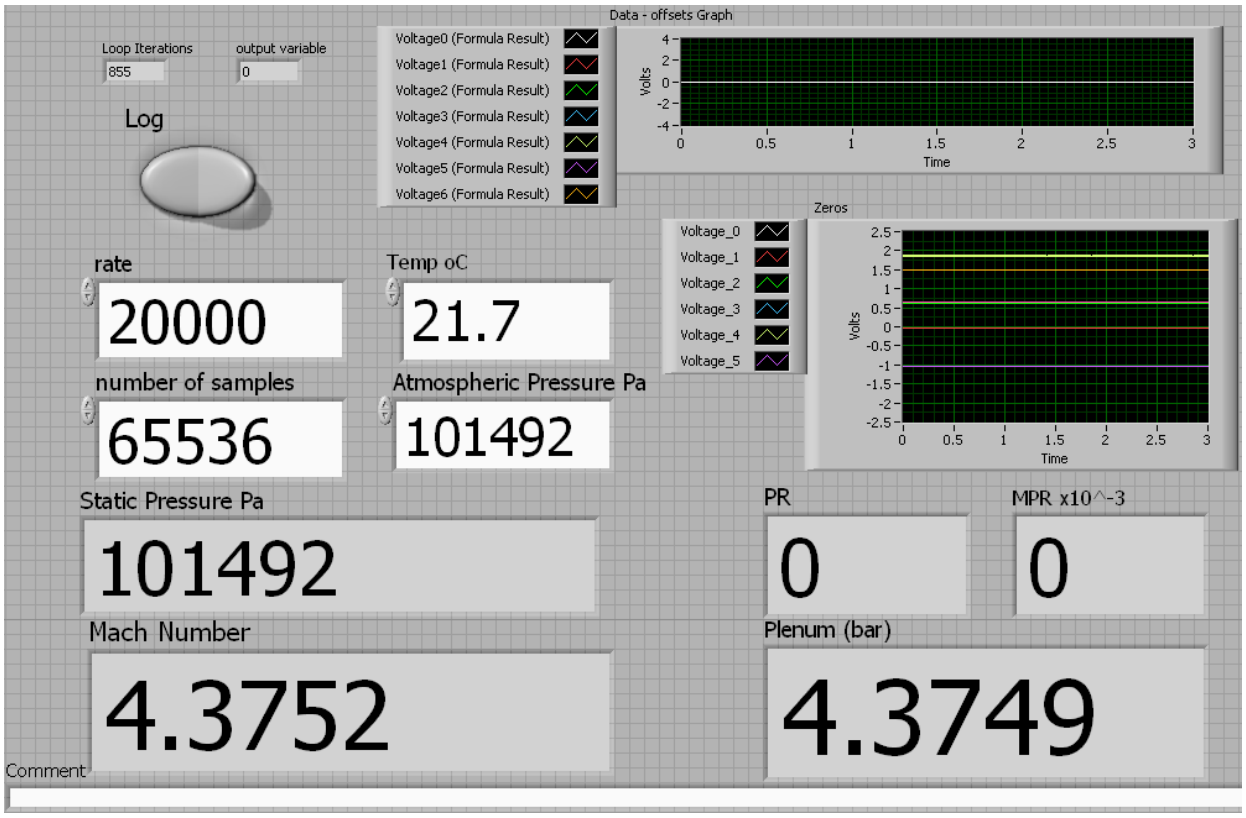


Screenshot of the labview frontend.

# Appendix D

# *Uncertainty analysis*

## *6.3 Pressure transducers*

### 6.3.1 Accuracy of the Pressure Transducers

The accuracy of the pressure transducers was given as a percentage of the full scale output, combing non-linearity and hysteresis errors (Table 29). The uncertainty in pressure for the worst case scenario was calculated for each transducer. In the case of the Druck pressure transducers, the uncertainty due to the accuracy of the transducer was:

$$\pm\frac{101325\times 0.1}{100}=101.3\ Pa \qquad \text{Equation 55}$$

Similarly, the uncertainty in pressure for the worst case scenario was calculated for the remaining pressure transducers and are summarized in Table 29**.**

| Manufacturer | Measurement | % Uncertainty of full scale output | Maximum pressure | Uncertainty in pressure (Worst case) |
|---|---|---|---|---|
| Druck PDCR 22 | Static pressure in test section | 0.1% | 101325 Pa | ±101 Pa |
| Setra 0-0.5 PSI Differential pressure transducer | Total pressure in settling chamber | 0.01% | 101325 Pa | ±10 Pa |
| Langham-Thompson Type: UP4/100G/325 s# 427 | Total pressure in jet plenum | 0.1% | 500000Pa | ±500 Pa |

Table 29 Summary of the percentage uncertainty of full scale output for the pressure transducer used in the experiment and their corresponding uncertainty in pressure in the worst case scenario

### 6.3.2 Resolution of the Acquisition Card

An additional source of uncertainty in static pressure measurement was the acquisition card used to transfer the data from the transducers. The acquisition card was a 16 bit card. This corresponded to $2^{16}$= 65536 output values. The maximum transducer output was 10 volts. The maximum resolution (r) of the measurements was therefore:

$$r = \frac{10}{65536} = 1.53 \times 10^{-4}\ V \qquad \text{Equation 56}$$

Using the calibration factor (Table 30) of the pressure transducers (*c)*, the resolution in pressure $r_{pres}$ was calculated (Table 30) using Equation 57:

$$r_{pres} = r \times c \qquad \text{Equation 57}$$

| Transducer | Calibration factor | Resolution in voltage | Resolution in pressure |
|---|---|---|---|
| Druck A (s# 14629) | 146391 | 1.53E-04 | 22.34 Pa |
| Druck B (s# illegible) | 14672 | 1.53E-04 | 2.24 Pa |
| Setra | 1369.8 | 1.53E-04 | 0.21 Pa |
| Langham | 3.03 | 1.53E-04 | 4.63 x$10^{-4}$ bar |

Table 30 Calibration factors and corresponding resolution in pressures for the transducers used in the experiment

### 6.3.3 Repeatability of the Pressure Measurements

The repeatability of the pressure measurements were tested by fourteen sets of experimental data. This data was recorded at a Mach number of 2.4. The tunnel was turned off between experimental runs and the Labview progamme reset. The deviation for a Mach number of 1.8 and 3.2 was expected to be in the same order of magnitude. The root mean square deviation is given by:

$$\sigma = \pm \sqrt{\frac{1}{(n-1)} \sum_{i=1}^{n} (x_i - x_m)^2} \qquad \text{Equation 58}$$

Where n is the number of samples, $x_i$ is the individual samples and $x_m$ is the mean of the individual samples.

Equation 58 was applied to the data set and the resulting root mean square deviation for each pressure transducer is summarized in Table 31.

| **Transducer** | **n** | **$x_m$** | $\sum_{i=1}^{n} (x_i - x_m)^2$ | **σ** |
|---|---|---|---|---|
| Druck A | 14 | 6588 Pa | 9764 | ±27.4 Pa |
| Druck B | 14 | 7406 Pa | 320 | ±4.96 Pa |
| Setra | 14 | 102007 Pa | 0.027 | ±0.05 Pa |
| Langham | 14 | 5.18 bar | 2.01 x$10^{-5}$ | ±1.24 x$10^{-3}$ bar |

Table 31 Uncertainty in pressure from repeatability study.

### 6.3.4 Total Uncertainty on Measurements

As the uncertainties are related a best estimate of the total uncertainty could be made by using addition in quadrature. These total uncertainties are presented in Table 32.

| Transducer | Quoted uncertainty | Data acquisition card uncertainty | Uncertainty from repeatability study | Total uncertainty |
|---|---|---|---|---|
| Druck A | ±101 Pa | ±22.34 Pa | ±27.4 Pa | ±107.0 Pa |
| Druck B | ±101 Pa | ±2.24 Pa | ±4.96 Pa | ±101.1 Pa |
| Setra | ±10 Pa | ±0.21 Pa | ±0.05 Pa | ±10.0 Pa |
| Langham | ±500 Pa | ±46.3 Pa | ±124 Pa | ±517.2 Pa |

Table 32 Total pressure transducer uncertainty

### 6.3.5 Uncertainty in Mach number measurements

$$\frac{P_0}{P} = \left(1 + \frac{\gamma - 1}{2} M^2\right)^{\frac{\gamma}{\gamma - 1}} \quad \text{Equation 59}$$

$$M^2 = \frac{2}{(\gamma - 1)} \left[ \left(\frac{P_0}{P}\right)^{\frac{\gamma - 1}{\gamma}} - 1 \right] \quad \text{Equation 60}$$

Assuming a constant value of 1.4 for γ Equation 60becomes:

$$M^2 = 5 \left[ {P_0}^{\frac{2}{7}} \cdot P^{\frac{-2}{7}} - 1 \right] \quad \text{Equation 61}$$

The uncertainty in the Mach number calculation can be then be found from:

$$\Delta M = \sqrt{5 \left[ \left( \frac{P_0 + \Delta P_0}{P - \Delta P} \right)^{2/7} - 1 \right]} - \sqrt{5 \left[ \left( \frac{P_0 - \Delta P_0}{P + \Delta P} \right)^{2/7} - 1 \right]} \quad \text{Equation 62}$$

Now P=(6588±105.74)Pa and $P_0$=(102007±10.26)Pa therefore the uncertainty in M=±0.02

### 6.3.6 Uncertainty in calculated pressure coefficient

The pressure coefficient is defined as:

$$C_p = \frac{P - P_\infty}{\frac{1}{2}\rho U^2} \qquad \text{Equation 63}$$

In the experiments this was calculated from Mach number total freestream temperature and pressure, and static pressure at the point of measurement. Equation 63 can be rewritten in terms of these variables giving:

$$C_p = 2 \cdot \left\{ \frac{P - P_{0\infty}\left[1 + \frac{\gamma - 1}{2} {M_\infty}^2\right]^{\frac{-\gamma}{\gamma - 1}}}{\frac{P}{R \cdot T_{0\infty}\left[1 + \frac{\gamma - 1}{2} {M_\infty}^2\right]} \cdot M \cdot \sqrt{\gamma R T_{0\infty}\left[1 + \frac{\gamma - 1}{2} {M_\infty}^2\right]}} \right\} \qquad \text{Equation 64}$$

Then using the uncertainty of the individual pressure transducers the error in pressure and Equation 64 the uncertainty in $C_p$ was found to be ±0.01

### 6.3.7 Uncertainty in calculated pressure ratio

Using the definition of pressure ratio (Equation 65) the uncertainties for each pressure transducer and typical values for each Mach number the uncertainty in pressure ratio can be calculated (Table 5).

$$PR = \frac{P_{0j}}{P_{\infty}} \qquad \text{Equation 65}$$

| | M=2.4 | M=3.2 |
|---|---|---|
| PR | ±PR | ±PR |
| 200 | 1.6 | 9.0 |
| 150 | 1.2 | 6.8 |
| 110 | 0.9 | 5.1 |
| 97 | 0.8 | 4.5 |
| 70 | 0.6 | 3.3 |
| 55 | 0.5 | 2.6 |
| 50 | 0.5 | 2.4 |

Table 33 Uncertainty in pressure ratio

## *6.4 Uncertainty in Fluctuating Pressures*

The uncertainty in fluctuating pressures was evaluated for the measurements of sound levels in decibels (SPL and OASPL). The uncertainty on the frequency of the tones was not evaluated, the calculation being very complex. The frequency resolution was calculated of 6.1Hz, which gave an idea of the accuracy in the tones frequency.

### 6.4.1 Accuracy of the Pressure Transducers

The accuracy of the high bandwidth Kulite pressure transducers was also given as ±0.1% of the full scale output. So the uncertainty in the unsteady pressure calculation was also approximately ±100 Pa in the worst case. This uncertainty in Pa can be converted in an uncertainty in decibels. From the SPL formula:

$$SPL = 20 \cdot \log\left(\frac{P_{fluc}}{P_{ref}}\right)$$ Equation 66

Taking a typical value for the fluctuating pressure measured in the tests ($p_{fluc}$=6500Pa), and a reference pressure of $p_{ref}$=2x10$^{-5}$Pa, the uncertainty of ±100Pa in pressure corresponded to an uncertainty of ± 0.13dB on the pressure fluctuation characteristics in decibels (both OASPL and SPL).

### 6.4.2 Resolution of the Acquisition Card

The same data acquisition card, with the same voltage resolution was used to measure the fluctuating pressures and time averaged pressures. Different calibration factors mean that the high bandwidth pressure transducers have a different pressure resolution. The voltage, pressure resolution and corresponding resolution in decibels was calculated for each Kulite transducer and is shown in Table 34.

| Kulite | Calibration factor | Resoultion in voltage | Resolution in pressure | Resolution in dB* |
|---|---|---|---|---|
| 1 | 30767 | 1.53E-04 | 4.69 | ±6.27 x10$^{-3}$ dB |
| 2 | 30938 | 1.53E-04 | 4.72 | ±6.31 x10$^{-3}$ dB |
| 3 | 30114 | 1.53E-04 | 4.60 | ±6.14 x10$^{-3}$ dB |
| 5 | -30712 | 1.53E-04 | -4.69 | ±6.26 x10$^{-3}$ dB |

Table 34 Voltage and pressure resolutions with corresponding resolution in dB for each Kulite. *Resolution in dB calculated using a typical $P_{fluc}$ of 6500 Pa.

### 6.4.3 Repeatability of the Pressure Measurements

Three sets of unsteady tests were carried out with a freestream Mach number of 2.4 and a pressure ratio of 50. Each test recorded 65,536 values (196,608 in total). The tunnel, jet and data acquisition programme were switched between tests. OASPL was calculated for each

micro-Kulite pressure transducer for each run. Equation 58, page 193 was then used to calculate the uncertainty of the measurement.

| Kulite | $x_m$ | $\sum_{i=1}^{n}(x_i - x_m)^2$ | σ |
|---|---|---|---|
| 1 | 121.277 dB | 0.167258 | ±0.289 dB |
| 2 | 126.165 dB | 0.076841 | ±0.196 dB |
| 3 | 120.255 dB | 0.671857 | ±0.58 dB |
| 4 | 122.252 dB | 0.144632 | ±0.269 dB |

Table 35 Uncertainty in OASPL from repeatability study.

### 6.4.4 Total uncertainty in fluctuating pressure measurements

As seen in previous estimation of total uncertainty can be made by addition in quadrature when the uncertainties are related. These total uncertainties are quoted in Table 6.

| Kulite | Quoted uncertainty | Data acquisition card uncertainty | Uncertainty from repeatability study | Total uncertainty |
|---|---|---|---|---|
| 1 | ±0.13 dB | ±6.27E-03 dB | ±0.29 dB | ±0.32 dB |
| 2 | ±0.13 dB | ±6.31E-03 dB | ±0.20 dB | ±0.24 dB |
| 3 | ±0.13 dB | ±6.14E-03 dB | ±0.58 dB | ±0.59 dB |
| 5 | ±0.13 dB | ±6.26E-03 dB | ±0.27 dB | ±0.30 dB |

Table 36 Total uncertainties for the high bandwidth pressure transducers.

# Appendix E

# *Matlab data processing code*

```
first_runno=input('Enter first run #: ','s');       % Ask user for run number
last_runno=input('Enter last run #: ','s');

for runno=str2double(first_runno):str2double(last_runno);

    filename=['Run_',num2str(runno),'.lvm'];      % Assign run# to filename
    data_V=dlmread(filename);                     % load in voltage data

    [N,M]=size(data_V);                       % N is number of samples
    fs=data_V(1,M);                           % sampling frequency
    t = (0:N-1)*(1/fs);                       % Time vector
    nochan=M-6;                               % number of channels to analyse
    data_P=zeros(N,M);
    %calibK=[30896 31000 30160 -30877 -30753];
    calibK=[30896 31000 30160 -30753];
    Patm=data_V(1,(M-5));
    Tatm=data_V(1,(M-4))+273.15;
    Pplenumbar=data_V(1,(M-3));
    Mach=data_V(1,(M-2));
    Pstatic=Patm*(1+((1.4-1)/2)*Mach^2)^-3.5;
    PR=Pplenumbar*100000/Pstatic;

    for i=1:nochan
        data_P(:,i)=calibK(i)*data_V(:,i)+Patm;
    end

    for k=1:nochan
        data=data_P(:,k);
        % Common data parameters
        lenblk=16384;                                   % block length
        overlap=lenblk/2;                               % overlap
        df=fs/lenblk;                                   % frequency resolution
        pref=2.0e-5;                                    % Reference frequency
        lenblk2=ceil(lenblk/2);                   % define the block 'half length'
        w=hanning(lenblk);                        % generate hanning window
        noblk=floor(1+(N-lenblk)/(lenblk-overlap));   % number of blocks
        time=1:1:N; time=(time-1)/fs;    % time array for plotting raw signal

        % set up matrices of zeros to be populated later
        y=zeros(lenblk,noblk);
        acy=zeros(lenblk,noblk);
        wacy=zeros(lenblk,noblk);
        FWACY=zeros(lenblk,noblk);
        FWACY2=zeros(lenblk2,noblk);
        PSD=zeros(lenblk2,noblk);
        PSDav=zeros(lenblk2,1);
        FFTav=zeros(lenblk2,1);

        % process data
        for j=1:noblk
            % arrange data into array of blocks, [lenblk,noblk]
            if j==1
                y(:,1)=data(1:lenblk);
            else
                low=1+(j-1)*(lenblk-overlap);
                high=lenblk+(j-1)*(lenblk-overlap);
```

```
            y(:,j) = data(low:high);
            clear low high
        end

        acy(:,j)=y(:,j)-mean(y(:,j)); % remove dc component blocks
        wacy(:,j)=w.*acy(:,j);        % window each block
    end

    % fft
    FWACY(:,:)=fft(wacy(:,:));   % isolate 1st 1/2 of data (2nd 1/2 is a
repeat)
    FWACY2(:,:)=FWACY(1:lenblk2,:);

    % psd
    PSD(:,:) = (abs(FWACY2(:,:)).^2 )/(lenblk^2*df);
    PSD=PSD*8/3;  % power correction for hanning window losses
    PSD(2:lenblk2-1,:)=2*PSD(2:lenblk2-1,:); % power*2, except 1st & last
points

    % average blocks
    for i=1:lenblk2
        PSDav(i)=mean( PSD(i,:) );
    end

    % spl
    SPL=zeros(lenblk2,1);
    SPLD=zeros(lenblk2,1);
    SPL(:)=20*log10(sqrt(PSDav(:))/pref);

    % oaspl, computed in time domain
    acx=data-mean(data);
    oaspl=20*log10(sqrt(mean(acx.^2))/pref);

    % setup freq axis
    freq=(fs/2)*(0:lenblk2-1)/lenblk2;

    % plot raw signal
    figtitle=['Run #: ' ,num2str(runno), ' Channel #: ' ,num2str(k)];
    figure('Name',figtitle ,'NumberTitle','off')
    subplot(2,2,1)
    plot(time,data_V(:,nochan),'k-','linewidth',1.0), hold on
    xlabel('Time [sec]','FontSize',10)
    ylabel('V','FontSize',10)
    title('Raw Signal','Fontsize',12)
    axis auto
    grid on

    Vmean=mean(data_V(:,k));
    Vmin=min(data_V(:,k));
    Vmax=max(data_V(:,k));
    Vamp=(Vmax-Vmin)*500;

    Pmean=mean(data_P(:,k));
    Pmin=min(data_P(:,k));
    Pmax=max(data_P(:,k));
```

```
        Pamp=(Pmax-Pmin);

        disp(['Run #: ',num2str(runno), '  Channel #: ',num2str(k)]);
        disp(['Mean Voltage: ',num2str(Vmean),' V','           Mean Pressure:
',num2str(Pmean),' Pa']);
        disp(['Max Voltage: ',num2str(Vmax),' V' ,'            Max Pressure:
',num2str(Pmax),' Pa']);
        disp(['Min Voltage: ',num2str(Vmin),' V','             Min Pressure:
',num2str(Pmin),' Pa']);
        disp(['Voltage  Amplitude:  ',num2str(Vamp),'  mV'  ,'       Pressure
Amplitude: ',num2str(Pamp),' Pa']);

        % plot FFT
        FWACY2=abs(FWACY2)/lenblk;
        FWACY2(2:lenblk2-1,:)=2*FWACY2(2:lenblk2-1,:);
        FWACY2=FWACY2*2; % hanning amplitude correction

        for i=1:lenblk2
            FFTav(i)=mean( FWACY2(i,:) );
        end

        subplot(2,2,2)
        plot(freq,FFTav,'k-','linewidth',1.0), hold on
        xlabel('Frequency [Hz]','FontSize',10)
        ylabel('Pa','FontSize',10)
        title('FFT','Fontsize',12)
        axis auto
        grid on, hold off

        % plot PSD
        subplot(2,2,3)
        plot(freq,PSDav,'k-','linewidth',1.0), hold on
        xlabel('Frequency [Hz]','FontSize',10)
        ylabel('Pa/Hz','FontSize',10)
        title('PSD independent from resolution','Fontsize',12)
        axis auto
        grid on, hold off

        % plot SPL
        subplot(2,2,4)
        plot(freq,SPL,'k-','linewidth',1.0), hold on
        xlabel('Frequency [Hz]','FontSize',10)
        ylabel('SPL [dB]','FontSize',10)
        title('SPL','Fontsize',12)
        axis auto
        grid on, hold off

        % output oaspl's to screen
        disp(['oaspl: ',num2str(oaspl),' dB']);
        disp(' ')

    end
end
clear all
```

# Appendix F

# *Comparison of Cobalt numerical results to ISL numerical & experimental results*

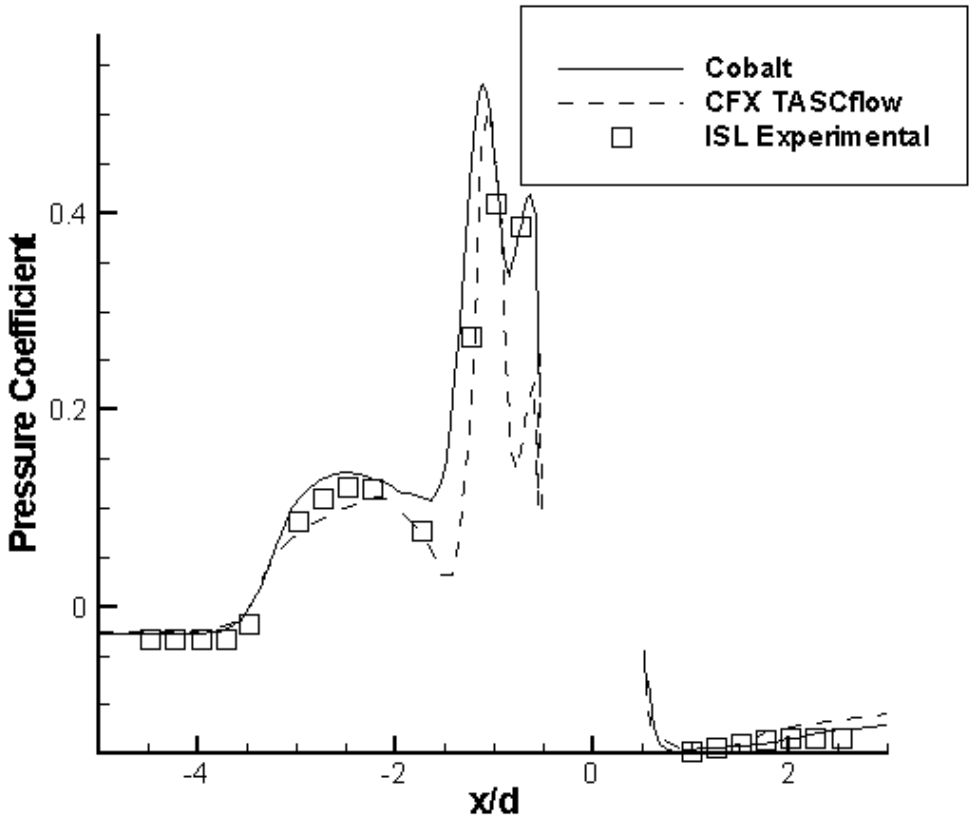


Figure 128 Coefficient of pressure in the longitudinal direction for the ISL BoR, PR=50.

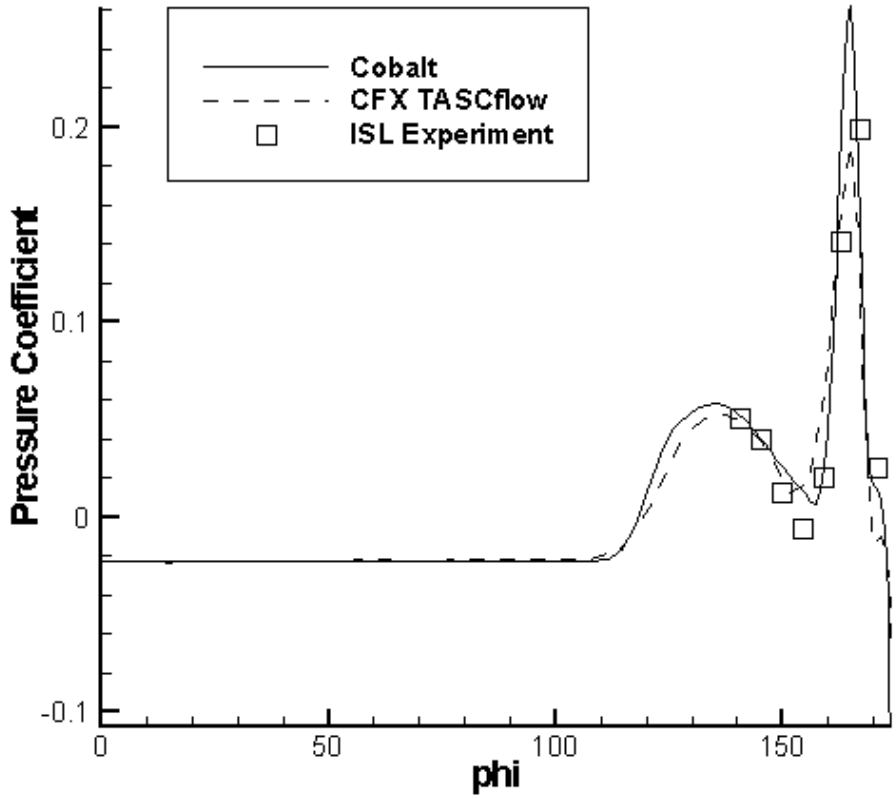


Figure 129 Coefficient of pressure in the circumferential direction for the ISL BoR, PR=50.

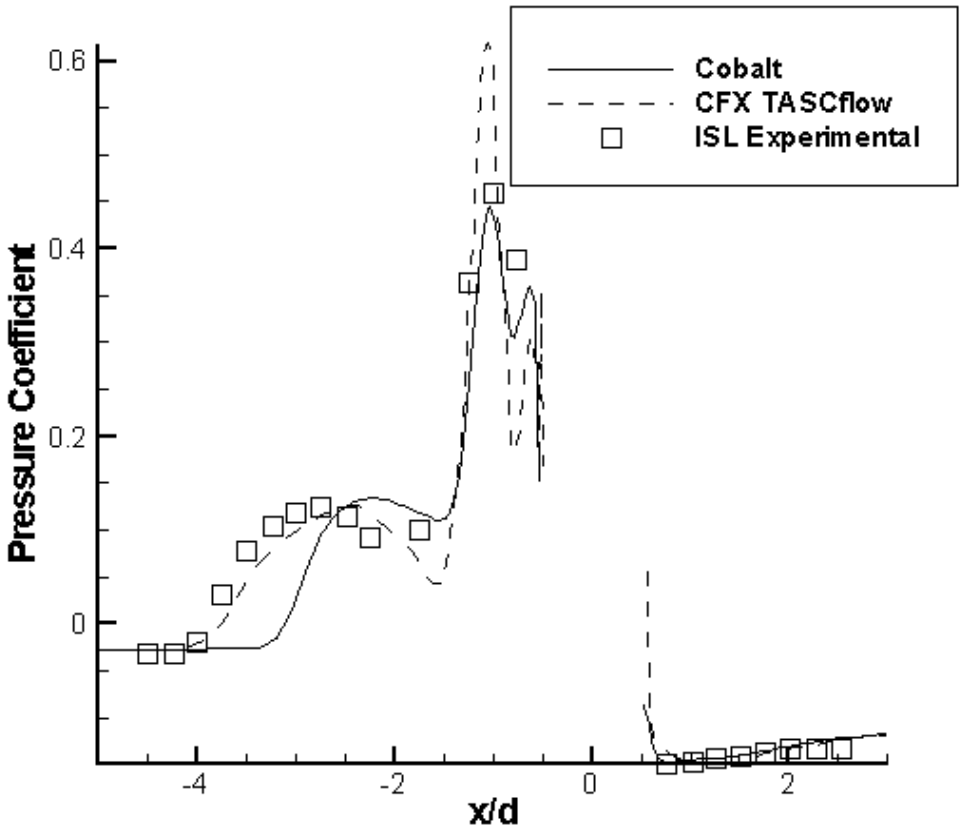


Figure 130 Coefficient of pressure in the longitudinal direction for the ISL BoR, PR=70.

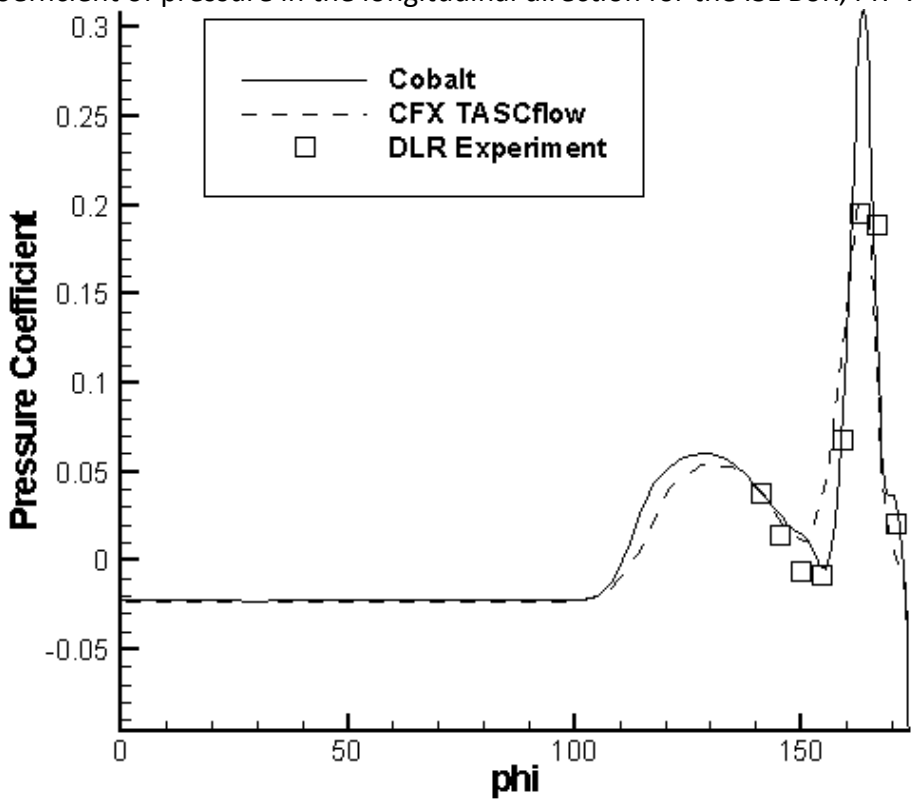


Figure 131 Coefficient of pressure in the circumferential direction for the ISL BoR, PR=70.

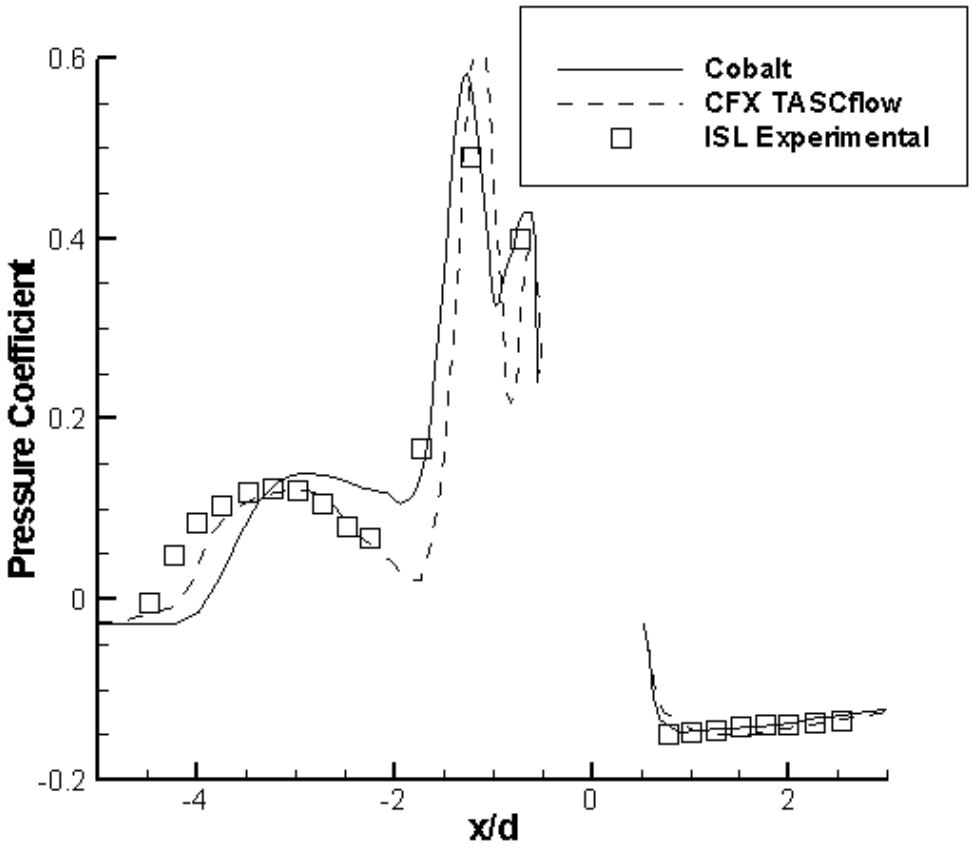


Figure 132 Coefficient of pressure in the longitudinal direction for the ISL BoR, PR=97.

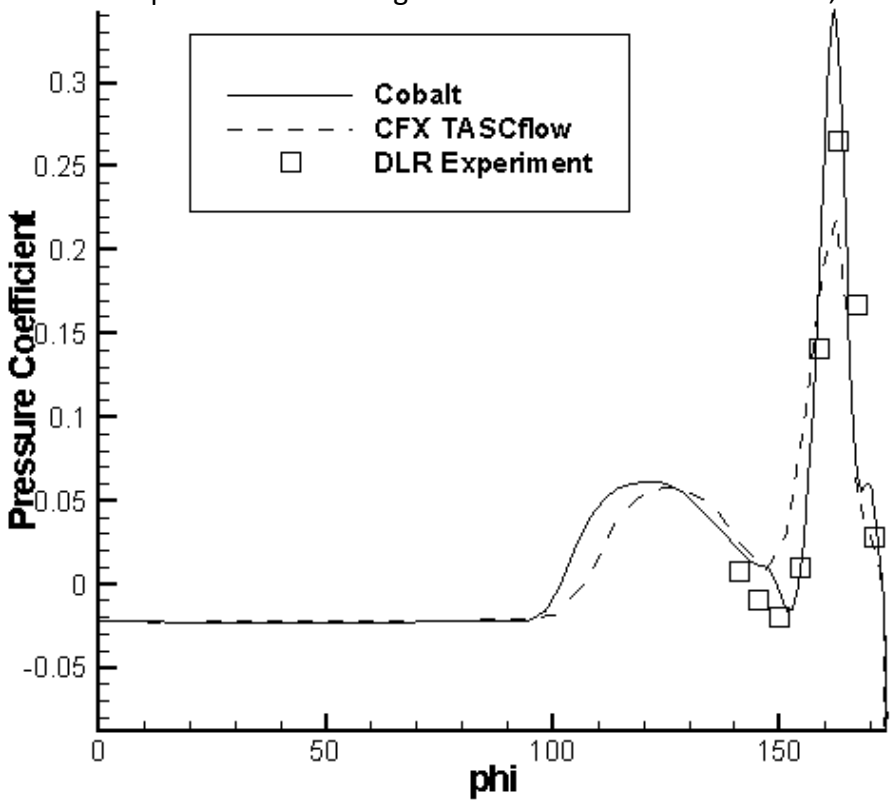


Figure 133 Coefficient of pressure in the circumferential direction for the ISL BoR, PR=97.

# Appendix G

# *Micro-Kulite data sheet*

kulite

# HIGH SENSITIVITY ULTRAMINIATURE IS® PRESSURE TRANSDUCER

## XCS-062 SERIES

- High Sensitivity
- Superior Signal To Noise Ratio
- Static And Dynamic Capability
- Wide Dynamic Range

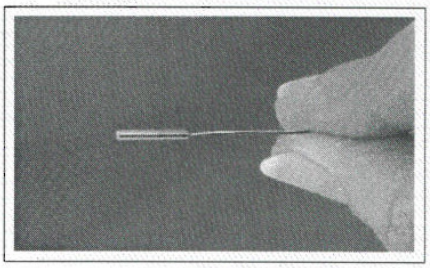

The XCS Series uses a diaphragm of advanced design which gives a substantially higher basic output allowing for high mV/psi sensitivities and improved signal to noise ratio.

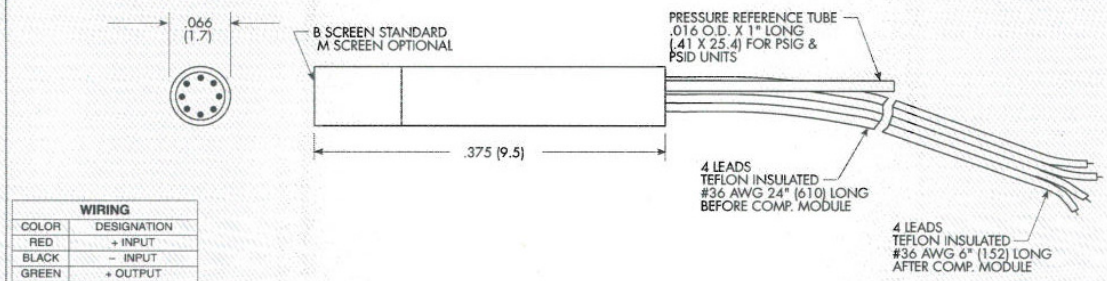


| WIRING | |
|---|---|
| COLOR | DESIGNATION |
| RED | + INPUT |
| BLACK | – INPUT |
| GREEN | + OUTPUT |
| WHITE | – OUTPUT |

NOTE: FOR INTERNAL COMPENSATION CONSULT FACTORY  CONSULT FACTORY FOR SPECS. ON SEALED GAGE

| | | | |
|---|---|---|---|
| **INPUT**<br>Pressure Range | 0.35<br>5 | 0.7<br>10 | 1.0 BAR<br>15 PSI |
| Operational Mode | Absolute, Gage, Sealed Gage, Differential | | |
| Over Pressure | 2 Times Rated Pressure With No Change in Calibration | | |
| Burst Pressure | 3 Times Rated Pressure | | |
| Pressure Media | All Nonconductive, Noncorrosive Liquids or Gases | | |
| Rated Electrical Excitation | 10 VDC/AC | | |
| Maximum Electrical Excitation | 12 VDC/AC | | |
| Input Impedance | 1000 Ohms (Min.) | | |
| **OUTPUT**<br>Output Impedance | 1000 Ohms (Nom.) | | |
| Full Scale Output (FSO) | 125 mV (Nom.)<br>50 mV (Nom.) for SG | 125 mV (Nom.)<br>50 mV (Nom.) for SG | 200 mV (Nom.)<br>100 mV (Nom.) for SG |
| Residual Unbalance | ± 5 mV (Typ.) | | |
| Combined Non-Linearity and Hysteresis | ± 0.25% FSO BFSL (Typ.) | | |
| Hysteresis | 0.1% (Typ.) | | |
| Repeatability | 0.1% (Typ.) | | |
| Resolution | Infinitesimal | | |
| Natural Frequency (KHz) (Typ.) | 150 | 175 | 200 |
| Acceleration Sensitivity % FS/g<br>Perpendicular<br>Transverse | <br>$1.5 \times 10^{-3}$<br>$2.2 \times 10^{-4}$ | <br>$1.0 \times 10^{-3}$<br>$1.0 \times 10^{-4}$ | <br>$7.0 \times 10^{-4}$<br>$9.0 \times 10^{-5}$ |
| Insulation Resistance | 100 Megohm Min. @ 50 VDC | | |
| **ENVIRONMENTAL**<br>Operating Temperature Range | -65°F to +250°F (-55°C to +120°C) | | |
| Compensated Temperature Range | 80°F to +180°F (25°C to +80°C) Any 100°F Range Within The Operating Range on Request | | |
| Thermal Zero Shift | ± 1% FS/100°F (Typ.) | | |
| Thermal Sensitivity Shift | ± 1% /100°F (Typ.) | | |
| Steady Acceleration | 10,000g. (Max.) | | |
| Linear Vibration | 10-20,000 Hz Sine, 100g. (Max.) | | |
| **PHYSICAL**<br>Electrical Connection | 4 Leads 36 AWG 30" Long | | |
| Weight | .2 Gram (Nom.) Excluding Module and Leads | | |
| Pressure Sensing Principle | Fully Active Four Arm Wheatstone Bridge Dielectrically Isolated Silicon on Silicon | | |

*Note: Custom pressure ranges, accuracies and mechanical configurations available. Dimensions are in inches. Dimensions in parenthesis are in millimeters.*
*Continuous development and refinement of our products may result in specification changes without notice - all dimensions nominal. (J)*

KULITE SEMICONDUCTOR PRODUCTS, INC. • One Willow Tree Road • Leonia, New Jersey 07605 • Tel: 201 461-0900 • Fax: 201 461-0990 • http://www.kulite.com

# Appendix H

# *Micro-Kulite calibration*

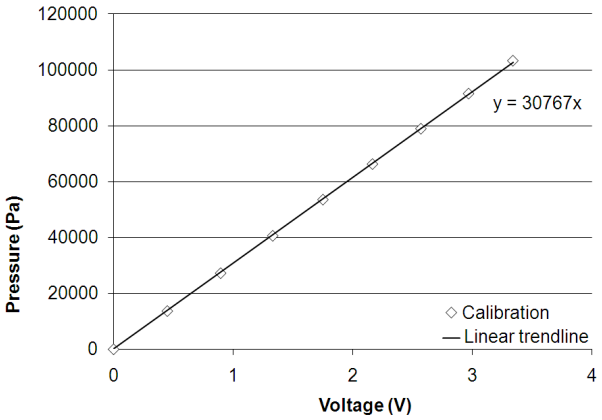


Calibration curve for micro-Kulite #1

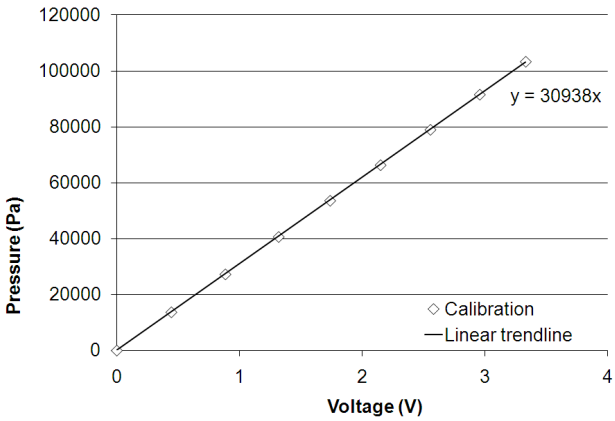


Calibration curve for micro-Kulite #2

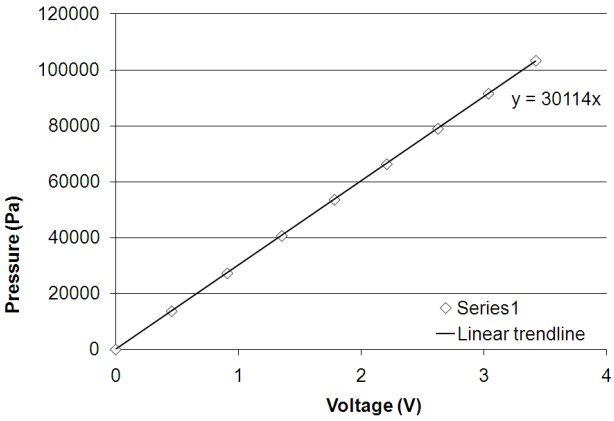


Calibration curve for micro-Kulite #3

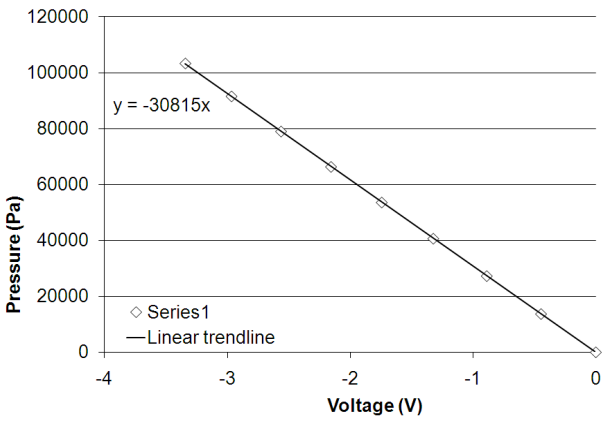


Calibration curve for micro-Kulite #4

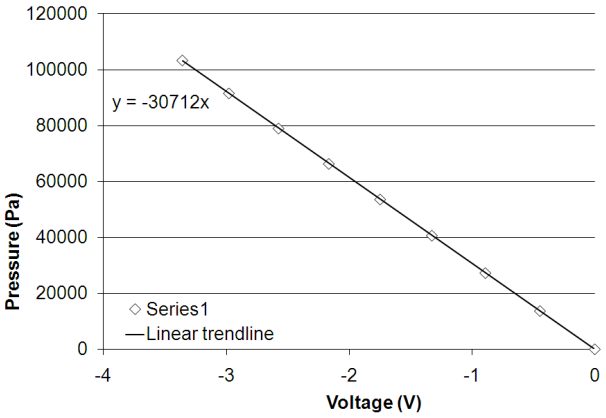


Calibration curve for micro-Kulite #5

# Appendix I

# *Micro-Kulite calibration*

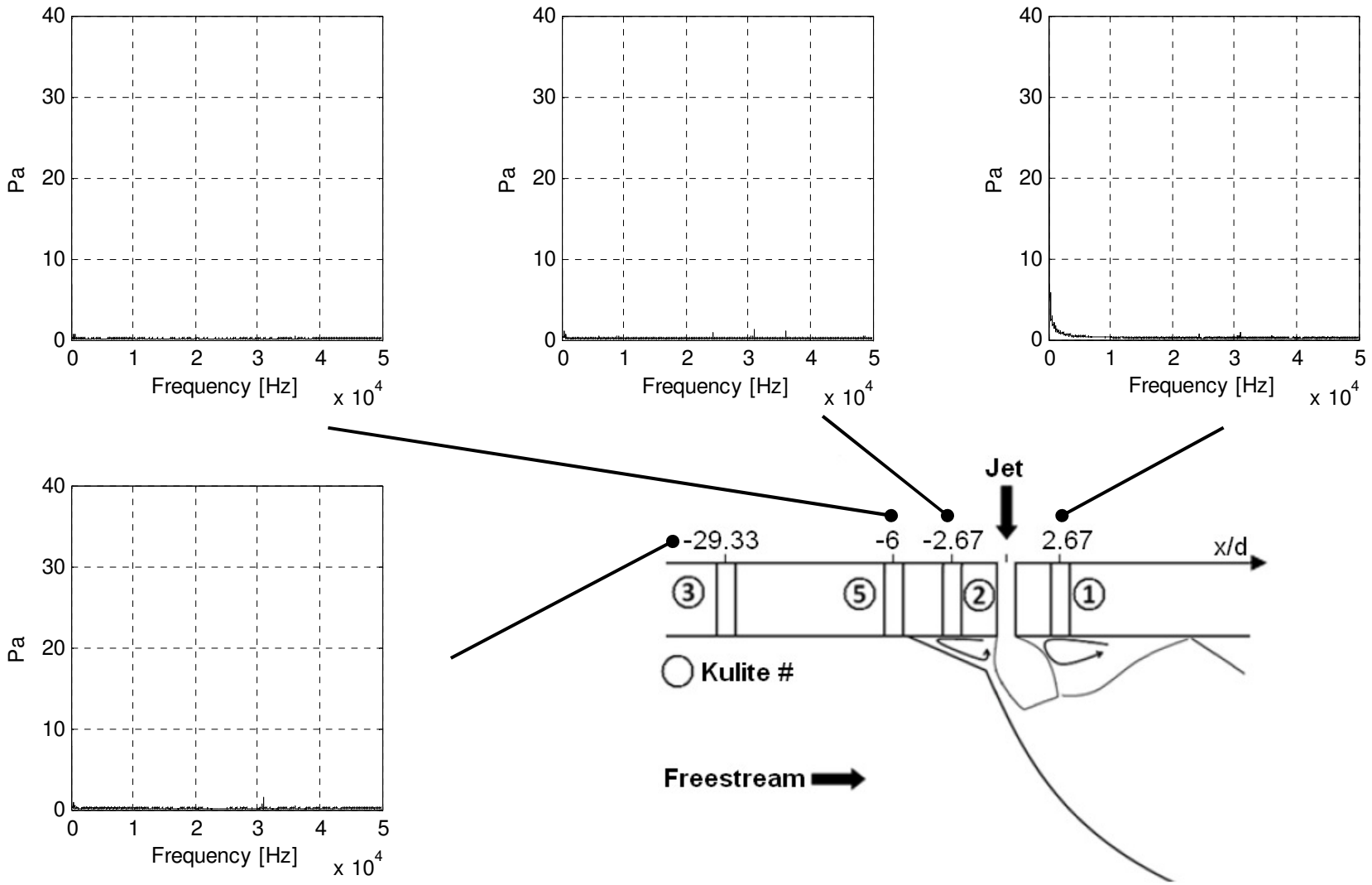


Figure 134 Pressure signal transformed into the frequency domain using a FFT, M=3.1, PR=200, δ=4.93.

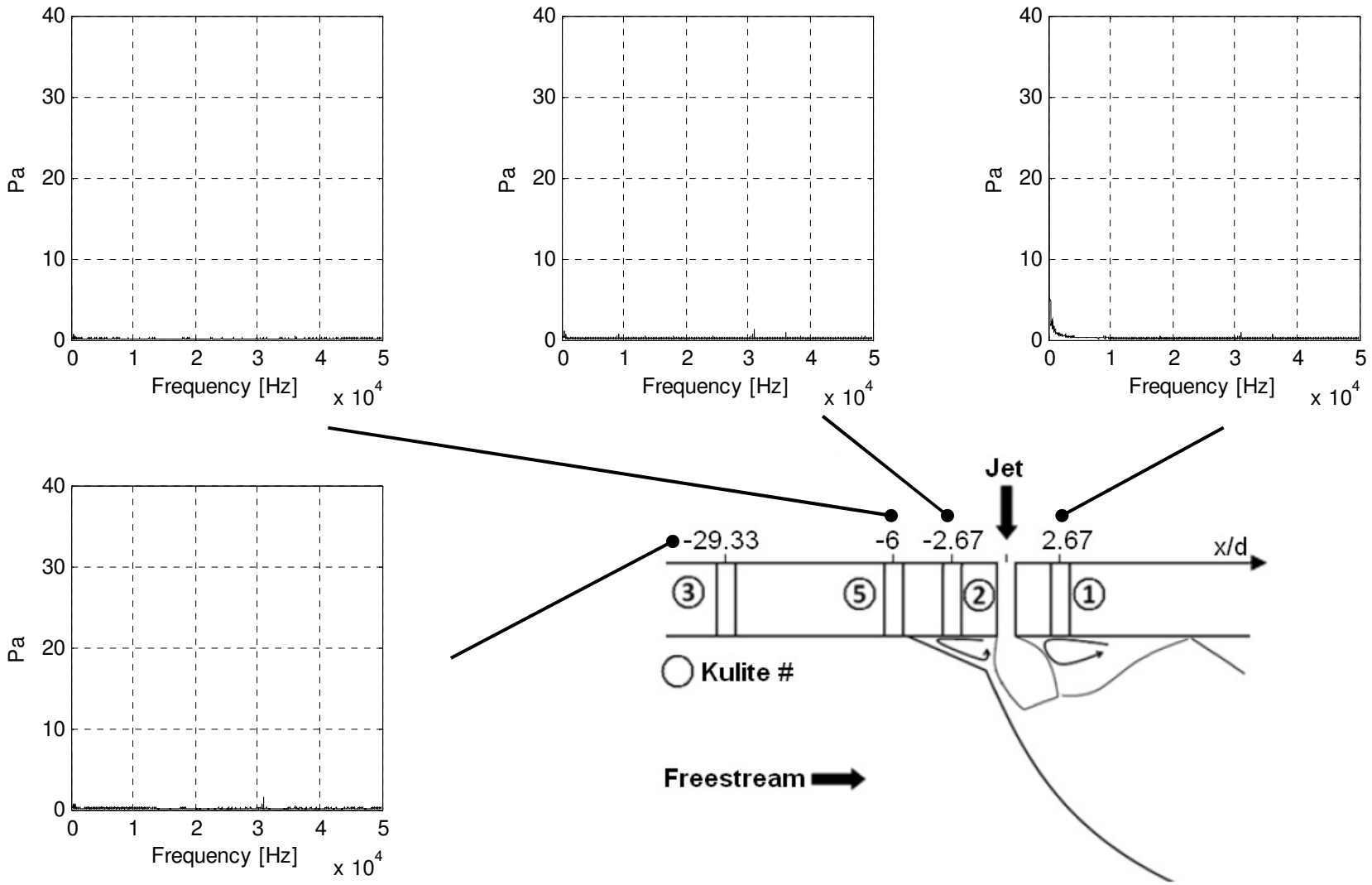


Figure 135 Pressure signal transformed into the frequency domain using a FFT, M=3.1, PR=150, δ=4.93.

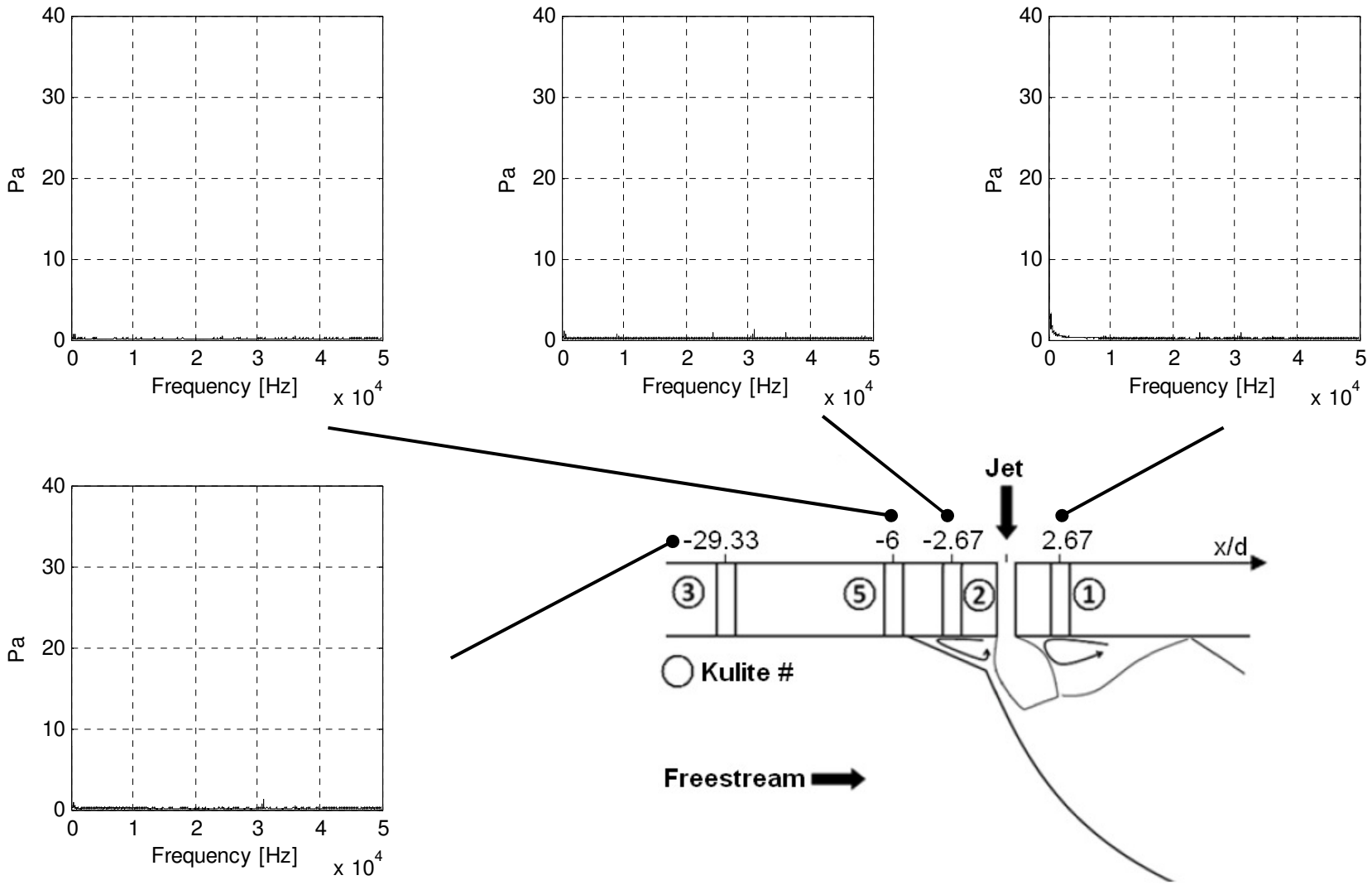


Figure 136 Pressure signal transformed into the frequency domain using a FFT, M=3.1, PR=110, δ=4.93.

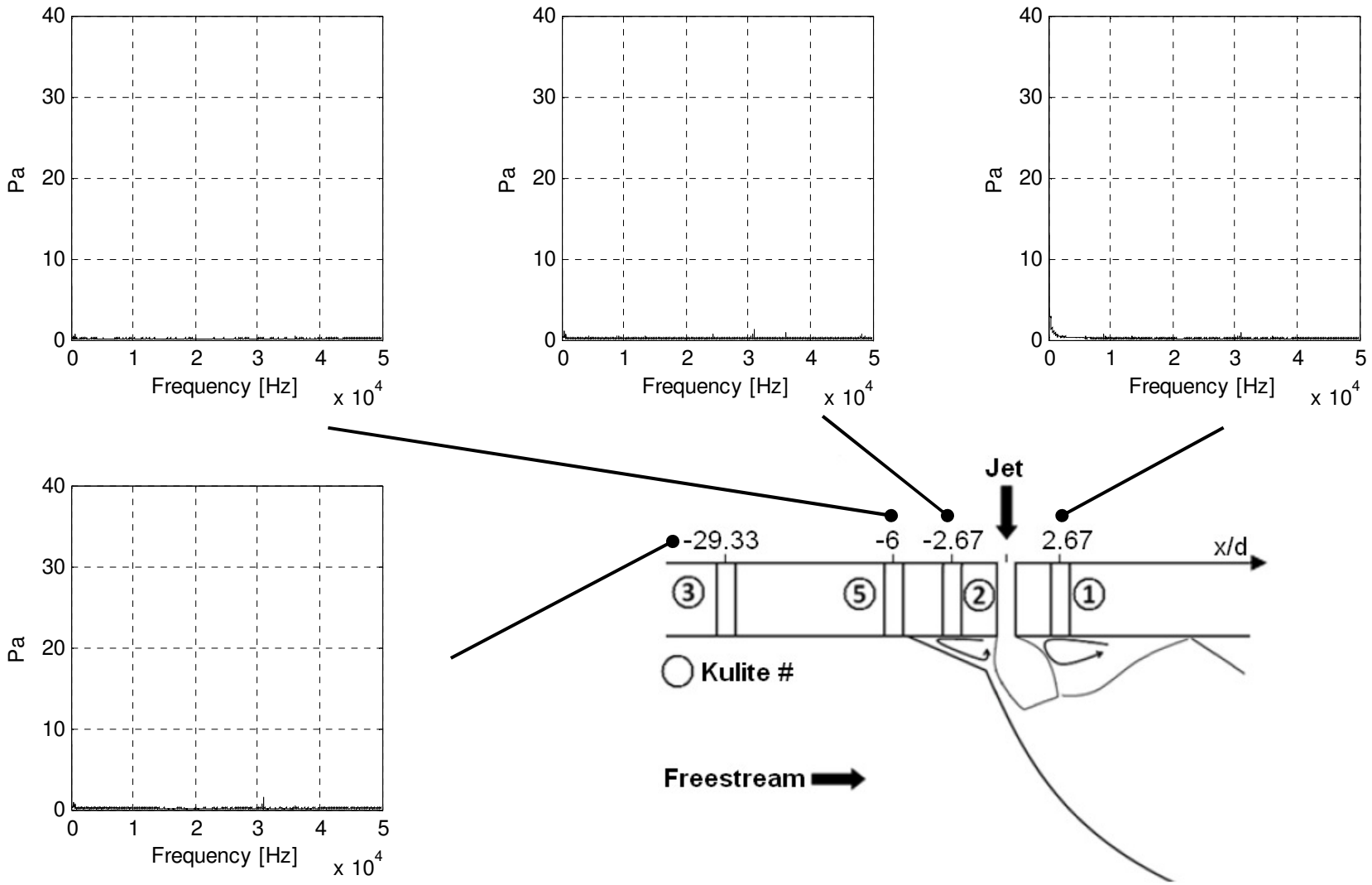


Figure 137 Pressure signal transformed into the frequency domain using a FFT, M=3.1, PR=97, δ=4.93.

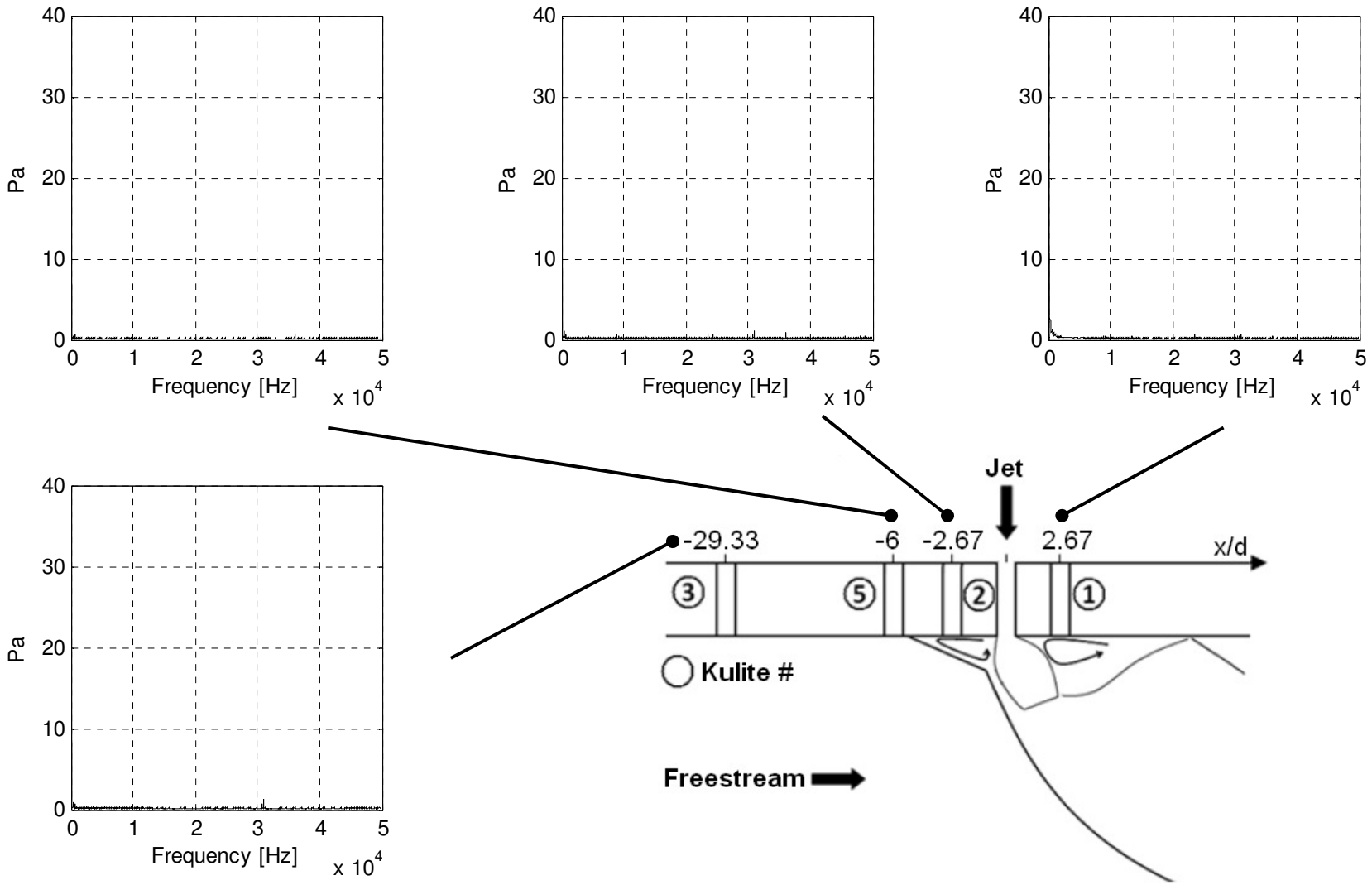


Figure 138 Pressure signal transformed into the frequency domain using a FFT, M=3.1, PR=70, δ=4.93.

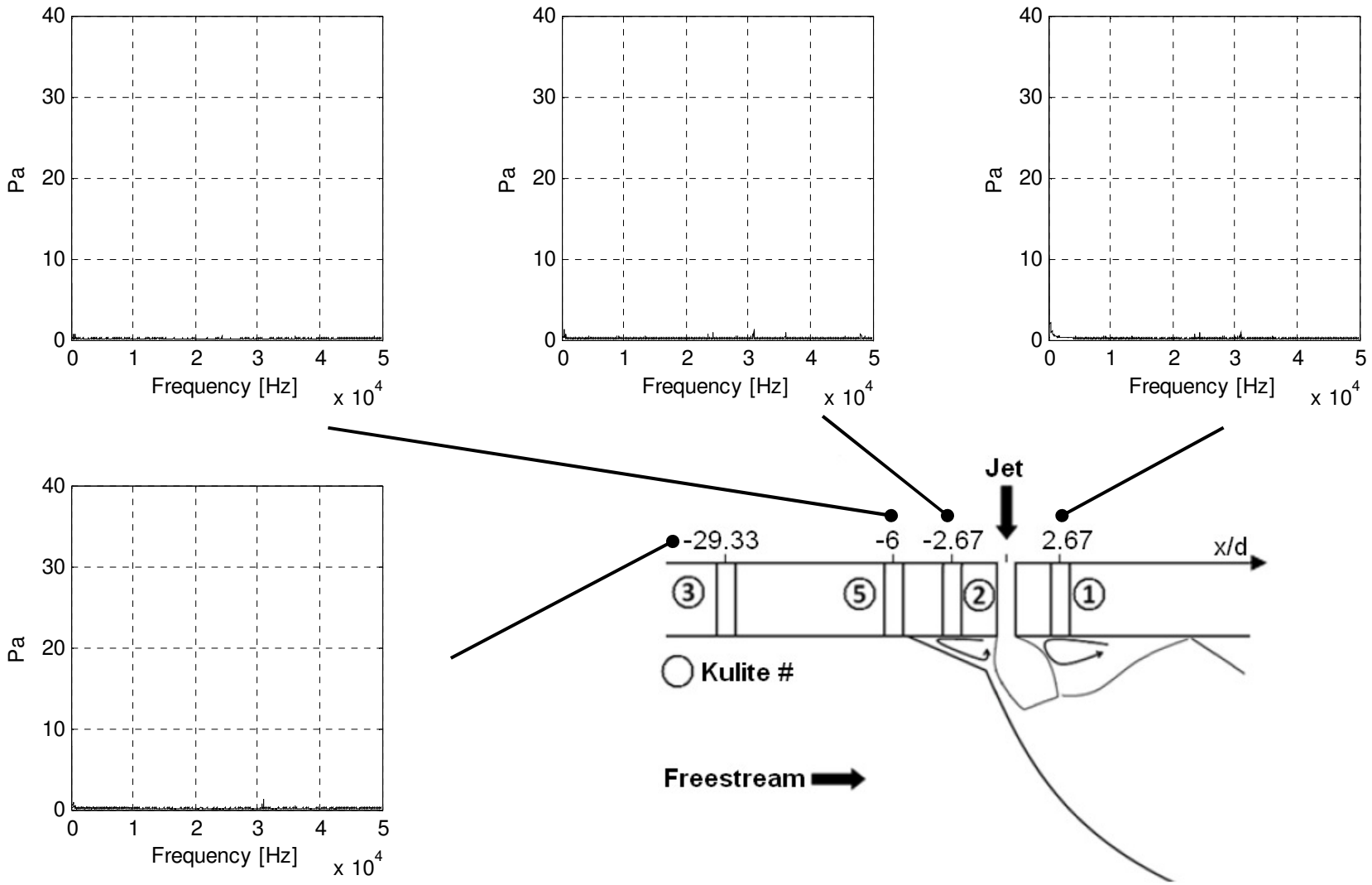


Figure 139 Pressure signal transformed into the frequency domain using a FFT, M=3.1, MPR=55, δ=4.93.

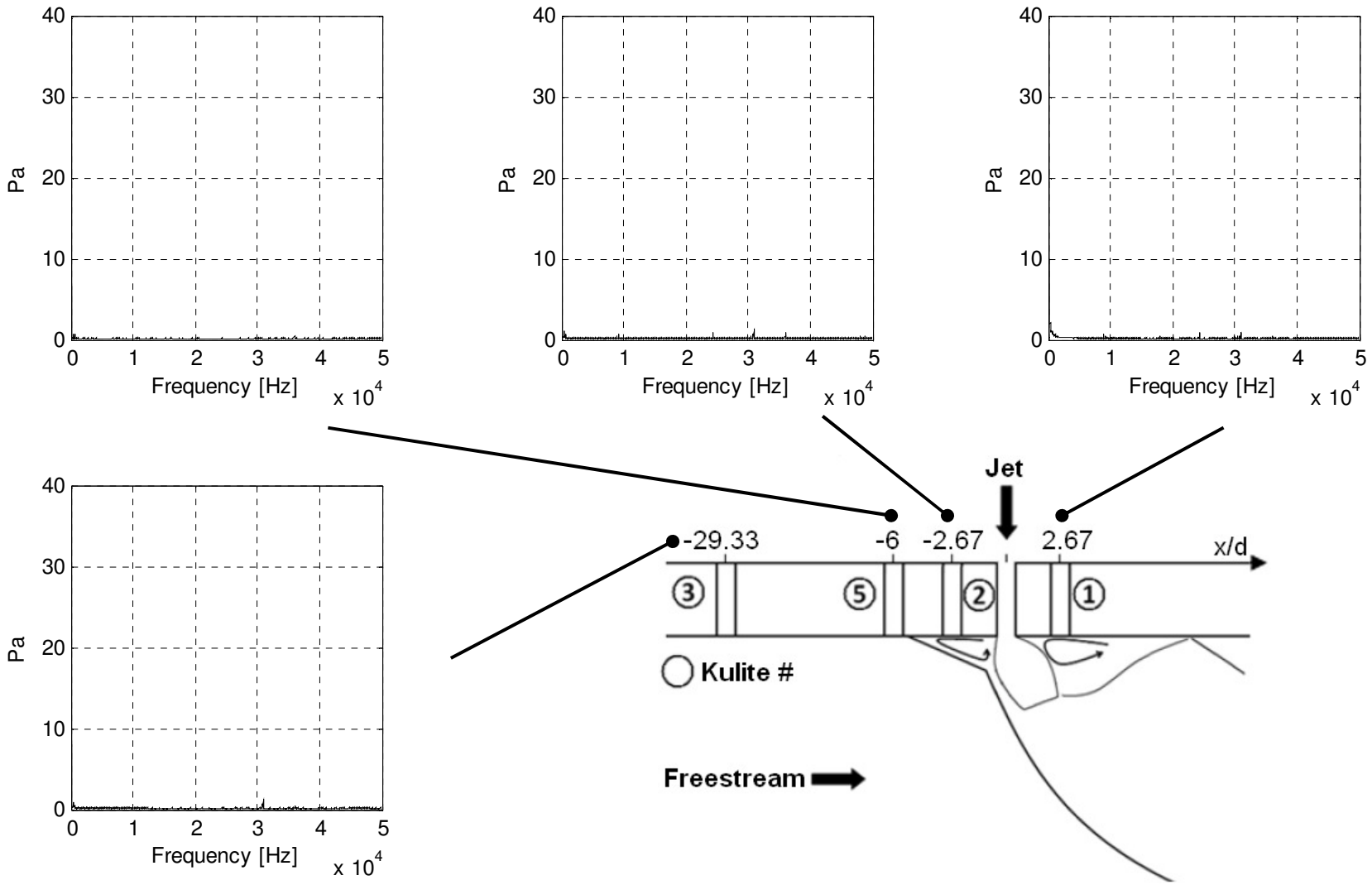


Figure 140 Pressure signal transformed into the frequency domain using a FFT, M=3.1, PR=50, δ=4.93.

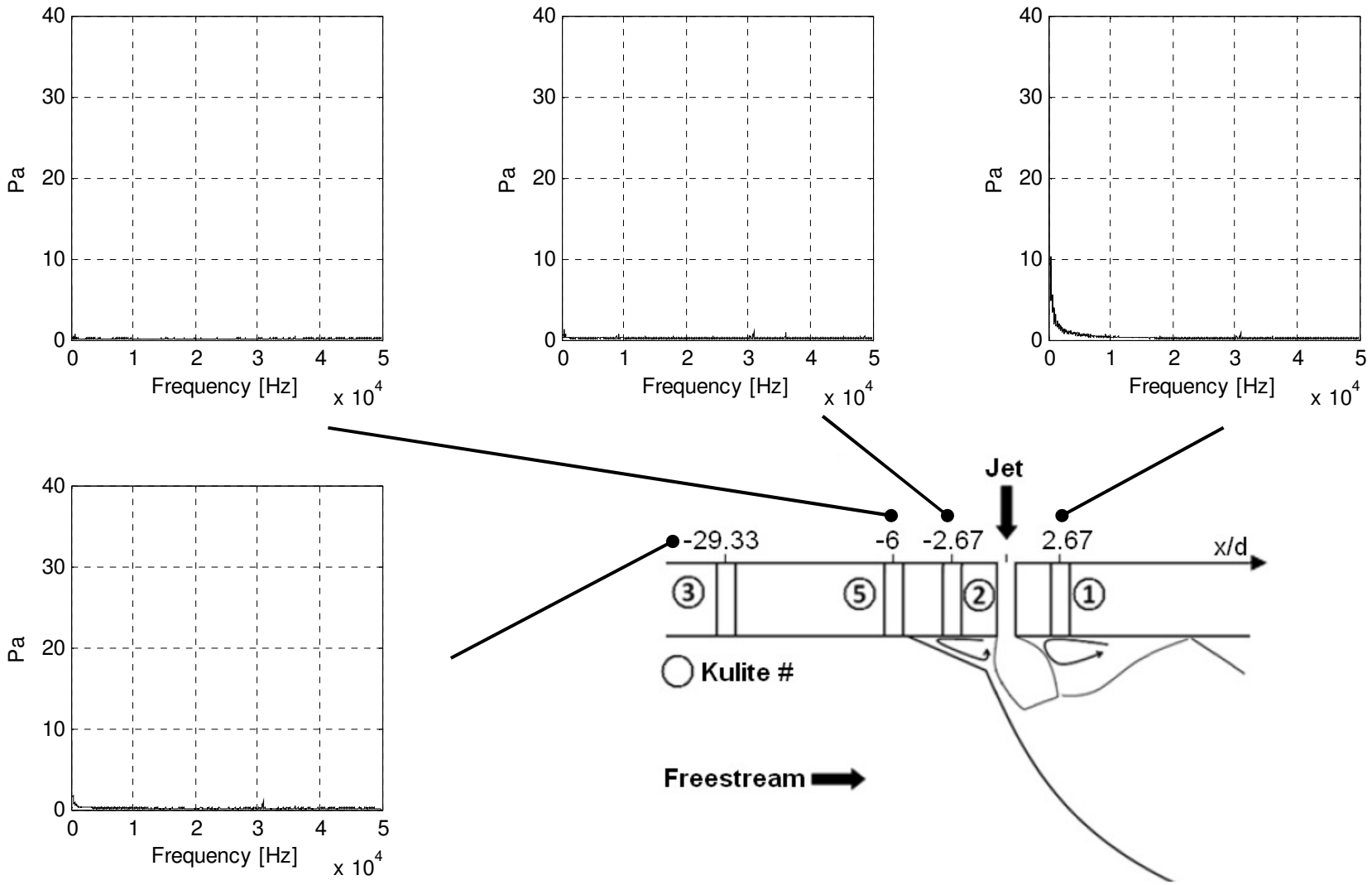


Figure 141 Pressure signal transformed into the frequency domain using a FFT, M=2.4, PR=70, δ=5.04.

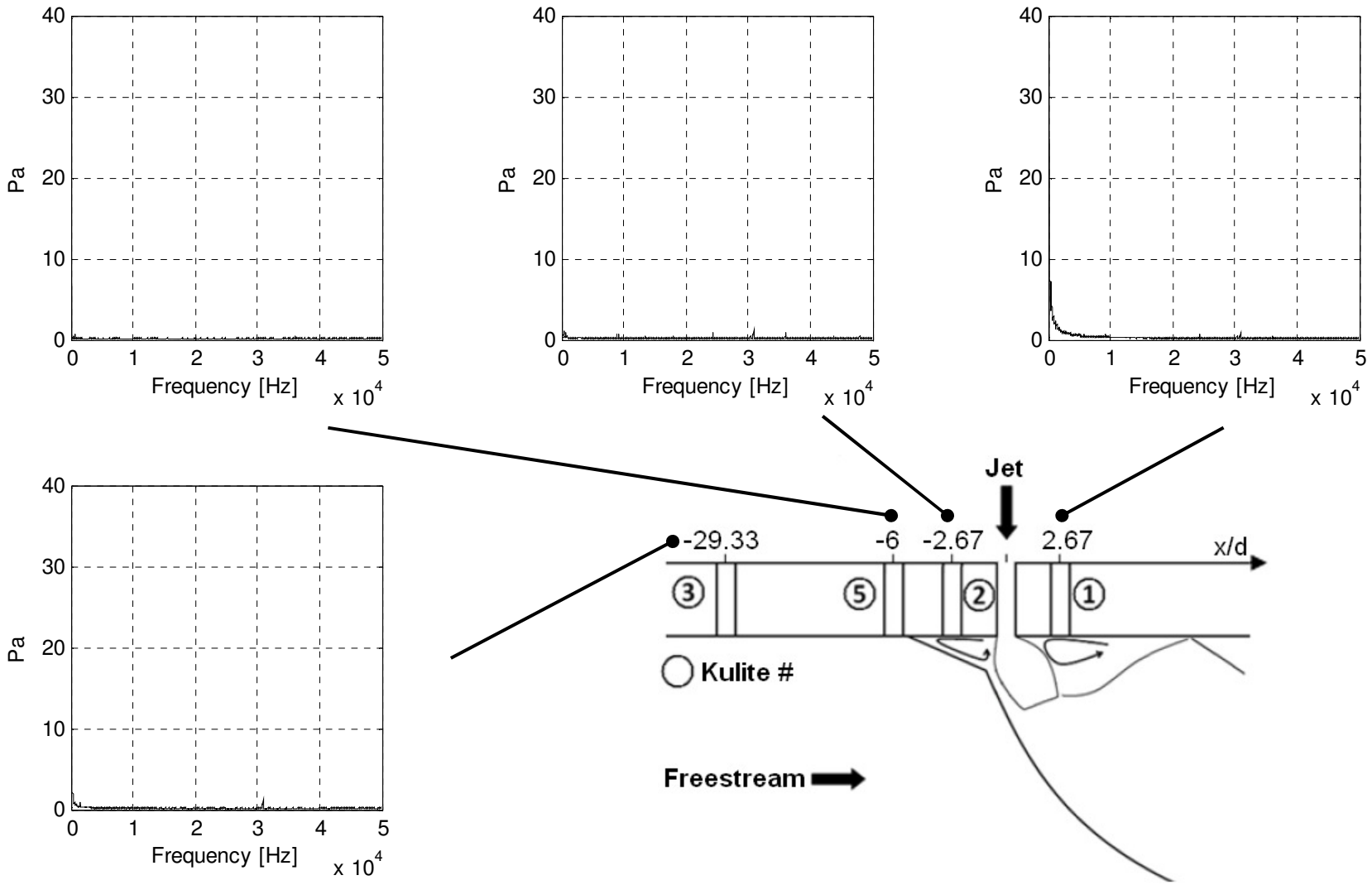


Figure 142 Pressure signal transformed into the frequency domain using a FFT, M=2.4, PR=55, δ=5.04.

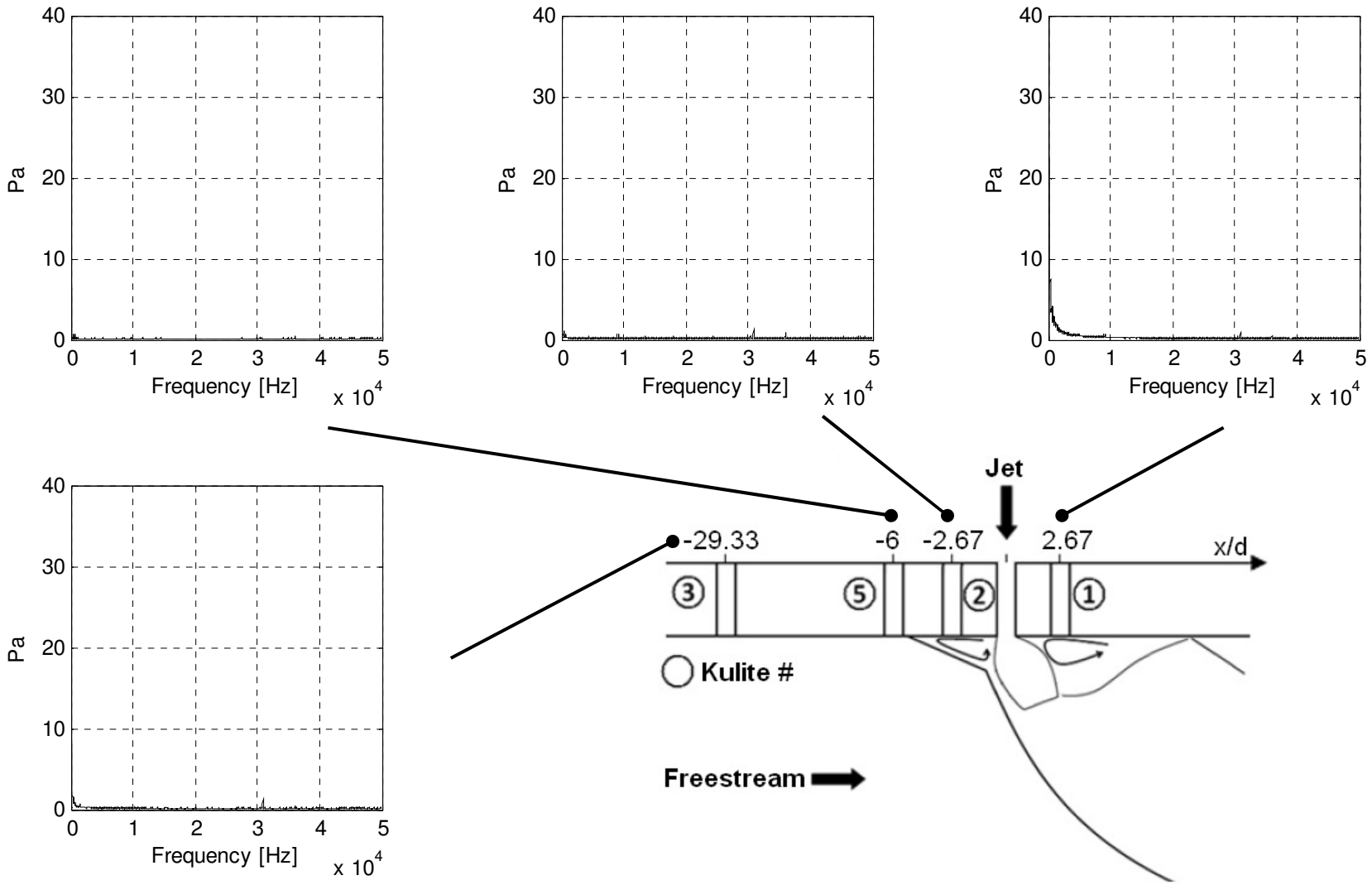


Figure 143 Pressure signal transformed into the frequency domain using a FFT, M=2.4, PR=50, δ=5.04.

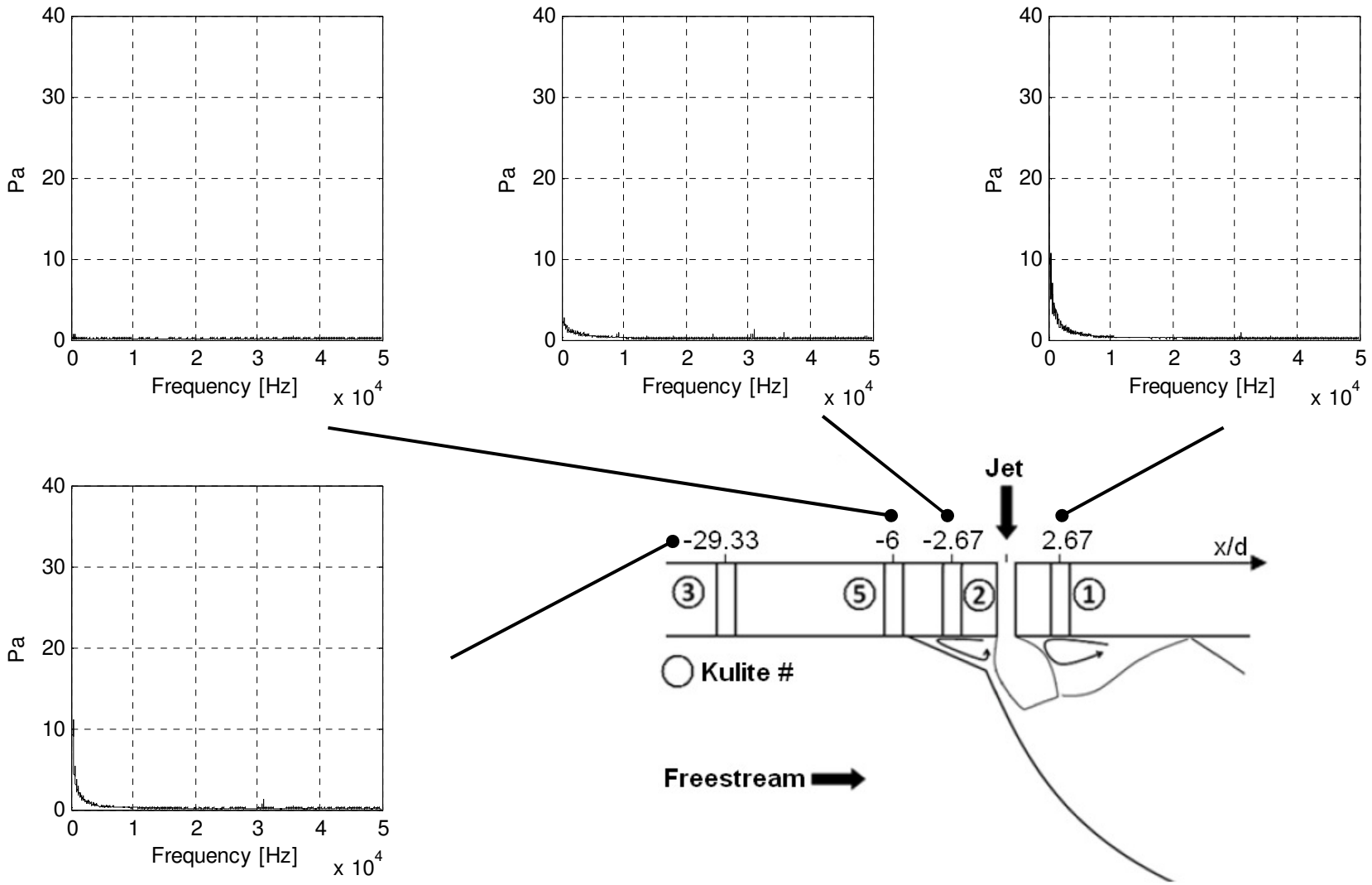


Figure 144 Pressure signal transformed into the frequency domain using a FFT, M=1.8, MPR=2.7, δ=4.55.

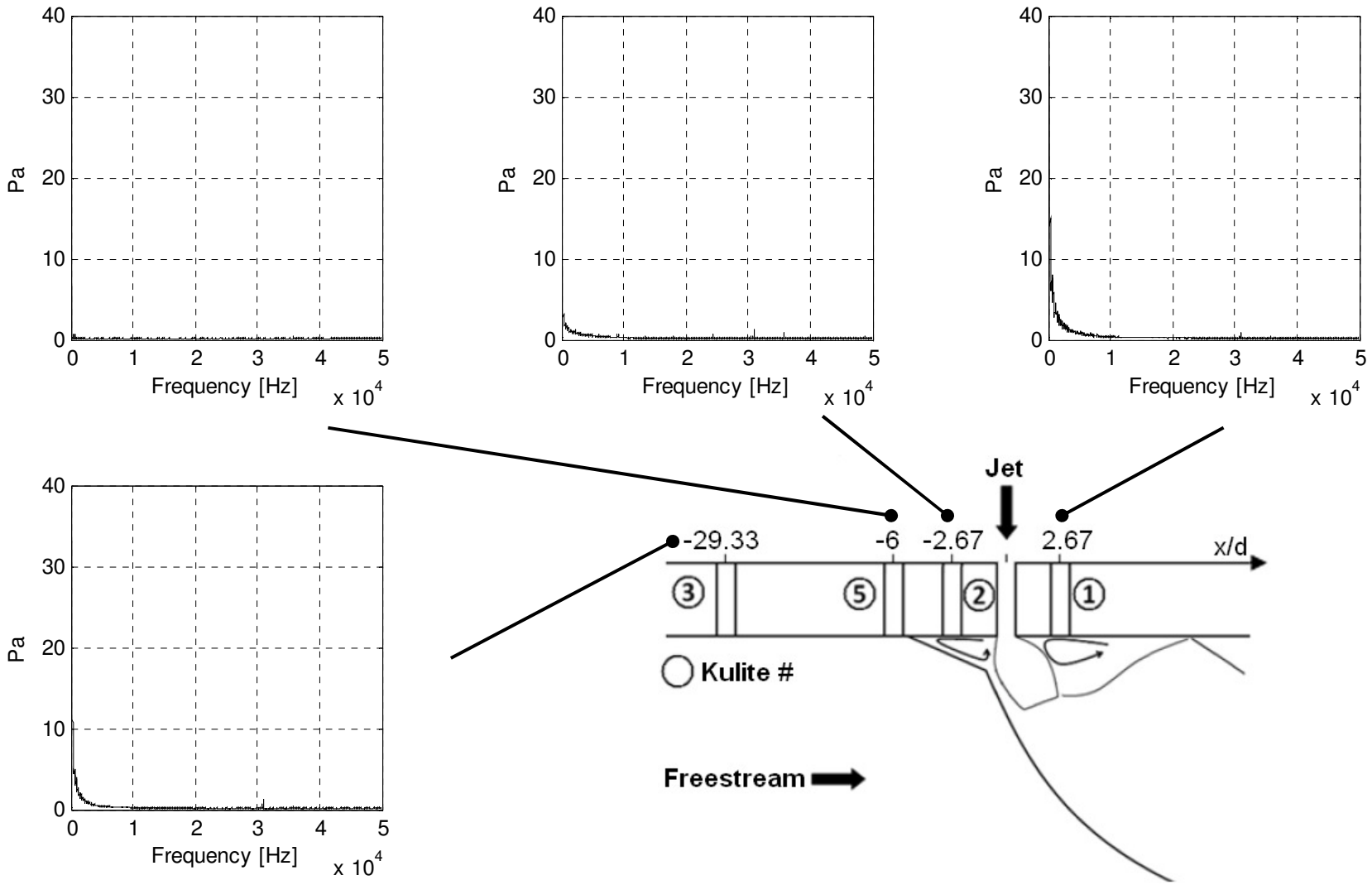


Figure 145 Pressure signal transformed into the frequency domain using a FFT, M=1.8, MPR=3.0, δ=4.55.

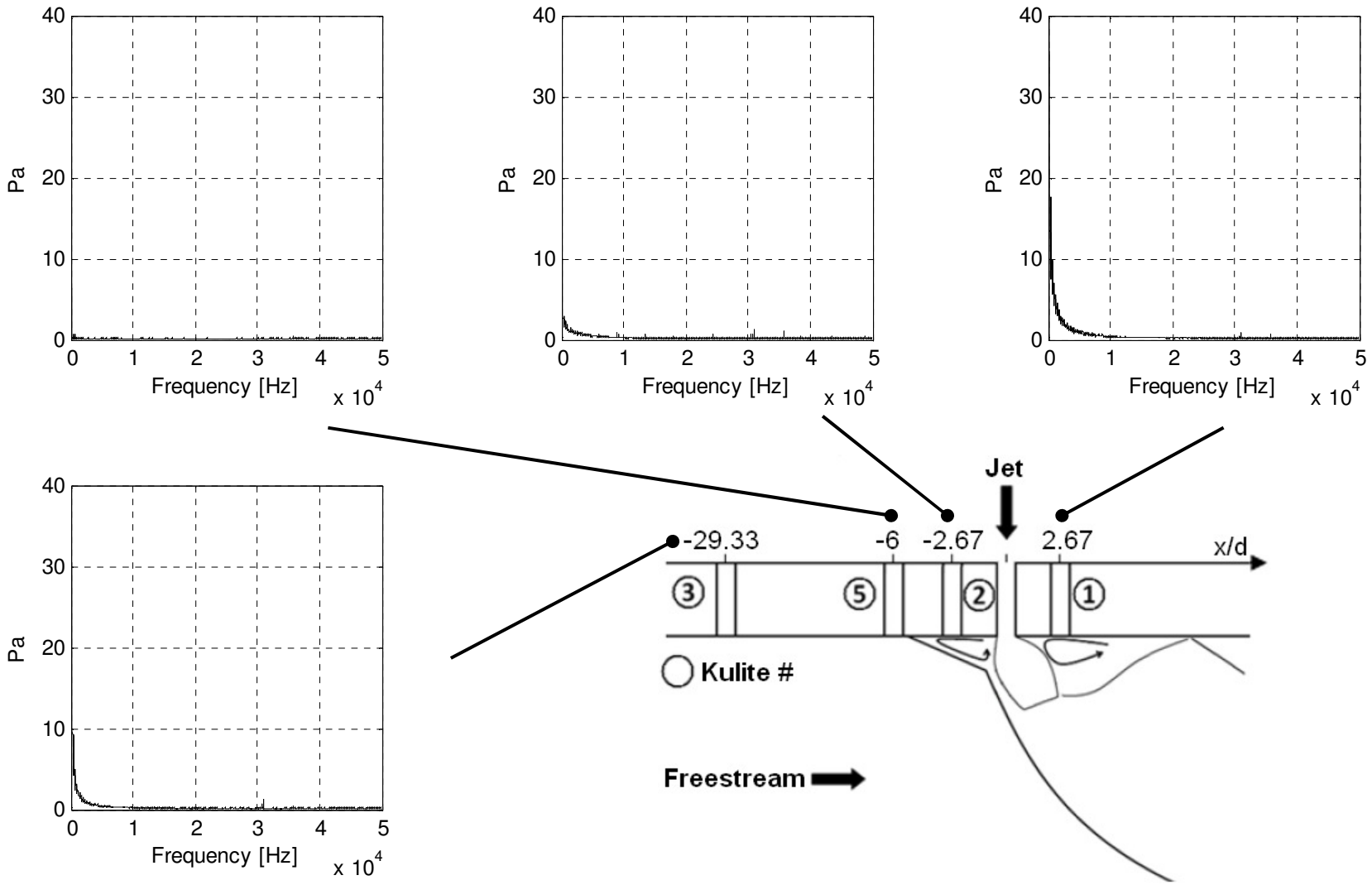


Figure 146 Pressure signal transformed into the frequency domain using a FFT, M=1.8, MPR=3.8, δ=4.55.

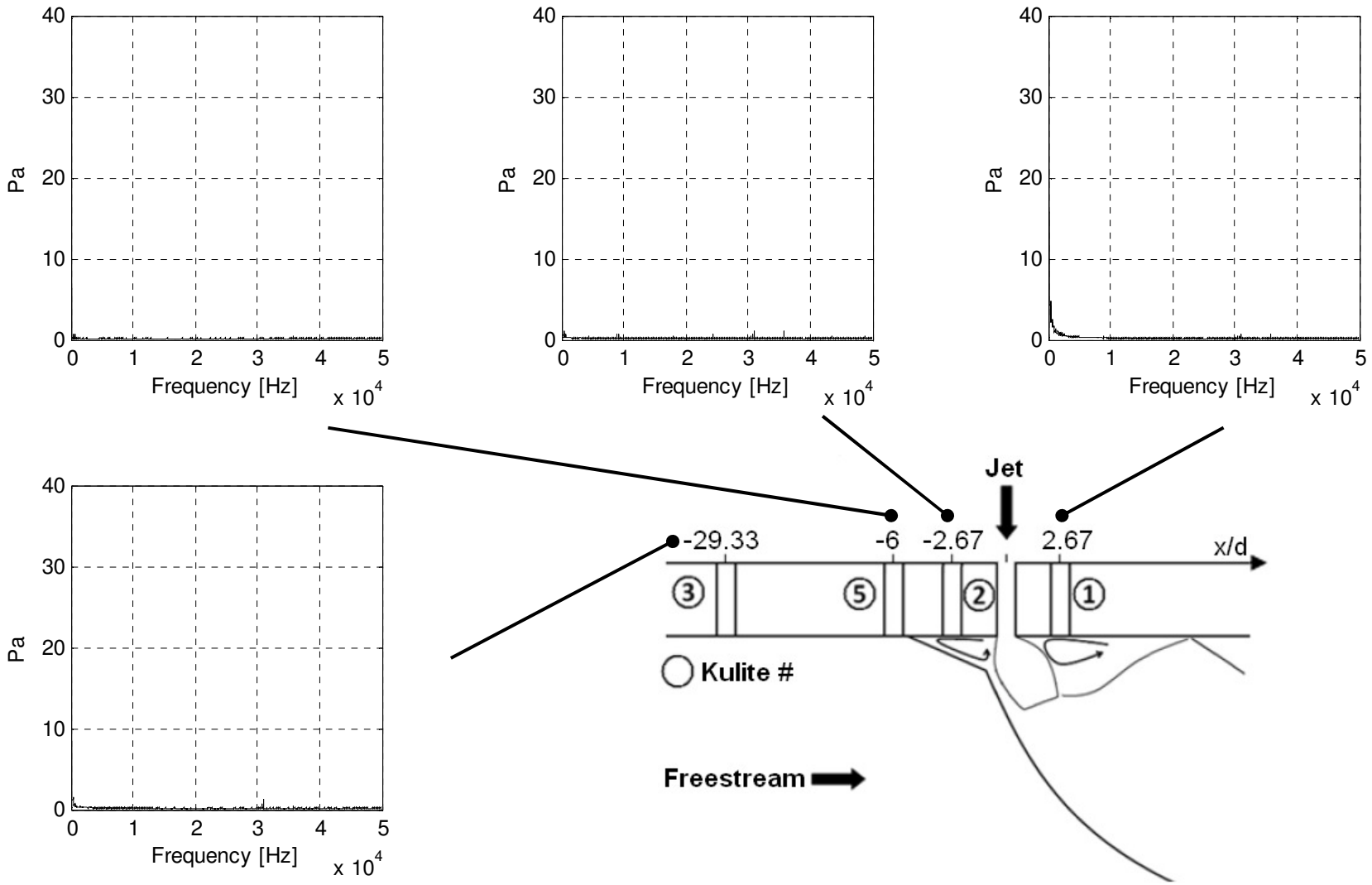


Figure 147 Pressure signal transformed into the frequency domain using a FFT, M=2.4, MPR=2.7, δ=5.04.

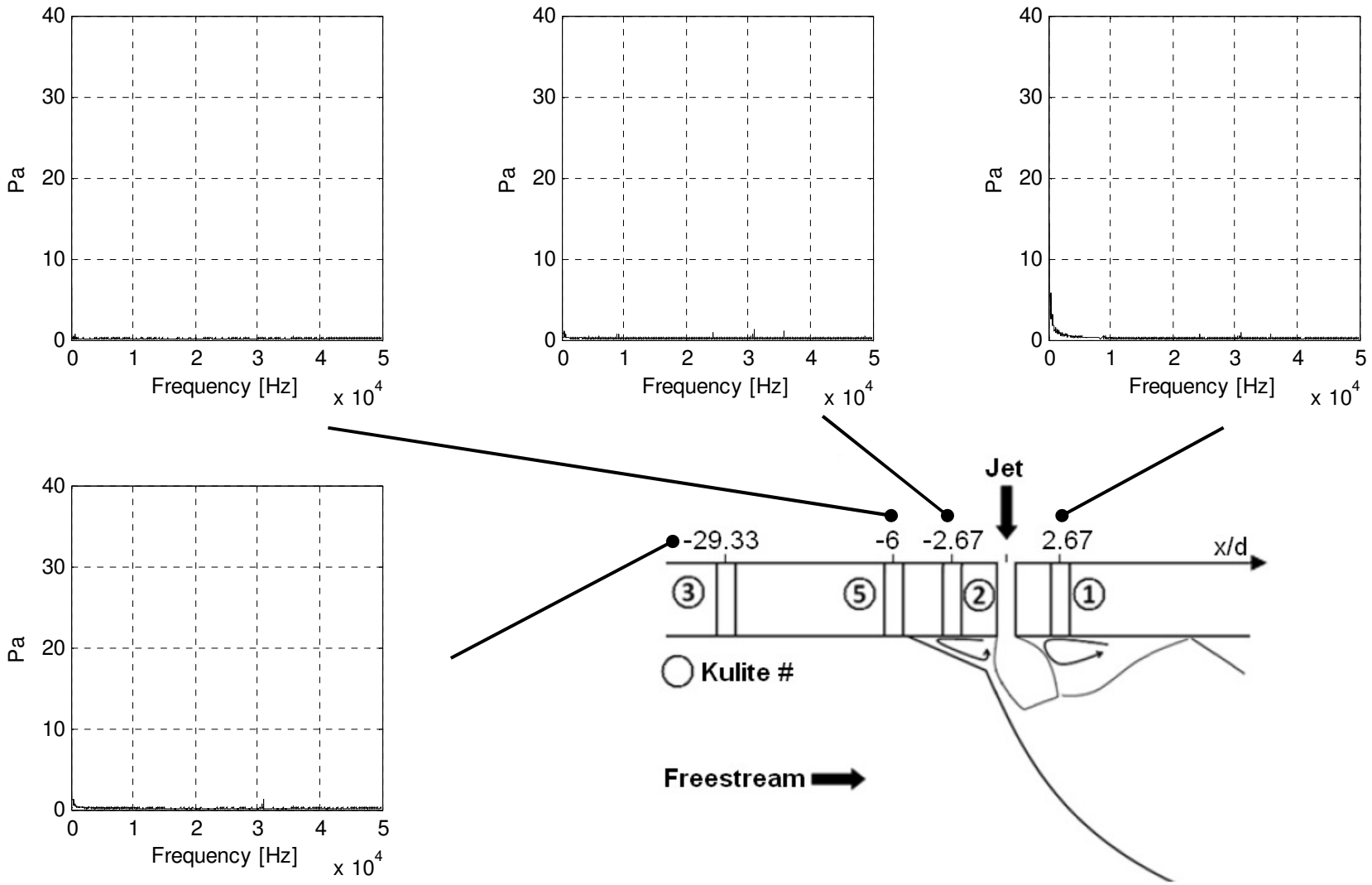


Figure 148 Pressure signal transformed into the frequency domain using a FFT, M=2.4, MPR=3.0, δ=5.04.

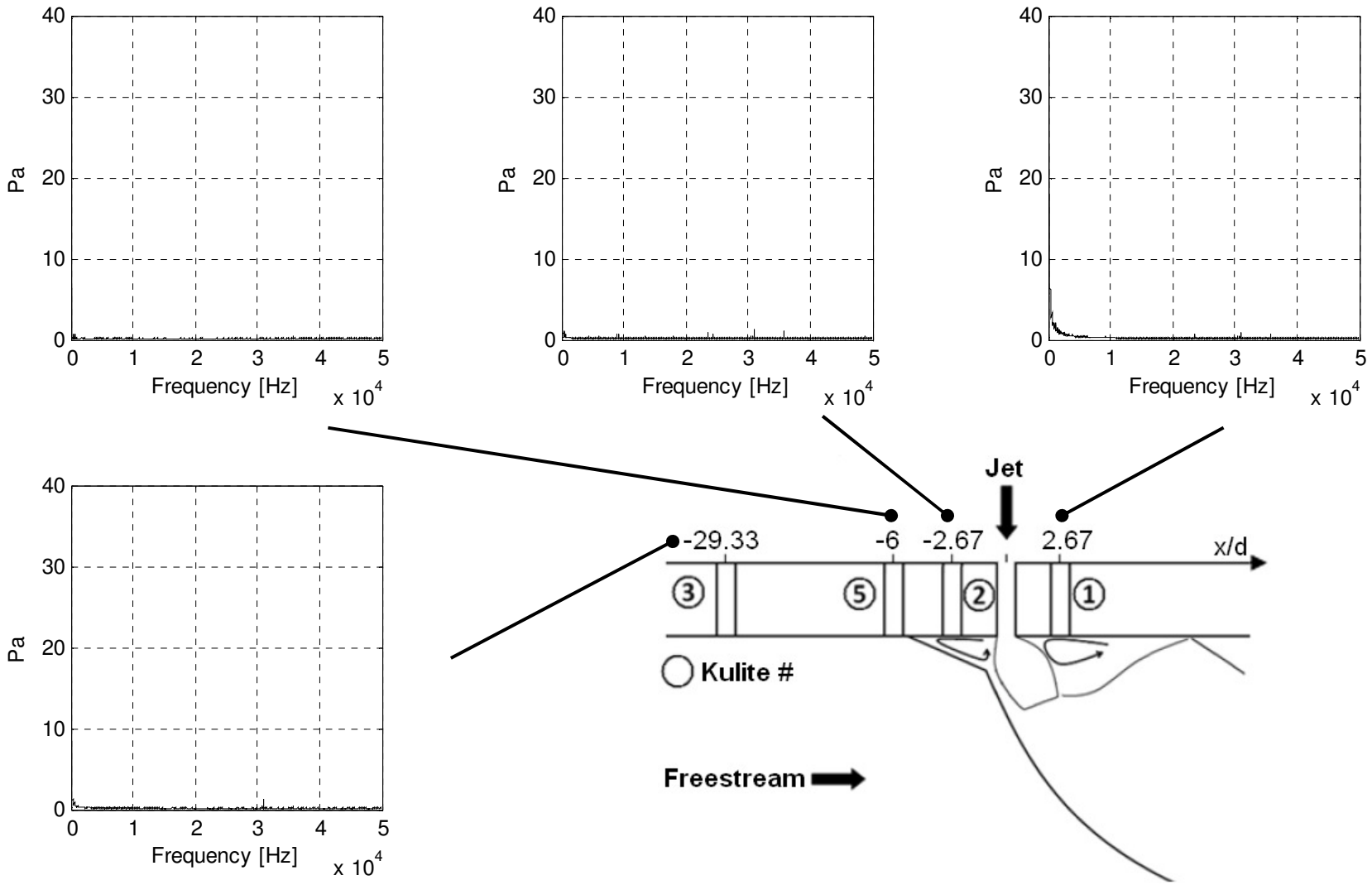


Figure 149 Pressure signal transformed into the frequency domain using a FFT, M=2.4, MPR=3.8, δ=5.04.

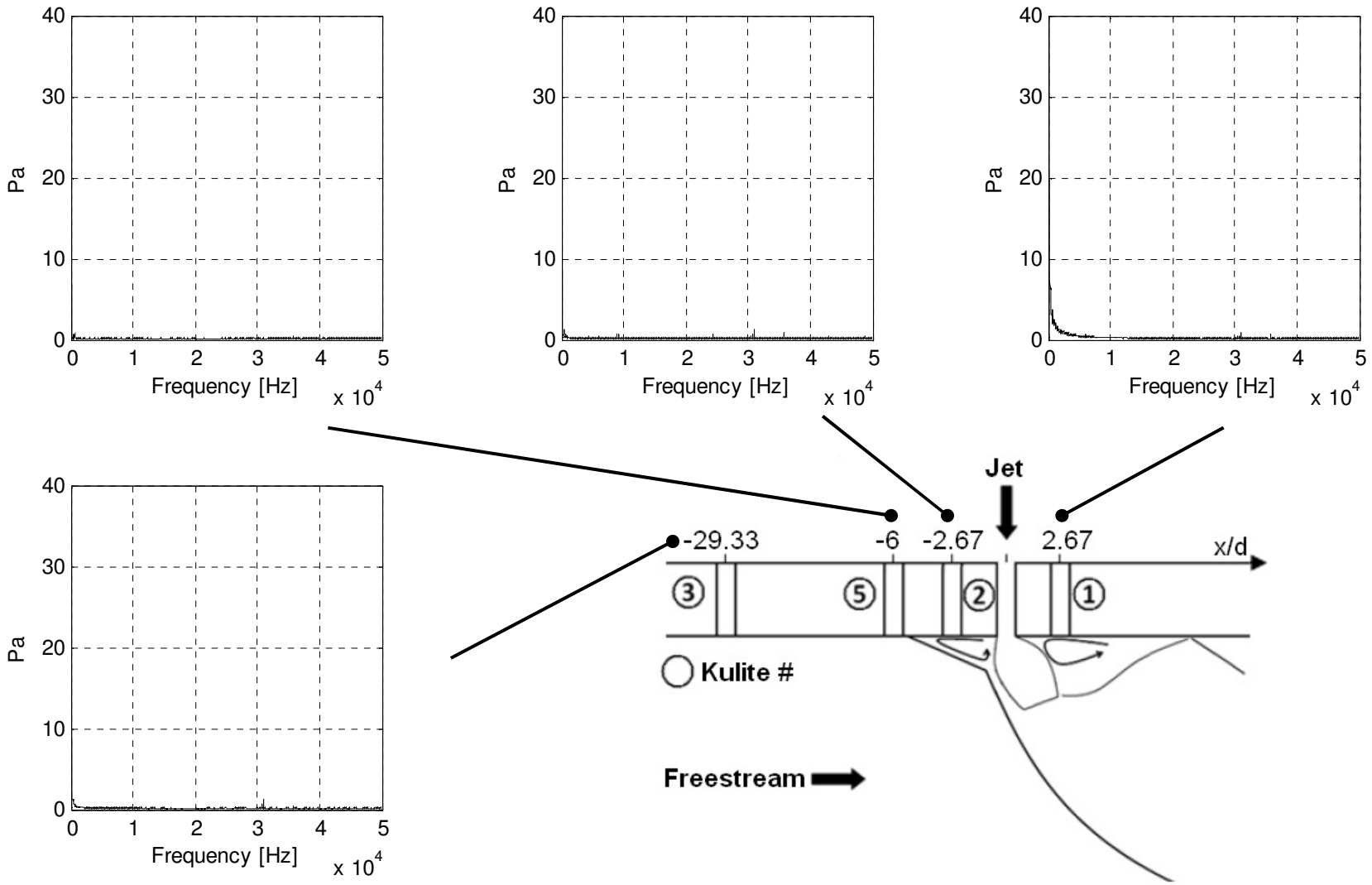


Figure 150 Pressure signal transformed into the frequency domain using a FFT, M=2.4, δ=5.04.

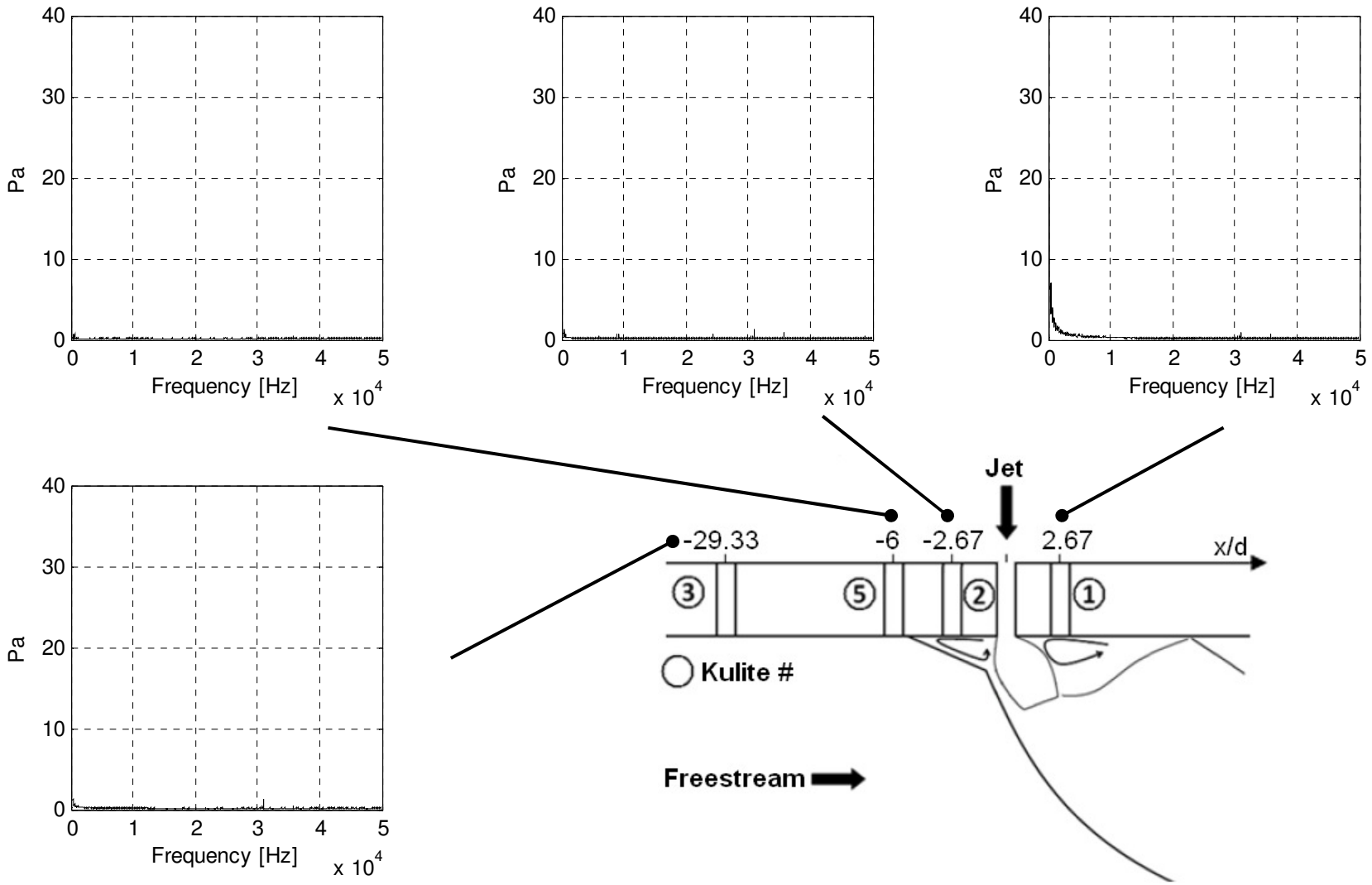


Figure 151 Pressure signal transformed into the frequency domain using a FFT, M=2.4, δ=5.04.

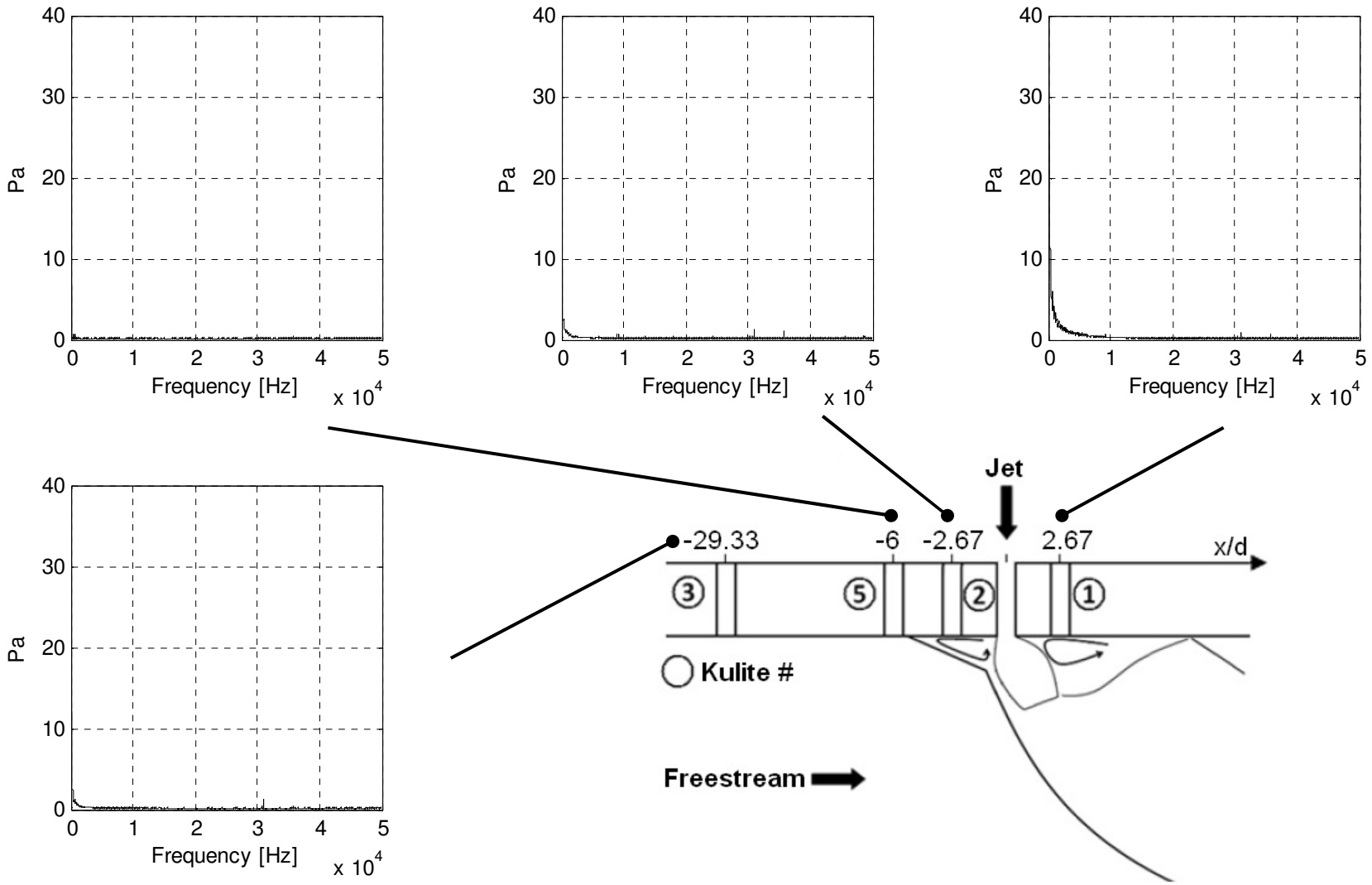


Figure 152 Pressure signal transformed into the frequency domain using a FFT, M=2.4, PR=70, δ=8.63.

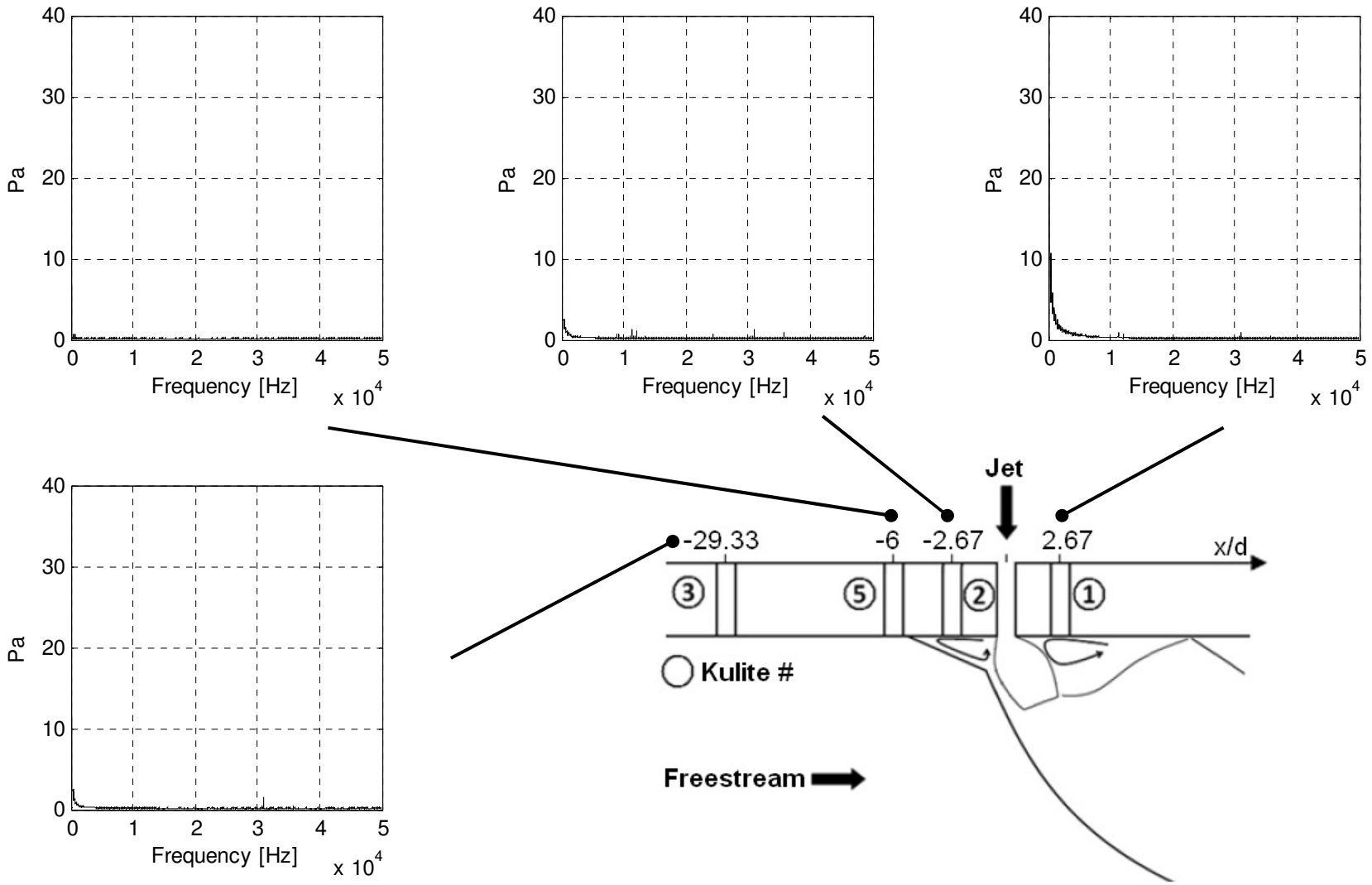


Figure 153 Pressure signal transformed into the frequency domain using a FFT, M=2.4, PR=55, δ=8.63.

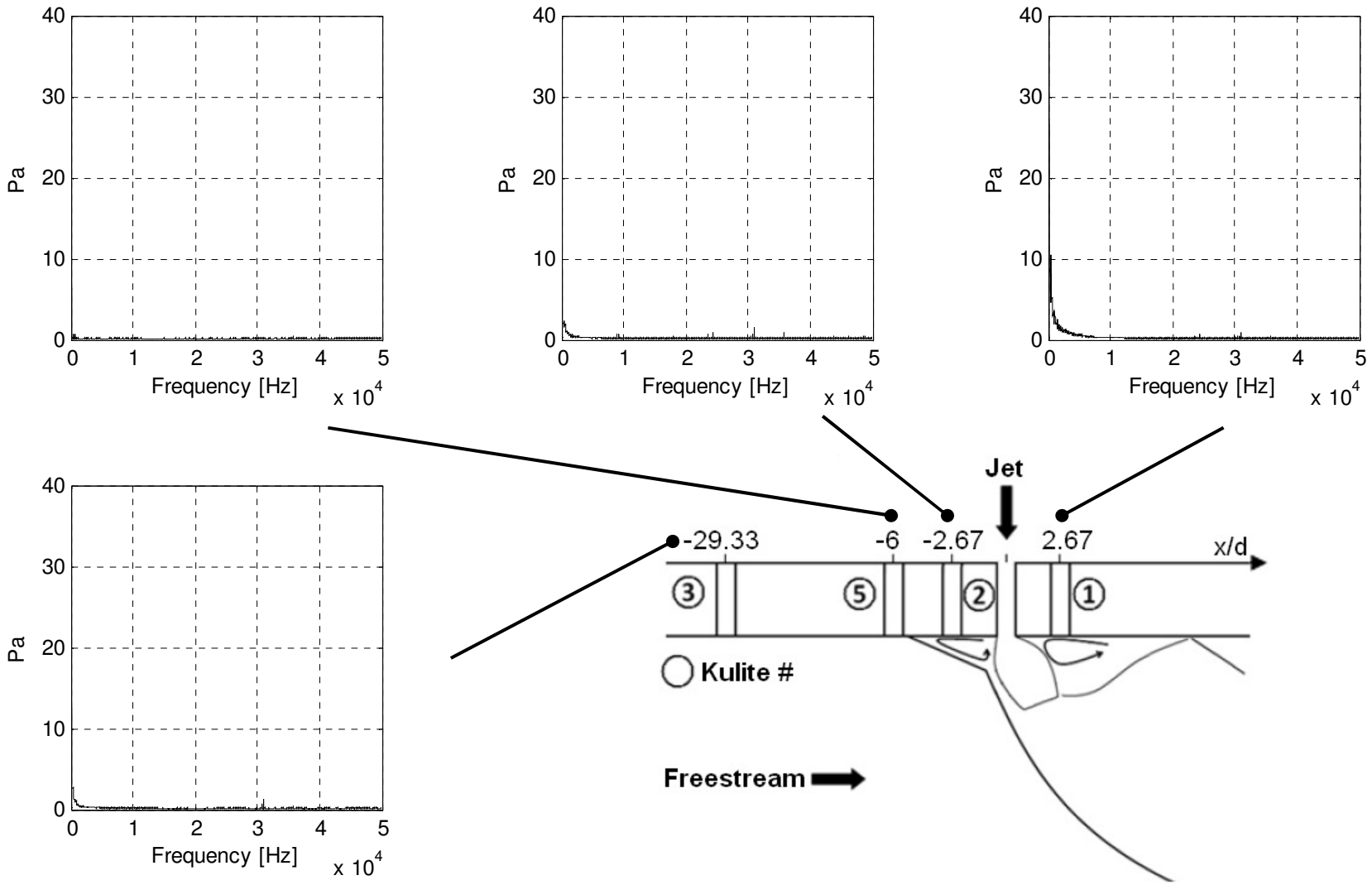


Figure 154 Pressure signal transformed into the frequency domain using a FFT, M=2.4, PR=50, δ=8.63.

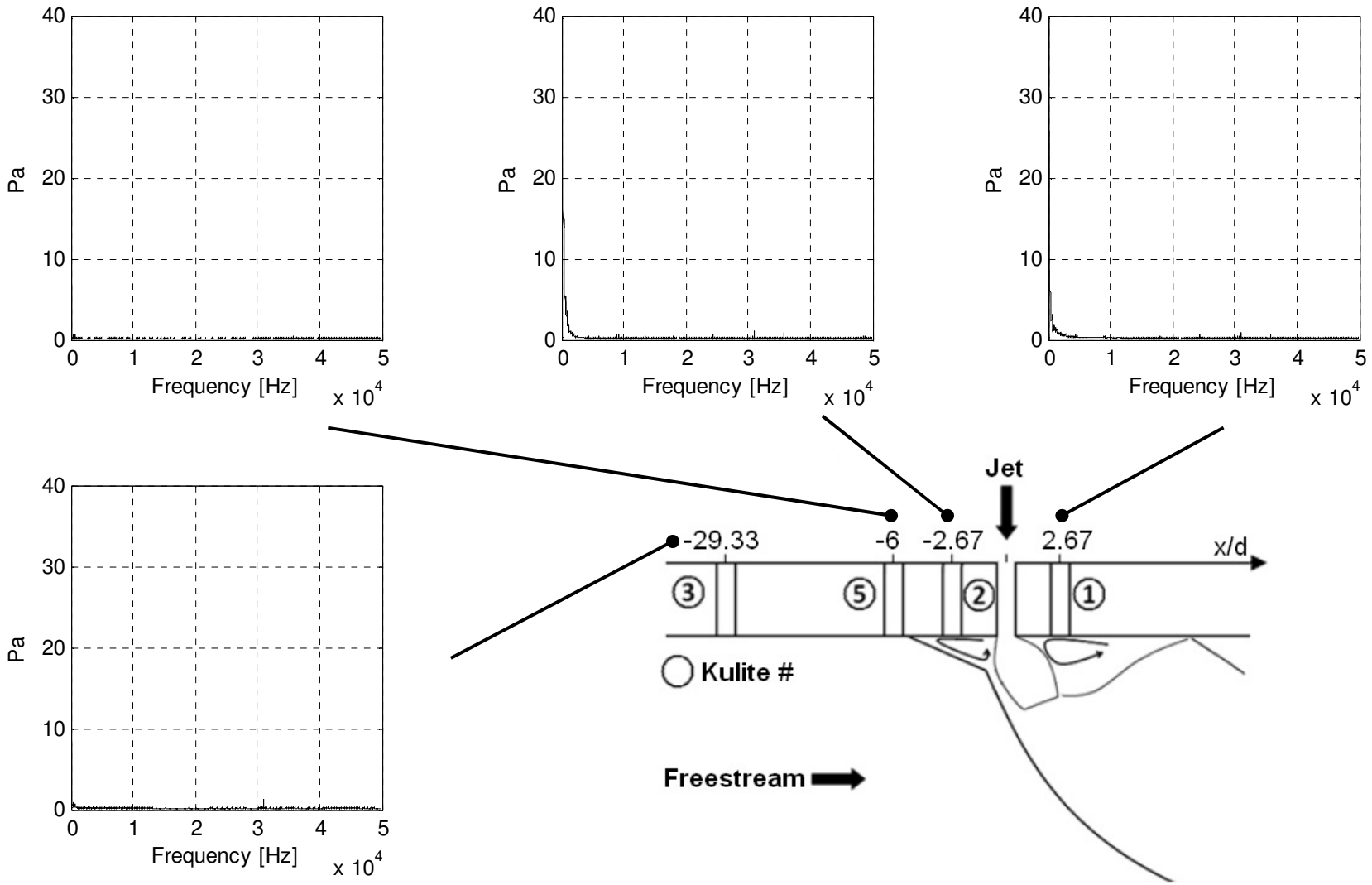


Figure 155 Pressure signal transformed into the frequency domain using a FFT, M=3.1, PR=200, δ=7.95.

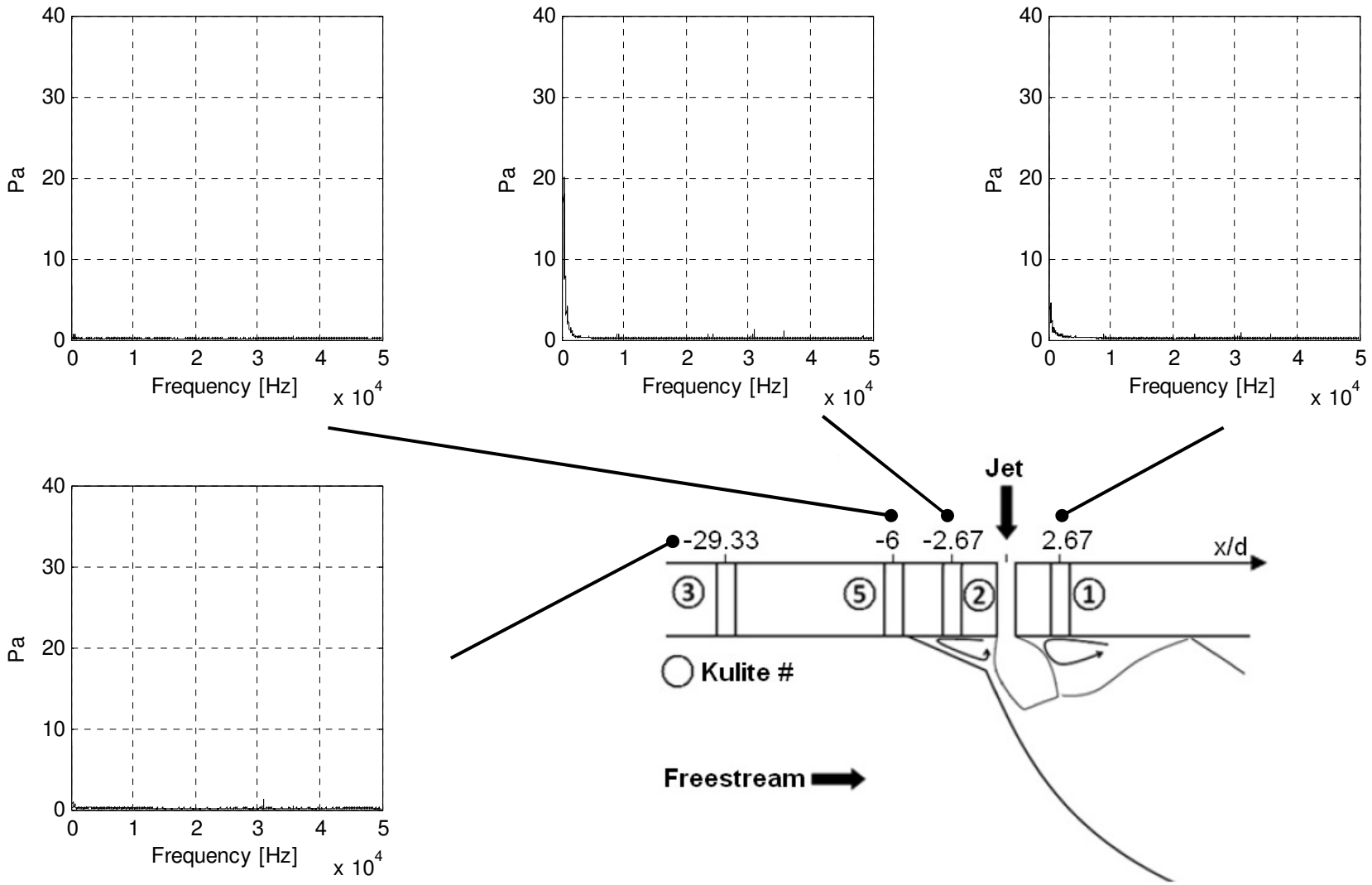


Figure 156 Pressure signal transformed into the frequency domain using a FFT, M=3.1, PR=150, δ=7.95.

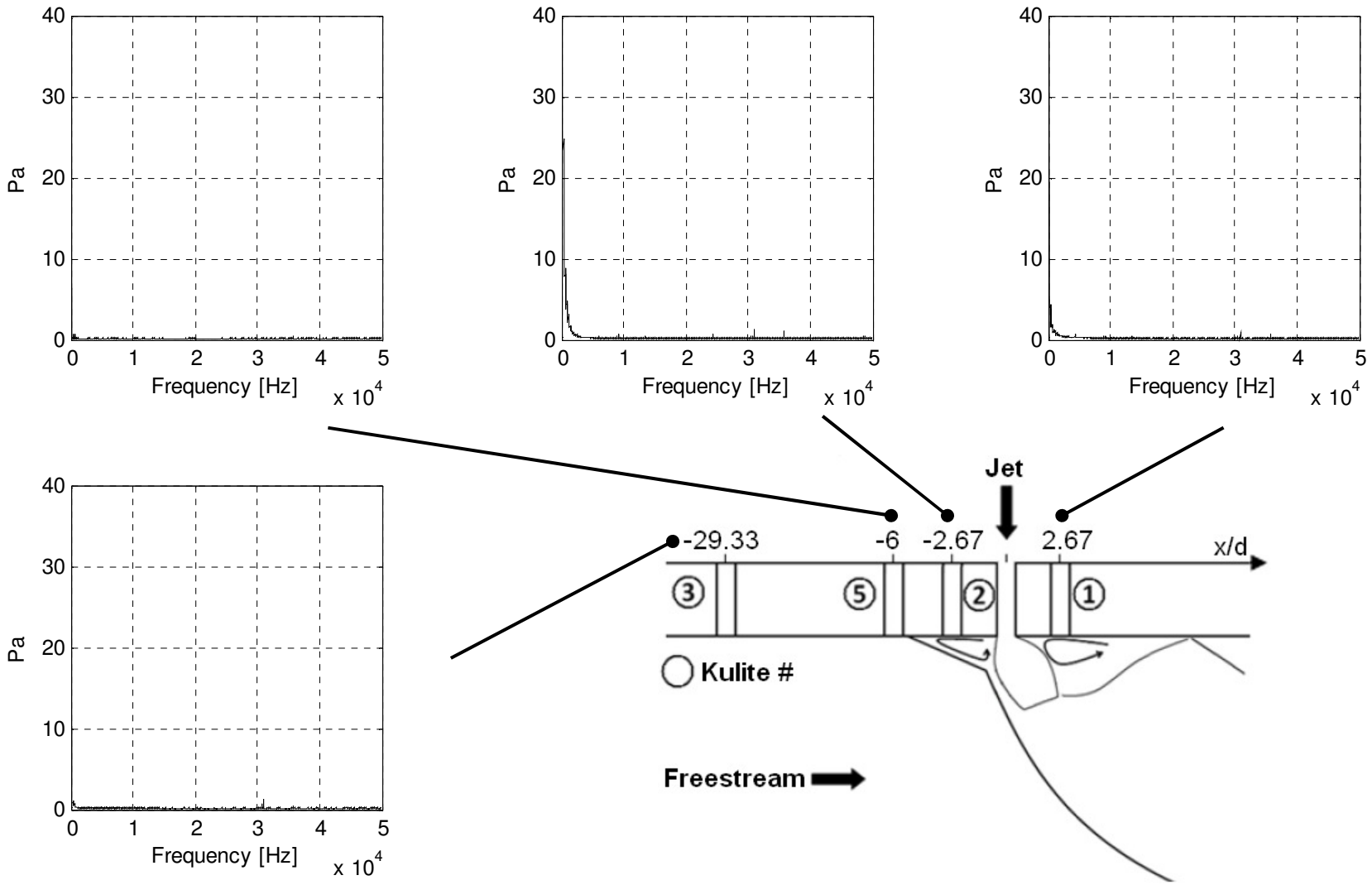


Figure 157 Pressure signal transformed into the frequency domain using a FFT, M=3.1, MPR=110, δ=7.95.

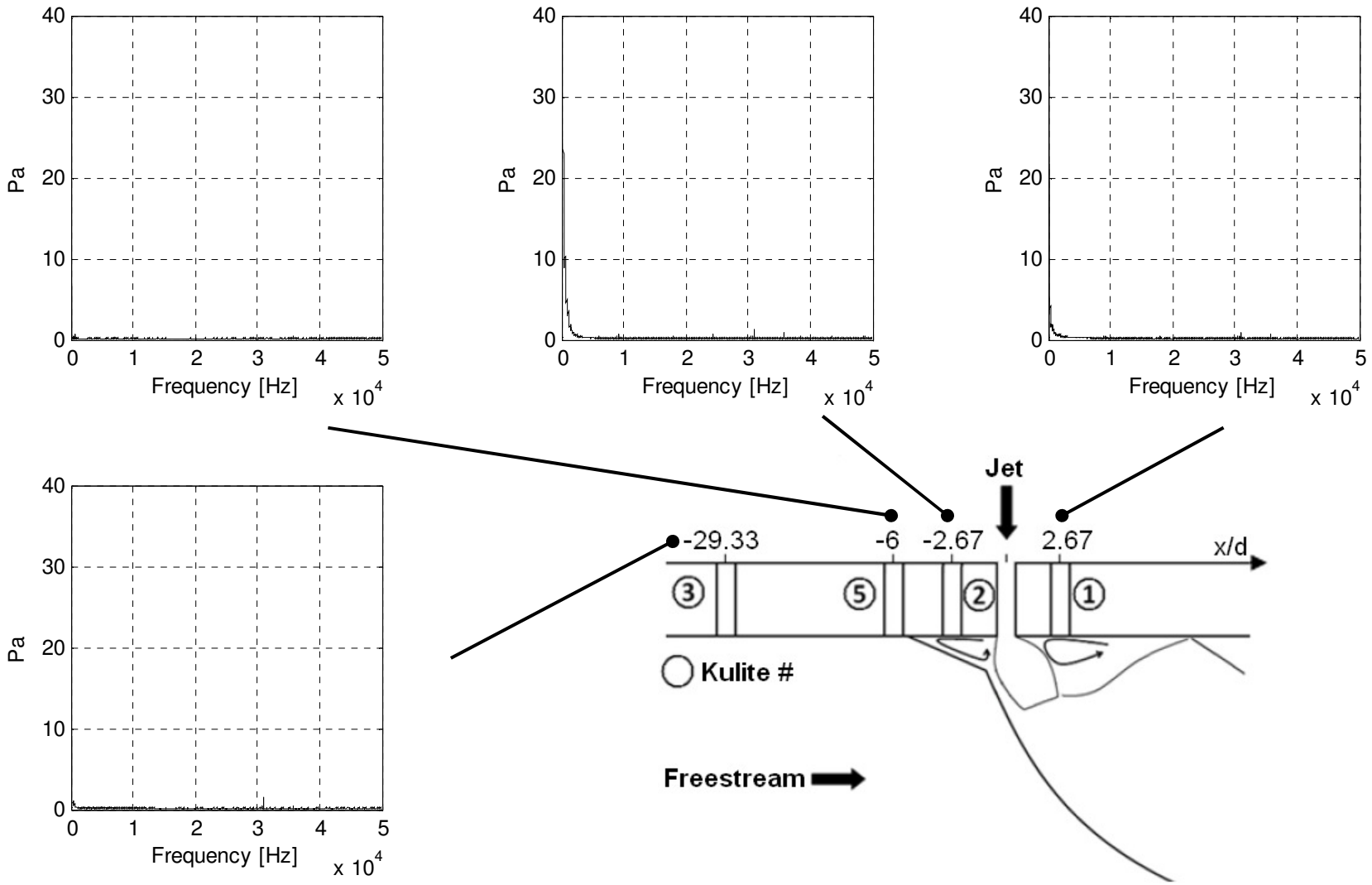


Figure 158 Pressure signal transformed into the frequency domain using a FFT, M=3.1, PR=97, δ=7.95.

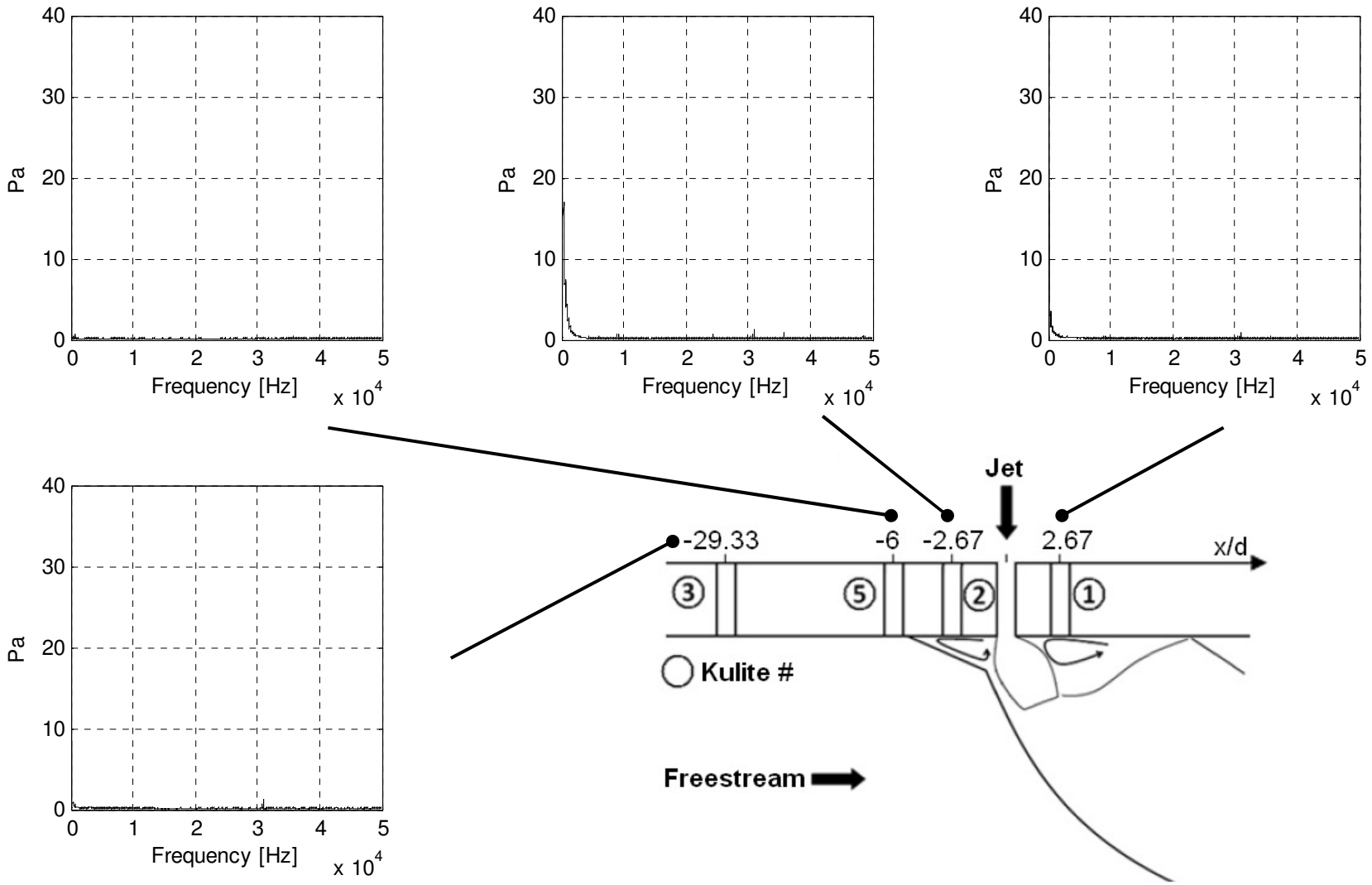


Figure 159 Pressure signal transformed into the frequency domain using a FFT, M=3.1, PR=70, δ=7.95.

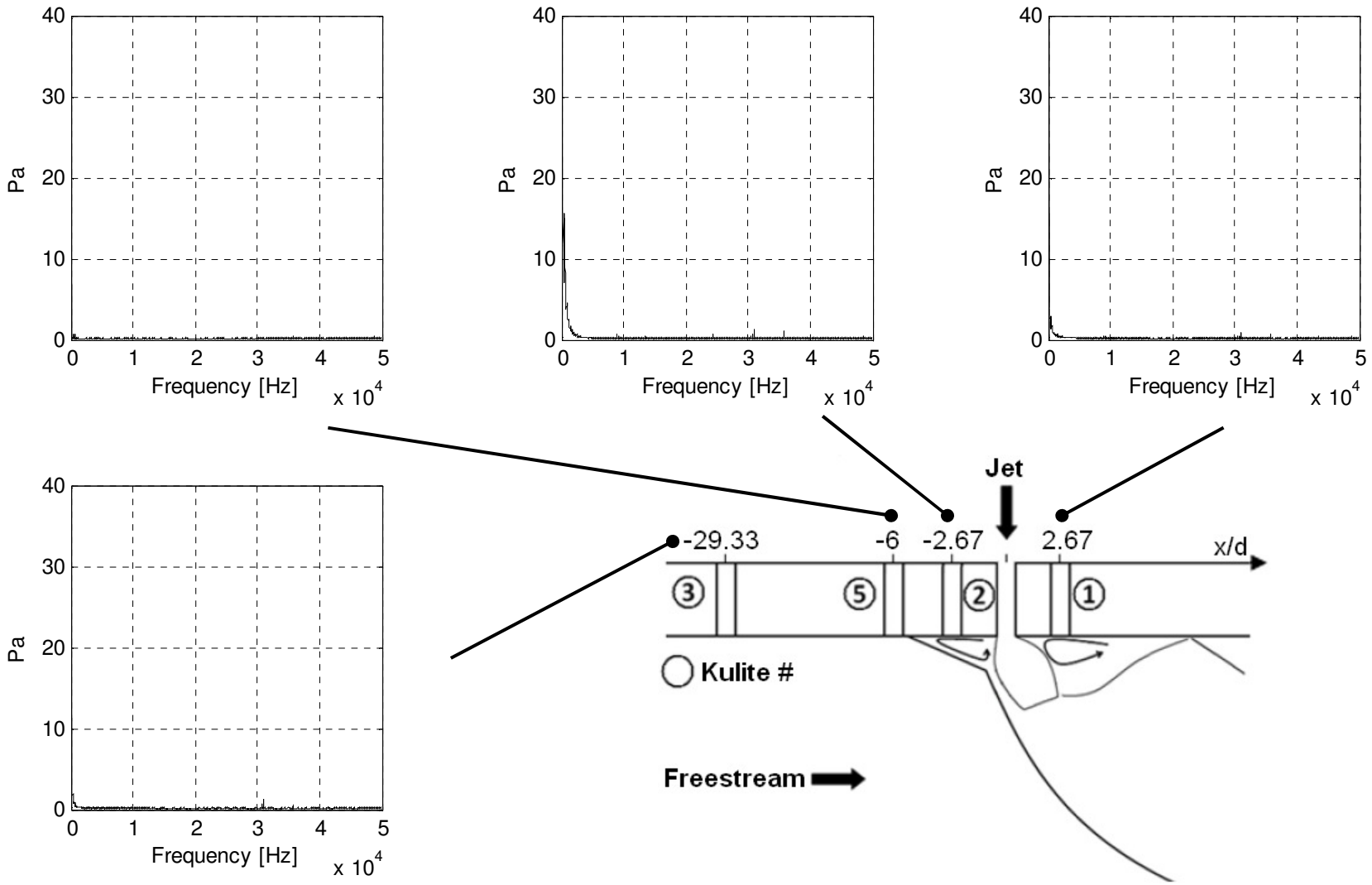


Figure 160 Pressure signal transformed into the frequency domain using a FFT, M=3.1, PR=55, δ=7.95.

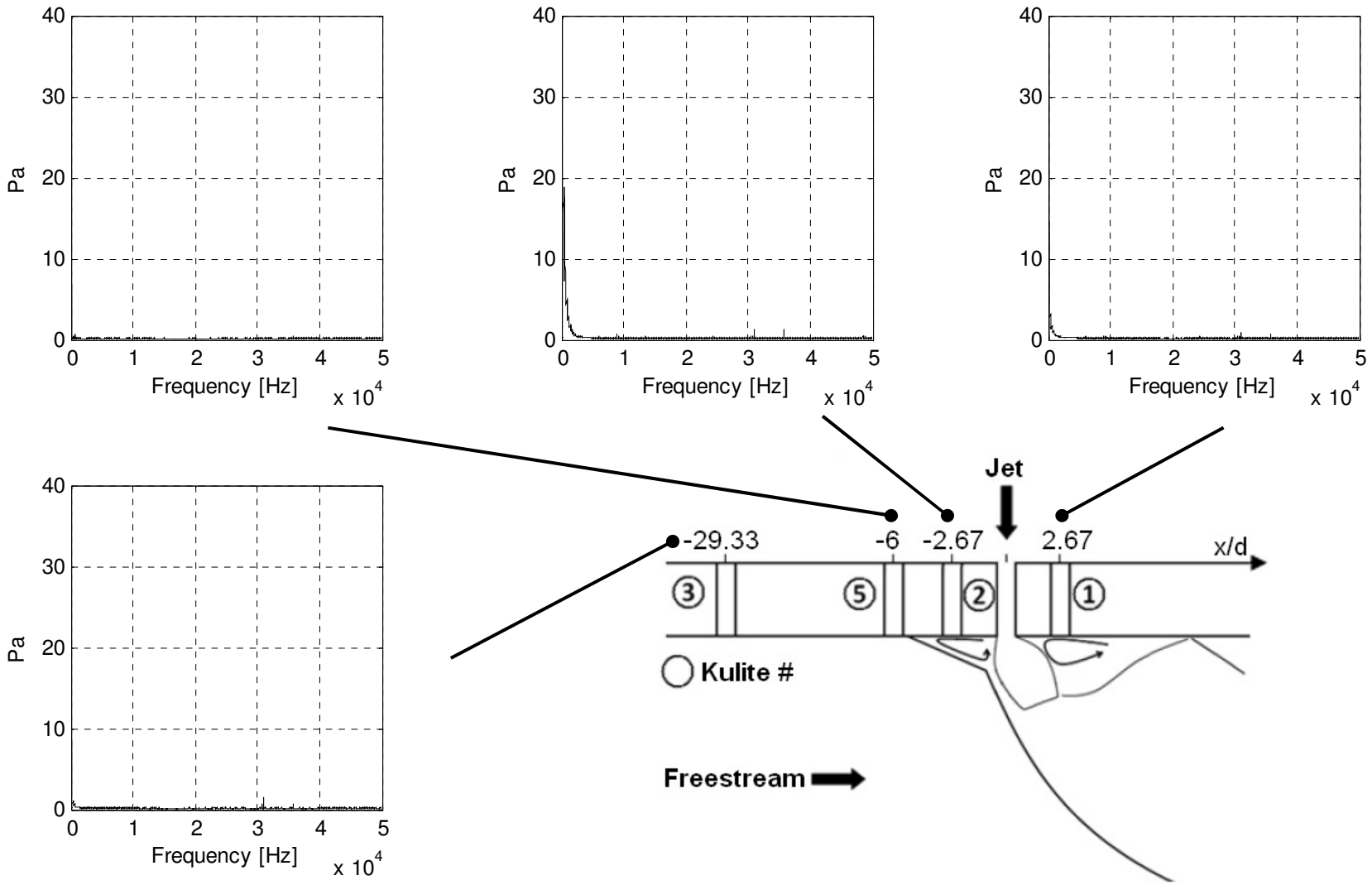


Figure 161 Pressure signal transformed into the frequency domain using a FFT, M=3.1, PR=50, δ=7.95.